nature

20 February 1997 Volume 385 Issue no 6618

Science and technology deserve better from Brussels

Delayed proposals for Europe's fifth Framework programme reflect political infighting. Research is likely to suffer as a result of poor leadership within the European Commission.

Anyone with even superficial knowledge of the history of the European Union (EU) knows that eighteen months can be a very short time in Europolitics. Yet that is all the time that remains before the European Commission needs to issue calls for proposals for the EU's fifth Framework programme (FP5) for research and development.

The commission has cut things too fine. Its new working paper on FP5 (see page 665) shows what disappointingly little it has achieved in filling in the details of the programme's proposed content since the commission's preliminary discussion paper was published last July. Given the rocky road to political approval that the commission has yet to travel, the chances of sticking to the planned timetable are remote.

Researchers should worry not just about a lack of new Eurofunds before FP5 starts, but also about whether support will be smooth once the programme is under way. Ironically, given the commission's need and professed intention to introduce greater flexibility and internal coordination, the new management structure proposed in the working paper is of such bewildering complexity that it threatens to paralyse progress.

Such worries would not be justified if the research community could rely on a ready acceptance of the formal FP5 proposal, complete with budget, that the commission is due to publish at the end of March. That would require ministers and members of the European Parliament to put aside their differences, and innumerable stakeholders, consulted at many stages of implementation, to withhold dissent. That appears unrealistic.

What has gone wrong? In its July paper, the commission, reflecting the wishes of all member states, as well as all other interested parties critical of the fourth Framework's scatter-gun approach, stated its intentions to concentrate money on fewer areas, to make its programmes more responsive to society's needs, to make management faster and more efficient and to make its operations more transparent. Given the commendable quantities of public consultations, transparency is undoubtedly being satisfied.

But the number and themes of programmes are effectively the same as in the current Framework. The familiar emphases on support for energy, transport, telecommunications, information and life-science industrial sectors are still there, albeit moving ever closer to the market-place. The enhanced attention to be given to the needs of small and medium-size companies is indeed essential, and there is thankfully no diminution of enthusiasm for the promotion of mobility and training of young scientists. But there is little sign of the concentration of effort that so many are calling for — an indicator, therefore, of battles to come.

There has been significant repackaging. This includes the new Eurojargon "key actions" which means, to quote a senior commission official, "internal coordination and external consultation around themes intended to be highly visible in the socioeconomic forum, which give rise to, and launch, large targeted programmes". Who wants to stiffen their sinews for that?

But the problems go deeper than the deployment of eye-glazing Eurospeak. The proposed FP5 structure is a matrix of three thematic programmes, broken down into the key actions, which are partly fed by three 'horizontal' programmes concerned with policy issues, such as training and international cooperation. The horizontal programmes also have their own independent budgets. Each of the six programmes will have to consult and coordinate with an endless list of other interests: national research programmes, European laboratories and other relevant EU activities such as social and economic assistance programmes, to name but a few.

But, at the end of the day, who is in charge of what? Who will decide when debate must end, and work begin? Who will sign the cheque and post it to the scientist? Commission officials have not been able to answer these simple questions. There is a lack of clarity that has already led to scandalous delays as turf battles have been fought between the research commission, which has prime responsibility for writing the proposal, and other commissions, such as agriculture, environment and transport, which wanted more control in defining research activities in their territories. Every battle has precipitated a new draft of the working paper. Draft thirteen is what has now been published, although the commission, not wishing to tempt fate, labels it "version 12-beta".

The EU co-decision process will then begin. Parliament (by a majority vote) and the Council of Ministers (unanimously) will both have to agree to content and cost. If achieved amicably, this could happen by the autumn. But it won't. Parliament will want more money to be spent than will ministers, and both will disagree with details of the proposed content, which, ironically, will probably lead to more actions being insisted upon, despite the fact that everyone wants 'concentration'. A conciliation process will prove necessary, adding up to six months to the process.

Once the general package has been approved, each action will have to survive further political scrutiny. That will be simpler, in that a unanimous vote within the Council of Ministers is not required, while parliament is required only to offer its opinion. However, as happened with the current Framework, the opinion of a quarrelsome parliament could be withheld for months. Pessimists would conclude that two-and-a-half years will pass between the commission's formal proposal and final approval, which would mean a delay of one year from the end of the fourth Framework.

Where should the blame be placed for this sorry state of affairs? The research commission's director general, Jorma Routti, is too rarely seen in Brussels, and appears to have been marginalized. But the buck stops with the research commissioner. To judge by performance and the standards set by her predecessors, Edith Cresson has shown a shameful lack of interest in science, too often failing to show up for important meetings and making no secret of her (time-consuming) ambition to return as soon as possible to French politics. Europe's researchers deserve better. □

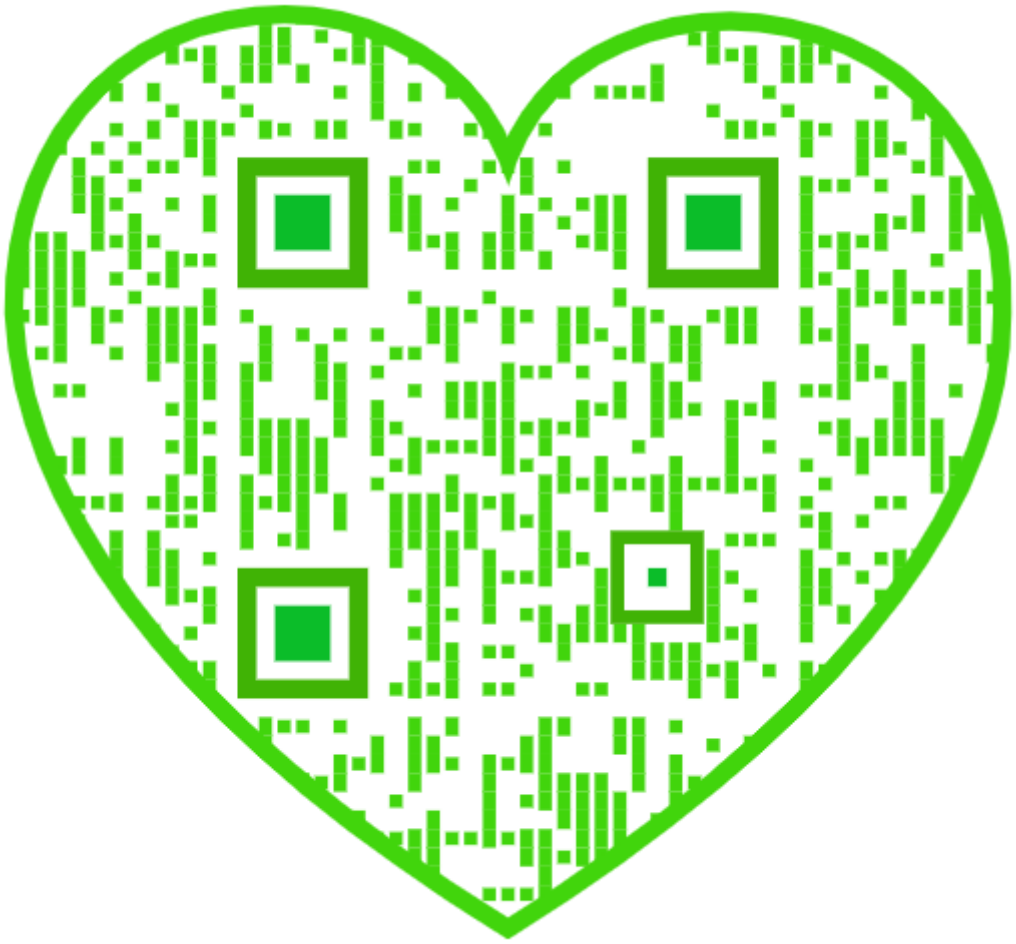

Japan's successful launch paves way for interplanetary missions

[TOKYO] The world's first space-based radiotelescope was launched last week by Japan's Institute of Space and Astronautical Science (ISAS). The event not only marked the start of a major international project in Very Long Baseline Interferometry (VLBI), but was also the first launch for ISAS using a more powerful launcher, the M-V rocket, which will open up opportunities for lunar and interplanetary missions.

The radiotelescope satellite was named the Highly Advanced Laboratory for Communications and Astronomy (HALCA) after launch. But it is more popularly known by the acronym VSOP, which stands for VLBI Space Observatory, Programme, and is also a grading of French brandy, a favourite drink of Masaki Morimoto of Japan's Nobeyama Radio Observatory who played a key role in dreaming up the project.

The satellite occupies a highly eccentric orbit ranging between a few hundred and 21,000 km in height. After a series of perigee-raising manoeuvres to bring it to higher altitude, the next critical step will be the opening of the telescope's eight-metre antenna.

If that is successful, the telescope will, operating in conjunction with ground-based telescopes, provide the longest baselines ever for VLBI of up to 30,000 km — three times those achievable on Earth. This will, for example, allow detailed imaging of the centre of active galaxies, as well as studies of spot sizes in maser sources (see *Nature* **381**, 463; 1996).

Furthermore, by linking up with the Australia Telescope in the Southern Hemisphere, the project offers the first all-sky mapping instrument for radioastronomy. Eventually, more than 25 ground-based radiotelescopes will join the project.

The M-V solid fuel rocket used to launch the satellite is considerably more powerful than its predecessor, the M-3SII. The launch marks the end of a bizarre era in which ISAS rockets were limited by government decree to a tail diameter of 1.41 metres, in order to prevent competition with the bigger National Space Development Agency. The rocket can launch large satellites of up to 1,800 kg into low Earth orbit and carry small payloads to the Moon and nearby planets.

The M-V's next mission, due for launch this summer, is Lunar-A, a spacecraft that will drop three penetrators from lunar orbit on to widely spaced locations on the Moon's surface. The penetrators, which have been designed to withstand impact at close to the speed of sound, will carry tiny seismometers, for measuring 'moonquakes', and heat flow probes. The data collected will be relayed to Earth via the orbiting spacecraft (see *Nature* **344**, 693: 1990).

Next year, ISAS is scheduled to send a probe to orbit Mars. The Planet-B mission will stretch the capabilities of the M-V rocket to its limits, and will require extremely lightweight onboard equipment to keep the spacecraft's weight down to 186 kg (excluding fuel) so that it can reach Mars with the limited thrust provided by the M-V rocket.

ISAS

Bright prospects? The launch of the M-V rocket ends a period of restriction on tail size.

Its main mission is to observe the upper martian atmosphere and its interaction with the solar wind. But it will also carry a camera and a dust counter (see *Nature* **353**, 8; 1991).

The most ambitious project of all, however, is the MUSES-C mission, scheduled for launch in January 2002. This will visit the asteroid Nereus, during its passage close to Earth, to collect a sample of the asteroid surface and return it to Earth in 2006. The spacecraft will use a novel 'ion thruster' in which xenon ions are accelerated by high-voltage electrodes to generate a small thrust.

On approaching the asteroid, which is only about 1 km in diameter and of unknown shape, the spacecraft will use instrumentation that includes an optical navigation camera, light detection and ranging, laser range finders and fan-beam sensors to select a suitable spot to touch down and grab a sample.

On return to Earth, a re-entry capsule will plunge straight into the Earth's atmosphere directly from the interplanetary return trajectory at a velocity of more than 12 km per second. The capsule will be subject to a heat transfer rate 30 times higher than that of the US Space Shuttle, and providing it survives, will then deploy a parachute for a soft landing. **David Swinbanks**

Insurers agree moratorium on gene data

[LONDON] **British insurance companies have provisionally agreed that, for an initial period of two years, they will not use genetic information about individuals in issuing life insurance policies linked to house mortgages for less than £100,000.**

But the companies are insisting on the right to access to the results of such tests if they have been carried out. And they will also be free to use genetic information in calculating policies covering mortgages whose value is greater than £100,000, and for other forms of life cover.

The guidelines, which were released this week, have been drawn up by a panel of the Association of British Insurers (ABI) in response to growing public concern at potential discrimination against those revealed to have a genetic susceptibility to a particular disease.

The guidelines are intended to act as minimum rules of behaviour for all insurance companies belonging to the ABI. Individual companies will be free to adopt more restrictive policies — such as refusing to use any genetic information in assessing life insurance risks — if they choose to do so.

The proposal inevitably represents a compromise. Insurance companies continue to insist that, if they do not retain the rights to raise insurance rates for those likely to develop a fatal disease, the result will be unfairly increased premiums for all policyholders. But many are aware of the bad publicity generated by their handling of the HIV issue. A question on application forms about whether an applicant had taken an HIV test has since been dropped.

"Insurance companies must continue to see the results of genetic tests so they can monitor developments and gauge any financial impact on their company," says Tony Baker, deputy director general of the ABI. "However, the industry will not ask anyone to take a genetic test when applying for life insurance." □

Europe reshuffles its scientific committees following BSE crisis

[PARIS] The European Commission has, as anticipated, announced a radical reform of its system of scientific advisory committees, removing them from commission departments whose interests could conflict with considerations of public health and consumer protection.

Jacques Santer, the president of the commission, was scheduled to outline the reforms in detail this week before the European Parliament. The measures are partly a response to criticisms by the press and parliament of the commission's handling of bovine spongiform encephalopathy (BSE).

The plenary session of the parliament was itself scheduled to consider the final report of its committee of inquiry into BSE. The parliament is expected to reject a proposal by a small number of its members to pass a motion of censure of the commission.

Under the planned reforms, the commission's scientific committees will be regrouped within a new 'department for scientific advice on health', located within the directorate for consumer policy (DG24), which itself will be renamed "consumer policy and protection of consumer health". The directorate will also be given responsibility for the commission's phytosanitary, veterinary and food inspection services, which were previously attached to the agriculture directorate.

The consumer directorate, which is overseen by commissioner Emma Bonino, will also be equipped with a new unit for the evaluation of public health risks. Completing these arrangements will be a high-level group made up of commissioners involved in human food safety, to be chaired by Santer himself.

The shake-up of the system of scientific advisory committees is designed to promote greater clarity and openness. The various scientific committees are at present attached to different directorates and operate in a haphazard fashion, with few clear rules governing such matters as how members and chairs of advisory committees are appointed. Also, it has often been almost impossible to find out who sits on committees, let alone obtain the minutes of their meetings.

To remedy this, all advisory committees will be brought under a steering committee which will be responsible for fixing standardized rules as to how committees should be established and operate. The steering committee will itself be built around the multidisciplinary scientific committee set up by the commission last July (see *Nature* 381, 724; 1996).

"This will be a totally different approach to scientific advice from what we have had in the past," says one commission official. "Now there will be a supercommittee watching the work of the others." Issues surrounding genetically modified organisms, for example, would now first be discussed by the steering committee. It would then decide on how work should be distributed among the various committees and what subgroups, if any, need to be specially created.

The commission and the steering committee will meet tomorrow (21 February) to work out details of how committees should operate. Under preliminary proposals, details of committee members and the minutes of their meetings would be made publicly available, possibly on the Internet.

Declan Butler

Chemists urge US to ratify weapons pact

[WASHINGTON] More than 140 chemists and biochemists belonging to the US National Academy of Sciences have added their voices to those urging the US Senate to move quickly to ratify the international Chemical Weapons Convention (CWC).

The treaty, which takes effect on 29 April, prohibits the development and use of chemical weapons and calls for signatories to destroy existing stockpiles.

Although more than 65 nations have already ratified the treaty — enough to bring the convention into force — neither the United States nor Russia is among them. And conservatives in Congress, led by Jesse Helms (Republican, North Carolina), who chairs the Senate Foreign Relations Committee, are threatening to hold up a vote to get their way on other foreign policy issues.

The petition by academy members, which was organized by Dudley Herschbach and Matthew Meselson of Harvard University, was due to be handed to the Senate majority leader, Trent Lott (Republican, Mississippi), this week. It asks him to work "as a matter of national urgency" to bring the convention to a vote before 29 April.

"If the Senate fails even to vote on the CWC ... the United States will have surrendered by default its essential leadership in combating the proliferation of chemical weapons," write the scientists.

Both the American Chemical Society and the American Physical Society have already written to the Senate in support of the CWC, and the Federation of American Scientists is organising a petition by Nobel prizewinners to urge ratification.

Only countries that have ratified the treaty by 29 April will be considered original signatories with full representation on the convention's governing council. Without a seat on the council, the United States would have no say in such matters as what threshold amounts of chemicals would be covered under the convention, according to Michael Walls of the Chemical Manufacturers Association (CMA), whose organization strongly supports ratification. The United States is also expected to contribute 25 per cent of the council's operating funds.

Although the treaty has wide bipartisan support, Lott will have to appease the conservative isolationist wing of his party, whose principal spokesman is Helms, to move the treaty out of the Foreign Relations Committee so it can come to a vote.

Two-thirds of the 100-member Senate need to approve ratification. The convention was on the verge of being approved last autumn before Bob Dole, the Republican presidential candidate, spoke out against it, forcing the Clinton administration to cancel what it regarded as a risky vote. Lott has appointed a group of ten senators, including himself and Helms, to work out a compromise with the White House.

Treaty supporters point out that the convention will take effect with or without the United States, and that the United States is already committed to destroying essentially all of its chemical weapons stockpile by 2005, at a projected cost of $12.4 billion. The cleanup is likely to be more expensive and to take longer than originally planned, according to a recent report by the congressional General Accounting Office (GAO).

Despite claims by opponents that the CWC would harm US chemical manufacturers, it is supported by virtually every affected industry and scientific group.

Manufacturers suspected of producing chemicals for weapons would be subject to inspection by international teams, but US industry groups are satisfied that confidential business information would be protected and that regular reporting requirements will not be onerous, according to Walls.

The consequences of non-ratification for US chemical manufacturers could be much worse, say supporters of the treaty. Beginning three years after the CWC takes effect, signatory nations would be prohibited from buying high-risk 'dual-use' chemicals (those with legitimate uses as well as being used for weapons) from non-signatories. These so-called 'Schedule 2' chemicals represent about $500–$600 million a year in business for US companies.

Tony Reichhardt

EU research plan fails to charm critics

[MUNICH] Draft proposals for the European Union (EU)'s next five-year research programme, published in Brussels last week, suggest that hopes for a greater concentration of EU research funds on fewer research topics may not materialize.

Furthermore, the proposals in the second working document on the EU's fifth Framework research programme (FP5), covering 1999 to 2003, reveal a complex management structure that many fear may be unworkable.

But EU officials defend the proposals as linking FP5 directly to the economic and social goals of member states. Furthermore, the proposals suggest that basic research could form up to 10 per cent of the overall budget, likely to be just over ECU13 billion ($15 billion). This is significantly more than in previous research programmes.

The proposals were adopted by the full commission last week after several weeks' delay. They confirm the commission's intention to divide research into six programmes, as envisaged in the first working paper published last July (see *Nature* **382**, 194; 1996), rather than the nineteen included in the current framework programme, FP4.

Themes within themes

But the six programmes are very broad, and are broken down into at least as many categories as in FP4. These would be linked by a complex management system involving considerable coordination and consultation.

Three of the main programmes are described as 'thematic', focusing on life sciences and the ecosystem, the 'user-friendly information society', and competitive and sustainable growth. Each thematic programme is in turn broken down into 16 'key actions', corresponding to specific social or economic priorities for the EU.

According to Jack Metthey, a member of the cabinet of the research commissioner, Edith Cresson, with responsibility for research policy, the commission sees the key actions as extending the task force idea launched two years ago to coordinate all EU research activities on a specific theme.

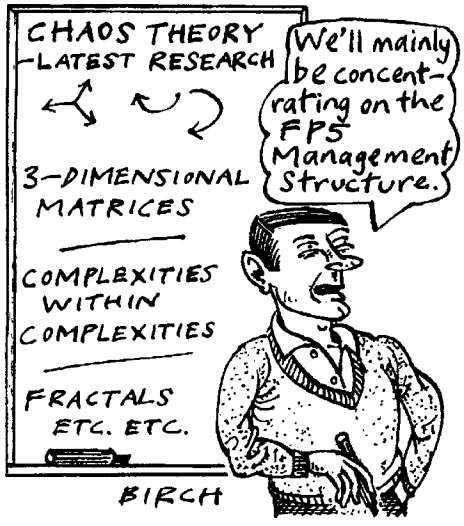

Each thematic programme also includes support for developing relevant generic technologies and basic research, as well as for large-scale infrastructures.

Three 'horizontal programmes' would have their own budgets but also feed into the thematic programmes, using a matrix management system. They cover international cooperation, innovation and the participation of small- and medium-sized enterprises, and improving human potential. Three other programmes will be carried out by the EU's Joint Research Centres and under the Euratom programme.

Cresson: 'simple, effective system'.

Observers in Brussels are concerned about the broad content of the proposals, and sceptical about how the proposed management system would work in practice.

In response, Metthey says that the breadth of the research activities will be reduced when a formal proposal is submitted to the European Council of Ministers — which represents the member states of the EU — and the European Parliament at the end of next month.

"This is a reflection document, not a formal commission proposal," he says, adding that the commission will respond to the reactions of industry interest groups and representatives of the basic research community, as well as to the recommendations of a five-year independent assessment of EU research activities, due out this week.

More management, more flexibility?

Metthey insists the proposal for FP5 "will definitely not grow beyond the six programmes, and it is our firm intention to reduce the number of key actions in our formal proposal". But achieving this may not be easy. Although all member states agree that the number of actions must be reduced, most are likely to defend those in which they have strong interests — and the programme needs the unanimous support of the Council of Ministers.

Metthey also denies that the planned management system is excessively complex, emphasizing its flexibility. Only three-fifths of each programme's budget will initially be fixed, enabling the commission to react quickly to new developments or emergencies, such as the scare over bovine spongiform encephalopathy (BSE).

Indeed, he suggests, the decision-making process will be much simpler and quicker, as the number of programme committees — made up of senior officials from member states — will be reduced in line with the number of programmes. Further, the adoption and implementation of FP5 requires twelve decisions, half the number for FP4.

And the emphasis on coordination between FP5 and other EU initiatives, as well as national research programmes and research programmes of non-EU European laboratories such as CERN, the European Particle Physics Laboratory and EMBL, the European Molecular Biology Laboratory, can only increase efficiency, he adds. The budget of the Training and Mobility of Researchers Programme, which includes a high proportion of basic research projects and networks, is expected to be doubled.

Larger funds for basic research

The document does not detail the amount of money the commission is likely to propose for FP5. But this is expected to be just slightly higher than the ECU13 billion spent on FP4. The basic research component, which, Metthey says, "is being regarded very sympathetically", could be about 10 per cent.

Richard Brook, head of the UK Engineering and Physical Sciences Research Council, says that, until the figures are added, "it is hard to see how the commission will translate its aspirations [for the concentration of programmes] into reality". It needs to clarify what it intends to leave out and how much money it would give to each action, he says.

He sees the proposed structure of FP5 with its six programmes as "reclassifying the family tree" without significantly changing the contents. And he fears that the flexibility theoretically allowed by the proposed matrix-style management system could be offset by the frictions likely to be generated by continuous debate.

Jan Borgmann, head of the EU's advisory body, the European Science and Technology Assembly, shares this concern. "The commission will have to do considerably more homework to explain how it thinks it could work in practice," he says.

Pierre Papon, director of the Observatoire des Sciences et Technologies in Paris, views the proposed broad spectrum of themes as unrealistic. "You can find almost everything" in the three thematic programmes, he says. But he approves the individual proposed key actions. Although there are too many, he says, they introduce some new ideas in line with EU general policy.

And Edith Cresson remains optimistic about the proposed system. She said in a speech last week that the management structure "will help to make the framework programme a simple and effective instrument capable of reacting rapidly to situations and needs".

Alison Abbott

EMBO panel gives biology in Finland a pat on the back . . .

[HELSINKI] Molecular biology and biotechnology research in Finland has been given a glowing report in a study by the European Molecular Biology Organization (EMBO), which attributes much of this success to the creation of a multidisciplinary centres-of-excellence programme.

Although the study, organized by the Finnish Medical Research Council and completed last month, points out that the fruits of the biotechnology effort have not yet been translated into industrial products, it says investments have so far been used wisely and that this should eventually pay off.

But the report also argues that, in order to perform optimally in future, Finland needs to develop expertise in bioinformatics and structural biology. It argues that the country needs a transgenic-mouse facility to allow its immunologists to achieve cutting-edge science. It also criticizes structural failures in Finland's training and research policies; most problematic, it says, is the low percentage of total research funds allocated competitively.

The main goal of the study was to evaluate the effectiveness of a major effort to promote molecular biology and biotechnology which took place between 1988 and 1995, at a cost of about FM480 million ($104 million). The EMBO review, which was coordinated by Lennart Phillipson, former head of the Heidelberg-based European Molecular Biology Laboratory, included an assessment of the work of 1,400 academic researchers in 175 different groups.

Down to the woods: natural resources have underpinned biotechnology research in Finland.

While praising the country's scientific achievements, the report points out that Finnish scientists are subject to too many evaluations — every year or so on average — from different bodies. "This is pointless and a distraction to scientists who must respond to such reviews instead of devoting most of their time to their research efforts," it says. The situation is exacerbated by a quirk in the law which means an academy can provide grants only for one year.

It also says there are too many graduate students and too few postdoctoral positions, and training is too long. The average age of PhD completion is between 30 and 35, when scientists are no longer eligible for many postdoctoral fellowships and are often less mobile because they have started families.

Olli-Pekka Heinonen, the minister of education, science and culture, says the government is aware of the shortcomings in the Finnish research structure highlighted by the EMBO report, and is attempting to correct them. "We may have been a little overenthusiastic about evaluating everything," he admits, adding that some relief may be in sight, as the law on research grants has now been changed to allow an academy to give longer-term awards, up to three years.

Heinonen also says that the government intends the new research funds to be allocated as far as possible through competition, and that it is studying ways of lowering the age of PhD completion.

Finnish scientists say they are pleased with the conclusion of the EMBO evaluation, which they hope will encourage the government to continue to provide generous funding for biotechnology.

"No-one knows exactly what the evaluation will develop into," says Mart Saarma, director of the University of Helsinki's Institute of Biotechnology, a centre of excellence that undergoes evaluations at least once a year. "But it will certainly be taken seriously, not least because it was conducted by an international panel selected independently by EMBO." Saarma says that small countries like Finland are particularly sensitive to the opinion of the outside world.

Alison Abbott

. . . as privatization windfall fills research coffers

[HELSINKI] Finland is to use the proceeds from the privatization of a series of state-owned companies related to the chemical, pulp and paper, and heavy metal industries to increase its research budget by 25 per cent over the next three years. The move will make it one of the biggest spenders on research in proportion to its size in the world.

Alongside a predicted continuation of the current trend towards more industrial financing of research, the extra money is expected to raise Finland's spending on research and development to 2.9 per cent of gross national product – at a time when the country's overall budget is being cut back.

According to the minister of education, science and culture, Olli-Pekka Heinonen, the windfall, worth a total of FM3 billion (US$650 million), will not remain a one-off injection of funds. He says the government is committed to maintaining the level of increase after 2000.

The decision substantially to increase spending on science is part of the Finnish government's efforts to strengthen the national economy and reduce unemployment through greater industrial innovation. As such, the money is already earmarked for pursuing strategic aims.

The cash is to be split 40:60 between science and technology. Half of the 40 per cent share allocated to science will go to the Academy of Sciences, Finland's main grant-giving body for basic science, to be distributed within four main priority areas.

Most of the academy's money will be used to extend and strengthen a special programme, launched in 1993, that provides generous support for multidisciplinary university research groups designated by the academy as 'centres of excellence'. Four of the current 17 centres of excellence conduct research in biotechnology and molecular biology.

The rest of the money will be used to develop the academy's new postdoctoral fellowship and graduate school programmes, and to promote the internationalization of Finnish science. The latter category includes promoting participation in the European Union's Framework research programmes, as well as collaborating with the neighbouring Baltic states and with Russia.

The other half of science's share of the windfall will go directly to Finland's 20 universities. This money will be used to upgrade equipment, increase the number of student places in strategic areas such as electronics, and expand graduate school programmes.

The cash injection continues a trend of rapid growth in Finnish research spending since the early 1980s. Apart from a few lean years during the general recession of the early 1990s, Finland has experienced the fastest growth in expenditure on research and development – both by the government and by industry – among members of the Organization for Economic Cooperation and Development.

At the same time as increasing research spending, the government will, through the Academy of Sciences, carry out an evaluation of all research activities in Finland, in order to establish how money should be distributed in future. This report on the state of Finnish research will be published later this year. **A.A.**

Chair of GMO panel resigns over maize

[PARIS] One of France's leading human geneticists has resigned as chairman of the committee that advises the French government on genetically modified organisms (GMOs), claiming that a recent decision by the French government to ban the cultivation of a transgenic maize has made his job impossible.

Axel Kahn, director of the INSERM Laboratory of Research on Genetics and Molecular Pathology at the Cochin Institute of Molecular Genetics in Paris, and chairman of the Biomolecular Engineering Commission, claims that the decision is inconsistent with an earlier decision by the government to seek permission for the import of the maize from the United States and the sale of the resulting crops.

Following a meeting of the French cabinet last week, Alain Juppé, the prime minister, announced that farmers would now be forbidden to grow the maize, which is produced in the United States by Ciba-Geigy, and was approved for import by the European Commission in December.

The modified maize contains a gene from the bacterium *Bacillus thuringiensis*, which makes it resistant to the European corn borer, a pest responsible for the loss of 5 to 10 per cent of the annual harvest. The maize also contains a herbicide-resistant gene, and a marker gene conferring resistance to the antibiotic ampicillin.

It was the French government that asked the European Commission (EC) in 1994 — after the Biomolecular Engineering Commission had approved the dossier — to approve marketing of the maize throughout the European Union. France continued to seek permission up to the time the commission finally approved import of the maize last December.

Furthermore the main benefits of the maize are to farmers, who will now be denied use of the seed. At the same time, the government earlier this month authorized consumption of the maize by animals and humans, apparently indicating that it feels that the environmental risks of the maize are greater than any risk to either human or animal health.

This conflicts with the outcome of two years of debate surrounding the approval of the maize within the European Union. Controversy centred not on environmental concerns but on the potential risks to humans of the maize's antibiotic-resistance gene which some — in particular the UK Advisory Committee on Novel Foods and Processes — argued might pass to bacteria in the gut of livestock and from there to humans (see *Nature* 383, 564, 1996).

Although transgenic plants in general raise environmental concerns, such as the risk of the transfer of herbicide-resistance genes to weeds, Ciba-Geigy's maize is widely considered to be free of such risks, as it does not cross with native European plants.

Juppé's decision appears to have been the result not of any new detailed study of the environmental risks of the maize but of a spontaneous response to a statement at the cabinet meeting by Corinne Lepage, the minister of environment, questioning the environmental safety of GMOs, and asking for a decision on the cultivation of the modified maize to be postponed.

The government goal is widely seen as an attempt to placate consumer and environmental organizations in the wake of the bovine spongiform encephalopathy (BSE) crisis. In a statement issued after the meeting, the environment ministry applauded the government's "concern to apply the precautionary principle [in the light of the environmental risks of GMOs]".

Kahn says that the decision has "left him with no choice but to resign". Although the Biomolecular Engineering Commission acts only as an advisory body, the government had asked it to represent France officially in defending the Ciba-Geigy application in Brussels.

The EC's approval of the maize was a "great success" for France, says Kahn, arguing that the government's new decision has destroyed both its own credibility and that of the Biomolecular Engineering Commission in international discussions. "If I were to go to a meeting in Brussels in future, people are going to ask 'will what Mr Kahn says be contradicted by his government tomorrow?'", he says. "I wouldn't have any credibility."

Kahn acknowledges that his resignation from the Biomolecular Engineering Commission, which he has chaired since its creation in 1986, has thrown France's well established system for approving GMOs into "crisis". It has authorized more than 450 field trials of transgenic plants, more than the total of all other European countries combined, and second only to the United States.

But he says that resigning was the "only honourable way" of forcing all those involved to clarify a "totally incoherent situation". The government has only two ways out, he asserts. Either it should concede that the "democratic debate" over GMOs in France now requires a complete review of the maize dossier, in which case imports should be banned, or it should revoke its ban on cultivation of the maize.

Kahn argues that the government's U-turn is also symptomatic of the disarray in scientific advisory systems that has been prompted by a series of scandals, including BSE and the contaminated blood and growth hormone affairs.

Being an expert is "extremely difficult" at present, says Kahn, arguing that the public's suspicion about the independence of experts has never been greater. The maize controversy may be an excellent opportunity to test in France the idea of whether lay consensus conferences can make progress in reconciling scientific advice, public opinion and political choices, he says.

Kahn, who has a high profile in public debates on scientific issues in France, says that he now intends to concentrate his public activities on the "combat" against what he claims is the most serious threat facing society — "scientific racism and genetic determinism based on an erroneous concept of genetics". An emerging convergence between genetic reductionism, ultraliberal economics and individualist ideologies raises an "enormous risk" that history is set to repeat itself, he warns. "It is very important to engage in this battle". **Declan Butler**

Three share Australian prize for telecoms

[SYDNEY] **The Australia Prize, worth A$300,000 (US$375,000) and awarded this year for research work in the field of telecommunications, has been shared by three researchers covering the range from theory to application.**

At the fundamental end of the spectrum, Allan Snyder (centre), a US researcher at the Australian National University in Canberra, was rewarded for his theory of guiding light, the blueprint for the development of optical fibres. Rodney Tucker (left), an electrical engineer at the University of Melbourne, was recognized for developing a tenfold expansion in the capacity of optical fibres.

Gottfried Ungerboeck (right), of IBM Laboratories, Zurich, Switzerland, received the award for trellis-coded modulation, the industry standard which made possible high-speed modems.

IMAGE UNAVAILABLE FOR COPYRIGHT REASONS

AUSPIC

In presenting the prize last week, John Howard, the prime minister, said his government was committed "very strongly to the central role of science and technology in the future of Australia". □

Sceptics and salmon challenge scientists

[SEATTLE] A sharp controversy has broken out around the scientific uncertainties involved in proposals to introduce a new, ecosystem-based approach to save dwindling salmon stocks found in the Columbia River basin, the main river system in the northwestern United States.

Plans to restore the stocks could include dynamiting four hydroelectric dams on the Snake River, the Columbia's largest tributary (see map), the annual meeting of the American Association for the Advancement of Science (AAAS) was told in Seattle last week.

But any such solution will face a mountain of opposition, not just from power and agricultural interests, but from a public that has grown deeply sceptical over the years as billions of dollars have been thrown at salmon conservation efforts in the river system, with little impact. The scepticism extends to the science behind it.

"Science has been part of our planning process for decades," says Ted Strong of the Columbia River Inter-tribal Fish Commission, a native American advocacy group. "It is attempting to take a lead role again, but it can't atone for the destruction it has already caused."

An annual salmon run of 16 million fish on the river system during the early part of this century has declined to around one million, according to the US National Marine Fisheries Service, with only ten per cent of these being spawned naturally. The rest are spawned in man-made hatcheries along the river system.

Dam destruction and genes

Overfishing of the stocks in the middle of the century is thought to have precipitated a decline which was compounded by the construction of extensive hydroelectric systems along the Columbia and Snake rivers. Hatcheries were supposed to compensate for the disruption caused by the dams. But some scientists think that they have actually contributed to the decline by weakening the gene pool of naturally born salmon.

Poor scientific understanding of the cause of the decline may undermine support for radical solutions, the AAAS meeting was told. According to John Etchart, a senior official with the Northwest Power Planning Council — a body set up by Washington, Oregon, Idaho and Montana to manage the river basin — the council is legally mandated to apply the best science.

But Etchart characterizes scientific knowledge of the issue as "unsettled and uncertain", adding that the fate of the proposal to breach the four dams on the Snake River "will turn on how certain we are of its benefits".

An independent scientific advisory group, chaired by Richard Williams, a population geneticist at the University of Idaho, has been established to advise the council. Last year, the group's brief was widened to advise the fisheries service, the main federal agency working on the issue, and the National Research Council in Washington helped to strengthen its membership and procedures.

The group's draft report, *Return to the river*, was recently published for public comment. It includes the dam-busting plan. Williams stresses that the report is not an action plan for the Columbia River basin, but rather a "conceptual foundation, based on established ecological principles", on which such a plan could be based.

The report argues that management of the Columbia system should aim to restore to the heavily managed river characteristics typical of a large, natural salmon river. In contrast with previous plans, which concentrated on local action to conserve specific species, it tackles the whole river, acknowledges its complexity as a system, and "recognizes the failures of the past", says Williams.

A plan to save the ecosystem, he says, should seek to preserve those stretches still operative — such as the Hanford Reach of the Columbia itself, the only free-flowing section of the river south of the Canadian border, which still yields 150,000 or 200,000 salmon a year — and to restore other parts of the river, then to reconnect these stretches.

But the good faith of these scientific advisers is questioned by Strong, whose talk was originally entitled "Is there too much science in the Columbia River Basin?", until organizers toned it down to the more restrained "Science in the Tribal Restoration Plan". Strong accuses scientists involved of arrogance towards nature, adding: "It isn't science that is offered: it is science that does not interfere with money-making on the Columbia."

Williams counters that tribal advocates want it both ways: they claim, with some justification, that the scientists have at last come round to their way of thinking, but they still argue that science can't be trusted to come up with ways to fix the problem. He worries that tribal advocates are more interested in continuing arguments than in embracing solutions.

These solutions are increasingly assumed to lie in destroying some of the dams. "We have turned a once-raging river into a series of reservoirs," says Donna Darm of the fisheries service. Salmon prosper on the Hanford Reach, where the Columbia is free-flowing, and only four dams — each with fish ladders — separate the spawning grounds from the Pacific Ocean, where the fish spend much of their adult lives before returning upstream to spawn.

But the additional four dams on the Snake River seem to be too much for the salmon to negotiate, Williams says. The decline in the overall salmon harvest in the Columbia basin was almost complete before these four dams were constructed but, Williams believes, the removal of the dams would restore natural salmon spawning on the Snake River and its tributaries in Idaho and western Montana.

Science and public perception

Darm says that their demolition would cost $1 billion, plus around $250 million a year in lost hydroelectric power. At present, around $450 million is spent each year on programmes to restore fisheries in the Columbia basin — although half of this goes on subsidies for the hydropower.

Attempts to restore the stocks could also be dogged by false public perceptions of what has gone wrong. According to Courtland Smith, a sociologist at Oregon State University, surveys have shown that the public considers "water quality" to be the main reason the salmon have gone, with overfishing by foreign fishermen in the Pacific Ocean the next biggest problem. Neither factor is viewed as significant by scientists or fishery managers.

"We've spent $2–3 billion on salmon recovery to date, and the results have been disappointing," says Etchart. "Science is not to blame, but it has played a part. There are serious questions about whether what we spend now [on fisheries management and research] is cost-effective."

Colin Macilwain

'Whistleblowers face blast of hostility'

[SEATTLE] Whistleblowers who alert authorities to alleged instances of scientific misconduct are facing an increasingly hostile environment in which colleagues, research administrators and even investigators called in to examine their claims are closing ranks against them, the annual meeting of the American Association for the Advancement of Science was told last week.

Despite laws that are supposed to protect them, whistleblowers often find themselves subjected to suspicion and investigation, according to Joan Sieber, a psychology professor at California State University. They are statistically likely to lose not only their job, professional friends and status, but even their home and spouse.

According to Robert Sprague, who himself blew the whistle in a celebrated case involving abuses of psychopharmacological research on disabled people, "the scientific community is moving toward suspicion of the whistleblower". It sees them as seeking to benefit, financially or otherwise, from their actions, although this is seldom the case, Sprague says.

Dan Greenberg, editor of the newsletter *Science and Government Report*, told the meeting that "the scientific establishment doesn't take misconduct seriously, except insofar as it needs to act to placate the political community". Greenberg said that now that Representative John Dingell (Democrat, Michigan), who protected whistleblowers and, as chairman of the House Investigations and Oversight Committee, pursued many well-known cases of alleged misconduct, is in the minority and stripped of his power, scientific leaders "just want to push the whole thing away".

In view of the potential dangers outlined by Sieber, would-be whistleblowers are offered a six-point plan on "how to keep your job" by C. K. Gunsalus, an attorney and administrator at the University of Illinois at Champaign-Urbana. Gunsalus was a member of the Ryan Commission, which last year produced a highly controversial report on scientific misconduct.

Gunsalus suggests that prospective whistleblowers should first show their information to someone they can trust who is in "at least as senior a position" as the subject of the complaint. If possible, they should do this twice, and listen carefully to the responses.

They should then assess what their actual goal is (to have a paper amended, for example), figure out exactly where the relevant documentation will be found, seek allies if possible, and find out the right person to take the allegation to. Only then should they decide whether to proceed.

Gunsalus describes the general response of scientists to misconduct charges as a "visceral" reaction. "We don't like tell-tales, and we don't like our dirty linen to be laundered in public," she says. She also points out that the total number of grievances and lawsuits brought to university administrators by faculty has shot up threefold in recent years. "Something is going on that has made everything [at the universities] much more contentious," she says.

The recommendations of the Ryan Commission are being considered by Donna Shalala, the health secretary, who has referred some of the more contentious ones to the White House. Shalala is expected to revise the process for dealing with misconduct in health research this year, in response to Ryan and to the well-publicized collapse of several high-profile cases at the Office of Research Integrity, which handles such cases in her department. **Colin MacIlwain**

Marconi's daughter sends out distress call about collection

[LONDON] The archives of Guglielmo Marconi (right), the inventor of wireless communication, which had been due for auction in April, are expected to be withdrawn from sale in the wake of a public outcry that included complaints from Marconi's daughter Elettra.

Some 1,000 individual lots, including prototype wireless equipment, documents, photographs and letters, which make up the Marconi Collection, were threatened with dispersal by public auction at Christie's, London, on 24 and 25 April.

But the sale now seems unlikely to go ahead, and a statement from the collection's owners, General Electric Company, which absorbed the Marconi company in 1968, says that discussion is taking place with the Science Museum in London and other parties in a bid to find a solution "which will ensure that the Marconi Collection remains intact and in this country".

Marconi moved to London in 1896 to patent his wireless telegraphy, which had been dismissed in his native Italy, and in the following year registered his Wireless Telegraph and Signal Company. He continued his research in England, and in 1901 successfully received a transatlantic radio signal in St John's, Newfoundland, that had been transmitted in morse code by a colleague in Cornwall, England.

Until this demonstration, radio waves had been received over 80 miles apart, and many scientists believed the waves would be unable to follow a longer curve around the Earth's surface. Marconi shared the Nobel prize for physics in 1909.

Marconi's work provided the foundation of today's terrestrial and satellite broadcasting, sea, air and cellular communications, space travel and radar. Last month, Christie's announced that their auction offered bidders "a unique chance to own a piece of the early days of the global communications industry".

But the news of the intended sale stirred up a flurry of comment in *The Times* newspaper, including letters from Marconi's daughter, Princess Elettra Marconi-Giovanelli, John Sutherland, the former managing director of Marconi Radar, the historian Lord Briggs, and archivists and wireless enthusiasts. The main criticism was that the value of the archive derives from its size and breadth, requiring that it be kept intact.

The collection, housed in Great Baddow, near Chelmsford, Essex, is closed to the public, but available for academic study. It includes such items as one of the first commercial wireless receivers, Marconi's diary recording the historic 1901 radio transmission, and a 'Marconigram' sent from the sinking liner Titanic in April 1912.

Christie's said last week that it is waiting for further instructions from General Electric. A spokesman from the company refused to specify the solutions being considered, but said that a final decision on the collection's fate, likely to include withdrawing it from public sale, is expected soon. Claire O'Brien

SPL

IMAGE UNAVAILABLE FOR COPYRIGHT REASONS

Scientists sign up to protest against French law on immigration

[PARIS] French scientists are supporting a growing campaign of civil disobedience launched last week by artists and intellectuals in protest at proposed legislation to control illegal immigration.

Opposition to the law — which comes up for a second reading in the National Assembly this week — has crystallized around a provision requiring citizens to ensure that the papers of their foreign guests are in order, and to declare their arrival and departure to the local authorities. Signatories to the campaign state that they refuse to respect the provision.

One of the texts already signed by hundreds of scientists says: "We French scientists do not accept that our country equips itself with xenophobic laws that would be ridiculous if they were not odious."

It goes on: "We do not want to be the only scientists in the world to be forced — unless we wish to become lawbreakers — to ask our foreign colleagues to prove the legitimacy of their presence in France before we invite them to spend the night! We refuse to get caught up in a spiral of denunciation like that in totalitarian countries, and a reminder of the darkest hours of our history."

One geneticist who has signed the text says that the idea of scientists treating their foreign colleagues in the way demanded by the law is "either stupid or mad". Alain Juppé, the prime minister, has condemned the campaign as a "serious act", and says he does not plan to change the law.

Polio campaign in Asia immunizes 250m infants

[GENEVA] **More than 250 million children under the age of five were successfully immunized against polio in December 1996 and January 1997 in a massive campaign organized by the World Health Organization (WHO). India, Bangladesh, Bhutan, China, Myanmar, Nepal, Pakistan, Thailand and Vietnam took part in a series of National Immunization Days, involving 2.6 million health workers in India alone. Since 1988, when WHO set itself the goal of eradicating polio worldwide by the year 2000, the number of cases has dropped from more than 35,000 to just 7,000 in 1995.**

Chirac asks academy to predict social changes

[PARIS] The French President, Jacques Chirac, has asked the Academy of Sciences to prepare a report on the big changes that can be expected in society early next century. He also asked the academy to produce recommendations to promote "the access of all to knowledge", and to guide politicians on the consequences of developments in information technology and the life sciences. The academy has welcomed the invitation with "lively interest" and has set up a committee to carry out the study. Some observers hope that it may equip itself with an Internet address — something the academy lacks at present.

US patents on ESTs 'to be permitted'

[SEATTLE] **An official from the US Patent and Trademark Office (PTO) said last week that the US government intends to allow patents to be granted for expressed sequence tags (ESTs), sequences of several hundred base pairs of DNA that uniquely identify full-length expressed genes. The statement was made during the annual meeting of the American Association for the Advancement of Science in Seattle, Washington State; no official confirmation has yet been issued by the PTO itself.**

Such a decision would clear up many years of uncertainty over whether these tiny markers of genetic information can be patented. But it would also be controversial. The official said that the decision was based on recognition that the 'utility' of ESTs lies in

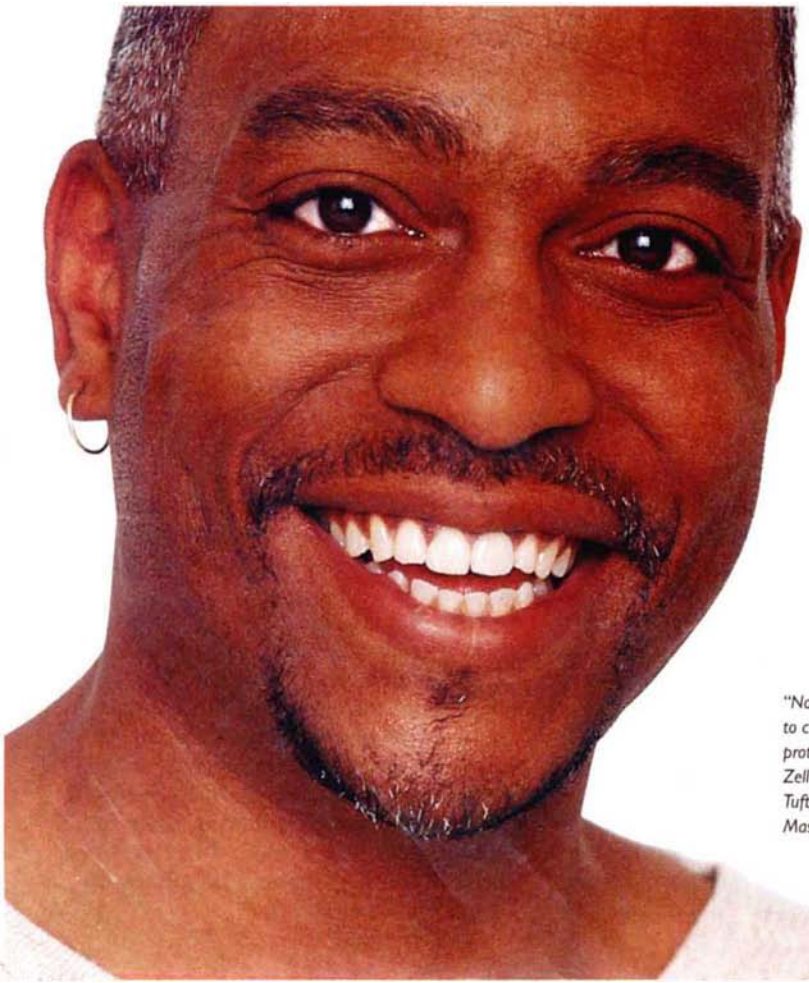

Malcolm is imp
by the new Pre
Protease be
it's a GST
fusion prot

"Not being a protein chemist, I just want to clone the gene, express it, isolate the protein and move on," says Malcolm Zellars, who's working on his post-doc at Tufts University Medical School in Boston, Massachusetts, USA.

Patent threat to research

Sir — The proposed Directive to the European Parliament and Council of the European Union on biotechnological patents (95/0350(COD)), currently under discussion, poses a threat to the future of scientific and medical research. Its potential consequences are as serious as those arising from the sweeping patent granted to the US company Biocyte on the use of all human blood cells from the umbilical cord of a newborn. This is being disputed by US and European medical groups because it threatens the free use of such cells for transplant purposes and in research (see E. Gluckman *et al.*, *Nature* **382**, 108; 1996).

The directive extends this type of commercial constraint on scientific and medical work to all organisms. A company has only to make use of a "microbiological process" in obtaining plants or animals to be able to patent them. It would then own them and be able to demand patent rights from anyone else wishing to work on them. The directive further states that the patent entitles the holder to prohibit third parties from exploiting them for industrial and commercial purposes. Applicants for research grants in the United Kingdom are now required to name the beneficiaries of their research. Most state-supported research in biotechnology can therefore be held to be for industrial and commercial purposes, and the patent holder could prohibit it even if patent rights are paid for use of the material.

Advances in biotechnology are already patentable under European patent law. What is at issue is whether these patents should be very much broader in scope than those in other fields, and, in particular, whether someone who isolates and characterizes natural material should be able to patent not just the method by which this was done but also the material itself. If this principle had been applied in chemistry, the elements would have been patented, and indeed, the directive does refer to "elements of plants and animals".

We do not doubt that biotechnology has an important role to play, but we do not accept the claim in the directive that the benefits we can expect are so vital and so urgent that special restrictions are called for. Moreover, as with all industrial innovations, there are dangers to be recognized and safeguards to be put in place, and by impeding research the new law would make it less likely that this will happen. Instead of helping biotechnology to make a responsible and useful contribution to medicine and agriculture, the present directive from Brussels succeeds only in threatening the very foundations of scientific research — free access to material and freedom to pursue promising lines of enquiry.

Howard Dalton *(Biological Sciences, University of Warwick)*; **Brian Goodwin*** *(Department of Biology, Open University, Walton Hall, Milton Keynes MK7 6AA, UK; e-mail: b.c.goodwin@open.ac.uk)*; **Mae-Wan Ho** *(Biology, Open University)*; **Jacqueline McGlade** *(Biological Sciences, University of Warwick)*; **Ghillean Prance** *(Royal Botanic Gardens, Kew)*; **Peter Saunders** *(Mathematics, Kings College London)*; **David Sherratt** *(Microbiology, University of Oxford)*; **John Maynard Smith** *(Biological Sciences, University of Sussex)*; **Roger Whittenbury** *(Biological Sciences, University of Warwick)*

*To whom correspondence should be addressed.

Not such a bad book

Sir — I did not see proofs of my review of *Triple-Helical Nucleic Acids* by V. N. Soyfer and V. N Potaman, and, in consequence of the editing, the printed result (*Nature* **385**, 218; 1997) was much more negative than I had intended. The book reviewed the structural aspects of triplex structures extremely well, yet in the published review these comments were submerged by my only negative comment, about the biological relevance.

My original sentence, "*Triple-Helical Nucleic Acids* presents a comprehensive and authoritative review of the current state of knowledge about most aspects of these novel structures, covering structural, molecular recognition and physical chemical aspects of triplex DNA in impressive detail", was shorn of all its positive adjectives. Moreover, the five 'scores' according to which I was asked to rate various aspects of the book became four in the version printed, and were inverted: thus a 2 ('excellent' on the scale I was asked to use) became ** (indicating only fair).

Overall, the result was unfair to the authors. I hope that the sales of this worthy volume are not adversely affected by this unfortunate occurrence.

David M. J. Lilley
Department of Biochemistry, University of Dundee, Dundee DD1 4HN, UK
e-mail: dmjlilley@bad.dundee.ac.uk

Improvement welcome

Sir — Philip Anderson's review of Per Bak's book *How Nature Works: The Science of Self-Organized Criticality* is seriously flawed[1]. Among other things, he claims that "Bak quotes two authors from Ilya Prigogine's institute who seem to have revived (20 years later and without attribution), the Pines–Shaham starquake theory...". By this statement, Anderson is implying plagiarism. That this is untrue can be simply proved by looking at the literature in question. Bak used the preprints that were subsequently published in refs 2 and 3. In ref. 2 (which derives the pulsar scaling law directly from original radioastronomical data), attribution is given in the following words: "We adopt the crust cracking model for pulsar glitches (M. Ruderman, *Ap. J.* **366**, 1991, 261; **382**, 1991, 576, 587)". The Ruderman papers quoted are the original papers that introduced the concept of neutron-star surface platelets. In ref. 3 (which presents the mass-accretion stress mechanism for pulsar glitches, which Bak, in his book, calls "speculative"), the attribution is given by: "This may be explained by the fact that pulsar glitches are starquakes (M. Ruderman, *Nature* **223**, 1969, 597; G. Baym and D. Pines, *Ann. Phys.* **66**, 1971, 816)". Anderson's name does not appear, nor should it.

Peter Morley
Department of Physics, University of Texas, Austin, Texas 78712, USA
e-mail: morley@linux.ph.utexas.edu

1. Anderson, P. W. *Nature* **383**, 772 (1996).
2. Morley, P. D. & Garcia-Pelayo, R. *Europhys. Lett.* **23**, 185–189 (1993).
3. Morley, P. D. *Astron. Astrophys.* **313**, 204–208 (1996).

Philip Anderson replies — The words "without attribution" referred only to the book's author, Per Bak, and not to the original authors, whose work I had not seen, and who I could assume gave proper references.

But my other comment remains valid. When Ruderman, Pines and Shaham abandoned the starquake theory, it was not to leave the field but because they felt the theory was physically untenable for almost all glitching pulsars. The amount of energy of elastic deformation that can be released in the well-understood Coulomb solid of the pulsar crust is many orders of magnitude below the size of a typical Vela-type glitch. After a brief flirtation with possible "core" solids they enthusiastically welcomed my suggestion of superfluid "vorticity jump" events, and various of the group Ruderman, Pines, Shaham, Alpar and Anderson published a series of papers together on this quite successful scenario. If we had yet heard of self-organized criticality, our discussion of glitch statistics might have been much improved, but we were a decade or two too early. We would welcome such an improvement of the model by Peter Morley.

Philip W. Anderson
Joseph Henry Laboratories of Physics, Princeton University, Princeton, New Jersey 08544, USA
e-mail: esz@pupgg.princeton.edu

A crisis in scientific morale

Scientists who work in biomedical fields cannot be objective observers of processes that go on in their own bodies. What is the rational solution to this dilemma?

Robert Pollack

So long as individual scientists believe, and behave according to the belief, that the essence of success in science is the freedom to discover the right experiment and then to do it according to one's own lights, all the social structures that connect scientists to one another will be based solely on each scientist's latest piece of individual work: a hobbesian world of each against all. Such a world is intrinsically unhappy, and profoundly unbiological as well, in the sense that no scientist's life, or work, can possibly go on indefinitely, as this sort of world demands.

This wilful miscalculation of the trajectory of a life can, paradoxically, lead to sudden demoralization in those scientists who have been around long enough to know better. As they reach an age and situation where 'peer review' means being judged by colleagues younger than their children, the absence of social structures that would validate anything about these researchers beyond their latest papers, makes for a reproducibly sad moment of isolation that often leads to bitterness and weird or obstructive behaviour.

These considerations feed a deeper malaise in the life sciences. In its disciplined way of looking at the natural world, any branch of science requires its practitioners to act as if they were observers, not participants. In all sciences, the first and last scientific instrument, the one that must be used in every experiment, is the scientist's brain. Scientists who choose human biology as their playing-field cannot fully meet the requirement that they observe their systems dispassionately, without dislodging themselves from their own bodies and minds.

The strain of trying to meet a standard of cool curiosity without flying apart into pieces imposes an unbearable distance between the biologist and his or her own biology. To relieve this strain, medical scientists have created the myth that their instruments and procedures somehow free them from the boundaries of their minds and bodies. This is the myth of absolute rational control of the scientist over her or his material, the notion that the metaphor of scientist as sculptor will not break down even when the sculptor and the sculpture are one and the same.

The conscious expression of this unconscious dilemma is a novel transformation of every scientist's dream of winning. Medical science, like any other science, is profoundly respectful of the score-card, allocating recognition only for precedence in demonstrating the correctness of a new model for how a piece of nature works. The dream of winning takes on an obsessive quality in the medical sciences once the subject of scientific study becomes the mind and body, and the reality of bodily mortality becomes unavoidable. The obsessive response to the certainty of biological death is the promise that a big enough win in the game of science will beat death itself, by conferring a form of immortality on the winner.

Discoveries that set the agenda for the future work of many other scientists do this after a fashion, permanently associating a lower-case version of a scientist's name with an aspect of nature: think of darwinian evolution or the watson–crick model of DNA. But in the medical sciences, belief in winning immortality of any sort is problematic, as it denies the biological reality only too plain from the data, that the eventual loss of self is inevitable.

I first saw how the life sciences could be driven by a fantasy of institutional scientific immortality quite early in my career, about 25 years ago, in a formative, odd conversation with Al Hershey, the Nobel prizewinning geneticist who had used a food blender and some radioactive bacteria in the late 1940s to show that the DNA of a virus—and not its protein coat—was its genetic material. Hershey told me his vision of heaven: you come into the lab every day forever, you do the same experiment you did the day before but with one small variation, and the results are just as exciting, important and new as they were the first time.

This notion of a model so interesting that testing it over and over again wins the game without any further creative thought, is also a product of the root fantasy of the biomedical sciences. Hershey's heaven cannot exist for students of life because they must deal with the facts of life: the first of these is the inevitability of death, the personal mortality of the experimenter. Hershey's myth serves the same function for those biologists who believe in it, as other myths about death serve in other religions: to keep their believers from having to confront this irrational, unbearable reality.

> Medical scientists have created the myth that their instruments and procedures somehow free them from the boundaries of their minds and bodies

Only faith or obsession — if they are not the same — can expect a method of observation of nature and the knowledge it yields, to

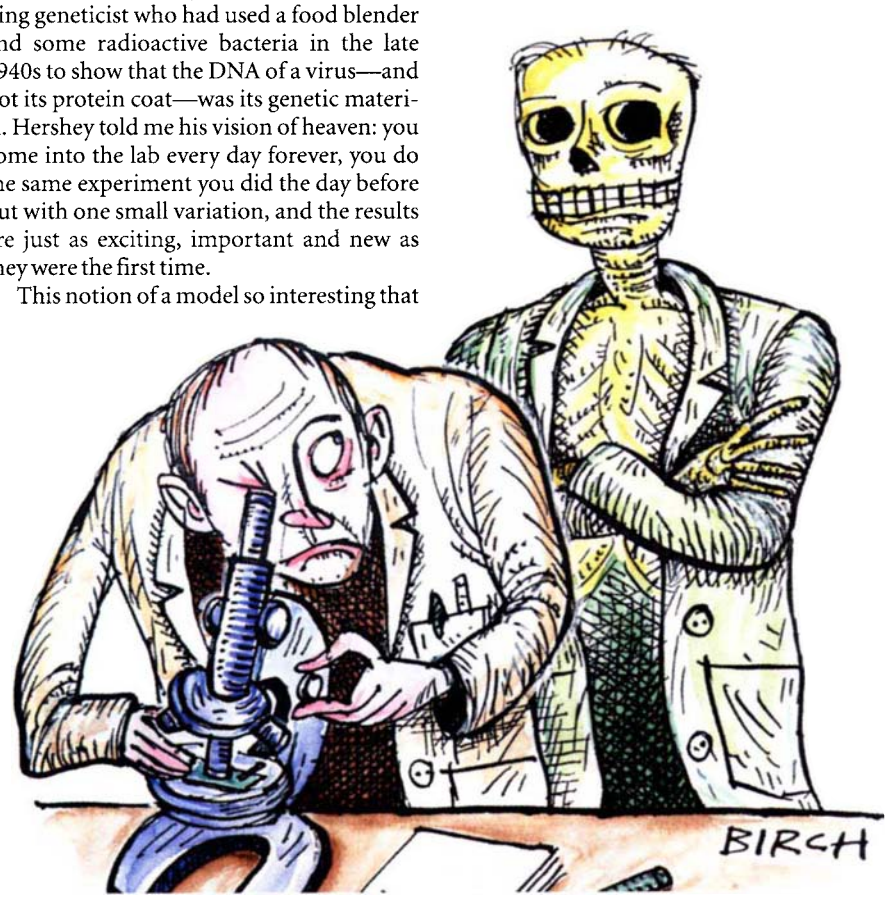

ANDREW BIRCH

set a person apart from the passage of time with its inevitable instant of personal ending. The underlying fantasy, that omnipotence of thought will bring immortality, is a notion inadmissible to rational analysis. This is why the conscious, operational, agenda of the life sciences masks the fantasy in the metaphorical cloak of institutional immortality.

The thinnest membrane of denial separates the notion of scientific immortality through priority of discovery from the deeper, older and wholly non-scientific dream of escaping one's own inevitable death. Personal mortality puts biologists in a quandary every time denial fails: to play the game well, they must never stop asking questions about our mortal bodies, but to play it with their own lives is to be sure that the answers—their own answers, their own models — are sometimes going to be truly frightening. Denial of the fear of nature's terrible power of mortality; projection of the suppressed wish not to be subject to nature, into a vision of nature as capable of bestowing immortality: these are the marks of a masked unconscious operating to create a biomedical science at war with its own stated purposes.

Visions like Hershey's heaven can have unexpected power when they are believed by the people who set the priorities of basic biomedical research. For example, many excellent scientists — their eyes fixed on their place in Hershey's heavens — have become completely averse to the idea that their work should be directed towards any goal beyond their own need to know the answer to their next experiment. Filled with this conviction, and thereby sustained in their faith that they have avoided the fact of mortality, they are easy prey to the habit of making promises to themselves, and to the rest of us, that they cannot keep, promises that hint that death itself may be put off indefinitely. It is not that science and medicine wish to avoid finding cures for diseases, it is that they are too strongly motivated by an irrational, unconscious need to cure death, to be fully motivated by the lesser task of preventing and curing disease simply to delay for a while the inevitable end of their patients' lives and, by extension, their own inevitable end.

About five years ago I decided to act on these observations: I resigned from my laboratory, which had been funded without interruption by the US National Institutes of Health and other government agencies for many years. I continue to write about the medical sciences, to teach the subject to undergraduates and graduate students, and to review manuscripts and grants. Instead of directing the work of a laboratory of my own, I am a consultant in the private sector, helping the research programme of AMBI Inc., a biopharmaceutical corporation.

Making this transition successfully is like crossing a highway on foot: oncoming drivers cannot afford to stop, unless they get into an accident themselves, and have to join you walking. Worse than being invisible (when I won a Guggenheim fellowship for my writing, one of my colleagues asked me, what's a Guggenheim?) is being condescended to: I recall the concerned, whispered attempt by a colleague to put me at ease by assuring me that I had simply entered scientific menopause.

...permanently associating a lower-case version of a scientist's name with an aspect of nature: think of darwinian evolution or the watson-crick model of DNA.

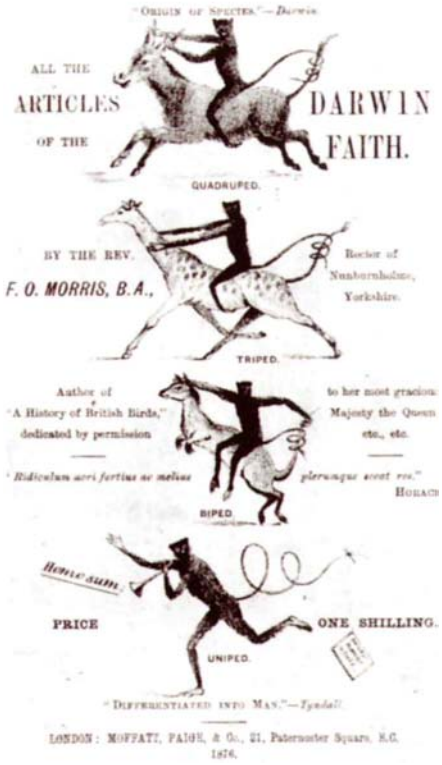

Eventually, I learned what smart women already know: menopause has its new freedoms, and even its pleasures. In terms of scientific morale, perhaps the most important of these is the discovery that it is possible to remain a scientist without running a laboratory. The mix that works for me involves writing, teaching, consulting and advising. My first book on science for the general public, *Signs of Life* (Houghton Mifflin, 1994), takes as its argument the notion that DNA is not merely an informational molecule, but is also a form of text, and that therefore it is best understood by analytical ways of thinking commonly applied to other forms of text, for example, books.

I am now completing my second book, on the difference between the outward, stable, inexorable time of science, and the inward, multiple, flexible time of consciousness, and the consequent problems science has in making sense of consciousness, and of that nasty diamond at its centre, each conscious person's knowledge of inevitable, personal mortality. These books have both been exercises in seeing patterns from insufficient data, and in that sense they are much like the science I used to do; the main differences are that I now write for the public rather than for a star panel of secret reviewers, and that I get paid by a publisher who pays taxes, rather than by a government agency spending tax money.

Having assembled this life for myself in the absence of any structures within the scientific community, I firmly believe that the crisis in morale among today's scientists—in my field, at least — stems not from money problems, nor from the stage of development the field is in, but from a failure by the scientists concerned to form themselves into proper, humane communities. It is never too late to begin the task of forming these communities, to introduce social structures that ameliorate the morale-puncturing competitiveness and anomic individualism of today's basic science, without in any way diminishing the intellectual rigour of the science itself.

No matter how porous the boundaries get between university-based and commercial-sector science, universities are likely to remain the main, if not the sole, source of new generations of scientists for a long time to come. For that reason alone, any changes in the social structure of science will need to take place among university professors in their departments, or else they will not have any lasting effect. We professors might as well begin our reforms in the most conservative way, by rediscovering and rededicating ourselves to the meaning of the title we hold. To 'profess' means openly to affirm. Affirmations are matters of the heart. Professors do not deserve the title, unless they are willing to take the time and make the effort openly to affirm something beyond their data, as data speak for themselves and need no affirmation. To be a professor, it seems to me, one must first have something of importance to oneself that needs affirming, and then one must affirm it. I affirm, for instance, that unconscious desires and fears, as well as data sets, drive the agendas of modern molecular biology. □

Robert Pollack is in the Department of Biological Sciences, Columbia University, New York, New York 10027, USA (e-mail: pollack@columbia.edu).

This article is based on the George Washington University symposium "Science in Crisis at the Millennium" on 19 September 1996.

A new age for type-II superconductors?

David R. Nelson

Many superconductors are rendered almost useless by the motion of string-like magnetic vortices. But because these vortices are hard to cut, it may be possible to pin them down using some very old techniques.

Many properties of materials depend crucially on defects. Soft metals bend irreversibly when dilute concentrations of defects called dislocation lines move in response to an applied stress. The Bronze Age began when early metallurgists added small concentrations of tin to copper to create a stronger and more effective material — the impurities work by pinning dislocations in place, thus preventing plastic deformation.

Similar problems arise when making superconductors work in high magnetic fields. The defects that must be pinned in place are now vortex lines, quantized bundles of magnetic flux where the magnitude of the superconducting wavefunction vanishes and its phase becomes undefined. On page 702 of this issue[1], Indenbom *et al.* use time-dependent supercurrents to twist these vortex lines into braided structures. In the process, they show that vortices resist being cut, and so highlight a possible change in strategies for vortex pinning, reminiscent of the revolution in metallurgy that led from the Bronze Age to the Iron Age.

Vortex lines are forced into type-II superconductors, the most promising materials for many applications, when the external magnetic field rises above 100 gauss or so. At low temperatures these defects crystallize into a regular triangular lattice of parallel lines aligned with the external magnetic field. Currents swirl around these vortex lines, much like the velocity field near a tornado, and vortices move in response to external electrical currents, just as dislocations move in soft metals when stress is applied[2]. Both motions are generally undesirable: moving vortices lead to a voltage drop and energy dissipation[3], and moving dislocations induce plastic deformations in metals.

The dissipation of energy caused by vortex motion means that any large sample of the material has some electrical resistance, even though the resistance vanishes locally away from the vortex cores. One simple way to ensure zero resistance would be to keep the magnetic field small and so expel vortices entirely from the sample. But in many applications, such as superconducting motors or the high-field magnets in magnetic resonance imagers, the intense fields generated act back on the superconducting wires to force vortices in. The only remedy so far has been to pin the troublesome vortex lines in place with point defects or precipitates of other phases in the host crystal, a technique similar to the incorporation of tin impurities in copper to produce bronze.

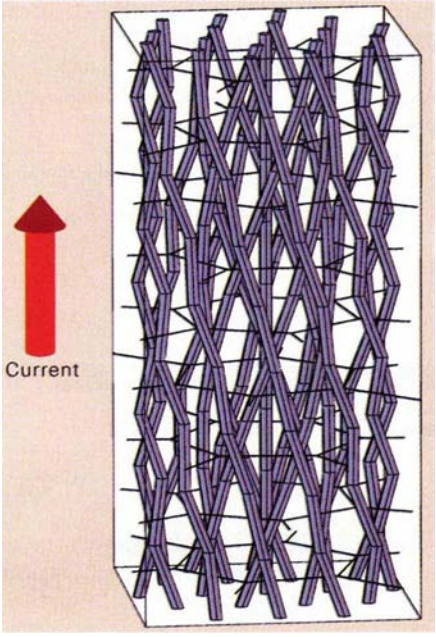

Figure 1 **A cage to stop superconductors misbehaving. In this scheme, a hexagonal lattice of screw dislocations would be introduced to fix the braided magnetic vortices (blue) in place.**

RANDALL KAMIEN, UNIV. PENNSYLVANIA

Unfortunately, this strategy does not work well in the new high-temperature superconductors, which are compounds consisting of highly conducting CuO_2 planes coupled weakly together. Although they remain superconducting up to relatively high temperatures (typically of order 100 K in zero magnetic field), thermal fluctuations and the weak coupling between CuO_2 planes make it very difficult to pin vortex defects by point imperfections even at liquid-nitrogen temperature (77 K). The weak coupling between planes leads to a fragile vortex lattice which melts even at relatively low temperatures.

Indenbom *et al.* worked with very clean rectangular samples of the high-temperature type-II superconductor $YBa_2Cu_3O_{7-\delta}$ under conditions of weak vortex-pinning. A background magnetic field parallel to the long axis of a rectangular sample controls the overall concentration of vortex lines. A small additional field is then applied perpendicular to the background direction, and induces screening currents (the currents that tend to keep magnetic fields out of superconductors). These currents exert a force that deforms the vortex lines already present in the sample.

Near the long edge of the sample, the current runs parallel to the vortex lines. Under these conditions, small deviations of the vortices from straight lines can be amplified into large helical-twist deformations. But because the vortex lines are difficult to cut, eventually their motion is inhibited, and so a higher current can flow before any resistance is encountered. (Beyond a critical level the current forces the vortices to move once more.)

By repeatedly reversing the direction of the screening currents, Indenbom *et al.* produce and study tornado-like helical 'twisters', each composed of thousands of vortex lines braided into very stable structures. The stability of these twisters shows that barriers to vortex cutting are high enough to have significant dynamical consequences, similar to the high viscosities in entangled polymer melts. Periodic screening currents generate creeping twister waves, which slowly travel into the interior. These wave patterns are again very stable, persisting for hours after the alternating current excitation is turned off. The relaxation requires only seconds in the absence of twist.

The generation of twisters by periodic deformations of vortex arrays has another metallurgical analogue: the Iron Age began when early materials scientists discovered how to make iron even stronger than bronze by supplementing the addition of impurities (typically carbon) with work hardening. When coat-hanger wire is bent back and forth repeatedly, the wire bends easily to begin with, but before it breaks it becomes quite stiff. The bending introduces more and more dislocation defects, and whereas low densities of dislocations make the material softer, eventually the dislocations become so concentrated that a traffic jam of entangled line defects develops. This tangle of lines becomes pinned as a single unit by impurities and boundaries between crystal grains, because the energy barriers to line crossing allow a few strongly pinned dislocation lines to hold the rest in place. Originally, carbon impurities were supplied by the blacksmith's forge, and work hardening by his hammer.

If the barriers to line crossing are indeed large, the electrical properties of type-II superconductors in a magnetic field could be improved by controlled entanglement of vortex lines. There are at least three ways to do this. One approach is to start at temperatures sufficiently high that the usual triangu-

lar lattice of defects is melted and entangled by thermal fluctuations. A rapid quench to low temperatures and a regime of high line-crossing barriers might then produce an entangled, polymer-like glassy state. Another is to inject splayed columnar defects of some sort into the sample, which can produce entangled ground states even at fairly high temperatures[4]. Finally, one could cool the lines in the presence of a current parallel to the average vortex direction, braiding the lines as in the new experiment[1].

A microscopic vortex configuration which might result from a constant current is shown in Fig. 1. Here, a regular hexagonal array of screw dislocation lines[5,6] has been superimposed on a conventional flux lattice to produce a configuration that is simultaneously crystalline in cross-section and entangled, while carrying a net current parallel to the lines. The structure is a compromise between the crystalline close packing favoured by inter-vortex interactions and the braiding induced by the current. Although this braided 'moiré state' was originally proposed[7] for chiral polymer crystals like DNA, it could also arise in type-II superconductors with currents parallel to the field direction.

The transition from the Bronze Age to the Iron Age was produced by trial and error, a process that took millennia. The metallurgical principles involved were only completely understood in the second half of this century. Superconductivity has been with us for only 86 years. It would be refreshing if ideas sketched above from basic research and fundamental science allow us to compress the time required to improve the electrical properties of superconductors. □

David R. Nelson is in the Physics Department, Harvard University, 17 Oxford Street, Cambridge, Massachusetts 01238, USA.

1. Indenbom, M. V. *et al. Nature* **385**, 702–705 (1997).
2. Hirth, J. P. & Lothe, J. *Theory of Dislocations* (Krieger, Malabar, FL, 1992).
3. Tinkham, M. *Introduction to Superconductivity* (McGraw-Hill, New York, 1996).
4. Hwa, T. *et al. Phys. Rev. Lett.* **71**, 3545–3548 (1993).
5. Wordenweber, R. & Kes, P. H. *Phys. Rev. B* **34**, 494–497 (1986).
6. Brandt, E. H. *Phys. Rev. B* **34**, 6514–6517 (1986).
7. Kamien, R. D. & Nelson, D. R. *Phys. Rev. E* **53**, 650–666 (1996).

Telomeres

Different means to common ends

David Shore

Telomeres — the structures that are found at the ends of eukaryotic chromosomes — have evolved to solve two problems: they ensure the complete replication of chromosome ends (which cannot be accomplished by known DNA polymerases), and they protect those ends from degradation or fusion[1]. In most organisms, telomeres are composed of variable numbers of simple repeat sequences (TTAGGG in vertebrates) that are produced by a special ribonucleoprotein called telomerase[2].

Cells must somehow monitor telomere length and use this information to regulate telomerase, which could otherwise add repeats to the end of the chromosome in an uncontrolled manner. How might such a process work? One hint has come from studies on the budding yeast *Saccharomyces cerevisiae*, which show that a telomere-repeat binding protein, Rap1p, negatively regulates telomere elongation[3]. Now, two reports on pages 740 and 744 of this issue, by van Steensel and de Lange[4] and by Cooper *et al.*[5], show that a newly discovered repeat-binding protein from a distantly related yeast, *Schizosaccharomyces pombe*, and the analogous human factor, also block the elongation of telomeres. The new work indicates that the mechanisms of telomere length regulation are highly conserved, and it provides a fresh perspective on the relationships between telomere length and both ageing and cancer.

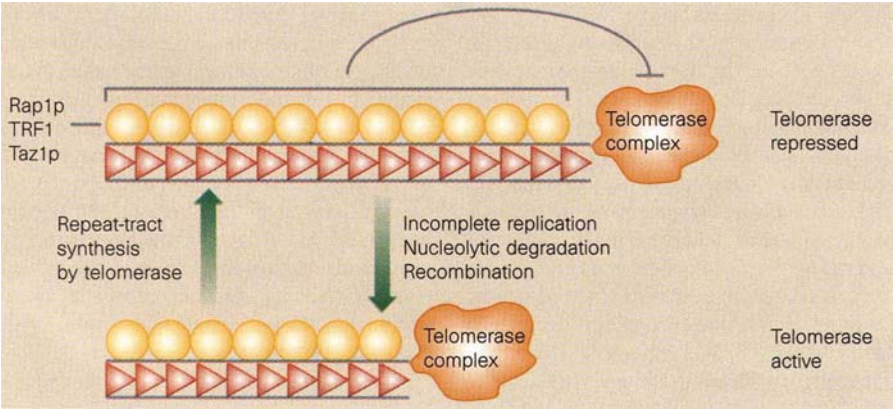

Figure 1 **The stabilization of telomere repeat tracts by the enzyme telomerase has been implicated in cancer, and the shortening of these tracts may be associated with ageing — but how is telomere length regulated? van Steensel and de Lange[4] have identified a human protein (TRF1) that binds to telomeres, and Cooper *et al.*[5] have isolated its analogue (Taz1p) in the yeast *S. pombe*. These proteins may prevent the elongation of telomere-repeat tracts by inhibiting telomerase.**

The variable length of telomere-repeat tracts has attracted considerable attention for two reasons. First, telomere tract shortening in somatic cells is associated with senescence, and it has been proposed to act as a molecular clock to prevent oncogenesis[6]. Second, telomerase is undetectable in most somatic cells, but it seems to be reactivated in many tumours, suggesting that telomere elongation might be an important — or even essential — step in tumour formation[7]. What is important to keep in mind is that telomere length in telomerase-containing tumour cells does not increase without bound, but is instead regulated at a constant average value. The same is true in germline cells, which also contain telomerase, and which regulate telomere length at a species-specific average value.

van Steensel and de Lange[4] report the first functional studies of a human telomere-repeat binding protein, TRF1 (ref. 8), and they suggest how it might work to regulate telomere length. They have stably overexpressed both full-length TRF1 and a dominant-negative mutant that reduces the binding of TRF1 to telomeres. Prolonged overexpression of wild-type TRF1 results in gradual telomere shortening, whereas the dominant-negative mutant abolishes detectable telomeric TRF1 staining (by indirect immunofluorescence), and causes pronounced telomere elongation. Both of these results point to the direct involvement of TRF1 in determining the length of telomeres in human cells. The authors suggest a simple model in which the amount of TRF1 that is bound to telomeric repeat tracts acts to regulate telomerase. The addition of wild-type protein increases the amount of TRF1 at telomeres — creating a negative signal for telomerase — whereas the depletion of functional TRF1 by the dominant-negative mutant leads to telomerase activation and telomere elongation.

Cooper *et al.*[5] have used a 'one-hybrid' approach to clone the *S. pombe* gene that encodes Taz1p (for telomere associated in *Schizosaccharomyces pombe*), a protein that binds to double-stranded DNA at telomeres. Remarkably, although the telomere-repeat sequences of *S. pombe*, *S. cerevisiae* and humans differ, all three repeat-binding proteins (Taz1p, Rap1p and TRF1, respectively) share similar (Myb-like) DNA-binding domains. Outside the DNA-binding domain, Taz1p has little homology with human TRF1, and no homology at all with Rap1p. Nonetheless, mutation of the *taz1*$^+$ gene creates two phenotypes that are strikingly similar to those seen in Rap1p carboxy-terminal truncation mutants — massive

elongation of the telomere-repeat tracts, and a complete loss of telomeric gene silencing or telomere positional effects[3,9]. So despite the absence of any clear sequence homology between these yeast proteins, they share two telomeric functions. But whereas the *taz1*$^+$ gene is not absolutely necessary for growth in *S. pombe*, Rap1p also works as an apparently essential transcriptional activator in *S. cerevisiae*[10].

A general theme to emerge from these studies is that proteins that bind to double-stranded telomere repeats negatively regulate telomere elongation. This concept was first suggested for Rap1p and its homologue in the related yeast *Kluyveromyces lactis*[11], and it may provide the key to understanding two central questions: how does the cell 'measure' telomere length, and how is this information used to regulate the length of telomeres?

One possibility is that a mechanism exists to sense the number of telomere-repeat binding proteins on the end of the chromosome. When this number exceeds a certain threshold, a signal is generated that blocks elongation by telomerase (Fig. 1). Alternatively, this signal might activate nucleolytic or recombinational processes that shorten telomere-repeat tracts. Incomplete replication or degradation events that remove repeat-tract binding sites would relieve the repression of telomerase, allowing subsequent elongation. This, in turn, would lead once again to the repression of telomerase.

Such a simple negative-feedback model could explain how germline cells or cancer cells (which contain active telomerase) can maintain a constant average telomere tract length. One prediction of the model is that telomere length is sensed by a mechanism that can discern the precise number of molecules that are bound to the telomere repeats. Direct evidence for such a mechanism has just been described for *S. cerevisiae*[12], and the experiments by van Steensel and de Lange[4] indicate that a similar protein 'counting' mechanism may be at work in human cells. So it is likely that TRF1 is directly involved in determining telomere length in germline cells, as well as in tumours.

With the outlines of a plausible model for the regulation of telomere length in view, the challenge will now be to understand the process in molecular detail. In *S. cerevisiae*, there is mounting evidence that length regulation by Rap1p is mediated by a pair of proteins called Rif1 and Rif2 (for Rap1-interacting factor)[13]. Are similar factors at work in *S. pombe* and mammalian cells? Although the principle of length regulation by a negative-feedback mechanism that involves repeat-binding proteins may be generally applicable, we should not be surprised to find that the details vary in different systems, or that additional mechanisms exist. Even in yeast, there seems to be an alternative pathway that can rapidly reduce an extremely elongated telomere to the size of its normal cohorts[14].

Finally, the putative target for regulation by telomere-tract binding proteins remains elusive, although attractive candidates have been identified in several systems — for example, telomerase subunits and proteins that bind specifically to the single-stranded protrusions at the very ends of telomeres. We can anticipate that a more detailed picture of telomere length regulation will emerge in the coming years, and this new perspective will certainly affect our view of the role of telomeres in senescence and tumorigenesis — the two problems that generated all of the excitement in the first place. □

David Shore is in the Department of Molecular Biology, University of Geneva, 30 quai Ernest-Ansermet, CH-1211 Geneva 4, Switzerland.

1. Zakian, V. A. *Science* **270,** 1601–1607 (1995).
2. Greider, C. W. & Blackburn, E. H. *Cell* **43,** 405–413 (1985).
3. Kyrion, G., Boakye, K. A. & Lustig, A. J. *Mol. Cell. Biol.* **12,** 5159–5173 (1992).
4. van Steensel, B. & de Lange, T. *Nature* **385,** 740–743 (1997).
5. Cooper, J. P., Nimmo, E. R., Allshire, R. C. & Cech, T. R. *Nature* **385,** 744–747 (1997).
6. Harley, C. B. in *Telomeres* (eds Blackburn, E. & Greider, C.) 247–263 (Cold Spring Harbor Laboratory Press, NY, 1995).
7. de Lange, T. *Proc. Natl Acad. Sci. USA* **91,** 2882–2885 (1994).
8. Chong, L. *et al. Science* **270,** 1663–1667 (1995).
9. Kyrion, G. *et al. Genes Dev.* **7,** 1146–1159 (1993).
10. Shore, D. *Trends Genet.* **10,** 408–412 (1994).
11. McEachern, M. J. & Blackburn, E. H. *Nature* **376,** 403–409 (1995).
12. Marcand, S., Gilson, E. & Shore, D. *Science* **275,** 986–991 (1997).
13. Wotton, D. & Shore, D. *Genes Dev.* (in the press).
14. Li, B. & Lustig, A. J. *Genes Dev.* **10,** 1310–1326 (1996).

Olfactory adaptation

The nose leads the eye

Geoffrey H. Gold and Edward N. Pugh Jr

Stimuli such as light, odours, hormones and other chemical signals, generate an intracellular response by altering the levels of intracellular second messengers. This type of signal transduction involves three components — a receptor protein that interacts directly with the stimulus; a guanine-nucleotide-binding (G) protein that is activated by the receptor; and an intracellular enzyme that is activated or inhibited by the G protein. Because a single receptor protein can activate a large number of G-protein molecules (each of which can interact with an intracellular enzyme molecule), this enzymatic cascade can provide enormous amplification. For example, vertebrate rods and certain invertebrate photoreceptors can respond reliably to as little as one photon of light.

But high transduction gain has a cost: a relatively weak stimulus can drive the signal-transduction mechanism into saturation. So G-protein-coupled mechanisms have evolved a variety of ways in which to desensitize (or adapt) to strong stimuli, allowing the cell to respond to stimuli over a wider range of magnitudes than would be possible with fixed, high gain. On page 725 of this issue, Kurahashi and Menini[1] show that of the many adaptation mechanisms that have been suggested, one seems to be dominant in newt olfactory receptor cells.

Odorants are detected by olfactory receptor cells in the nasal cavity. These cells

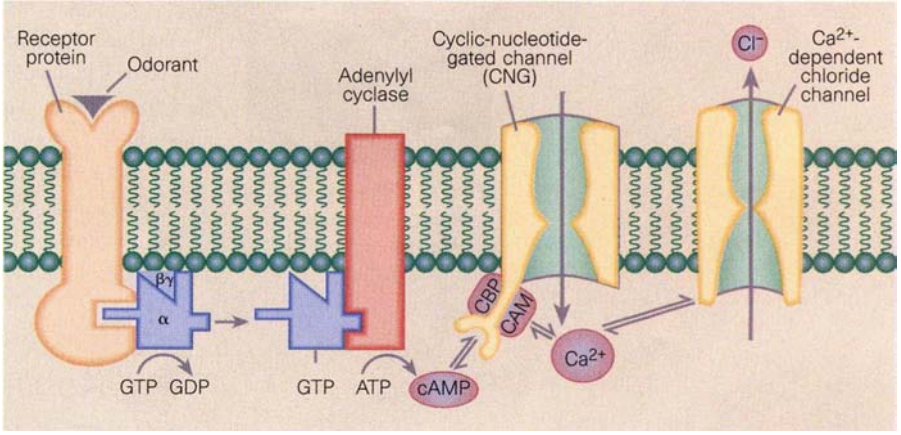

Figure 1 **To avoid becoming saturated by weak stimuli, sensory cells desensitize (or adapt). By studying olfactory receptor cells, Kurahashi and Menini[1] have explained exactly how adaptation occurs in response to odorant molecules. Following binding of the odorant to its receptor, G-protein-mediated activation of adenylyl cyclase leads to the production of cyclic AMP (cAMP), which activates a cyclic-nucleotide-gated (CNG) cation channel. Activation — and subsequent opening — of the channel allows an influx of Ca^{2+}, which evokes a response to the odorant by activating a Ca^{2+}-dependent chloride channel. But Ca^{2+} also mediates adaptation, by desensitizing the CNG channel through which it entered the cell. Desensitization is thought to be mediated by calmodulin (CAM) and possibly also by a new calcium-binding protein (CBP). (Figure adapted from ref. 10.)**

mediate G-protein-dependent activation of adenylyl cyclase, which in turn produces the intracellular messenger, cyclic AMP (Fig. 1). Cyclic AMP depolarizes the cell by activating cation-selective cyclic-nucleotide-gated (CNG) ion channels[2]. These channels are highly permeable to Ca^{2+} (refs 3, 4), leading to a rise in the concentration of intracellular Ca^{2+} which has two opposing effects: it activates a depolarizing Ca^{2+}-dependent Cl-conductance that amplifies the current generated by cAMP[5], and it causes the cell to adapt[3].

Several mechanisms by which Ca^{2+} can evoke an adaptive response have already been proposed, varying from inhibition of cAMP production[6] or stimulation of cAMP hydrolysis[7], to Ca^{2+}-mediated desensitization of the CNG channel[8]. However, receptor-protein phosphorylation has also been shown to decrease the activity of adenylyl cyclase[9], and this mechanism is not dependent on Ca^{2+}.

How can the relative importance of these putative adaptation mechanisms be determined? An advantage of working with sensory receptors is that their responses can be measured electrophysiologically, with excellent time resolution and sensitivity. Kurahashi and Menini[1] first studied the effect of a pulse of odorant on the response that was evoked by a second pulse of the same odorant. They showed that the first (adapting) stimulus did indeed decrease the response to the second stimulus but, more importantly, the adapting stimulus shifted the dose–response relationship to higher concentrations of the odorant.

The authors next examined the effect of the first pulse of odorant on the current that was evoked by a subsequent pulse of cAMP (produced by photoactivation of caged cAMP). Surprisingly, the current that was evoked by the caged cAMP was reduced by the same amount as the response to the second pulse of odorant. So adaptation seems to occur after the production of cAMP, ruling out receptor-protein phosphorylation and inhibition of adenylyl cyclase as being part of the adaptation mechanism.

Kurahashi and Menini[1] also showed that the decay rate of the response to odorants is affected very little by adaptation, arguing against the involvement of Ca^{2+}-dependent stimulation of cAMP hydrolysis. So they conclude that Ca^{2+}-mediated desensitization of the CNG channel is the dominant mechanism of olfactory adaptation (Fig. 1). This is remarkably simple — an influx of Ca^{2+} through the CNG channel decreases the affinity of the channel for cAMP, thereby decreasing response amplitude and sensitivity. The authors attribute the Ca^{2+}-mediated desensitization of the CNG channel to the effect of calmodulin (with which Ca^{2+} interacts) on the channel[8]. However, calmodulin-independent desensitization has also been described[10], and the relative importance of the calmodulin-dependent and -independent mechanisms is not yet known.

As most (if not all) odorants are detected by the cAMP pathway[2], desensitization of CNG channels may be a common mechanism of adaptation for odorants. Interestingly, the vertebrate rod and cone photoreceptors also use CNG channels to generate an electrophysiological response. Moreover, adaptation of photoreceptors — like that of olfactory receptors — is triggered by the change in the intracellular concentration of Ca^{2+} that accompanies the response to the stimulus[11], and calmodulin-dependent changes in the affinity of the CNG channel for cyclic GMP have been found in both rods[12] and cones[13]. However, the direction of stimulus-triggered changes in the concentrations of cyclic nucleotide and Ca^{2+} are opposite: in olfactory receptors, the concentrations of cAMP and Ca^{2+} increase in response to odorants whereas, in photoreceptors, cGMP and Ca^{2+} decrease in response to light.

In photoreceptors, the stimulus-triggered decline in Ca^{2+} acts through calmodulin to restore some CNGs to the open state. The lower levels of intracellular Ca^{2+} also lead to the activation of guanylyl cyclase, which again results in increased opening of the CNG channels[14]. The open state leads to depolarization of the photoreceptors, and provides a greater output-voltage range for the response to incremental changes in illumination. But although the channel-opening effects of Ca^{2+} are functionally 'adaptive', neither explains the 5–20-fold decrease in amplification that occurs during exposure of photoreceptors to light[15–17], and which involves a change in the gain of an early transduction intermediate[18], even though this decrease is known to be caused by a decline in the concentration of Ca^{2+} (refs 15, 17, 18). So Kurahashi and Menini[1] have given those who study adaptation in olfactory receptors 'one up' on those tracking down the mechanisms of light-adaptation in photoreceptors — the latter are still on the hunt for the mechanism(s) that underlie a major Ca^{2+}-dependent gain-control process. □

Geoffrey H. Gold is at the Monell Chemical Senses Center, Philadelphia, Pennsylvania 19104-3308, USA. Edward N. Pugh Jr is in the Department of Psychology, University of Pennsylvania, Philadelphia, Pennsylvania 19104-6196, USA.

1. Kurahashi, T. & Menini, A. *Nature* **385**, 725–729 (1997).
2. Brunet, L. J., Gold, G. H. & Ngai, J. *Neuron* **17**, 681–693 (1996).
3. Kurahashi, T. & Shibuya, T. *Brain Res.* **515**, 261–268 (1990).
4. Frings, S., Seifert, R., Godde, M. & Kaupp, U. B. *Neuron* **15**, 169–179 (1995).
5. Lowe, G. & Gold, G. H. *Nature* **366**, 283–286 (1993).
6. Sklar, P. B., Anholt, R. R. H. & Snyder, S. H. *J. Biol. Chem.* **261**, 15538–15543 (1986).
7. Borisy, F. F. *et al. J. Neurosci.* **12**, 915–923 (1992).
8. Liu, M., Chen, T.-Y., Ahamed, B., Li, J. & Yau, K.-W. *Science* **266**, 1348–1354 (1994).
9. Boekhoff, I. & Breer, H. *Proc. Natl Acad. Sci. USA* **89**, 471–474 (1992).
10. Balasubramanian, S., Lynch, J. W. & Barry, P. H. *J. Membr. Biol.* **152**, 13–23 (1996).
11. Matthews, H. R., Murphy, W., Fain, G. L. & Lamb, T. D. *Nature* **334**, 67–69 (1988).
12. Hsu, Y.-T. & Molday, R. S. *Nature* **361**, 76–79 (1993).
13. Hackos, D. H. & Korenbrot, J. I. *Biophys. Soc. J.* **72**, A115 (1997).
14. Hodgkin, A. L. & Nunn, B. J. *J. Physiol. (Lond.)* **403**, 439–471 (1988).
15. Lagnado, L. & Baylor, D. A. *Nature* **367**, 273–277 (1994).
16. Jones, G. J. *J. Physiol. (Lond.)* **487**, 441–451 (1995).
17. Gray-Keller, M. P. & Detwiler, P. B. *Neuron* **17**, 323–331 (1996).
18. Matthews, H. R. *J. Gen. Physiol.* **109**, 141–146 (1997).

Archaeology

Plus c'est le même chews

This small piece of used chewing gum (actual size) is 6,500 years old. It was found in a bog at Bökeberg in Sweden, and similar ancient chewing gum has been discovered at sites all over Northern Europe. What was it made of?

It is clearly some sort of natural tar. Pine resin was one possibility — it is easily prepared, and has been used as chewing gum historically. But analysis of tar from several sites by Elizabeth Aveling at the University of Bradford points to another source: birch-bark (*Br. Archaeol.* no. 21, 6; 1997). Birch-bark tar was used for many other purposes at the time, including glue and waterproofing. Ötzi, the alpine 'Ice Man' found in 1991, had his axe stuck together with it, for example.

From the size of the tooth marks, the birch-bark gum was mostly chewed by children and teenagers. "Although the taste cannot be described as pleasant," Aveling writes of gum made in the lab, "neither is it entirely unpleasant — and who knows what appealed to the mesolithic palate?" It doesn't appear to be narcotic. Did it help remove loose milk teeth or to fight plaque? Was it used as a pacifier, as a disinfectant for sore throats, or was it just chewed to disgust adults?

Some ingenuity and effort was needed to make the stuff. The bark must be heated to drive out the sap, but if it is heated in air it simply chars. Neolithic people could have used sealed jars, but ceramics are unknown before about 5,600 years ago, so how the mesolithic cultures made it is a mystery.

As for the most obvious question — does your chewing gum lose its flavour underground over the millennia? — sadly no one has been allowed to taste the ancient gum to find out.

Stephen Battersby

Neurobiology

Memory floxed

Richard G. M. Morris and Roger J. Morris

As the generations come and go, new memories are made while old ones fade away. The arrival of a new generation of mouse mutants, together with advances in their electrophysiological assessment, have now been heralded with the publication of four papers by Susumu Tonegawa, Eric Kandel and their colleagues, in *Cell*[1–4]. The importance of these new approaches goes well beyond the data obtained — they are a step towards bridging the intellectual divide between *in vivo* systems and cellular accounts of neuronal memory mechanisms.

Tonegawa and colleagues[1–3] have broken new ground by creating a mouse in which a targeted gene (a subunit of an excitatory glutamate receptor) has been inactivated, but only in specific neurons within a subregion of the hippocampus known as CA1. Many of these neurons are 'place' cells: they fire impulses only when the mouse is at a certain location. In an analysis of learning and place cells in the mutant mice, they find that they learn a spatial task poorly; that brain slices from them show a precise regional deficit in an important form of synaptic plasticity; and that single-neuron recordings in the whole animals reveal peculiarities in the firing pattern in the CA1 region. Kandel and colleagues[4] describe a mouse that has an engineered alteration in synaptic plasticity of a different kind, but which also shows changes in the patterns of cell firing.

The first generation of mouse mutants that were developed to explore memory and behaviour were created using homologous recombination to inactivate genes of interest[5]. Powerful though this technique may be, the regionally and temporally unrestricted nature of the resulting gene deletion can lead to developmental defects or premature death, and other pleiotropic effects can play havoc with attempts to interpret the effect of the deletion in the adult brain. Some of these problems are avoided by using the Cre/loxP system to restrict inactivation of the targeted gene to a specific subset of cells (see panel). Building on Mark Mayford's characterization of the α-calcium–calmodulin-dependent kinase II promoter (*αCaMKII*)[6], Tsien *et al.*[1,2] produced a mouse in which the gene for the R1 subunit of the *N*-methyl-D-aspartate (NMDA) receptor was excised only in CA1 pyramidal neurons.

Having trapped their mouse, it was time to get it to tell its tale. The R1 subunit mediates a slow-rising and long-lasting excitatory postsynaptic current that is critical for certain forms of synaptic plasticity[7] and spatial learning[8] in the hippocampus. The mutants had no detectable NMDA-receptor-mediated currents in the CA1 region, yet signalling was normal in other parts of the hippocampus. Moreover, whereas long-term potentiation (LTP) and long-term depression were absent in the CA1 neurons, short-term plasticity was intact. The mice also showed reduced spatial learning in a water-maze (where the animal is required to use distal cues to swim to a platform that is hidden in a large pool).

These findings confirm, with greater anatomical precision, earlier studies using antagonists to the NMDA receptor, and they add one crucial piece of information. Gene deletion — even with the Cre/loxP system used here — is a chronic treatment, allowing the neural circuitry to develop compensatory mechanisms. Other hippocampal synapses support LTP, but (as these mice show) they cannot compensate for defective CA1 pyramidal neurons in supporting learning.

Striking new findings were obtained using single-cell recording techniques. The skull of a 30-gram mouse might seem to be too small to support a headcap containing a moveable electrode headstage and impedance-reducing circuits. But in a technical *tour de force*, McHugh *et al.*[3] miniaturized the device that was first developed by Bruce McNaughton and John O'Keefe, and they were rewarded for their efforts with two new results. First, although the CA1 pyramidal cells that fired in localized areas of space ('place fields') were clearly observed, the areas that they covered were larger in

Restricting gene inactivation to a subset of neurons

Cre is a bacteriophage recombinase that excises DNA between a pair of palindromic sequences called loxP sites[11]. If the loxP sites are introduced into a mouse so as to flank a targeted gene (referred to as the floxed gene, for 'flanked by loxP'), that gene will be excised in cells that express active Cre[12].

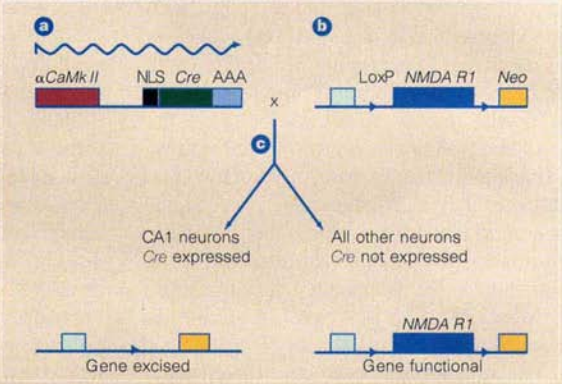

Transgenic technology – pro-nuclear injection of DNA into a fertilized oocyte – is used to express Cre. The *Cre* gene is placed under the control of regulatory elements that cause the Cre protein to be expressed only in specific subsets of cells. Tonegawa's group[1–3] used the promoter for the α-subunit of Ca^{2+}-calmodulin protein kinase II (*αCaMKII*) (**a**), a gene that is normally expressed postnatally in forebrain neurons[13]. The promoter (red) was added upstream of the *Cre* gene (dark green), and a nuclear localization signal (black) was added to the 5′ end of *Cre* to ensure the transport of Cre to the nucleus. A polyadenylation signal (light blue) was added to the 5′ end.

The expression pattern of the *αCaMKII* promoter is influenced by where the construct inserts into the host genome – a factor that varies in every transgenic line made. Fortunately, in one cell line, *Cre* was expressed in almost all CA1 pyramidal neurons, and only in these cells.

Tonegawa's group created a second line of transgenic mice by homologous recombination in embryonic stem cells. The flanking loxP sites were specifically introduced into introns so as not to inactivate the targeted (*NMDAR1*) gene (**b**): so the floxed gene was functionally normal unless the Cre recombinase was also expressed. The transgenic mice were then produced by injecting the floxed embryonic stem cells into a blastocyst.

The two elements were brought together by mating the mice, then backcrossing to obtain the F_2 recombinant generation, in which some mice were homozygous for floxed *NMDAR1*, and contained one copy of the *Cre* gene whose expression was restricted to CA1 neurons (**c**). In these mice, the *NMDAR1* gene was excised (in the third postnatal week of life) only from CA1 pyramidal neurons[2].

R.J.M. & R.G.M.M.

total and more scattered than normal. And second, whereas cells with overlapping place fields normally show correlated activities, there was little evidence of this in the NMDA-receptor R1 mutants. NMDA-receptor-mediated plasticity therefore seems to sharpen place-field specificity, helping to ensure that a coordinated place-cell-encoded signal is transmitted to downstream brain areas from the hippocampus.

Although McHugh *et al.*[3] provide exciting evidence for the importance of CA1 NMDA receptors in spatial learning and place-field determination, both of these effects are consequences of the gene deletion, and the impaired spatial learning may not necessarily be due to the change in place fields. A different possibility is that the hippocampus is involved in remembering recent events (at least temporarily) with respect to the spatial context in which they occur, and that the mutants are poorer in remembering events. In other words, spatial knowledge may develop in a secondary manner, through the consolidation of many memories of similar events.

Part of the reason for being suspicious about the idea that a subtle place-field defect could account for the learning deficit is that access to the information that is encoded in place cells cannot alone enable an animal to navigate effectively. Consider a mouse that wanted to go from place A to place B, avoiding place C. The cells for each place will fire if, and only if, an animal is in that place, so how could the mouse at place A access information relevant to approaching B, but not C, by using place cells without going to B or C in the first place? Head-direction units[9] and other spatial features of hippocampal unit activity could be part of the picture. Our concern here is to make the logical point that we should be cautious about assuming that an abnormality in place-cell properties is the only basis of a deficit in place navigation.

The place-field analysis done by Rotenberg *et al.*[4] also bears on this point. They studied transgenic mice that expressed a calcium-independent form of CaMKII, and which had previously been shown to lack LTP under certain conditions[10]. Whereas wild-type controls showed normal place-cell firing, the place-field locations of the mutants were unstable across successive recording sessions; this result is consistent with the idea of the hippocampus being a memory system in which events are remembered in relation to where they happen.

Cell-specific gene excision will be applied to other brain regions and developmental stages as soon as suitable promoters become available. The most eagerly awaited advance is the introduction of an inducible promoter that will express *Cre* in response to a systemically administered drug such as tetracycline[6] or tamoxifen. This should help to get around the problems of altered development (for example, the possibility of a cryptic developmental defect in the CA1 region), and it will allow more powerful behavioural analyses in which animals are tested with or without inactivation of the targeted gene.

The technical difficulty of single-cell recording in mice may limit its frequent application to mutants. However, in the case of memory, place fields are specified directly in relation to the animal's behaviour rather than, as with LTP, in response to an electrophysiological stimulus that is given independently of behaviour. Single-cell recording is therefore a welcome addition to the electrophysiological arsenal that is used to assess the role of specific genes in neural plasticity. □

Richard G. M. Morris is in the Centre for Neuroscience, University of Edinburgh, Edinburgh EH8 9LE, UK. Roger J. Morris is in the Department of Experimental Pathology, UMDS Guy's Hospital, London SE1 9RT, UK.

1. Tsien, J. Z. *et al. Cell* **87**, 1317–1326 (1996).
2. Tsien, J. Z., Tonegawa, S. & Huerta, P. T. *Cell* **87**, 1327–1338 (1996).
3. McHugh, T. J., Blum, K. I., Tsien, J. Z., Tonegawa, S. & Wilson, M. A. *Cell* **87**, 1339–1349 (1996).
4. Rotenberg, A., Mayford, M., Hawkins, R. D., Kandel, E. R. & Muller, R. U. *Cell* **87**, 1351–1361 (1996).
5. Thomas, K. R. & Capecchi, M. R. *Cell* **51**, 503–512 (1987).
6. Mayford, M. *et al. Science* **274**, 1678–1683 (1996).
7. Collingridge, G. L., Kehl, S. J. & McLennan, H. *J. Physiol. (Lond.)* **334**, 33–46 (1983).
8. Morris, R. G. M., Anderson, E., Lynch, G. S. & Baudry, M. *Nature* **319**, 774–776 (1986).
9. Taube, J. S., Muller, R. U. & Ranck, J. B. *J. Neurosci.* **10**, 436–447 (1990).
10. Mayford, M., Wang, J., Kandel, E. R. & O'Dell, T. J. *Cell* **81**, 891–904 (1995).
11. Kilby, N. J., Snaith, M. R. & Murray, J. A. H. *Trends Genet.* **9**, 413–421 (1993).
12. Gu, H., Marth, J. D., Orban, P. C., Mossmann, H. & Rajewsky, K. *Science* **265**, 103–106 (1994).
13. Burgin, K. E. *et al. J. Neurosci.* **10**, 1788–1798 (1990).

Palaeoclimatology

Cool tropical punch of the ice ages

Christopher Charles

It seems incongruous, but many climatologists now believe that the key for unlocking the mysteries of the ice ages may be found in the tropics. Climate model simulations conducted by Webb *et al.*[1], published on page 695 of this issue, suggest a surprisingly effective means for cooling the ice-age tropics and, consequently, the entire Earth's surface. Meanwhile, three other studies — two in this issue, by Beck *et al.*[2] (page 705) and Bard *et al.*[3] (page 707), and one in *Paleoceanography* by Curry and Oppo[4] — describe observations, from various geological archives, of tropical sea surface temperature that combine to imply that the tropical oceans are dynamically involved in glacial cycles.

Anyone who has experienced the wrath of storms or droughts accompanying El Niño knows that even a relatively subtle redistribution of sea surface temperature in the tropics can influence climate globally. It wouldn't be unreasonable, therefore, to suppose that the tropical ocean was partially responsible for several of the most puzzling aspects of ice ages — the enormous amplification of small, orbitally induced changes in seasonality to produce huge ice sheets, the apparent interhemispheric synchroneity of glaciation, or the dramatic millennial-scale climate oscillations inferred from records such as the polar ice cores. But resolving where, when, by how much and (especially) why the tropical ocean cooled during glacial episodes remains remarkably difficult. The issue goes beyond merely interpreting the geological record; determining the behaviour of the tropical ocean during ice ages provides one measure of the general sensitivity of the Earth's climate system to any perturbation, including possible future anthropogenic effects.

It is well known that the ice ages as a whole were paced by variations in the Earth's orbital geometry that dictated the seasonal distribution of solar radiation over tens to hundreds of thousands of years[5]. Once mature, ice sheets several kilometres thick — for example, the Laurentide, which presided over North America roughly 20,000 years ago — undoubtedly helped maintain the cold conditions by cooling and drying the surrounding air and by reflecting solar radiation. However, the tropics were far removed from any direct influence of the ice sheets, and any orbitally induced changes in insolation should have been insignificant for the tropical ocean. So it is not straightforward to identify an external force capable of provoking the tropics into joining the ice ages.

Nevertheless, in the past two years a flood of geochemical and glaciological evidence[6–9] has cast serious doubt on the long-standing view that surface temperatures of the tropical oceans were relatively invariant throughout glacial cycles — the conclusion drawn by the CLIMAP project[10] conducted in the 1970s. Yet the matter is far from settled. Universal acceptance of these new data depends on the development of a physically plausible mechanism for sustained cooling of the tropics during ice ages, and the satisfactory reconciliation of disparate evidence for the temperature history of tropical oceans.

In view of these uncertainties, Webb *et al.*[1] set out to establish the requirements for tropical cooling in an atmospheric general circulation model. Their results run diametrically opposite to conventional wisdom —

by assuming essentially modern ocean heat transport in combination with other glacial boundary conditions (large ice sheets, lowered atmospheric CO_2), they found that the model produced widespread cooling throughout the tropics and subtropics. The cooling resulted from the fact that modern patterns of ocean transport in a glacial world created heat divergence in broad areas of the subtropics.

Once established, this initial condition then led to an array of feedbacks involving the model's radiation balance: evaporation rates fell, drastically reducing the water vapour in the atmosphere and therefore its greenhouse capacity; moisture (and latent heat) convergence in the tropics decreased; low clouds increased with enhanced vertical stability, raising the albedo. Upon equilibrium, the simulated surface temperature was a whopping 8 °C cooler globally (relative to modern simulations), including a 5.5 °C cooling in the tropics.

The implication is that an ocean-circulation scheme often considered necessary for deglaciation — an active thermohaline 'conveyor' delivering oceanic heat polewards — may, in certain circumstances, actually cool the Earth's surface through tropical feedbacks, driving the climate system to an intensely glacial state. Those who subscribe to the orthodox view that the North Atlantic was cold during glacial episodes because of a weakened conveyor circulation may be sceptical of this new hypothesis. To support the idea that, during glacial periods, the polewards transport of heat in the surface ocean was as vigorous as today, Webb *et al.* build on the evidence for a shallow overturning cell in the North Atlantic, one that probably produced so-called Glacial North Atlantic Intermediate Water[11].

Atmospheric general circulation models are not really equipped to deal with this type of argument about specific ocean-circulation regimes (or issues such as how the system might switch out of the cold state, or how ice sheets and decreased atmospheric CO_2 came about initially). So there are a number of questions that Webb and colleagues' simulations cannot address. However, in general, a dynamical ocean mechanism for cooling the tropics has several appealing advantages.

For example, it could explain the somewhat heterogeneous pattern of ice-age temperature change that emerges if one accepts the inferences from various geological records; unlike other possible mechanisms (such as changes in greenhouse gases), there would be no reason to expect a completely uniform response of tropical temperatures if ocean dynamics were involved. Also, the rapid, high-amplitude oscillations observed in many tropical records are more easily explained by the effects of ocean circulation, such as that proposed by Webb *et al.*, than by other conceivable influences; levels of atmospheric carbon dioxide[12], for example, changed too little and too gradually to be effective, and fluctuations in the other greenhouse gases (water vapour, methane) perhaps represented feedback amplifiers but were not the original cause of variation in tropical temperatures.

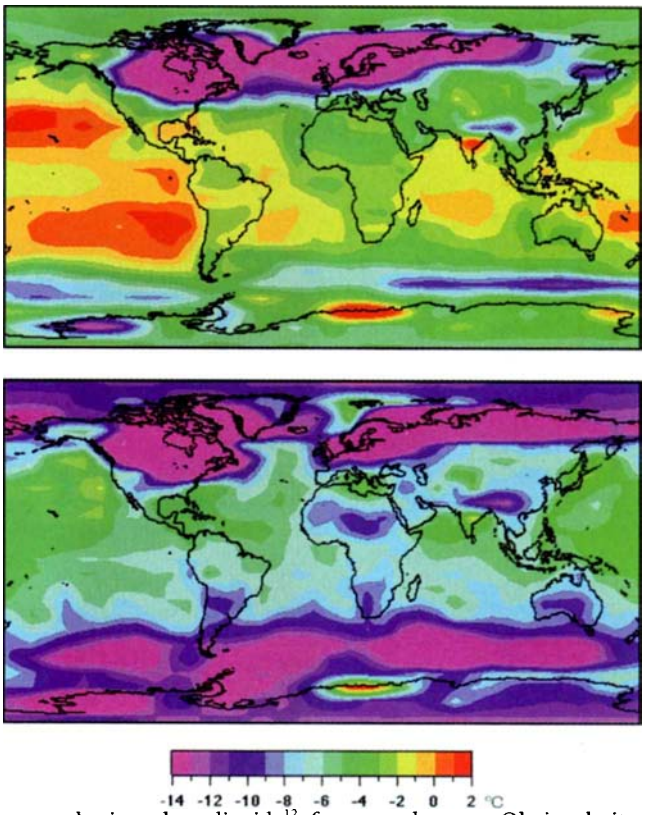

Figure 1 **Simulating ice-age climate: two experiments with the atmospheric general circulation model at the Goddard Institute for Space Studies. Top, the difference between modern annual average air temperature and the surface air temperatures for a standard ice-age climate simulation (using initial conditions from CLIMAP[10]). Bottom, as above, but showing the consequences of Webb and colleagues'[1] incorporation of modern patterns of heat transport in the oceans. Except for regions such as the North Atlantic, most of the Earth's surface, including the tropics, becomes substantially cooler.**

The three observational papers[2–4] highlight all of these considerations. Using a temperature index based on sedimentary alkenones, Bard *et al.*[3] demonstrate that temperature changes in the tropical Indian Ocean (of up to 3 °C) were strikingly well-correlated with glacial ice volume, and perhaps even with millennial-scale climate fluctuations in the Northern Hemisphere. Five-year-long segments of coral, analysed and dated with remarkable precision by Beck *et al.*[2], suggest that the tropical South Pacific remained quite cold (5 °C or more colder) until late into the last deglaciation, warming very rapidly after about 10,500 years ago to modern temperatures. Finally, from measurements of the isotopic composition of deep- and surface-dwelling foraminifera in a single sediment core from the Atlantic, Curry and Oppo[4] show that the variability in tropical sea surface temperatures (of 2–4 °C) was linked directly to deep-ocean circulation changes, even on millennial timescales.

Each of these records carries its own uncertainties (for example, the exact scaling of alkenone variability to temperature is open to question). But there is little doubt from these data that changes in sea surface temperatures in all tropical oceans took an active part in ice-age cycles, and that these temperatures could change abruptly.

Obviously, it will be necessary to produce a more comprehensive array of records extending at least through the Last Glacial Maximum (20,000 years ago). The difficulty is twofold: tropical deep-sea sediments with adequate resolution are rare; with corals, on the other hand, resolution is no problem, but finding and sampling a long continuous sequence is quite a challenge.

If nothing else, Webb and colleagues' simulations provide a useful focus for further investigation, because they emphasize the importance of understanding the variability in sea surface temperatures in regions such as the subtropical North Pacific (Hawaii). For those of us in the business of reconstructing the Earth's climate history, it is comforting to think that the secrets of the ice ages may be divulged in a place where, afterwards, one could sip drinks from a coconut. □

Christopher Charles is in the Scripps Institution of Oceanography, La Jolla, California 92093-0220, USA (e-mail: ccharles@ucsd.edu).

1. Webb, R. S., Rind, D. H., Lehman, S. J., Healy, R. J. & Sigman, D. *Nature* **385**, 695–699 (1997).
2. Beck, J. W., Récy, J., Taylor, F., Edwards, R. L. & Cabioch, G. *Nature* **385**, 705–707 (1997).
3. Bard, E., Rostek, F. & Sonzogni, C. *Nature* **385**, 707–710 (1997).
4. Curry, W. B. & Oppo, D. W. *Paleoceanography* **12**, 1–14 (1997).
5. Hays, J. D., Imbrie, J. & Shackleton, N. J. *Science* **194**, 1121–1132 (1976).
6. Guilderson, T .P., Fairbanks, R. G. & Rubenstone, J. L. *Science* **263**, 663–665 (1994).
7. Stute, M. *et al. Science* **269**, 379–383 (1995).
8. Thompson, L. G. *et al. Science* **269**, 46–50 (1995).
9. Schrag, D. P., Hampt, G. & Murray, D. W. *Science* **272**, 1930–1932 (1996).
10. CLIMAP Project Members *Science* **191**, 1131–1138 (1976).
11. Duplessy, J. C. *et al. Paleoceanography* **3**, 343–360 (1988).
12. Raynaud, D. *et al. Science* **259**, 926–934 (1993).

NATURE

100 YEARS AGO

In view of the importance which attaches to Dr. Yersin's discovery of the plague virus and its anti-toxin, the following notes on his work may be of interest.... While at Tonkin, in the spring of 1894, he received the request from the French Government to proceed to Hong Kong to study the plague which had recently broken out there. Yersin started off on his mission, and arrived in Hong Kong a few weeks after the plague had commenced its terrible career in that city – a career which had already claimed the lives of 300 Chinese, and which was yet to exact a tribute of over 100,000.... In these infected districts, one of the first things which attracted Yersin's attention was the extraordinary number of dead rats which lay about in all directions in the houses as well as in the streets; but, on inquiry, he soon learnt that this rat-mortality was a well-known forerunner of the plague, that the latter usually attacks animals such as rats and mice, and in the country districts swine and buffalos, before it touches human beings. An examination of these dead rats showed that their symptoms differed in no way from those which characterise the plague in man, and the extreme susceptibiity of these animals furnished Yersin at once with a valuable means of tracking out the virus.

From *Nature* 18 February 1897.

50 YEARS AGO

The system used at the Royal Cancer Hospital to record information numerically about cancer patients so that it can be transferred to a punched card and sorted mechanically is described by D. W. Smithers, K. M. H. Branson and H. O. Hartley.... The essential features of the system are the compilation of a special record card from notes on the patient, the information on the card being such that it can be expressed in numerical form and is suitable for rapid analysis by mechanical means. Filling in this card is the only extra clerical work required of the medical man.

From *Nature* 22 February 1947.

Many more extracts like these can be found in *A Bedside Nature: Genius and Eccentricity in Science, 1869–1953*, a 266-page book edited by Walter Gratzer. Contact David Plant (e-mail: subscriptions@nature.com).

Asthma

Blocking adenosine with antisense

Peter J. Richardson

Over the past decade, the widely recognized growth in the incidence of asthma has increased the need for new therapies. The aim of any asthma therapy is to control the inflammation and hypersensitivity of the airways that result from the condition. The purine adenosine has been implicated in both the development of bronchial hypersensitivity and the control of inflammation, so adenosine receptors have been suggested as possible therapeutic targets.

On page 721 of this issue, Nyce and Metzger[1] confirm that adenosine is involved in an animal model of allergic asthma, by using antisense oligodeoxynucleotides (ODNs) to reduce the number of adenosine A_1 receptors in the lung. The observed decrease in the constriction of airways confirms that the adenosine A_1 receptor is a potential therapeutic target for allergic asthma, and the results also show the potential of ODN-mediated control of gene expression in the treatment of a common disease.

In asthma, narrowing of the airways is caused by the exaggerated sensitivity of smooth muscle to constricting agents and inflammatory damage. In allergic asthma, a normally innocuous stimulus — such as the house-dust mite — causes the release of 'mediators' from mast cells (Fig. 1). These mediators constrict the airways, cause increased secretion of mucus (so blocking the already narrow airways) and attract inflammatory cells, particularly eosinophils and basophils, into the lungs. These inflammatory cells release enzymes that damage the surface epithelium, and other agents that both constrict the airways and attract more inflammatory cells, which in turn cause further damage.

ODNs act by sequence-specific hybridization to messenger RNA (Fig. 2). They then selectively prevent the translation of the RNA message into protein, and promote degradation of the message by ribonucleases. The potential of this approach lies in the ability to produce antisense ODNs that will hybridize to a message that has been transcribed from any gene of known sequence. Because the coding sequences of many human genes are already known, and the remainder will probably be identified in the near future, we may soon be able to inhibit the expression of any gene. There are problems associated with ODN-based therapy — particularly in terms of ODN stability and access to the target cells. However, the lung is an ideal tissue for testing the potential of the ODN approach because it has a large surface area for adsorption, and ODNs can easily be administered by aerosol.

It is particularly pleasing to see that Nyce and Metzger[1] have successfully used ODNs to control the synthesis of a specific protein. Four aerosol doses reduced the number of adenosine A_1 receptors in the lungs of allergic rabbits by around 75 per cent. As a result of this treatment, the airway constriction that was triggered by either adenosine itself, by histamine (which is a measure of airway hypersensitivity), or by the dust-mite allergen, was attenuated. Moreover, another ODN was almost as effective in reducing the level of the bradykinin B_2 receptor in these rabbits, illustrating the gene-specificity of the technique.

Do these results have any bearing on human asthma? Considerable progress has been made in identifying the processes and mediators that are involved in mast-cell activation (degranulation), inflammatory-cell infiltration and the development of airway hyper-reactivity[2]. Mast cells are generally thought to be critical for the development of asthma, suggesting that agents that can cause long-term inhibition of mast-cell degranulation may be of therapeutic benefit[3].

Two interesting changes that occur in the human lung with the onset of asthma are an

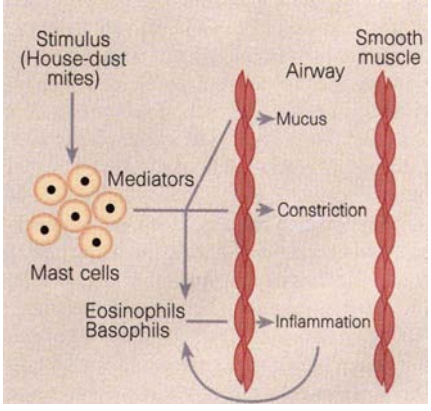

Figure 1 **The allergen-induced activation of mast cells is central to allergic asthma — mediators released from these cells have many effects, including airway constriction and the recruitment of inflammatory cells. Adenosine, acting through A_1 receptors, may increase the sensitivity of mast cells to allergens, promote airway constriction and mucus secretion, and stimulate inflammatory cells such as eosinophils and basophils.**

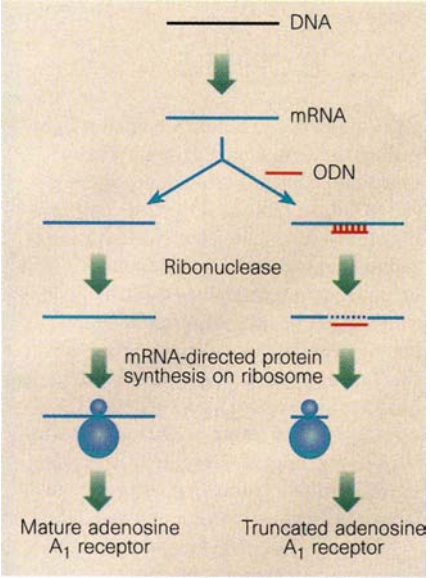

Figure 2 **Nyce and Metzger[1] have used antisense oligodeoxynucleotides (ODNs) to selectively inhibit the synthesis of adenosine A_1 receptors in rabbit lungs. Transcription of messenger RNA from the gene for the A_1 receptor is followed by synthesis of the receptor protein on ribosomes. The ODN consists of deoxynucleotides that are linked by phosphorothioate linkages (which confer stability to DNA-degrading enzymes). The ODN hybridizes by Watson–Crick base-pairing to the mRNA, to generate a substrate for ribonucleases, particularly RNase H, which degrade the RNA portion of the hybrid. ODNs must be long enough to hybridize only to the mRNA of interest, they need to be stable, and they must be able to enter cells and activate ribonucleases. As the mRNA no longer encodes the full-size protein, fewer receptors are synthesized, and the normal turnover of the adenosine A_1 receptor reduces the total number of receptor molecules.**

increase in the mucosal concentration of adenosine, and the appearance of the adenosine A_1 receptor. The A_1 receptor is one of four known cell-surface adenosine receptors, and it is very difficult to detect in normal lung tissue[4]. But in the asthmatic lung, its presence is associated with the ability of adenosine to induce bronchoconstriction — an effect that is not seen in normal lungs. So adenosine and the A_1 receptor seem to be central players in the development of airway hypersensitivity and the inflammatory response to allergens.

It is now important that we understand how, and where, the adenosine A_1 receptor exerts its effects in the human asthmatic lung. There is already evidence that adenosine can activate mast cells, and that this is probably how it elicits bronchoconstriction in asthmatic patients[5,6]. But in normal lungs, the adenosine A_3 receptor is thought to mediate the adenosine-dependent activation of mast cells[7], and it is not clear whether the A_1 receptor can mediate mast-cell activation in the asthmatic lung.

There is also evidence that the adenosine A_1 receptor elicits bronchospasm in the absence of mast-cell activation[8], so the A_1 receptor may have many effects — for instance, on neural pathways, smooth muscle, and other inflammatory cells. In addition, the A_1 receptor activates some inflammatory cells that are inhibited by the adenosine A_2 receptor[9,10], suggesting that ablation of the A_1 receptor in the asthmatic lung would result in adenosine-mediated inhibition of inflammatory-cell function. To clarify this rather confusing situation, the site at which A_1 receptors are expressed in the asthmatic lung needs to be determined. Interestingly, theophylline, which blocks both A_1 and A_2 receptors, is used to treat asthma, although its mechanism of action is not restricted to adenosine-receptor blockade. But now, in the light of Nyce and Metzger's results[1], it would be interesting to investigate the effects of selective antagonists or ODNs to the A_1 (and presumably A_3) receptors in human asthma. □

Peter J. Richardson is in the Department of Pharmacology, University of Cambridge, Tennis Court Road, Cambridge CB2 1QJ, UK.

1. Nyce, J. W. & Metzger, W. J. *Nature* **385,** 721–725 (1997).
2. Warner, J. A. & Kroegel, C. *Eur. Resp. J.* **7,** 1326–1341 (1994).
3. Wasserman, S. I. *Am. J. Resp. Crit. Care Med.* **150,** S39–S41 (1994).
4. Dixon, A. K., Gubitz, A. K., Sirinathsinghji, D. J. S., Richardson, P. J. & Freeman, T. C. *Br. J. Pharmacol.* **118,** 1461–1468 (1996).
5. Holgate, S. T. *et al.* in *Topics and Perspectives in Adenosine Research* (eds Gerlach, S. & Becker, B.) 614–624 (Springer, Berlin, 1987).
6. Polosa, R. *et al. Am. J. Resp. Crit. Care Med.* **151,** 624–629 (1995).
7. Linden, J. *Trends Pharmacol. Sci.* **15,** 298–306 (1994).
8. Meade, C. J., Mierau, J., Leon, I. & Ensinger, H. A. *J. Pharmacol. Exp. Ther.* **279,** 1148–1156 (1996).
9. Cronstein, B. N. *et al. J. Immunol.* **148,** 2201–2206 (1992).
10. Peachell, P. T. *et al. J. Pharmacol. Exp. Ther.* **256,** 717–726 (1991).

Quantum optics

The amazing atom laser*

Keith Burnett

The word laser now has a strong emotional impact, conjuring up images of space-battles and high-tech surgery. There was a time when this strange acronym, as yet unloved by science-fiction writers, conjured up nothing at all to a general audience. What is more, scientists thought of the laser as nothing more than a curiosity brought forth by optical physicists and engineers, fascinating perhaps, but little more. It was termed, admittedly by the unkind, 'a solution in search of a problem'.

We now have the beginnings of a new type of solution — a new type of laser. This is not a source of light but of matter, in the form of alkali atoms. In the 27 January issue of *Physical Review Letters*[1], a group at MIT led by Wolfgang Ketterle describe an 'output coupler' that allows pulses of matter to escape in a narrow beam from a trapped Bose–Einstein condensate (Figs 1 and 2). In the 31 January edition of *Science*[2], the same group show that this beam is coherent, an essential test of laser behaviour.

The possibility of an atom laser should not be such a shock if we recall that all matter has a wave-like nature, just like light, with each particle's de Broglie wavelength determined by its momentum. So if light is made of waves and can be produced in laser form, why not a laser-like source of matter waves?

The problem is how to do it. In the case of light, we rely on a very important property of photons. Energy is first put into a material form — the excited states of atoms or molecules — and then re-emitted in the form of photon energy packets; lasers are possible because photons can be created with exactly the same direction and speed as those that are already travelling through the medium. This means that the number of photons travelling through a laser medium can become enormously amplified. This property was elucidated first by Einstein and Bose in their studies of the implications of wave mechanics for the theory of radiation.

So can this idea be extended from photons to other particles, such as atoms? Indeed it can, if, like photons, the particles are Bose–Einstein particles (bosons for short). All particles are either bosons, with an integral number of spin units,

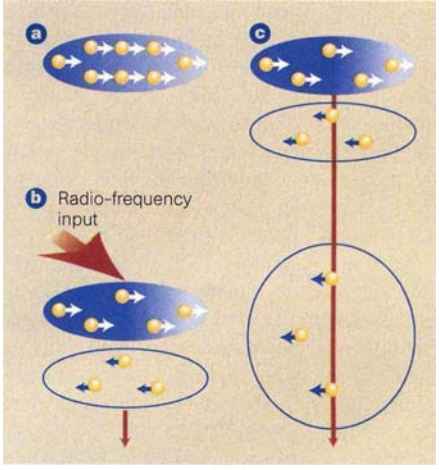

Figure 1 **Radio leakage. The magnetically trapped Bose–Einstein condensate (a) is separated into two states with opposing spins by a radio-frequency input (b). The state with flipped spin is no longer held by the magnetic trap, and so falls out (c).**

*This article is reprinted from the 6 February issue (*Nature* **385,** 482–483; 1997). Because of a production error, an incomplete version of the article appeared in the US edition of *Nature*, for which we apologize.

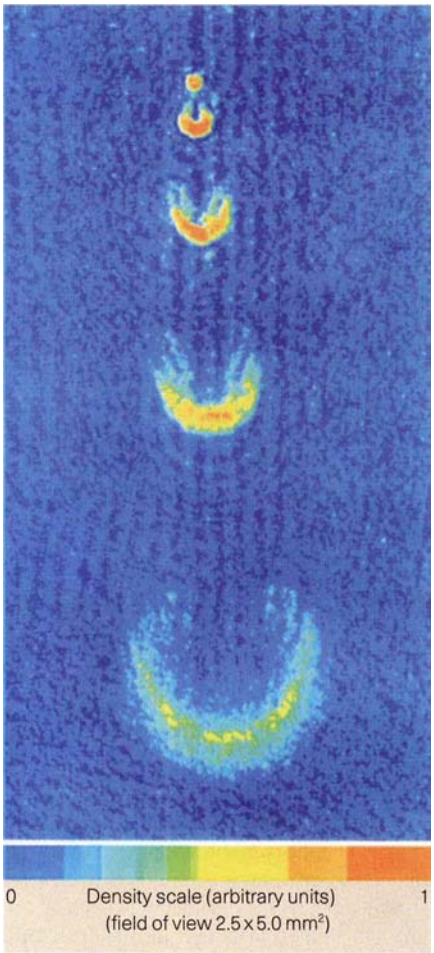

Figure 2 **The atom laser in action. Drops of coherent sodium fall under gravity, about five milliseconds apart.**

or fermions, with half-integral spin. The crucial physical difference between the two is that no two fermions can occupy the same quantum state, so coherent behaviour is impossible.

Most alkali metals are bosons, so a bunch of alkali atoms can join together in identical states of motion. At sufficiently low temperatures, Einstein and Bose showed that the propensity to do this sets in with a vengeance, and all the atoms condense into the lowest-energy state — hence the term Bose–Einstein condensation. It is done in practice by cooling a magnetically trapped gas of atoms to extraordinarily low temperatures, below a microkelvin. So far, no other way has been found to make a pure laser-like assembly of atoms. A Bose–Einstein condensate was first made using rubidium in 1995, at the Joint Institute for Laboratory Astrophysics in Colorado[3], and later that year at MIT.

In the new experiments at MIT, they have made the next step in producing a laser-source of atoms: the smooth transference from the magnetic box in which the atoms are corralled to an atomic beam[1] (Fig. 1). At present, the beam is simply collimated by the magnetic fields of the trap, but in principle it can be directed at will (for animations and other details see http://bink.mit.edu/dallin/news.html#matterwave). Ketterle and colleagues have also shown how to test the properties of the beam very precisely[2]. They made a pair of sources, shining both of them on a screen, and looking at the regions where they overlap. If two such beams are coherent (that is, pure enough in wavelength) then a regular pattern of stripes will be observed on the screen, just as the MIT group saw.

These experiments have produced exquisite results that can go directly into the textbooks. There are other aspects of laser light, such as continuous output and stable intensity, that cannot yet be reproduced in the matter beam, and many would want to reserve the term atom-laser for the next generation of sources. But what cannot be doubted is that a huge step has been made towards making laser-like sources of atomic de Broglie waves a tool for science and technology.

The new source shares many of the practical advantages of laser light. It is an intense, precisely directed, beam of matter. It should be possible to focus such a beam using diffraction gratings or the equivalent of lenses for atomic waves — an atom passing through a laser beam that has an intensity gradient feels a position-dependent force, so a beam with the right geometry acts as a lens. Therefore, atoms can be directed to a point or feature on a material surface, for example. This is precisely what we need to produce systems on the nanometre scale, such as micro- (or rather nano-) electronic circuits.

Coherent matter waves may also surpass laser light beams as fundamental measuring sticks. The spacing between the lines on the ruler is set by the beam's wavelength, which is around a half a micrometre for visible light. But with matter waves, the wavelength can be tuned by changing their speed (light, of course, moves with a fixed speed in a given medium) and one should be able to produce matter waves with wavelengths a hundred times smaller than that of a visible photon. Accurate, continuous-wave atomic clocks will permit a wide range of new measurements. Atom-laser interferometers may be the best gyroscopes and accelerometers, making more precise measurements of gravity than ever before. They will also be used to test certain quantum theories that predict a divergence from conventional quantum behaviour on large scales. □

Keith Burnett is in the Clarendon Laboratory, University of Oxford, Parks Road, Oxford OX1 3PU, UK.

1. Mewes, M.-O. *et al. Phys. Rev. Lett.* **78,** 582–585 (1997).
2. Andrews, M. R. *et al. Science* **275,** 637–641 (1997).
3. Anderson, M. H., Ensher, J. R., Matthews, M. R., Wieman, C. E. & Cornell, E. A. *Science* **269,** 198–201 (1995).

Daedalus

Sheets of light

Optical fibres can not only transmit light-pulses; they can amplify them. When illuminated by a suitable pumping radiation, an erbium-doped silica fibre becomes a distributed laser, amplifying the pulses that travel along it. Daedalus is now extending the principle to two dimensions.

Imagine, he says, an optically transparent flat sheet a wavelength or so thick, doped with lasing material, and coated onto a transparent support of lower refractive index. Pump-radiation shines into the sheet through the support; a number of optical emitters around its periphery can launch pulses into it on command.

These pulses would travel and amplify out in two dimensions. Where they hit the edges of the sheet they would be reflected back into it. Where two such pulses passed through each other, each would lose gain as it entered a region depleted of excited states by the previous passage of the other. Highly complex energy distributions would develop; the whole thing would be an extremely subtle optical computer.

More usefully, however, it would be a splendid flat visual display screen, lit by the pumping radiation beamed into it from behind. Its brightness at any point would depend on the local attenuation of this radiation. This in turn would depend on how recently it had been depleted by the passage of a pulse. Any possible picture could be generated by a suitable choice of pulse-patterns from the emitters around the edge of the sheet. To compute the pattern needed to generate a given picture would be very tricky; but the resulting scanless high-resolution image could be updated continuously at megahertz rates.

A simpler and cheaper two-dimensional laser would be an oil slick on water. Such a slick can be a few wavelengths thick, or even thinner. It has optically smooth surfaces; its refractive index exceeds that of water and could trap radiation within it by total internal reflection, even in the presence of ripples. It could easily dissolve a suitable lasing organic erbium complex. And it could cover a huge area.

A pond or lake covered by a lasing slick would be a wonderful trap for solar energy. This powerful optical pump would excite it not in pulse mode, but continuously. The lake could be ringed with immersed reflectors, except for a small region bearing a photovoltaic-cell array. The intercepted energy would bounce around the slick till it hit the photocells and was absorbed. All the energy captured by the whole lake would be neatly delivered to that one point.

David Jones

Giant female or dwarf male spiders?

Explanations of the difference in size between male and female spiders usually assume male dwarfism, thus implying that males, rather than females, have changed in size[1–3] (but see refs 4–6). A well-known case of sexual dimorphism is the orb-weaving tetragnathid spider genus *Nephila* (Fig. 1), in which female body length is up to six times greater than that of the 'dwarf' males. Dimorphism could evolve by a change in the size of females or males, or even both. Without information on historical patterns of size change in each sex, it is difficult to distinguish whether females are giants, males are dwarfs, or both.

Vollrath and Parker[6] used life-history data on *N. clavipes* in their Letter to illustrate the evolution of sexual size dimorphism in taxa with sedentary females and roving males. High mortality among searching males should bias the adult sex ratio towards females, reduce competition between males, and favour male dwarfing by early maturation. So dimorphism in *Nephila* should be due to evolutionary size reduction in males, and males should mature in fewer moults than their 'undwarfed' sister taxa.

We have reconstructed the phylogeny[7–9] of several orb-weaving spider lineages that include dimorphic taxa, including *Nephila* (Fig. 2). Female *Nephila* (and other nephilines like *Nephilengys* and *Herennia*) are much larger than their ancestors. Males are of similar size or even larger. It seems likely that male nephilines are not dwarfs, but the females are giants. Likewise, there is no definitive evidence that nephiline males mature in fewer moults than their monomorphic ancestors (few data are published), but females do take more moults to mature than their ancestors[10,11]. Although Vollrath and Parker's model could apply to verified cases of male dwarfism, it may not be appropriate in *Nephila*.

Figure 1 **The golden orb spider *Nephila clavipes* male (top) and female (bottom).**

In fact, evolution of dimorphism among orb-weaving spiders is much more complex. The phylogeny (Fig. 2) suggests ten changes in dimorphism status: four gains and six losses (hence reversion to monomorphism). Changes in male and female body size are substantially decoupled. In all 79 genera in the analysis (and in spiders generally) females are larger than males. Of these genera, 23 contain one or more species in which the difference is large enough to qualify as 'dimorphism' (Fig. 2). Many of these dimorphic genera are very close relatives, so that most cases of dimorphism represent simple inheritance from a common ancestor, not independent origins of dimorphism in every dimorphic species.

In their regressions of male on female body size, Vollrath and Parker did not take close phylogenetic relationships into account but treated each species as an independent data point, so artefactually inflating the sample size and possibly misconstruing statistical significance[12]. Until the data are reanalysed properly, claims of significantly different sexual size ratios in different taxa or foraging guilds should be viewed with caution.

In summary, phylogenetic reconstruction suggests a different view from that of Vollrath and Parker: dimorphic species of the orb-weaving spider taxa shown here, and especially in *Nephila*, are more likely to be due to female giantism than male dwarfism. Dimorphism seems to have appeared and disappeared over time in various ways. The biology of each of these evolutionary pathways may be distinctive and require its own explanation. More data may change the phylogenetic reconstruction presented here, but the basic point remains: sexual size dimorphism is the ratio of two quantities, either of which may have changed. Without a phylogeny to distinguish between the possibilities, the application of models devoted to one mechanism can go awry.

Jonathan A. Coddington
Department of Entomology, National Museum of Natural History, Smithsonian Institution, Washington DC 20560, USA
Gustavo Hormiga
Department of Biological Sciences, George Washington University, Washington DC 20052, USA
Nikolaj Scharff
Department of Entomology, Zoological Museum, University of Copenhagen, Copenhagen DK 2100, Denmark

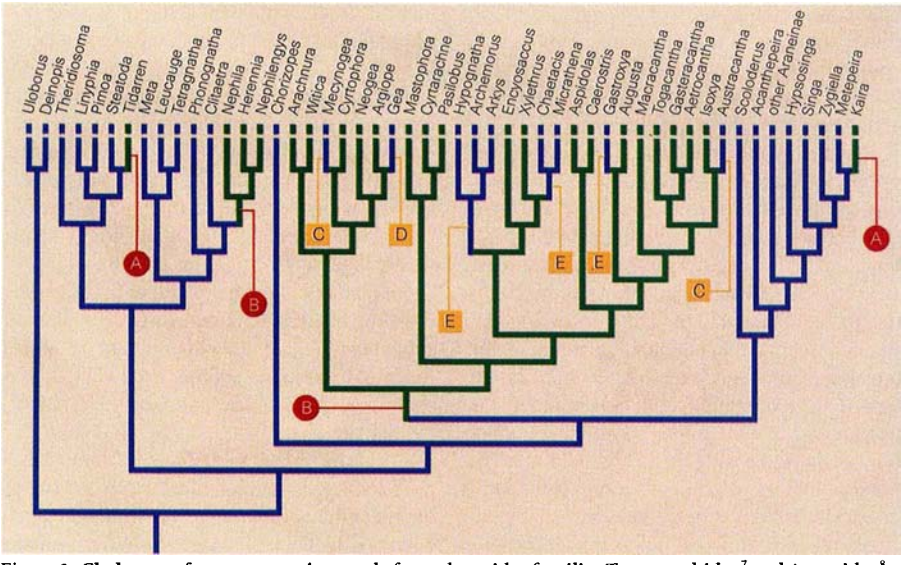

Figure 2 **Cladogram for a taxonomic sample from the spider families Tetragnathidae[7] and Araneidae[8], plus their outgroups[9] ('other Araneinae' include 22 genera, none of them relevant to reconstructing the history of dimorphism). Green and blue branches indicate dimorphic and monomorphic lineages, respectively. For every genus (taken from museum specimens and the literature) body size was expressed as mean adult body length. We used Wagner (linear) parsimony[13–15] to reconstruct the history of mean body-size change of each sex in each family and computed female/male size ratios on all branches (dimorphism is defined as a ratio ≥ 2 or ≤ 0.5). If overlapping ranges at adjacent branches made it ambiguous as to whether a change had occurred, we conservatively assigned no change. Red circles, origin of dimorphism; yellow squares, reversal to monomorphism. A, males decrease, females increase; B, females increase; C, males increase; D, males and females decrease; E, females decrease.**

1. Darwin, C. *The Descent of Man, And Selection in Relation to Sex* (Murray, London, 1871).
2. Elgar, M. A., Ghaffar, N. & Read, A. F. *J. Zool.* **222**, 455–470 (1990).
3. Vollrath, F. *Z. Tierpsychol.* **53**, 61–78 (1980).
4. Head, G. P. *Evolution* **49**, 776–781 (1995).
5. Gerhardt, U. *Z. Morphol. Okol. Tiere* **1**, 567–618 (1924).
6. Vollrath, F. & Parker, G. A. *Nature* **360**, 156–159 (1992).
7. Hormiga, G., Eberhard, W. G. & Coddington, J. A. *Aust. J. Zool.* **43**, 313–364 (1995).
8. Scharff, N. & Coddington, J. A. *Zool. J. Linn. Soc.* (in the press).
9. Griswold, C. E., Coddington, J. A., Hormiga, G. & Scharff, N. *Zool. J. Linn. Soc.* (in the press).
10. Bonnet, P. *Graellsia* **29**, 183–200 (1975).
11. Robinson, M. H. & Robinson, B. *Smithson. Contr. Zool.* **218**, 1–22 (1976).
12. Felsenstein, J. *Am. Nat.* **125**, 1–15 (1985).
13. Farris, J. S. *Syst. Zool.* **19**, 83–92 (1970).
14. Swofford, D. & Maddison, W. P. *Math. Biosci.* **87**, 199–229 (1987).
15. Maddison, W. P. & Maddison, D. R. *MacClade: Analysis of Phylogeny and Character Evolution*, version 3.0 (Sinauer, Sunderland, MA, 1992).

Vollrath and Parker reply — Spider males are smaller than females, with very few exceptions[1,2]. This sexual dimorphism is an ancient trait: males are marginally smaller in liphistiid spiders ('living fossils' with a segmented abdomen)[3] and trapdoor spiders[4]. Compared with 'modern' labidognath spiders[5–7], these 'primitive' orthognath spiders typically have more instars (moulting stages) and larger body size. Coddington *et al.* raise two important questions. First, does modern *Nephila* have larger females and smaller males than its ancestors? Second, did ancestral females have fewer instars, and males more, than the average for this taxon?

Answering these questions with morphological data alone is difficult, if not impossible, especially if the cladistic hypothesis is contested (see refs 8–10). It may be more profitable to seek answers in life-history data. Puzzling life-history traits (measured on the species level) are often best explained by models[11]. Our[1] puzzle was the very real observation that males of the golden orb spider *N. clavipes* are much smaller than their females, although all measured reproductive advantages suggested selection for a larger male size[12]. In females, large size always benefits fecundity[13–15].

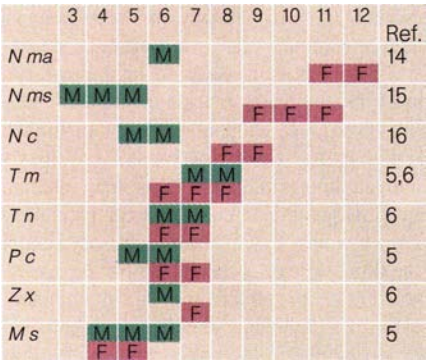

Figure 3 **Number of moults in 'tetragnathid' spiders. M, males; F, females. *N ma, Nephila maculata; N ms, N. madagascariensis; N c, N. clavipes; T m, Tetragnatha montana; T n, T. nigrita; P c, Pachyganthat clercki; Z x, Zygiella x-notata; M s, Meta segmentata.* The original data (refs given) have been normalized to count from the instar (stadium) that leaves the eggsac (all have 1 extra larval instar inside the eggsac). Note that in the ancestral *Atypus karschi*[4] males mature in 8 or 9 and females in 9–11 instars; males of the 'living fossil' *Liphistius*[3] have between 10 and 31 instars. Generally, the more instars, the larger the spider.**

Our model[1] is designed to predict the extent of sexual dimorphism in a species (see also ref. 16). It trades off the mortality rate of each sex (which favours early reproduction, and hence smaller adult body size) against the reproductive advantages of later maturation (being bigger can mean laying more eggs or gaining greater mating prospects). The ratio of the evolutionarily stable body sizes for the two sexes generates the 'evolutionarily stable strategy' of sexual dimorphism. Thus we did not set out to prove absolute selection to reduce male size, but instead predicted quite generally the *relative* size of the two sexes from life-history traits that can be measured in the field and the laboratory.

When related to data about *N. clavipes* and similar species, the model predicted a general trend for dwarf males (dwarf relative to females) to occur in species with 'sit-and-wait' habits as opposed to searching and hunting habits: males must rove (and consequently suffer high mortality) to find females that are sedentary. A simple cladistic analysis (using accepted traits on a family level) seemed to confirm this trend and validate our model (Fig. 3 of ref. 1). The best confirmation is the discovery[17] of true dwarf males in a mygalomorph (ancestral) spider living in a marginal, high-mortality habitat, where the burrowing females are less at risk than the roving males.

When proposing female giantism (as opposed to male dwarfing) for *N. clavipes*, Coddington *et al.* make various assumptions. They claim that the males are typical for this taxon in size and instar number whereas the females are atypical in both. But in fact the data are ambiguous (Fig. 3). First, it seems that *Nephila* is unusual for tetragnathids (and most other spiders) in having non-overlapping male/female instar numbers. Second, *Nephila* can have rather few male instars. Third, the number of female instars is indeed large for tetragnathids, and so is body size. But this is an ancestral trait and could be fitted to phylogenetic hypotheses placing *Nephila* near the beginning of the ecribellate branch of orb weavers[8,10]. This would imply that other tetragnathids have a reduced number of instars. Finally, *Nephila* might not even be a true tetragnathid[8,10].

It is never easy to decide how to read phylogenetic information. But the pertinent point of the controversy of mini males versus giant females is that we desperately need more life-history data on unusual spiders, that is, species with extreme or absent sexual size dimorphism. This is the only way to solve a puzzle that intrigued Darwin and many researchers since: a puzzle that concerns the difference between male and female sizes, not their absolute values.

Fritz Vollrath
Department of Zoology, Universtetet B135, DK-8000 Aarhus C, Denmark
Geoff A. Parker
Department of Evolutionary Biology, PO Box 147, University of Liverpool, Liverpool L69 3BX, UK

1. Vollrath, F. & Parker, G. A. *Nature* **360**, 156–159 (1992).
2. Head, G. P. *Evolution* **49**, 776–781 (1995).
3. Schwendinger, P. J. *Zool. Scripta* **19**, 331–351 (1990).
4. Miyashita, T. *Acta Arachnol.* **41**, 177–186 (1992).
5. Schaefer, M. *Zool. Jb. Syst. Jena* **103**, 127–289 (1976).
6. Juberthie, C. *Bull. Soc. Hist. Nat. Toulouse* **89**, 299–318 (1954).
7. Bonnet, P. *Bull. Soc. Entomol. France* **1926**, 67–69 (1926).
8. Eberhard, W. G. *Evolution* **36**, 1067–1095 (1982).
9. Shear, W. A. in *Spiders: Webs, Behavior and Evolution* (ed. Shear, W. A.) 364–400 (Stanford Univ. Press, 1986).
10. Coddington, J. A. in *Spiders: Webs, Behavior and Evolution* (ed. Shear, W. A.) 319–363 (Stanford Univ. Press, 1986).
11. McNamara, J. M. & Houston, A. I. *Nature*, **380**, 215–221 (1996).
12. Vollrath, F. *Z. Tierpsychol.* **53**, 61–78 (1980).
13. Robinson, M. H. & Robinson, B. *Smithson. Contr. Zool.* **218**, 1–22 (1976).
14. Bonnet, P. *Bull. Soc. Zool. France* **54**, 501–523 (1929).
15. Vollrath, F. *Verh. Naturwiss. Verein. Hamburg* **26**, 277–289 (1983).
16. Parker, G. A. *J. Fish Biol.* **41**, (suppl. B) 1–20 (1992).
17. Main, B. Y. *Acta Zool. Fenn.* **190**, 273–278 (1990).

A gene family of silicon transporters

Silicon is essential in biological systems, affecting development and cellular metabolism[1–4]. In polymerized form, as silica, it is a biological material with valuable structural characteristics[2]. Yet little is known at the molecular level about how cells transport, process and use silicon. Here we report the isolation and functional expression of complementary DNAs encoding silicon transporters from the marine diatom *Cylindrotheca fusiformis*. These cDNAs represent members of a previously undescribed gene family, and provide insight into the molecular basis of silicon transport across biological membranes and cellular silicon processing.

In certain diatom species, silicon transport increases tenfold after DNA synthesis begins and increases to a similar extent when silicon levels are low[5]. When silicon is re-supplied, transport levels rapidly decrease[5]. These changes are probably due to the synthesis and degradation of specific transport proteins[5]. We have generated cDNA libraries from silicon-responsive genes[6], and here identified six cDNAs with identical common sequence. These were derived from messenger RNA whose levels responded (Fig. 1a) as would be expected of a silicon transporter[5]. After cloning the 3′

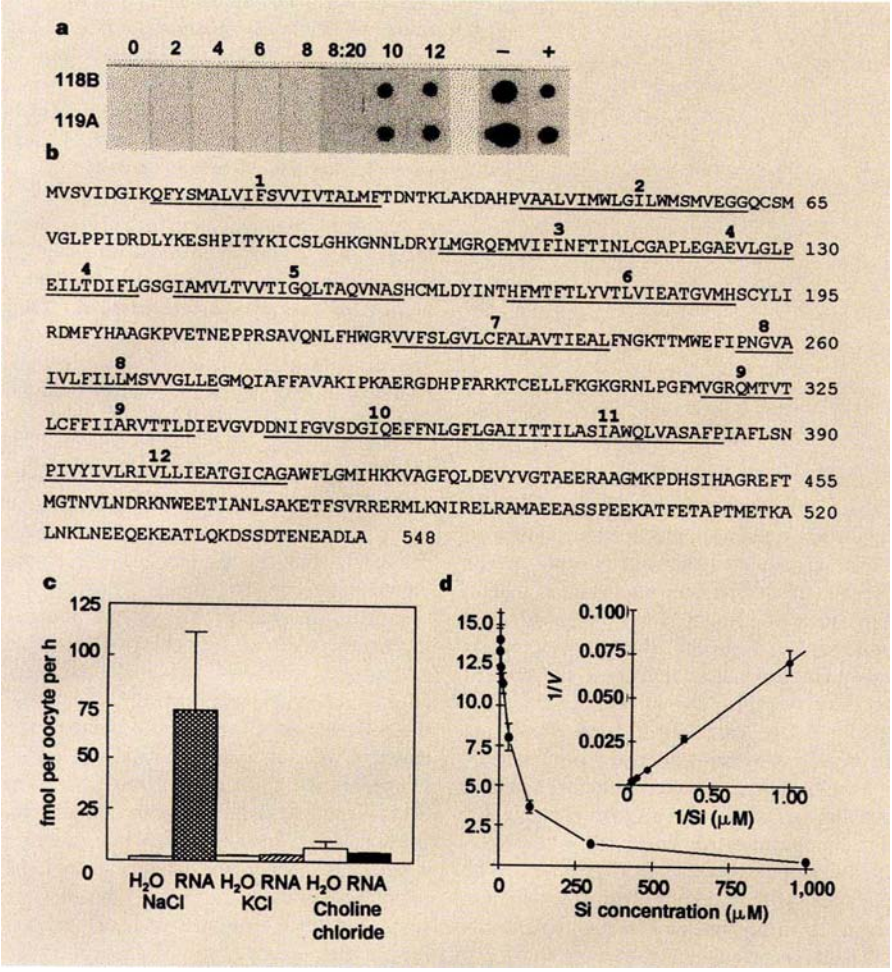

Figure 1 a, **Expression levels of mRNA encoding potential silicon transporters during the cell cycle and in response to silicon starvation and recovery. Clones[6] are indicated on the left. Conditions of silicon starvation (−) and replenishment (+) and the time (in h) after reillumination during a light/dark synchrony are indicated. In the light/dark synchrony, DNA synthesis began at 8 hr 20 min. (See ref. 6 for experimental details.)** b, **Deduced amino-acid sequence of the combined DNA sequences of clone 119A and its 3′ RACE[7] products (GenBank accession no. U63417). Potential membrane-spanning regions are underlined and numbered above. Amino-acid residue numbers are indicated on the right.** c, **$^{68}Ge(OH)_4$ uptake in water and SIT1 RNA-injected oocytes assayed under conditions of 115 mM NaCl, KCl or choline chloride. For uptake experiments, the original untranslated region of the SIT1 clone was modified, increasing expression levels 4.7-fold.** d, **Competition for $^{68}Ge(OH)_4$ uptake in RNA-injected oocytes by increasing amounts of unlabelled silicic acid (Si). Inset, Lineweaver–Burke plot of data, accounting for the isotope-dilution effect[8], reveals a K_s of 30 μM.**

end using a rapid-amplification of cDNA ends (RACE) technique[7], translation of the complete sequence of the longest clone (1,662 base pairs) revealed an open reading frame of 548 amino acids (Fig. 1b). The open reading frame has no significant match to any other known sequences, and our analysis suggests that it has 12 potential transmembrane regions (Fig. 1b), a common motif in transport proteins.

To test directly whether the cDNA encodes a silicon transporter, we injected RNA transcribed *in vitro* from the clone into *Xenopus laevis* oocytes and assayed them for the uptake of germanium [$^{68}Ge(OH)_4$], as a silicon analogue tracer[5,8]. Uptake of $^{68}Ge(OH)_4$ for water-injected control oocytes showed background levels. With RNA-injected oocytes, we observed significant uptake, up to 84 times higher than background. Uptake is sodium-dependent (Fig. 1c), as shown previously in diatom whole-cell uptake experiments[9].

Unlabelled silicon added in increasing amounts competes for germanium uptake (Fig. 1d), also as shown in diatoms[8]. A half-saturation constant (K_s) of 30 μM (V_{max} = 436 fmol per oocyte per h) for silicon uptake was determined (Fig. 1d inset), accounting for the isotope-dilution effect[8]. These data show that we have isolated a cDNA encoding a silicon transporter from the diatom; we named this clone SIT1 (silicon transporter 1).

We have isolated at least five additional types of SIT1 homologous clones from cDNA and genomic libraries (unpublished data), indicating that SIT1 is a member of a previously undescribed gene family. The amino-acid sequences are 90% identical in the potential transmembrane region, but are much less highly conserved (45–57% identity) in the carboxy-terminal portion. The carboxy-terminal end is sometimes responsible for targeting transport proteins to specific cellular locations[10]. It is therefore possible that these genes encode silicon transporters targeted to different cellular compartments.

To our knowledge, this is the first time that clones encoding proteins that interact specifically with silicon, and that transport silicon, have been isolated and functionally characterized. Further characterization of the SIT gene family will be valuable in extending our understanding of how silicon is transported and processed in the cell and how it affects cellular metabolism, as well as in devising biomimetic approaches to silicification.

Mark Hildebrand, Benjamin E. Volcani
Marine Biology Research Division, Scripps Institution of Oceanography, University of California, San Diego, La Jolla, California 92093-0202, USA
Walter Gassmann*, Julian I. Schroeder
Department of Biology and Center for Molecular Genetics, University of California, San Diego, La Jolla, California 92093-0116, USA

1. Bendz, G. & Lindqvist, I. (eds) *The Biochemistry of Silicon and Related Problems* (Plenum, New York, 1978).
2. Simpson, T. L. & Volcani, B. E. (eds) *Silicon and Siliceous Structures in Biological Systems* (Springer, New York, 1981).
3. Evered, O. & O'Connor, M. (eds) *Silicon Biochemistry: Ciba Foundation Symposium 121* (Wiley, Chichester, 1986).
4. Epstein, E. *Proc. Natl Acad. Sci. USA* **91**, 11–17 (1994).
5. Sullivan, C. W. *J. Phycol.* **13**, 86–91 (1977).
6. Hildebrand, M. *et al. Gene* **132**, 213–218 (1993).
7. Frohman, M. A., Dush, M. K. & Martin, G. R. *Proc. Natl Acad. Sci. USA* **85**, 8998–9002 (1988).
8. Azam, F. *Planta* **121**, 205–212 (1974).
9. Bhattacharyya, P. & Volcani, B. E. *Proc. Natl Acad. Sci. USA* **77**, 6386–6390 (1980).
10. Verhey, K. J., Hausforff, S. F. & Birnbaum, M. J. *J. Cell Biol.* **123**, 137–147 (1993).

*Present address: Department of Plant Biology, 111 Koshland Hall, University of California, Berkeley, California 94720-3102, USA.

Hydration in electrical double layers

The interaction between two surfaces separated by an electrolyte (an electrical double layer) is a fundamental determinant of the behaviour of colloids. Direct measurement of this interaction[1,2] revealed a strong, approximately exponential, short-range repulsion that has been interpreted as an effect of the hydration structure surrounding the ions. This exponential consists of a series of steps (at high electrolyte concentrations) and oscillations (at lower concentrations)[3,4]. There is still no generally accepted explanation for strong exponential

repulsion. In their recent Review Article[5] Israelachvili and Wennerström suggest that it is caused by the finite size of adsorbed hydrated counterions. Here I report calculations of the interaction between surfaces in an aqueous solvent showing that the repulsion is related to the hydration of ions in the double layer, although the full picture is more complex than originally envisaged.

My calculation is based on oscillatory ion–ion potentials of mean force obtained in molecular model simulations[6,7] and adopted into the primitive model of electrolytes[8]. Using this much-improved primitive model, I calculated the double-layer interaction using the anisotropic hypernetted chain (AHNC) method[9]. The calculation procedure is well defined, and there are no free parameters. The largest error is probably that associated with the ion–water potentials used in the simulations.

The potential of mean force between ions or ionic groups can be represented as a sum of the asymptotically exact Coulomb force in a dielectric continuum, the core interaction, and the oscillatory contribution from the hydration structure of ions. Using the potentials evaluated[6,7] for NaCl ion pairs, I calculated the interaction of surfaces with a high negative charge in NaCl electrolyte. Before 'switching on' the hydration part of the potential, one finds conventional double-layer repulsion typical of a dielectric continuum solvent (see Fig. 1).

When the hydration potential is included in the calculation, the altered behaviour corresponds closely to observations in two respects. First, at large separations, I found asymptotically exact exponential decay, but with greatly reduced magnitude. From measurements at separations larger than 20 Å it seems that most counterions have adsorbed to the surface[1]. Second, when surfaces are brought closer together, a much stronger repulsion is observed (the 'hydration force' in refs 1–4).

AHNC calculations show that accurate solutions of the primitive model indicate a higher counterion density near a surface and hence a more effective screening of the surface charge than suggested by the Poisson–Boltzmann equation. Including the oscillatory potential of mean force between the ions in the calculations greatly increases the tendency towards increased counterion density, as counterions near a surface assume separations corresponding to the minima of the mutual potential. This denser layer of favourably packed hydrated counterions (the Stern layer) extends about 6–7 Å away from the surface and causes the apparent reduction of the surface charge or surface potential.

If surface separations are decreased to about 14 Å, denser surface layers come into contact, resulting in stronger repulsion that

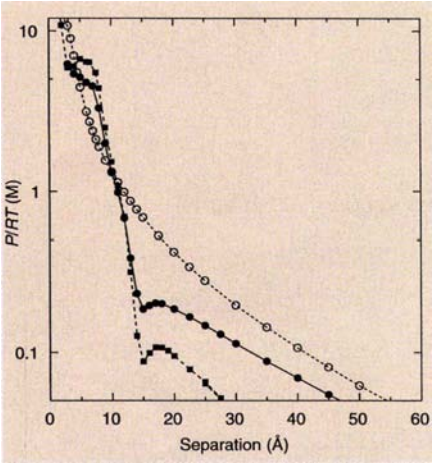

Figure 1 **Calculated double-layer repulsive pressure P (R is the gas constant and T the temperature) between smooth surfaces with a uniform negative charge of 0.334 C m^{-2} (corresponding to mica, which is used in most experiments). Separation is measured from the centre of counterions touching the surface and zero separation corresponds to one layer of hydrated counterions between the surfaces. In experiments, this definition of zero probably corresponds to surfaces in electrolyte solution brought into contact, and was used in ref. 4. The results correspond to electrolytes 0.025 M NaCl, both with (filled circles) and without (open circles) the hydration potential, and 0.1 M NaCl with the hydration potential (squares).**

resembles a distinct new exponential force. Figure 1 shows that this is not an additional hydration repulsion, but merely a return to the level expected without hydration. For NaCl at the concentrations considered here, experiments[4] also show several small steps superimposed upon the approximately exponential repulsion. Because the present method averages over solvent states before the pressure calculation, steps resulting from solvent layering are not reproduced.

Ion–ion potentials of mean force cannot yet be calculated accurately enough for a fully quantitative comparison between measurements and calculations. The Na^+–Na^+ potential of mean force, which is the most important pair in the present calculation, is available from two studies[7,10] compared in Fig. 7 of ref. 7. Although the results are in qualitative agreement, the depth of the oscillatory potential wells is different. Best numerical agreement with direct double-layer measurements[4] would correspond to a potential intermediate between these two studies[4,7]. Nevertheless, my calculation confirms the concept[1] that the hydration structure of ions significantly influences the double-layer pressure of strongly charged surfaces and provides a physical picture of how this is produced by a change in the structure of the Stern layer.

S. Marčelja
Department of Applied Mathematics, Research School of Physical Sciences and Engineering, The Australian National University, Canberra 0200, Australia

Israelachvili and Wennerström reply—Marčelja's theoretical analysis is an important development in our understanding of the electrostatic interactions between charged surfaces in aqueous electrolyte solutions. The analysis supports our recent suggestion[5] that monotonically repulsive 'hydration forces' are not due to structured water layers propagated away from a surface, but to the osmotic effect of hydrated ions electrostatically trapped between two approaching surfaces. By taking into account the molecular nature of the solvent, Marčelja has developed a quantitative description of electrostatic double-layer repulsion, but the underlying qualitative entropic mechanism remains the same.

Marčelja's analysis brings out another important feature, namely, hydrated ion effects need not necessarily make the overall interaction more repulsive. By virtue of the intrinsic oscillatory component of the effective ion–ion pair potential caused by the molecularity of the solvent (a solvent that is assumed to be composed of discrete, finite-sized molecules rather than one that is treated as a structureless continuum), the resultant, spatially averaged, monotonic surface–surface interaction can be less repulsive over certain distance regimes than would be predicted by the simple Poisson–Boltzmann equation. Monotonically varying 'hydration forces' should be more correctly referred to as spatially averaged (oscillatory) solvation forces, especially when one is talking in general terms, because these forces are not unique to water and arise with other liquids (solvents) and surfaces.

J. N. Israelachvili
Department of Chemical Engineering, University of California, Santa Barbara, California 93106, USA
H. Wennerström
University of Lund, Physical Chemistry 1, Chemical Centre, PO Box 124, S-221 00 Lund, Sweden

1. Pashley, R. M. *J. Colloid Interface Sci.* **83**, 531–546 (1981).
2. Pashley, R. M. & Israelachvili, J. N. *J. Colloid Interface Sci.* **97**, 446–455 (1984).
3. Pashley, R. M. & Israelachvili, J. N. *J. Colloid Interface Sci.* **101**, 511–523 (1984).
4. McGuiggan, P. M. & Pashley, R. M. *J. Phys. Chem.* **92**, 1235–1239 (1988).
5. Israelachvili, J. N. & Wennerström, H. *Nature* **379**, 219–225 (1996).
6. Guàrdia, E., Rey, R. & Padró, J. A. *Chem. Phys.* **155**, 187–195 (1991).
7. Guàrdia, E., Rey, R. & Padró, J. A. *J. Chem. Phys.* **95**, 2823–2831 (1991).
8. Zhong, E. C. & Friedman, H. L. *J. Phys. Chem.* **92**, 1685–1692 (1988).
9. Kjellander, R. & Marčelja, S. *J. Chem. Phys.* **82**, 2122–2135 (1985).
10. Pettitt, B. M. & Rossky, P. J. *J. Chem. Phys.* **84**, 5836–5844 (1986).

Genius triumphs over jealousy

The Very First Light: The True Inside Story of the Scientific Journey Back to the Dawn of the Universe
by John C. Mather and John Boslough
BasicBooks: 1996. Pp. 328. $27.50

Joseph Silk

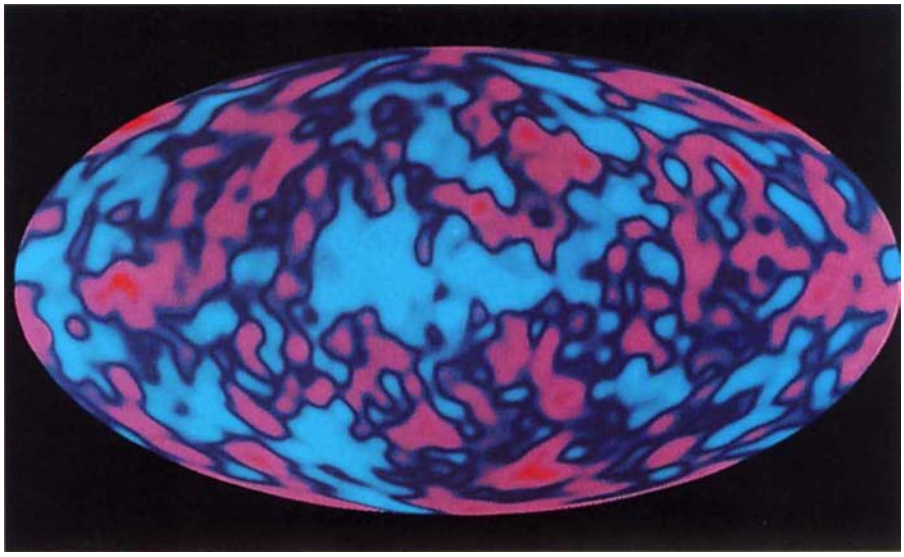

NASA/SCIENCE PHOTO LIBRARY

God's blotted handwriting: COBE found fluctuations in the early Universe, but caused a PR stink.

Large scientific collaborations breed infighting. Sometimes this stimulates the progress of an experiment, but more often the acrimony leaves bitter scars. The COBE satellite project, which mapped cosmic background radiation for four years after its launch in November 1989, involved more than 1,500 participants at its peak. Yet two scientists stand out from the crowd, John Mather and George Smoot.

Mather was the prime mover behind the satellite. A NASA scientist, he developed a key experiment on board which measured the spectrum of the cosmic microwave background, the 'fossil' radiation from the beginning of the Universe. After a series of disconcerting vicissitudes that culminated in the Challenger shuttle disaster, Mather oversaw the repackaging of COBE into a Delta spacecraft, in which role it made a major discovery within the first nine minutes of data-taking: the purity of the microwave black-body spectrum.

In the 1950s, Ralph Alpher, Robert Herman and their mentor, cosmologist George Gamow, had predicted that the relic fossil radiation from the Big Bang should fill the observable Universe with a diffuse microwave glow. In the 1980s several experiments, one of which was a by-product of Mather's own work, purportedly demonstrated that there were unanticipated deviations from the black-body spectrum predicted by proponents of the Big Bang theory. Cosmologists were in a quandary.

The COBE team maintained absolute secrecy about their results for two months until Mather, addressing a meeting of the American Astronomical Society in January 1990, showed a slide of the spectrum with absolutely no perceptible deviations from a black body. The spectral accuracy surpassed that of the best laboratory black body.

On seeing the slide, the audience spontaneously erupted into a standing ovation. Few moments in science have provided such a dramatic confrontation of prediction and observation. But the press reports were muted, perhaps because a black-body spectrum is not very familiar to the public.

All that changed on 23 April 1992, however, when front pages of newspapers around the world reported the discovery of ripples or intensity fluctuations in the cosmic microwave background radiation. Again, over the previous three decades cosmologists had persevered in their search for such ripples, the elusive seeds for large-scale structure in the Universe.

The newspapers attributed the discovery to a team seemingly dominated by one individual, George Smoot, a scientist at Lawrence Berkeley Laboratory in California. Smoot was the primary developer of the mapping instrument on board COBE. Such accolades as Stephen Hawking's "the greatest discovery of the century, if not of all time" accompanied banner headlines. (Although the epoch-making discovery was soon confirmed, the sky maps of the fluctuations that appeared in the press showed mostly experimental noise rather than the more subtle cosmic signal.)

Smoot's hard-working colleagues were, unsurprisingly, embittered at his moment of fame. And consternation set in at NASA headquarters at the lack of attribution to the heroic effort by the space agency that had spanned two decades. How did this public relations fiasco come about?

The answers are spelled out in *The Very First Light* by Mather and science writer John Boslough. The efficiency of the public relations office at Lawrence Berkeley, along with Smoot's acquiescence in its role, is held to blame. Their embargoed press release was circulated to journalists one day before the press conference at which the results were announced. The journalists telephoned the world's cosmologists for comments. Years of pent-up frustration were released. Dick Bond at Toronto and Michael Turner at Chicago simultaneously and independently described the fluctuations as the "Holy Grail of cosmology". Joel Primack at Santa Cruz compared it to seeing "the handwriting of God". The crescendo of expectation culminated in the press conference where Smoot stated that "if you are religious, it is like seeing God".

By this stage, the damage had been done. Within days Smoot was signed up by the well known literary agent John Brockman to write the book of the COBE story with science journalist Keay Davidson, netting them millions but irreversibly inflating the popular science book market. Little wonder that Smoot has become somewhat unpopular with some of his former colleagues who are now busily developing a sequel to COBE, to be launched by NASA at the turn of the century. Smoot is not involved in that enterprise.

The Very First Light is largely an appealing book, with vivid descriptions of how administrators, scientists and engineers combined to carry off a marvellous success, but it is not all fair. The authors do Smoot an injustice by failing to recognize that it was his persistence and experimental know-how that led to the first definitive measurement of the dipole anisotropy in the cosmic microwave background. Mather and Boslough credit another group with the primary role, and Smoot's group only as one of several that confirmed the result.

A section of the book attributed to interviews by Boslough describes Smoot as the "bad egg" in a large team of hard-working scientists. Smoot is depicted as the jealous scientist holding up other team members from announcing the results, yet as head of the team he would have been credited regardless of when the results were announced. But the very same pages reveal a more plausible interpretation: Smoot, along with a senior team member, David Wilkinson, are portrayed as sceptical arch-

conservatives, unwilling to let the young Turks get away with announcing preliminary results that might later turn out to need substantial modification or withdrawal.

The course of cosmology is littered with such failures. Against the odds — and because of the experimental genius of two remarkable scientists, Mather and Smoot — COBE turned out to be a great success. □

Joseph Silk is at the Institut d'Astrophysique, 98 bis, Boulevard Arago, F-75014 Paris, France. He is on leave from the University of California, Berkeley, USA.

Flying yellow kangaroos

Tree Kangaroos: A Curious Natural History
by T. F. Flannery, R. Martin and A. Szalay. Illustrated by P. Schouten
Reed Books Australia: 1996. Pp. 202. A$100

Jared M. Diamond

In 1981, I finally succeeded in getting dropped by helicopter into New Guinea's highest, largest, most remote unexplored mountain range, the uninhabited Foja Mountains, which rise like an island out of lowland swamps. I dreamed of discovering there a population of diprotodonts, the rhinoceros-like giant marsupials that became extinct after humans arrived elsewhere in New Guinea and Australia. In the event, I had no luck with diprotodonts but did find New Guinea's long-lost golden-fronted bowerbird, as well as a remarkable large mammal.

The mammal was yellow, red and pink, with spots and stripes, about 1.5 metres long, and resting on the ground. It looked like a kangaroo but did not behave like one: when it saw me, it jumped up a tree.

No, I was not delirious with malaria. The strange apparition was a tree-kangaroo, one of a group of at least 10 species belonging to the genus *Dendrolagus* and confined to New Guinea and tropical Australia. Tree-kangaroos are among the world's most unusual and most difficult-to-study large mammals. One quarter of the known taxa have been discovered only within the past decade, including two of the most divergent — a striking black-and-white species with a white star on its forehead, and a large black species with a strong smell. Little has previously been known about them, and most of that was unpublished or in obscure publications.

That has now changed with the publication of this book, whose text is by Timothy Flannery, Roger Martin and Alexandra Szalay, and whose magnificent paintings of every species and subspecies are by Peter Schouten. The book is full of new information ranging from anatomical dissections to results of radio-tracking under unspeakably miserable field conditions.

Unknown to science until 1990: golden-mantled tree-kangaroo.

Unlike the well known, open-country, terrestrial animals that the word 'kangaroo' conjures up to most of us, tree-kangaroos are largely arboreal. To reach that niche required a zigzag evolutionary sequence of adaptations.

From arboreal, clambering, possum-like ancestors with prehensile tails, kangaroos became highly modified for hopping on the ground, and then evolved a new set of adaptations to trees to become tree-kangaroos. One remarkable species — discovered only three years ago — has in turn shed those adaptations to become the sole terrestrial species of tree-kangaroo.

The lifestyle of arboreal tree-kangaroos required them to reverse millions of years of kangaroo evolution in many respects: saving weight by a 25 per cent reduction in muscle mass; developing long, strong, curved claws; big, powerful grasping forearms, and a rotator cuff in the shoulder (shared with humans but not with other kangaroos or most other mammals) to permit overhead use of the forearm; hind-feet that twist so the soles can face each other to grasp a tree trunk; hair whorls to shed rain (also shared with humans); and a tail tufted with long fur in some species, used as a counterbalance in climbing and as a rudder in 'flight'.

Those 'flights' are actually jumps to the ground from a height of 20 metres or more in the canopy. I know of no other big mammal that survives drops from such a height, even landing on rocks — imagine trying to do it yourself. But tree-kangaroos often make such leaps to avoid danger. The loud thuds of falling tree-kangaroos as they hit the ground were among the distinctive sounds that I heard daily in the Foja Mountains. The text gives hints of the ways in which the animals' bones, muscles and ligaments must have become modified to withstand such shocks.

Adaptations to diet are equally interesting. Most species are leaf-eaters, but some take roots and fruit, and a couple have been observed in zoo cages to hunt and kill birds. Faced with a hard-to-digest, toxic, bulky leaf diet of low nutritional value, tree-kangaroos evolved a low metabolic rate. They decrease rather than increase their metabolic rate at low ambient temperatures; spend 90 per cent of their time 'doing nothing' (that is, sitting and digesting); and have a complex stomach of several chambers, and regurgitate and rechew food, like cows chewing the cud.

A glance inside the stomach is guaranteed to disgust even the most hardened gastroenterologist: among the leaf fragments crawl more than 100,000 nematode worms of various shapes and sizes. The worms digest leaves, excrete usable nutritious compounds, and finally yield up their bodies (to the tree-kangaroo's acid-secreting stomach compartment?) which are far more digestible to the host than are the original leaves. So the worms may not be parasites but gut symbionts — an astonishing departure from the usual pattern of microbes as gut symbionts in ruminants, termites and other herbivores.

The authors describe differences between species in anatomy, altitudinal distribution (hot lowland rainforest to freezing subalpine scrub), odour (from chest or cloacal glands), scrotal weight (possibly correlated with differences in breeding system) and colour (ranging from black or black and white to red and yellow, and including some of the most brightly coloured of mammals). But these are only a few examples of the surprises held in store for us by tree-kangaroo biology.

This book is aimed not so much at the few dendrolagophiles among us, nor even at mammalogists in general, but at any biologist looking for a goldmine of scarcely explored adaptations — or just looking for a gorgeous book.

Jared M. Diamond is in the Department of Physiology, University of California Medical School, Los Angeles, California 90095-1751, USA.

Out of the shadow of the guillotine

André-Marie Ampère: Enlightenment and Electrodynamics
by James R. Hofmann
Cambridge University Press: 1996. Pp. 406. £40, $49.95

David Cahan

Most scientists and historians of science know André-Marie Ampère (1775–1836) solely as the founding father of electrodynamics, in particular as the creator of an elegant law of electrodynamic force. Yet Ampère's interest in electrodynamics came rather late in his career and lasted only six years, from 1820 onwards. Before then, as James R. Hofmann shows well, Ampère placed first mathematics, then chemistry, at the centre of his interests, while philosophy remained an abiding concern throughout his life.

Hofmann has put Ampère's scientific and philosophical activities at the heart of his biography, but he has also sought to relate those activities to the larger contexts of Ampère's personal life and the professional world of French science and learning during the first third of the nineteenth century. The result is a thorough and scholarly biography that gains its coherence through contextual narration rather than through pursuit of a particular theme.

This lack of a leitmotiv in Ampère's life and work seems to have issued from his idiosyncratic upbringing, emotionally turbulent personal life and unrequited spiritual longings. Ampère, the son of a bourgeois and devoutly Roman Catholic family, spent most of his childhood in rural southeastern France. He received no formal education. His earliest and lasting ideas about the nature of science came from his readings of Buffon on natural history, of Rousseau on botany, of the works of Descartes, and of d'Alembert's and Diderot's *Encyclopédie*. These and other sources gave him a love of the direct experience of nature, of classifying and ordering it according to 'natural' schemes, and a taste for philosophy and mathematics.

In 1792, Ampère's happy childhood and teenage years of unsystematic and self-taught learning abruptly ended when his father was guillotined as an anti-revolutionary. The Ampères became poorer and André-Marie experienced a near total physical and mental breakdown. According to Hofmann, this was one source of his subsequent depressions. Another was a pair of short-lived marriages, first to a sickly spouse, then to a swindling one. To support himself and his only child, Ampère first became a private tutor and then a secondary-school mathematics and science teacher. Both his devotion to Christianity and his intermittent attraction to spiritualist and mesmerist sects should give us pause in seeing him as an Enlightenment figure, as suggested by Hofmann's subtitle.

IMAGE UNAVAILABLE FOR COPYRIGHT REASONS

MARY EVANS/EXPLORER

Ampère: never became part of the inner circle of the scientific community.

In 1804, after producing a memoir on mathematics and acquiring a powerful patron in Paris, Ampère was appointed to the Ecole Polytechnique. Although he spent the rest of his career in Paris, he never became part of the inner circle of the scientific community. Nevertheless, it was not until he rubbed shoulders with members of the French scientific élite that he realized the high standards needed to produce first-rate scientific and mathematical research. Both before and after the decisive year of 1820, he devoted much time to pleasure-less teaching and administration; to the pursuit of philosophy; and to dealing with his personal discontents and (until the 1820s) frustration at a lack of professional recognition.

Before 1820, Ampère's scientific work was not particularly distinguished. His best efforts were in mathematics, where he classified partial differential equations. Yet he felt no calling for mathematics — he did it simply to earn a living and, in 1814, to gain a position at the Paris Institut. His mathematical work had, at least then, little importance, and nothing to do with the outstanding contemporary work in the foundations of the calculus (above all, that by his student Augustin-Louis Cauchy) and in the development of the Fourier series.

Similarly, in chemistry, Ampère sought to classify the elements through a speculative scheme using the geometry of atomic structure, but his work was largely ignored. In physics, too, he remained an outsider: before 1820, he did little more than adopt Augustin Jean Fresnel's new wave theory of light and teach physics. Ampère's work before 1820 served in effect as an apprenticeship in scientific research.

Hofmann devotes nearly one-third of his study to Ampère's creative work in electrodynamics between 1820 and 1826, concentrating first on his search for experimental foundations for a phenomenological law of electrodynamic forces and for his theory of magnetism, and then on his mathematical and experimental work on the Biot-Savart law and Poisson's theory of magnetism. Hofmann emphasizes the ether-mechanical foundation of Ampère' s work in optics and electrodynamics. In con-

New in paperback

Sexual Selection: Mate Choice and Courtship in Nature
by James L. Gould and Carol Grant Gould
Scientific American Library (W. H. Freeman), $19.95, £14.95
"Finally, we have a thought-provoking (and unashamedly 'sociobiological') account of the role of sexual selection in shaping human evolution and culture. The Goulds write clearly yet with authority… and lace the text with many fascinating facts and examples." Rory Howlett, *Nature* **342**, 318 (1989).

Animal Minds and Human Morals: The Origins of the Western Debate
by Richard Sorajbi
Duckworth/Cornell University Press, £16.99, $15.95
"This is an impressive, important and thought-provoking book. It is clearly written and, although much of it deals with the details of Greek thought, the structure is plain and the index is excellent." Mary Midgley, *Nature* **368**, 363–364 (1994).

Hidden Histories of Science
edited by Robert B. Silvers
Granta, £7.99.
"Even where the substance inflames, the literary excellence assuages." Walter Gratzer, *Nature* **374**, 838–839 (1995).

Science and the Founding Fathers: Science in the Political Thought of Thomas Jefferson, Benjamin Franklin, John Adams & James Madison
by I. Bernard Cohen
Norton, £10.95, $15.95
"[Cohen] is well placed to judge the influence of scientific thought on early American political life. Historians and scientists should find this book rewarding, a reminder of the days when science and society marched hand in hand." J. Reynolds, *Nature* **376**, 477 (1995).

trast to several other historians, he stresses the experimental basis, origins and methods of Ampère's electrodynamics. He argues that "Ampère's experimentation [in electro-dynamics] was almost always guided by predetermined goals; his initial agenda was to specify a mathematical expression for a phenomenological force law and to determine the circuits followed by the electric currents he believed existed within magnets".

Hofmann also points out that Ampère did not seek quantitative precision nor, unlike Faraday, did he seek experimental novelties. Rather, he preferred deductive analysis and confirming experimentation to inductive generalizations. He believed that his electrodynamics had originated in the same way as, and paralleled in its argumentative form, Newton's gravitational theory.

Here, as throughout his study, Hofmann devotes much analysis to Ampère's philosophy of science and metaphysics, in particular elucidating his overall research programme and assessing the means by and extent to which he achieved it.

After the publication in 1826–27 of his essay on the theory of electrodynamic phenomena, Ampère ceased work in this field. His research during the final decade of his life was anticlimactic: he again occupied himself with the unfruitful pursuit of problems of classification.

Although he was elected in 1824 to the Collège de France (as the experimental, not the theoretical, professor of physics), he continued to remain an outsider to the scientific community. His lack of training, his temperament and his fervent yet unrequited pursuit of metaphysics had turned him, as Hofmann shows, into a scientist-philosopher *sui generis*.

David Cahan is in the Department of History, University of Nebraska–Lincoln, 612 Oldfather, PO Box 880327, Lincoln, Nebraska 68588-0327, USA.

The framework of feelings

The Emotional Brain: The Mysterious Underpinnings of Emotional Life
by Joseph LeDoux
Simon & Schuster: 1996. Pp. 384. $25

Raymond J. Dolan

The progress of cognitive neuroscience towards an understanding of mind is beyond question, but one component has so far proved intractable — emotion. With few notable exceptions, the preferred strategy of cognitive neuroscience in dealing with emotion has been to ignore it. Given that so much of everyday experience is shaped by emotion, it is difficult to understand how any concept of mind devoid of emotion can be taken seriously.

The Emotional Brain by Joseph LeDoux represents an important step in bringing emotion back into mainstream cognitive neuroscience. It follows a notable work by Antonio Damasio, *Descartes' Error* (published by Grosset/Putnam). Both can be viewed as part of a process of rehabilitation for cognitive neuroscience from a long-standing state of emotional denial.

Whereas Damasio attempted to provide a comprehensive theory of emotion, LeDoux focuses on fear. This is justified by reference to the fact that fear represents a class of emotion that is conserved across species, so neurobiological data from other species can provide important clues about the probable organization of fear in the human brain. This focus also avoids the cul-de-sac that characterizes debate within psychology about what constitutes an emotion and whether there are fundamental emotions.

The account of emotion emphasized here is unashamedly neurobiological. Its historical antecedents are the anatomical and physiological theories of James Papez, Paul MacLean and Donald Hebb. These approaches were limited by an attempt to account for all emotions in terms of the function of a single brain system.

As Leslie Brothers has pointed out, this had the unfortunate consequence of a reification of emotion in the concept of the limbic system, a concept now viewed as fundamentally flawed. LeDoux takes the position that there is no such thing as a single, all-inclusive emotion faculty, but that there are distinct systems that mediate particular emotions.

LeDoux's contribution to the understanding of fear has been considerable. His work is exemplary in bridging anatomical localization and neurobiological mechanisms of emotion. LeDoux and colleagues have shown that a critical mammalian system for responding to fear involves the thalamus and amygdala. Critical processing related to fear takes place in the amygdala, whose outputs can be functionally and anatomically separated into different components of a fear response, for example autonomic responses.

Emotional disturbances represent the commonest form of human psychopathology. The social, cognitive or pharmacological mechanisms of these disturbances have been emphasized in research efforts over the past 30 years. Much of this work is speculative, in that it lacks a plausible, anatomically grounded, neurobiological account of emotion.

The pathological counterparts of fear include anxiety, phobias and post-traumatic stress disorder, and LeDoux proposes that aberrant activation of a fear system is likely to be fundamentally important in these areas. The goal of psychopathological research must be to provide models for such aberrant activation. In other words, how does processing that supports acquired fear gain access to systems mediating innate fear responses?

An obstacle to understanding emotion has been the issue of the centrality of conscious emotion. LeDoux points out that an absence of awareness is the rule for much of mental life. He assumes that in animals with a capacity for conscious awareness, emotional feelings will be present, although this is not central to understanding emotion.

This concept has much in common with Jerry Fodor's notion of modular systems, whose activity is assumed to be automatic, obligatory and cognitively impenetrable. In this framework, it is the outputs of emotionally specific modular systems that are available as experienced feelings. Provocatively, he concludes that conscious feelings are at best red herrings in the pursuit of an understanding of emotion. However, by the same token, so also are other outputs from a fear-processing system, including autonomic and other behavioural responses.

This view of emotion is clearly distinct from William James' notion of fear as the perception of physical responses; both feelings of fear and its autonomic concomitants are effects of activity within a system specialized for the detection of danger, and the system that detects fear constitutes what is fundamental.

Psychology makes a clear distinction between cognition and emotion, and LeDoux implicitly subscribes to this dichotomy. The critical issue here is the absence of any unanimity about the definition of cognitive. If cognition refers to systems that embody a transformation of inputs, then emotion can also be construed as cognitive. In this framework, what distinguishes emotion from other modes of cognition is the evaluative nature of these transformations.

What is most gratifying in this book is that, for once, the neurobiological mechanisms of emotion are put centre-stage. Generous reference is made to other modes of enquiry wherever this illuminates the author's general thesis. The style of writing is highly accessible, and LeDoux's musical and literary references reveal a man clearly in touch with his own emotional feelings. All said, *The Emotional Brain* is a stimulating and thoughtful work and is essential reading for any serious student of human emotion. □

Raymond J. Dolan is in the Wellcome Department of Cognitive Neurology, Institute of Neurology, Queen Square, London WC1N 3BG, UK.

Influence of ocean heat transport on the climate of the Last Glacial Maximum

Robert S. Webb*, David H. Rind†, Scott J. Lehman‡, Richard J. Healy†§ & Daniel Sigman§

* *NOAA-NGDC Paleoclimatology Program, 325 Broadway, Boulder, Colorado 80303, USA*
† *NASA-GISS, 2880 Broadway, New York, New York 10025, USA*
‡ *INSTAAR and Department of Geological Sciences, University of Colorado, Boulder, Colorado 80309, USA*
§ *Woods Hole Oceanographic Institution, Woods Hole, Massachusetts 02543, USA*

A series of climate simulations using an atmospheric general circulation model shows that maintaining ocean heat transport at close to present-day values, but with otherwise glacial boundary conditions, leads to an enhanced cooling, particularly in the tropics. This is in agreement with recent geochemical evidence from fossil corals, ground waters, and ice. Near-modern ocean heat transport may have been sustained in all ocean basins during the Last Glacial Maximum in order to balance the formation and export of Glacial North Atlantic Intermediate Water.

Until recently, most palaeoclimate reconstructions for the Last Glacial Maximum (LGM) indicated an average 8 °C cooling over land and ocean in the middle to high latitudes[1], up to 6 °C cooling over land in the tropics[1–6], and little change in tropical sea surface temperatures (SSTs)[7,8]. Previous global climate modelling experiments[1,9–13] have been unable to produce the large cooling over tropical land areas when using generally accepted glacial boundary conditions and LGM SSTs from CLIMAP[7,8], indicating little or no cooling of the tropical ocean. However, new palaeotemperature estimates from the Sr/Ca ratio in Barbados corals[14] and noble-gas concentrations in fossil ground waters from near sea level in Brazil[15] indicate a 5 °C tropical ocean cooling, and directly challenge the CLIMAP LGM SST reconstruction for the tropics.

Rather than specifying fixed CLIMAP LGM SSTs as a boundary condition in simulations presented here, we have chosen instead to specify the modern grid-by-grid transport of energy through the ocean (after a modest correction for lowered glacial sea level) to simulate LGM SSTs and associated climate conditions. The resulting simulations indicate that incorporating near-modern ocean heat transport (OHT), reduced glacial atmospheric CO_2 levels, large terrestrial ice sheets, together with feedback mechanisms involving atmospheric water vapour, clouds, and Southern Hemisphere sea ice, are sufficient to lower annual-average global surface temperature by 8 °C and tropical SSTs by 5.5 °C.

Ocean heat transport has been estimated previously using the NASA-GISS $8° \times 10°$ atmospheric general circulation model (AGCM)[16] for both modern and CLIMAP SST distributions and associated boundary conditions. These OHTs were generated by diagnosing the grid-by-grid convergence of ocean heat required to maintain a prescribed SST field and integrating the zonal-average convergences from south to north[17,18] (Box 1). We have made similar OHT calculations for a modern climate but with glacial land–sea distributions (sea level 120 m lower and areas occupied by ice sheets at the LGM defined as land; Fig. 1) to ensure that our simulations conserved energy (hereafter, 'near-modern OHTs'). Although reduced relative to modern, the near-modern OHTs in the Atlantic Ocean were consistently greater than OHTs estimated for LGM climate with CLIMAP SSTs[7,8,18] (Fig. 1). Near-modern OHTs in the Pacific Ocean although slightly elevated relative to modern, were not as large as OHTs estimated for LGM climate with CLIMAP SSTs[7,8,18] (Fig. 1). Global ocean heat convergences (OHCs; Fig. 1) associated with the near-modern OHTs, like modern OHCs, are greater than CLIMAP-inferred values at high northern latitudes (primarily an Atlantic basin effect); however, in the subtropics neither the near-modern nor modern OHCs are as large as those inferred for CLIMAP SSTs (primarily a Pacific basin effect; Fig. 1).

Today's pattern of OHT is northward throughout the Atlantic, balancing a southward equator-to-pole transport of ocean heat in the Pacific and Indian oceans. This general pattern is a consequence of both the basin-scale, wind-driven circulation (which does not transport heat poleward of ~45° in any basin) and the large-scale thermohaline or 'conveyor' circulation[19,20]. A primary feature of the latter is the cooling and sinking of saline surface waters in the subpolar North Atlantic to form North Atlantic Deep Water (NADW). Because this water-mass is largely exported to other basins (where it upwells and is re-warmed), a compensatory return flow at or near the surface is required. The continental positions demand that this be achieved around either or both the southern tips of South America and Africa, resulting in a northward transport of heat in both the North and South Atlantic. If the formation and export of NADW were to cease entirely, there would be no demand for inter-basin exchange of water and ocean heat, and a pattern of Atlantic OHT much like that calculated from CLIMAP SSTs would result (Fig. 1). Early geochemical investigations of the abyssal circulation determined that the formation of NADW weakened markedly during the last glaciation[21–23], consistent with the pattern of OHTs inferred from CLIMAP SSTs. However, later investigations have shown clearly that a shallower deep water-mass formed instead (Glacial North Atlantic Intermediate Water)[24–29]. Recent geochemical box-modelling studies[30], and a comparison of modern and LGM distributions of the $^{231}Pa/^{230}Th$ ratio in sediments (ref. 31) indicate that this water-mass was exported to the Southern Ocean at rates comparable to the export of NADW today. As this export would demand an inter-basin exchange of ocean water and heat more like today's than the one inferred from CLIMAP SSTs, we chose to examine the result of maintaining near-modern OHTs under glacial forcing on LGM climate.

Climate model simulations

We have run climate simulations with the NASA-GISS AGCM[16] at $8° \times 10°$ (latitude versus longitude) resolution. We performed a LGM simulation (LGM-A) using these near-modern OHTs, orbital

Box 1 Ocean heat convergence and transport calculations[17]

Ocean heat convergences and associated transports are calculated as the amount of energy advected either into or from each grid box by the ocean that would be required to maintain prescribed SSTs given the energy contribution to each grid box by the atmosphere. Within the GCM, the ocean heat convergence for each grid box is the residual amount of heat necessary to balance the sum of model-provided surface atmospheric energy fluxes:

Ocean heat convergence = net solar radiation + net thermal radiation + latent heat flux + sensible heat flux + precipitation heat flux

Northward ocean heat transports (OHTs) for each ocean basin are calculated as the latitudinally integrated sum of ocean heat convergence for each grid box starting from 90° S and ending at 90° N. The application of modern OHTs in a modern climate experiment will result in predicted SSTs and atmospheric conditions that are nearly identical to the comparable experiment with fixed modern SSTs. Likewise, application of CLIMAP OHTs in an LGM climate experiment will result in predicted SSTs and atmospheric conditions that are nearly identical to the comparable experiment with fixed CLIMAP SSTs.

forcing[32] appropriate for 18,000 yr ago, lowered sea level, LGM terrestrial ice sheets, and modern atmospheric CO_2 levels. A second LGM simulation (LGM-B) was run identical to LGM-A except that a glacial atmospheric CO_2 level of 200 p.p.m. (ref. 33) was specified. Both of these simulations were designed to be directly comparable with a previous NASA-GISS AGCM LGM simulation[11] run using similar glacial boundary conditions, CO_2 set at the glacial level of 200 p.p.m. (LGM-C), and SSTs fixed from CLIMAP[7,8] with implied OHT/OHC as a climate forcing that is very different from modern.

The new palaeoclimate simulations, LGM-A and LGM-B, showed respectively 4.6 °C and 8 °C reductions in global annual-average surface air temperature relative to the modern control simulation (Table 1; Fig. 2). The cooling in both simulations resulted from global increases in planetary albedo, surface albedo, snow cover, ocean ice cover, and both total and low-level clouds, as well as decreases in evaporation over the ocean and in atmospheric water vapour concentrations (Table 1; Fig. 2). Although the reduction of CO_2 in LGM-B contributed only 0.6 °C in direct cooling, the consistently larger feedbacks in this simulation, including a 37% decrease in atmospheric water vapour, resulted in a global cooling almost double that simulated in LGM-A. Based on previous energy-balance diagnostics[11,34], we estimate that the cumulative effects of changes in radiative forcing sum to 5.5 °C cooling in the global annual-average surface air temperature for LGM-A and 8.8 °C cooling for LGM-B (Fig. 3a, Table 1). The dominant radiative cooling was due to reductions in atmospheric water vapour and high clouds which decreased greenhouse forcing, and increases in low clouds which raised the planetary albedo. The small discrepancies between the model simulated temperatures (4.6 and 8 °C) and our estimates for the cumulative effects (5.5 and 8.8 °C) can be attributed to unaccounted for and/or overlapping feedbacks among the various radiative forcing components.

Within the tropics (16° N to 16° S), LGM-A exhibited a 2.7 °C reduction in annual-average surface air temperature and SST relative to the modern control run, whereas LGM-B showed a 5.7 °C reduction in air temperature and 5.5 °C reduction in SST (Table 1). We estimate that tropical cooling due to changes in the vertical distribution and amount of clouds was 2.8 °C in LGM-A and 4.3 °C in LGM-B. The greater cloud-related cooling in LGM-B is primarily an albedo effect driven by a large (7%) increase in low-level clouds compared to a smaller increase (3.4%) in LGM-A (Table 1), an expected result in view of previous analyses of the NASA-GISS AGCM showing that lower SSTs invariably lead to an increase in low clouds[35]. Atmospheric water vapour within the tropics decreased by 23% in LGM-A and 35% in LGM-B, contributing 1.9 °C and 3.8 °C of cooling, respectively. From energy-balance diagnostics for the tropics[11,34], we estimate that the cumulative effects of changes in the radiative forcing sum to 2.5 °C cooling in annual-average surface air temperature for LGM-A and 7.3 °C cooling for LGM-B (Table 1, Fig. 3b). Whereas most feedbacks contribute to tropical cooling, reductions in the atmospheric flux of static energy out of the tropics, and orbitally forced changes in insolation each contributed some warming to the tropics in both LGM-A and LGM-B (Table 1).

Compared to the previous NASA-GISS LGM simulation using fixed SSTs from CLIMAP[7,8] and CO_2 set at glacial levels (LGM-C)[11], LGM-A and B exhibit much greater cooling (Table 1). All of these LGM experiments exhibit significant increases in global planetary albedo primarily associated with large terrestrial ice sheets and expansion of Southern Hemisphere sea ice; however, increases in the planetary albedo in LGM-C were not as large as those in LGM-A and B, reflecting differences in the amount of low-cloud cover and sea-ice cover. The zonal averages of surface air temperature anomalies (Fig. 2) show significantly lower temperatures at all latitudes in LGM-B, whereas the coolings in LGM-A and -C are concentrated in the high latitudes. Evaporation over the ocean in the subtropics is decreased in both LGM-A and B, whereas evaporation is increased or near-modern in LGM-C in response to significantly warmer subtropical SSTs reconstructed by CLIMAP[7,8] (Fig. 2). Within the tropics, zonal-average surface air temperatures in LGM-A and B were 1.1 and 4.1 °C lower, respectively, than in the fixed-SST experiment, LGM-C. Atmospheric water vapour in LGM-A and -B decreased by 22% and 37% globally, respectively, in contrast with only a 12% decrease in experiment LGM-C.

Zonal-average tropical SSTs in the near-modern OHT experiments are 1.4 °C (LGM-A) and 4.2 °C (LGM-B) lower than in the control experiment, in contrast to the 1.2 °C cooling reconstructed by CLIMAP (Table 1). On the other hand, maintaining near-modern OHTs result in LGM SSTs that are 4.1 °C (LGM-A) and 2.9 °C (LGM-B) higher than reconstructed by CLIMAP for the high-latitude North Atlantic (39° to 70° N). However, much of this discrepancy is in the 47° to 55° N latitude band, where SSTs for the different LGM simulations vary between extremes of 6.7 °C and 0.2 °C. Such low temperatures are generally acknowledged to be outside the sensitivity range of SST estimation techniques employed by CLIMAP (that is, $\leqslant$5 °C)[36]. The annual-average, global sea-ice coverage increased, relative to modern, by 1.6% in LGM-A and 5.5% in LGM-B, whereas, based on the CLIMAP reconstruction, a 4% increase in global sea ice was prescribed in LGM-C. The increase in global sea-ice coverage in LGM-B is dominated by the expansion of Southern Hemisphere sea ice in summer. Comparisons of the zonal-annual averages show LGM-B produced significantly greater Southern Hemisphere sea-ice coverage than reconstructed by CLIMAP, whereas LGM-A produced less (Fig. 2). In the northern North Atlantic, sea-ice cover in LGM-A and in LGM-B was reduced relative to the CLIMAP reconstruction in the central portion of the basin reflecting the greater northern penetration of ocean heat, while approximately the same amount of sea ice was simulated off the coasts of North America and Europe. The locally elevated OHC also resulted in slightly warmer temperatures for North Hemisphere subsurface sea ice between 39° and 70° N, around − 4 °C for LGM-A and B versus almost − 5 °C in LGM-C with CLIMAP SSTs. The newly simulated sea-ice distributions (LGM-A and -B) are similar to the reconstructed sea surface salinity field for the LGM North Atlantic, showing high salinities (little or no seasonal sea-ice cover) penetrating north to Iceland in the central portion of the basin[37].

The dominant feedback contributing to greater cooling in

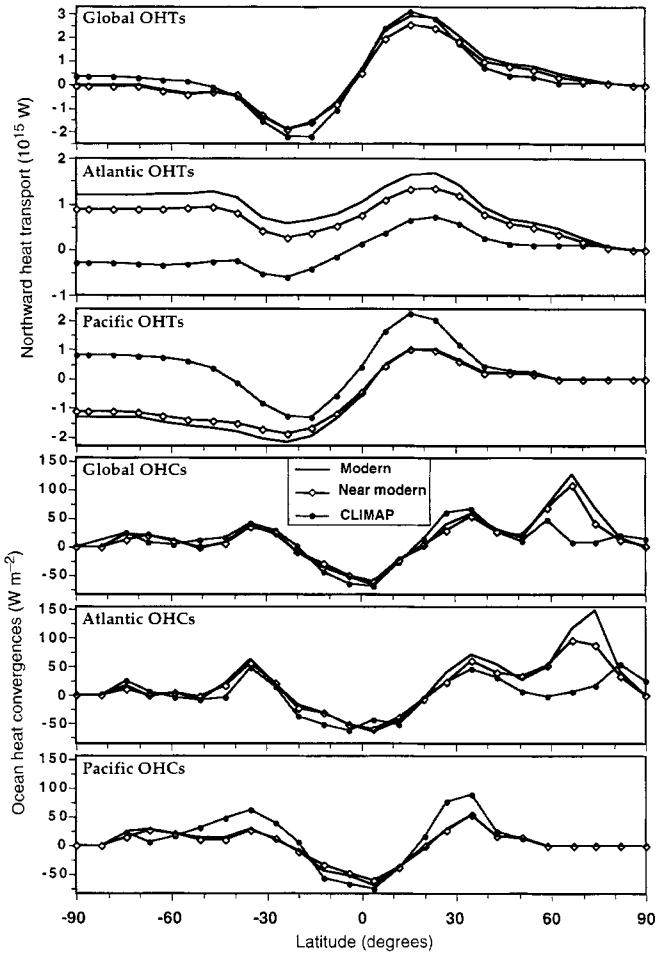

Figure 1 Model-generated annual ocean heat transports (OHTs) and ocean heat convergences (OHCs). Latitudinal zonal averages are shown for the globe, and for the Atlantic and Pacific oceans. The results of three simulations are shown; the modern-climate control experiment (solid black line[4]); the LGM experiment with CLIMAP SSTs (line with filled circles); and the 'near-modern' climate experiment with LGM land-sea distribution (line with open diamonds).

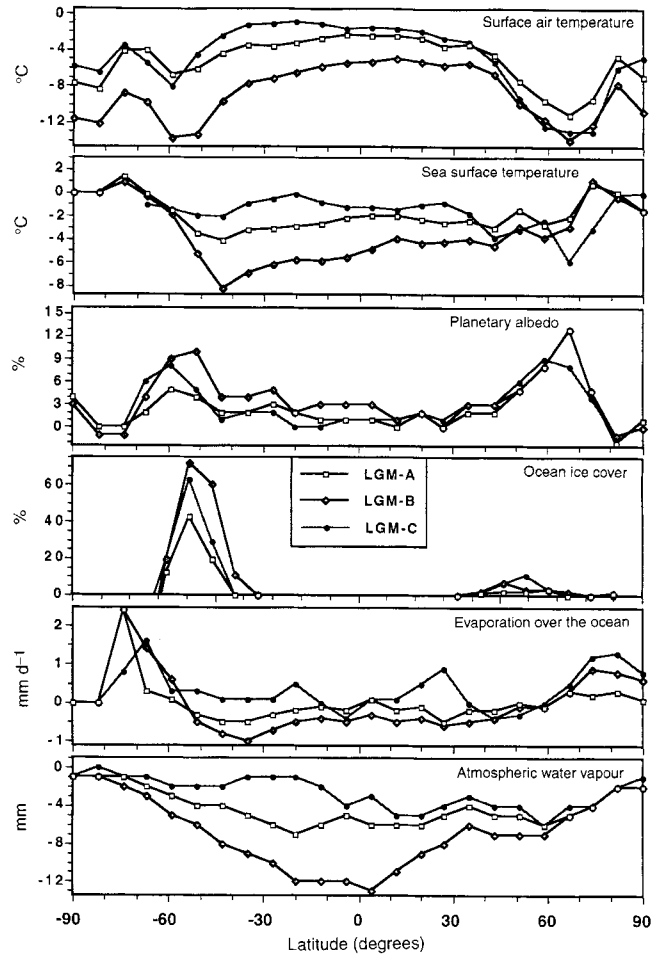

Figure 2 Latitudinal zonal-mean anomalies (experiment minus control) between the modern control climate and the simulated LGM climate: LGM-A (line with open boxes), LGM-B (line with diamonds), and LGM-C (line with filled circles).

LGM-A and B than in LGM-C was changes in evaporation over the Pacific ocean in the subtropics, an area that today is a significant source of heat and water vapour for the atmosphere[38]. Within LGM-C, the sharp gradient of CLIMAP LGM SSTs between the subtropics and the middle-to-high latitudes of the Pacific resulted in high OHCs in the subtropics relative to those associated with modern SST distributions (Fig. 1). Evaporation rates therefore increased in the subtropics in order to balance the increased convergence of ocean heat. The increase in evaporation over the north and south subtropical Pacific in LGM-C was sufficient to compensate for decreases elsewhere, moderating any changes in global atmospheric water content in response to cooler glacial conditions. In contrast, amongst otherwise glacial boundary conditions, the near-modern subtropical OHCs in LGM-A and B result in a decrease in evaporation throughout the subtropics relative to modern, and an even larger decrease relative to LGM-C. The reduction in the subtropics as a source of water vapour for the global atmosphere was amplified in the tropics by a decrease in Hadley circulation in response to lower temperature gradients, which reduced the equatorward flux of water vapour. The combined effects of maintaining near-modern subtropical OHCs (a reduction in OHC relative to CLIMAP), a reduction in atmospheric water vapour, glacial atmospheric CO_2 level, LGM ice sheets, enhanced heat storage in sea ice, and changes in the vertical distribution of clouds are sufficient to have cooled the Earth by 8 °C, and the tropics by 5.5 °C.

In comparison with the 5 °C LGM cooling reconstructed from Barbados corals[14] and noble gases in fossil ground waters from Brazil[15], LGM-B simulated conditions 4.8 °C colder at Barbados and 5.7 °C colder in northeastern Brazil. In contrast, LGM SSTs reconstructed by CLIMAP were less than 2 °C lower than present for Barbados and associated surface air temperatures (experiment LGM-C) were 2.6 °C lower than present for northeastern Brazil. Recent oxygen isotopic measurements in ice cores suggest an 8–12 °C cooling of annual-mean air temperature during the LGM at 6,048 m above sea level in northern central Peru[39]. The simulated cooling at 6,000 m and 8° S was 5.7 °C in LGM-A and 9.3 °C in LGM-B, but only a 2.1 °C cooling was simulated at this location in LGM-C. The annual-average 0 °C isotherm in the tropics dropped by nearly 700 m to ~4,100 m above sea level in LGM-A and by 1,300 m to ~3,500 m above sea level in LGM-B, bracketing the observed LGM snowline depression of 900–1,000 m (ref. 6). In contrast, LGM-C simulated less than a 350-m descent in the 0 °C isotherm in the tropics. The improved match between the palaeoclimate data and the simulated tropical surface air temperatures throughout the lower troposphere of LGM-A, and especially LGM-B, indicate that glacial boundary conditions combined with near-modern OHTs are

Table 1 Global and tropical mean annual anomalies for climate model variables

Variable	LGM-A		LGM-B		LGM-C	
	Global	Tropics	Global	Tropics	Global	Tropics
CO_2 change (p.p.m.)	0.0	0.0	115 (−0.6)	115 (−0.6)	115 (−0.6)	115 (−0.6)
Solar irradiance ($W m^{-2}$)	−0.10	0.75 (0.75)	−0.10	0.75 (0.75)	0.00	0.00 (0.0)
Surface air temperature (°C)	−4.62 (−5.5)	−2.68 (−2.5)	−8.06 (−8.8)	−5.68 (−7.3)	−3.72 (−4.4)	−1.55 (−3.3)
Sea surface temperature (°C)	−1.32	−2.68	−3.49	−5.53	−2.3[7]	−1.25
Ground albedo	4.04 (−1.6)	0.25 (−0.2)	6.15 (−2.4)	0.25 (−0.2)	4.10 (−1.6)	0.00 (0.0)
Land surface albedo	7.29	0.50	7.95	0.50	6.30	0.00
Snow cover (%)	7.00		11.20		8.20	
Ocean ice cover (%)	1.6		5.50		4.10	
Total cloud cover (%)	0.60 (−1.4)	−0.88 (−2.8)	1.30 (−1.8)	−0.38 (−4.3)	0.10 (−0.7)	5.85 (−2.0)
Low cloud cover (%)	2.30	3.40	4.00	7.08	1.50	1.30
High cloud cover (%)	−1.50	−6.08	−2.30	−6.25	−0.90	−3.00
Planetary albedo	2.32	1.75	3.65	3.50	2.10	0.75
Atmospheric water vapour (mm)	−4.90 (−2.5)	−6.00 (−1.9)	−8.60 (−4.0)	−12.25 (−3.8)	−3.00 (−1.5)	−3.50 (−0.6)
Net radiation at the surface ($W m^{-2}$)	−6.5	−6.50	−11.7	−12.75	−5.7	−3.75
Sensible heat flux ($W m^{-2}$)	−1.1	−0.50	−3.1	−2.50	−1.2	0.25
Latent heat flux ($W m^{-2}$)	7.9	2.75	14.8	11.50	3.3	2.50
Static energy flux out of tropics ($10^{14} W m^{-2}$)		12.0 (1.7)		6.0 (0.85)		−1.0 (−0.15)
Precipitation ($mm d^{-1}$)	−0.27	−0.23	−0.51	−0.58	−0.11	−0.05
Soil moisture (mm)	0.00	2.00	3.00	2.25	0.00	2.50

These anomalies are for experiment minus control run. Estimated radiative contributions to temperature change are shown in parentheses. See text for explanation of experiment names.

not only an effective way to cool tropical SSTs, but also permits the model to simulate a reduction in temperature aloft without extreme changes in lapse rates.

OHTs and climate sensitivity

Our results indicate that the new cooler tropical LGM temperatures inferred from coral material and noble gases in fossil ground waters could have resulted from the combined effects of forcing by glacial boundary conditions and of OHTs maintained at near-modern levels during the LGM. In this scenario, high rates of intermediate water formation in the North Atlantic would have been balanced by near-modern transports of ocean heat in the Pacific and Indian basins. Previous climate model simulations have sown that the direct effect of the ice sheets is restricted to a relatively large cooling in northern middle-to-high latitudes[9], whereas modest cooling in low latitudes occurs primarily in response to an overall decrease in atmospheric greenhouse capacity[1,9–13]. In contrast to either the modern climate or our LGM simulations with near-modern OHTs, the previous simulations using CLIMAP LGM SSTs included an implicit increase of OHTs and OHCs as a significant climate forcing mechanism in both the northern and southern subtropical Pacific (Fig. 1) that limits the extent of glacial cooling. Our new simulations indicate that maintaining near-modern OHTs under glacial conditions leads to enhanced global cooling resulting from reductions in evaporation over the subtropical ocean which lead to decreases in global atmospheric water vapour. This cooling mechanism is significantly amplified in response to the effects of reduced levels of CO_2 with greater feedbacks involving atmospheric water vapour, Southern Hemisphere sea-ice growth, and cloud cover changes. The version of the NASA-GISS model used in this study has previously been shown to display enhanced tropical sensitivity related to the explicit representation of cloud generation, penetrative convection and aspects of the hydrological cycle[40]; however, we do not believe that this enhanced tropical sensitivity is the primary explanation for our LGM modelling results. The primary feedback driving enhanced cooling under glacial boundary conditions in these experiments is a change in evaporation controlled by maintaining near-modern OHCs in the subtropical Pacific with high- and low-latitude feedback mechanisms playing less dominant roles. The importance of this feedback mechanism in our simulations highlights the need to re-evaluate CLIMAP LGM SST reconstructions in the Pacific[41], with special attention to the temperature gradient marking the transition between subtropical and subpolar waters.

Our simulations provide a mechanism to cool the tropics by 5–6 °C in accordance with the growing body of new evidence for colder LGM tropical temperatures[14,15,39]. The associated amplified global cooling at the LGM displayed in experiment LGM-B also may have implications for the potential magnitude and distribution of anthropogenic climate change. The simulated 8 °C cooling of global temperature in LGM-B implies a much greater climate sensitivity ($>1\,°C\,W^{-1}m^{-2}$) to a total glacial forcing of $7.1\,W m^{-2}$ (ref. 42) than previous estimates ($0.5\,°C\,W^{-1}m^{-2}$ for a 3.7 °C cooling[11], $0.7\,°C\,W^{-1}m^{-2}$ for a 5 °C cooling[42]). Current IPCC assessments[43] conclude that 'the sensitivity of global mean surface air temperature to doubling CO_2 ($4\,W/m^2$ radiative forcing) is unlikely to lie outside the range 1.5 to 4.5 °C', with a best estimate of 2.5 °C (ref. 43), and an implied $0.6\,°C\,W^{-1}m^{-2}$ climate sensitivity. Although climate sensitivity may not be symmetric for warming and cooling, from a cold-climate perspective a

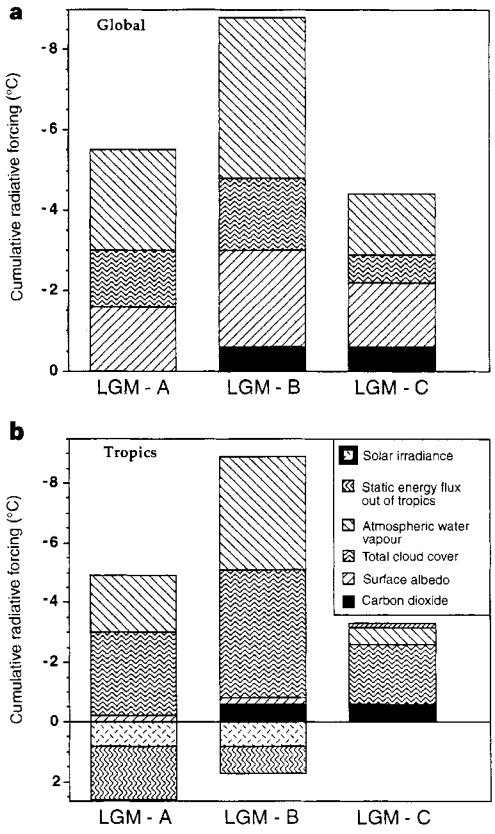

Figure 3 Contributions to the global (**a**) and the tropical (**b**) mean temperature reduction between the modern control climate and simulated LGM climate. Values shown are for the approximate contribution of each component with negative values indicating cooling and positive numbers indicating warming (for example, changes of solar irradiance and static energy flux out of the tropics, as shown in **b**, contribute some warming in LGM-A and B).

$1\,°C\,W^{-1}\,m^{-2}$ climate sensitivity to a $4\,W\,m^{-2}$ radiative forcing may be more appropriate than suggested by IPCC (leading to 4 °C warming), and suggests that inferred climate sensitivity for increased CO_2 under conditions of global warming may be higher than IPCC 'best' estimates[43]. While debate persists on the role and sensitivity of both the tropics and the ocean in future climate change scenarios, our results suggest that under LGM boundary conditions, maintaining near-modern patterns of energy transport from the tropics to high latitudes through the ocean leads to enhanced subtropical and tropical cooling, and cools the Earth. The evidence[6,14,15,39] and possible mechanism for tropical cooling described in this Article undercut arguments that tropical SSTs have changed little throughout the Cenozoic era[44] and that such stability will persist in the future[45]. We recognize that these results could be model-dependent and may reflect how processes are parametrized in the GISS AGCM in comparison to other AGCMs or more complicated coupled ocean–atmosphere–ice sheet models. However, if the coral SSTs and groundwater reconstructions for the LGM temperature are correct, then the $7.1\,W\,m^{-2}$ (ref. 42) glacial forcing requires a climate sensitivity of the order of that shown in our GISS AGCM simulations. □

Received 2 September 1996; accepted 9 January 1997.

1. COHMAP *Science* **241,** 1043–1052 (1988).
2. Colinveaux, P. A. *et al. Clim. Change* **32,** 19–33 (1996).
3. Bush, M. B., Colinveaux, P. A., Wiemann, M. C., Piperno, D. L. & Liu, K. B. *Quat. Res.* **34,** 330–345 (1990).
4. Bonnefille, R., Roeland, J. C. & Guiot, J. *Nature* **346,** 347–349 (1990).
5. Webster, P. J. & Streten, N. A. *Quat. Res.* **10,** 279–309 (1978).
6. Rind, D. & Peteet, D. *Quat. Res.* **24,** 1–22 (1985).
7. CLIMAP Project Members *Science* **191,** 1131–1138 (1976).
8. CLIMAP Project Members *Map Chart Ser.* MC-36 (Geol. Soc. Am., Boulder, 1981).
9. Broccoli, A. J. & Manabe, S. *Clim. Dyn.* **1,** 87–99 (1987).
10. Manabe, S. & Hahn, D. G. *J. Geophys. Res.* **82,** 3889–3911 (1977).
11. Hansen, J. *et al. Climate Processes and Climate Sensitivity* 130–163 (Geophys. Monogr. 29, Am. Geophys. Union, Washington DC, 1984).
12. Manabe, S. & Broccoli, A. J. *J. Atmos. Sci.* **42,** 2643–2651 (1985).
13. Rind, D. *J. Geophys. Res.* **92,** 4241–4281 (1987).
14. Guilderson, T. P., Fairbanks, R. G. & Rubenstone, J. L. *Science* **263,** 663–665 (1994).
15. Stute, M. *et al. Science* **269,** 379–383 (1995).
16. Hansen, J. *et al. Mon. Weath. Rev.* **111,** 609–662 (1983).
17. Miller, J. R., Russell, G. L. & Tsang, L. C. *Dyn. Atmos. Oceans* **7,** 95–109 (1983).
18. Miller, J. R. & Russell, G. L. *Paleoceanography* **4,** 141–155 (1989).
19. Gordon, A. *J. Geophys. Res.* **91,** 5037–5046 (1986).
20. Broecker, W. S. *Oceanography* **4,** 79–89 (1991).
21. Boyle, E. A. & Keigwin, L. D. *Science* **218,** 784–787 (1982).
22. Boyle, E. A. *Annu. Rev. Earth Planet. Sci.* **20,** 245–287 (1992).
23. Curry, W. B. & Lohmann, G. P. *Quat. Res.* **18,** 218–235 (1982).
24. Oppo, D. W. & Fairbanks, R. G. *Earth Planet. Sci. Lett.* **86,** 1–15 (1987).
25. Duplessy, J. C. *et al. Paleoceanography* **3,** 343–360 (1988).
26. Bertram, C. J., Elderfield, H., Shackleton, N. J. & MacDonald, J. A. *Paleoceanography* **10,** 563–578 (1995).
27. Oppo, D. W. & Lehman, S. J. *Science* **259,** 1148–1152 (1993).
28. Boyle, E. A. & Keigwin, L. D. *Nature* **330,** 35–40 (1987).
29. Sarnthein, M. K. *et al. Paleoceanography* **9,** 209–267 (1994).
30. Sigman, D. & Lehman, S. J. *Eos* **46,** F284 (1995).
31. Yu, E.-F., Francois, R. & Bacon, M. P. *Nature* **379,** 689–694 (1996).
32. Berger, A. *J. Atmos. Sci.* **35,** 2362–2367 (1978).
33. Raynaud, D. *et al. Science* **259,** 926–934 (1993).
34. Pollack, J. B. *et al. J. Clim.* **6,** 1719–1742 (1993).
35. Rind, D. *J. Atmos. Sci.* **43,** 3–24 (1986).
36. Imbrie, J. & Kipp, N. G. in *Late Cenozoic Glacial Ages* (ed. Turekian, K. K.) 71–181 (Yale Univ. Press, New Haven, 1971).
37. Duplessy, J.-C. *et al. Oceanol. Acta* **14,** 311–324 (1991).
38. Peixoto, J. P. & Oort, A. H. *Physics of Climate* (Am. Inst. Physics, New York, 1992).
39. Thompson, L. G. *et al. Science* **269,** 46–50 (1995).
40. Rind, D. *J. Atmos. Sci.* **44,** 3235–3268 (1987).
41. Moore, T. C. *et al. Mar. Micropalaeontol.* **5,** 215–247 (1980).
42. Hansen, J., Lacis, A., Ruedy, R., Sato, M. & Wilson, H. *Explor. Res.* **9,** 142–158 (1993).
43. Intergovernmental Panel on Climate Change Working Group I *Climate Change, The Supplemental Report to the IPCC Scientific Assessment* (Cambridge Univ. Press, 1992).
44. Matthews, R. K. & Poore, R. Z. *Geology* **8,** 501–504 (1980).
45. Lindzen, R. A. *Bull. Am. Meteorol. Soc.* **71,** 288–299 (1990).

Acknowledgements. The connection between AGCM results and ocean palaeochemistry grew out of a meeting of the palaeoclimate module of the NOAA-LDEO-SIO Climate Consortium. We thank D. M. Anderson, J. T. Overpeck, M. Chandler, K. Hughen, G. L. Russell, J. R. Miller, W. B. Curry, A. J. Broccoli and M. K. England for discussions and reviews of the manuscript. This work was supported by the NOAA-NGDC Paleoclimatology Program, NASA Climate Program Office, and the US National Science Foundation.

Correspondence should be addressed to R.S.W. (e-mail: rwebb@ngdc.noaa.gov). Model results presented in this Article are available at the World Data Center-A for Paleoclimatology (http://www.ngdc.noaa.gov/paleo/paleo.html).

Visibility of scattered broad-line emission in Seyfert 2 galaxies

Charlene A. Heisler*, Stuart L. Lumsden† & Jeremy A. Bailey†

* *Mount Stromlo and Siding Springs Observatory, Institute of Advanced Studies, The Australian National University, Weston Creek Post Office, Canberra, ACT, 2611, Australia*

† *Anglo-Australian Observatory, PO Box 296 Epping, NSW 2121, Australia*

Active galaxies are thought to be powered by the accretion of gas onto a central massive black hole. Seyfert galaxies—the most common examples of nearby active galaxies—are separated into two classes based on their emission line widths[1]. Seyfert 1 galaxies exhibit broad emission lines that are attributed to ionized gas within 1 pc of the black hole, whereas the spectra of Seyfert 2 galaxies show only narrower emission lines, believed to originate from a much larger region around the core. The 'unified model' for Seyfert galaxies attributes these differences to the presence of a dusty torus of dense molecular gas surrounding the black hole[2]: the orientation of Seyfert 2 galaxies is such that the broad-line region is obscured. The detection[3] in the polarization spectrum of broad emission lines scattered into our line of sight by free electrons in NGC1068 (the prototypical Seyfert 2 galaxy) and other Seyfert 2 galaxies[4–8] has strengthened this view, but all of these galaxies were subject to selection biases. Here we report the results of a systematic search for polarized broad emission lines in a well defined sample of Seyfert 2 galaxies. We show that the ability to detect scattered broad emission lines is related to the far-infrared colours, in the manner predicted by the unified model.

Since the discovery of a hidden broad-line region (HBLR) in NGC1068, about 12 additional HBLRs have been detected by spectropolarimetry in Seyfert 2 galaxies[4–8]. Unfortunately, all previous studies are known to be biased in their continuum polarization properties, with samples chosen to be either highly polarized or having rising polarization in the red. Such characteristics are not typical of Seyfert galaxies in general. In addition to these biases, there have been very few non-detections published, and there has been no consistency in ensuring non-detections are at the same signal-to-noise ratio in percentage polarized flux. To overcome these problems, we have chosen a sample of Seyfert 2 galaxies in an objective manner using the isotropically emitted far-infrared fluxes.

Here we report the results of our spectropolarimetric survey of a well defined infrared-selected sample of Seyfert 2 galaxies. Our flux-limited sample was chosen from the IRAS Faint Source Catalog, Version 2, to include all southern Seyfert 2 galaxies at declination $\delta < +20°$, with $|b| > 25°$ (where b is Galactic latitude), and with high-quality detections at 12, 25, 60 and 100 μm, a 60-μm flux limit of $f_{60} > 5$ Jy, a far-infrared (FIR) luminosity cut-off of $\log(L_{FIR}/L_{\odot}) > 9.85$, and a far-infrared flux ratio of $f_{60}/f_{25} < 8.5$ to exclude normal spirals dominated by the cool disk component. The classification[1] of a galaxy as a Seyfert 2 is based on our own optical spectra. We include galaxies that lie close to the borderline of Seyferts and 'low-ionization nuclear emission-line region' (LINER) galaxies in optical line diagnostic diagrams. The total sample consists of 16 Seyfert 2 galaxies (see Table 1).

We have uncovered a previously unknown HBLR in the galaxy IC3639. The region of the spectrum near Hα is shown in Fig. 1. The total flux spectrum (Fig. 1a) shows the narrow line emission typical of Seyfert 2 galaxies. The polarized-flux spectrum (Fig. 1b), reveals a broad component to Hα in addition to the narrower line emission.

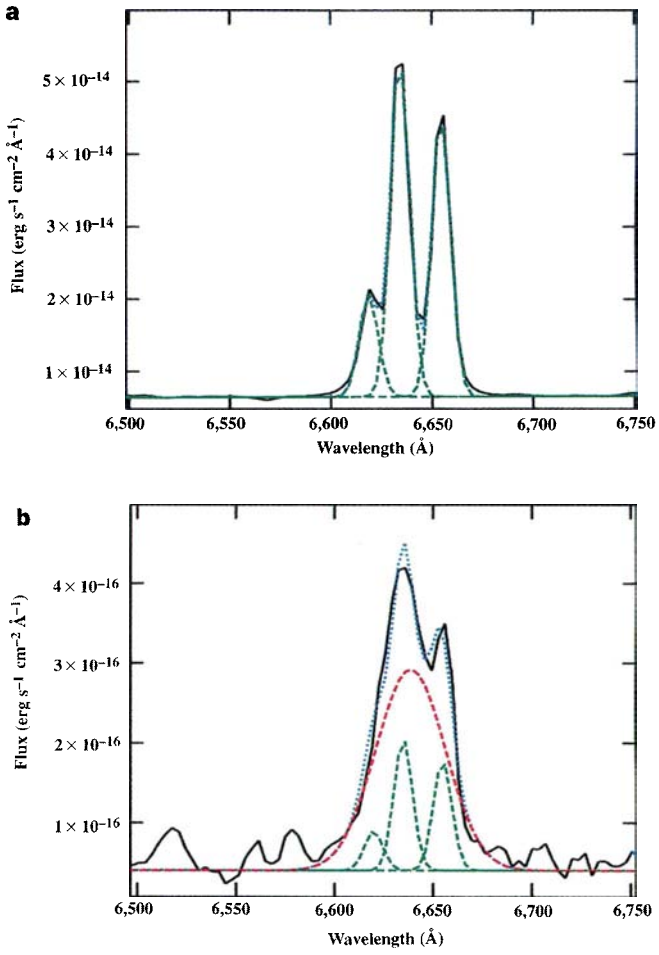

Figure 1 a, Direct light spectrum of IC3639 (solid black line) showing gaussian fits to the narrow lines [N II] 6,548 Å, Hα and [N II] 6,548 Å (dashed green lines). The sum of the three gaussian fits is represented by the dotted blue line. The line profiles of the Hα and [N II] complex are well fitted by three gaussians all having full-width at half-maximums (FWHM) ~320 km s^{-1}. **b**, Polarized light spectrum of IC3639 (solid black line), illustrating the broad component of Hα. The fit to the broad line was obtained by initially using the narrow line fits obtained from the direct light spectrum (dashed green lines) and fitting an additional component to the observed profile in polarized light. The additional broad component is centred at Hα and has FWHM ~1,860 km s^{-1} (dashed red line). The sum of the fitted profiles is represented by the dotted blue line.

The most striking result of our survey is given in Fig. 2. Those galaxies with detected HBLRs should have warmer FIR colours ($f_{60}/f_{25} < 4$) and smaller internal extinctions as measured by the Balmer decrement, compared to Seyferts for which HBLRs are not detected. The segregation between HBLRs and non-HBLRs as a function of far-infrared spectral index is most obvious for the shorter wavelength ratios, f_{60}/f_{25} and f_{60}/f_{12}, with the HBLRs having flatter far-infrared spectral indices. Although the distribution of the 60 μm to 100 μm colour is slightly bluer for HBLRs, the far-infrared flux ratio f_{60}/f_{100} does not prove to be as good at discriminating between HBLRs and non-HBLRs as do FIR flux ratios at shorter wavelengths. This survey confirms previous speculation[6,9,10] that galaxies with HBLRs have generally flatter FIR spectra.

Radio observations made with the Parkes–Tidbinbilla Interferometer (PTI) at 2.3 GHz exist for the entire sample[11–13]. This interferometer is sensitive only to structures with brightness

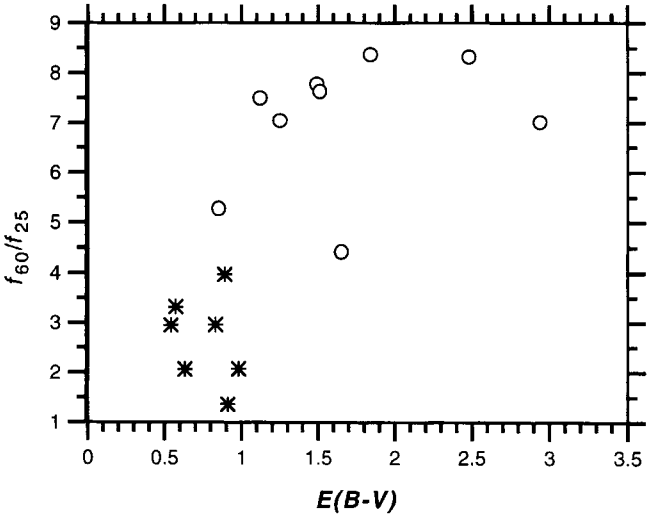

Figure 2 Correlation between internal extinction $E(B-V)$, far-infrared flux ratio and the detectability of an HBLR in the IRAS-selected Seyfert 2 sample. (f_{60} indicates the flux at 60 μm, f_{25} the flux at 25 μm.) Stars, HBLR detected; open circles, no HBLR detected. Optical spectropolarimetric observations were obtained at the Anglo-Australian Telescope during 16–18 August 1995. The half-waveplate module, built by the University of Hertfordshire, was used in conjunction with the RGO spectrograph, the 270R grating and the 25-cm camera, giving a spectral resolution of 8.4 Å. Our observations yield a 3σ detection at 0.5% polarization.

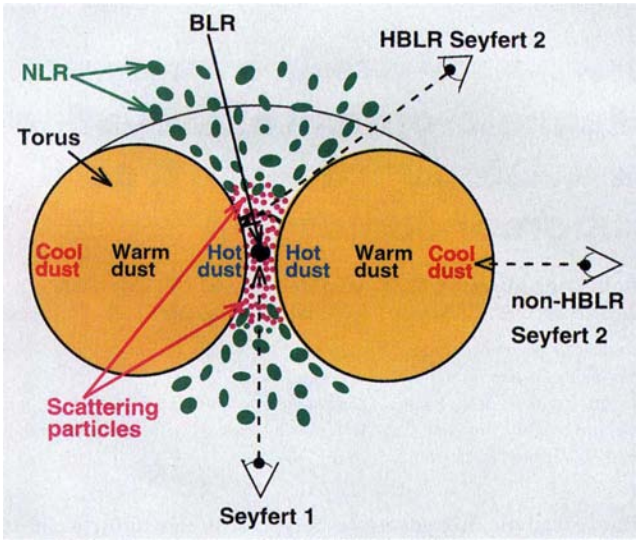

Figure 3 Schematic diagram (not to scale) of the central region of a Seyfert galaxy illustrating the effect of viewing angle on infrared colours and ability to detect the broad-line region (BLR). We have indicated the BLR which has a typical size of <1 pc, the narrow-line region (NLR) clouds located <1 kpc from the BLR, and the scattering particles located <300 pc from the BLR. The temperature of the dust in the torus decreases radially outwards. The viewing angles producing the Seyfert 1, hidden broad-line region (HBLR) Seyfert 2 and non-HBLR Seyfert 2 galaxies are illustrated. An edge-on view will result in an optical spectrum which is characteristic of a Seyfert 2 with 'cool' infrared colours, and relatively large values of internal extinction, due to obscuration by the cool dust in the outer regions of the torus. A face-on viewing angle will provide a direct view of the BLR and of the hot dust at the inner edge of the torus resulting in a Seyfert 1 spectrum and 'hot' infrared colours. At intermediate viewing angles, the BLR is detected only by scattered light, the far-infrared colours have 'warm' dust temperatures, and the internal extinction to the NLR will be small relative to an edge-on orientation.

temperatures $>10^5$K, and sizes <0.1 arcsec, which corresponds to <35 pc at the mean redshift, $z = 0.018$, of our sample (assuming a Hubble constant $H_o = 75\,\mathrm{km\,s^{-1}\,Mpc^{-1}}$). Thus, the PTI detects radio emission from compact sources associated with active galactic nuclei, but does not see extended star-formation regions with typical brightness temperatures $<10^4$ K. There is no significant difference in the detection rate for HBLR and non-HBLR Seyfert 2 galaxies, with 71% and 67% containing compact radio cores, respectively. These observed detection rates are consistent with that found for other samples of Seyfert 2 galaxies. The PTI results indicate that the HBLRs and non-HBLRs are drawn from the same parent population of galaxies containing an active galactic nucleus.

The above results can not be explained by either a distance or a luminosity effect. The redshift and FIR luminosity distributions are similar for HBLRs and non-HBLRs. The Kolmogorov–Smirnov statistical test for the cumulative distributions of the redshift and FIR luminosity, shows that we can reject the hypothesis that the HBLRs and non-HBLRs samples are different at the 96% and 98% confidence level, respectively. There is no segregation between the HBLRs and non-HBLRs with respect to overall polarization percentage or with continuum polarization as a function of wavelength.

The results presented here are best understood within the context of the unified model, which asserts that a Seyfert 2 galaxy would appear as a Seyfert 1 galaxy if viewed at an angle such that the torus was oriented face-on. Because the inner side of the torus that obscures the broad-line region 'sees' the radiation from the active galactic nucleus directly, the dust temperature there is high ($T_{\mathrm{dust}} > 1{,}000$ K), and contributes mostly at 12 and 25 μm. However, the torus may have significant opacity even in the mid-infrared, so that only the longer wavelengths (>50 μm) could be assured of escaping directly. Unless we see part of the inner face of the torus almost directly, the 12- and 25-μm radiation will be reprocessed to longer wavelengths, and the galaxy will have 'cool' FIR colours. This is consistent with theoretical models[14–16] which indicate that an increase in the inclination of dust tori causes steepening of spectral indices at FIR wavelengths, and observational data[17–19] which indicate that Seyfert 1 galaxies have flatter far-infrared ratios, f_{25}/f_{12} and f_{60}/f_{25}, compared to Seyfert 2 galaxies. Detailed modelling[20] of the well known HBLR, NGC1068, indicates that the viewing angle is 55°, while observed structure of the ionization cone[21] suggests that the opening angle of the torus is 60°. Thus if the inclination of the torus were increased by only 5°, NGC1068 would appear as a Seyfert 1. So the Seyfert 2 galaxies with HBLRs detected via spectropolarimetry represent Seyfert 1 nuclei surrounded by a torus that is viewed at an angle intermediate between Seyfert 1 and non-HBLR Seyfert 2 galaxies.

The larger extinction observed in the non-HBLR Seyfert 2 galaxies (Fig. 2) is attributed to an edge-on line of sight, which passes through a larger amount of dust in the torus. A major implication of our results is that the scattering particles producing the observed polarized broad lines must lie very close to or possibly within the plane of the torus. A similar proposal was put forward by Miller and Goodrich[4], who attributed the lack of high-polarization Seyfert 2 galaxies with nearly edge-on disks to a bias in their sample against edge-on Seyfert 2 galaxies as a result of scattering occurring very close to the nucleus. A schematic diagram which describes how the results of our survey fit within the concept of unification between Seyfert 1 and Seyfert 2 galaxies is displayed in Fig. 3.

The fact that dust is inhibiting our view of the HBLR in the Seyfert 2 galaxies with colder far-infrared colours points to the limitation of optical spectropolarimetry for studying these objects, and underlines the benefit of moving to longer wavelengths where the effects of extinction are decreased. Assuming that all Seyfert galaxies contain suitable scattering particles, we predict that broad polarized lines of Brγ will be detected in the Seyfert 2 galaxies with

Table 1 Sample of bright Seyfert 2 galaxies

Galaxy name	Other names	z	f_{60}/f_{25}	HBLR?	Ref.	PTI flux density (Jy)
NGC0034*	Mrk 938	0.01978 ± 0.00004	7.01	No	This work	0.004
NGC1068	M77, Arp37	0.00379 ± 0.00001	2.07	Yes	2	0.086
NGC1143		0.02822 ± 0.00010	8.37	No	This work	0.004
IRAS05189 − 2524		0.04256 ± 0.00018	3.97	Yes	7	<0.003
NGC4388		0.00842 ± 0.00000	2.96	Yes†	7	<0.006
IC3639	Tol1238 − 364	0.01096 ± 0.00002	3.32	Yes	This work	0.013
MCG − 3 − 34 − 63		0.01718 ± 0.00018	2.06	Yes	7	0.026
NGC5135		0.01372 ± 0.00006	7.04	No	This work	<0.005
IRAS19254 − 7245		0.06171 ± 0.00027	4.42	No	This work	0.033
IC5063	PKS2048 − 57	0.01135 ± 0.00002	1.36	Yes	6	0.152
NGC7130	IC5135	0.01615 ± 0.00005	7.78	No	This work	0.014
NGC7172		0.00859 ± 0.00001	7.50	No	This work	0.003
NGC7496		0.00550 ± 0.00002	5.28	No	This work	0.007
NGC7582		0.00525 ± 0.00002	7.63	No	This work	<0.005
NGC7590		0.00532 ± 0.00002	8.32	No	This work	<0.003
NGC7674	Arp182	0.02901 ± 0.00008	2.95	Yes	4	0.039

z indicates redshift (adopted from the NASA/IPAC Extragalactic Database-NED; f_{60}/f_{25} is the far-infrared 60 μm to 25 μm flux ratio adopted from NED; HBLR? indicates whether a hidden broad-line region has been detected via optical spectropolarimetry; Ref. is the published reference for spectropolarimetry observation. The rightmost column gives the PTI flux density at 2.3 GHz; upper limits are quoted at five times r.m.s. noise in the fringe-frequency spectrum. These flux densities are taken from refs 11-13 and R. Norris (personal communication).
* The classification of NGC 0034 as a Seyfert 2 galaxy is somewhat controversial. Based on our own spectra we classify this galaxy as a marginal LINER/Seyfert 2 galaxy. It has been classified as a Seyfert 2 by several authors[22,23] while others claim that it is not a Seyfert 2 galaxy[24,25]. We retain this galaxy in our sample noting that it lies on the boundary of LINER/Seyfert 2 in optical line ratio diagnostic diagrams.
† The signal-to-noise for the polarized flux spectra obtained by Young *et al.*[7] is consistent with what we have obtained for our sample. Although a broad component is fitted to the polarized spectra at Hα (ref. 7), the detection is regarded as tentative. We regard NGC4388 as containing an HBLR, and note that this classification is tentative; a misclassification of this one object will not significantly alter the conclusions presented in this Letter.

intermediate far-infrared colours, and would provide a strong confirmation of the unified model. Such observations are now feasible using current near-infrared spectropolarimeters. □

Received 18 October 1996; accepted 16 January 1997.

1. Osterbrock, D. E. *Astrophysics of Gaseous Nebulae and Active Galactic Nuclei* 308–381 (University Science Books, Mill Valley, USA, 1989).
2. Antonucci, R. R. J. *Annu. Rev. Astron. Astrophys.* **31,** 473–521 (1993).
3. Antonucci, R. R. J. & Miller, J. S. *Astrophys. J.* **297,** 621–632 (1985).
4. Miller, J. S. & Goodrich, R. W. *Astrophys. J.* **355,** 456–467 (1990).
5. Tran, H., Miller, J. S. & Kay, L. *Astrophys. J.* **397,** 452–456 (1992).
6. Inglis, M. D. *et al. Mon. Not. R. Astron. Soc.* **263,** 895–902 (1993).
7. Young, S. *et al. Mon. Not. R. Astron. Sco.* **281,** 1206–1242 (1996).
8. Hines, D. C. & Wills, B. J. *Astrophys. J.* **415,** 82–92 (1993).
9. Hutchings, J. B. & Neff, S. G. *Astron. J.* **101,** 434–446 (1991).
10. Kay, L. in *The First Stromlo Symposium: The Physics of Active Galaxies* (eds Bicknell, G. V., Dopita, M. A. & Quinn, P. J.) 265–266 (ASP Conf. Ser. Vol. 54, Astron. Soc. Pacific, San Francisco, 1994).
11. Roy, A. L., Norris, R. P., Kesteven, M. J., Troup, E. R. & Reynolds, J. E. *Astrophys. J.* **432,** 496–507 (1994).
12. Heisler, C. A., Norris, R. P., Jauncey, D. L., Reynolds, J. E. & King, E. A. in *Proc. 4th Asia Pacific Meeting and Workshop* (ed. King, E. A.) 166–177 (ATNF, Sydney, Australia, 1996).
13. Norris, R. P., Allen, D. A., Sramek, R. A., Kesteven, M. J. & Troup, E. R. *Astrophys. J.* **359,** 291–295 (1990).
14. Pier, E. A. & Krolik, J. H. *Astrophys. J.* **418,** 673–686 (1993).
15. Granato, G. L. & Danese, L. *Mon. Not. R. Astron. Soc.* **268,** 235–252 (1994).
16. Efstathiou, A. & Rowan-Robinson, M. *Mon. Not. R. Astron. Soc.* **273,** 649–661 (1995).
17. Giuricin, G., Mardirossian, F. & Mezzetti, M. *Astrophys. J.* **446,** 550–560 (1995).
18. Maiolino, R., Ruiz, M., Rieke, G. H. & Keller, L. D. *Astrophys. J.* **446,** 561–573 (1995).
19. Spinoglio, L., Malkan, M. A., Rush, B., Carrasco, L. & Recillas-Cruz, E. *Astrophys. J.* **453,** 616–633 (1995).
20. Young, S., Hough, J. H., Axon, D. J., Bailey, J. A. & Ward, M. J. *Mon. Not. R. Astron. Soc.* **272,** 513–527 (1995).
21. Pogge, R. W. *Astrophys. J.* **345,** 730–751 (1989).
22. Veilleux, S., Kim, D.-C., Sanders, D. B., Mazzarella, J. M. & Soifer, B. T. *Astrophys. J. Suppl. Ser.* **98,** 171–217 (1995).
23. Veron-Cetty, M.-P. & Veron, P. *Astron. Astrophys. Suppl. Ser.* **65,** 241–258 (1986).
24. Mulchaey, J. S., Wilson, A. S. & Tsvetanov, Z. *Astrophys. J. Suppl. Ser.* **102,** 309–367 (1996).
25. Osterbrock, D. E. & Dahari, O. *Astrophys. J.* **273,** 478–488 (1983).

Acknowledgements. We thank J. Hough for discussions on spectropolarimetry of AGN; R. Norris for introducing us to the PTI as an effective tool for uncovering AGN cores, and for discussions; R. Antonucci for reviewing this manuscript and for comments and suggestions. This research has made use of the NASA/IPAC Extragalactic Database (NED) which is operated by the Jet Propulsion Laboratory, California Institute of Technology, under contract with NASA.

Correspondence should be addressed to C.A.H. (e-mail: heisler@mso.anu.edu.au).

Magneto-optical observation of twisted vortices in type-II superconductors

M. V. Indenbom*†, C. J. van der Beek*, V. Berseth*, W. Benoit*, G. D'Anna*, A. Erb‡, E. Walker‡ & R. Flükiger‡

* *Institut de Génie Atomique, Département de Physique, Ecole Polytechnique Fédérale de Lausanne, CH-1015 Lausanne, Switzerland*
† *Institute of Solid State Physics, 142432 Chernogolovka, Moscow District, Russia*
‡ *Département de Physique de la Matière Condensée, Université de Genève, CH-1211 Genève, Switzerland*

When magnetic flux penetrates a type-II superconductor, it does so as quantized flux lines or vortex lines, so called because each is surrounded by a supercurrent vortex. Interactions between such vortices lead to a very rich and well characterized phenomenology for this 'mixed state'. But an outstanding question remains: are individual vortex lines 'strong', or can they easily be cut and made to pass through one another? The concept of vortex cutting was originally proposed to account for dissipation observed in superconducting wires oriented parallel to an applied magnetic field, where the vortex lines and transport current should be in a force-free configuration[1–6]. Previous experiments, however, have been unable to establish the vortex topology in the force-free configuration or the size of the energy barrier for vortex cutting. Here we report magneto-optical images of $YBa_2Cu_3O_{7-\delta}$ samples in the force-free configuration which show that thousands of vortex lines can twist together to form highly stable structures. In some cases, these 'vortex twisters' interact with one another to produce

wave-like dynamics. Our measurements also determine directly the current required to initiate vortex cutting, and show that it is much higher than that needed to overcome the pinning of vortices by material defects. This implies that thermodynamic phases of entangled vortices[7–10] are intrinsically stable and may occupy a significant portion of the mixed-state phase diagram for type-II superconductors.

The flux structures were visualized using a magneto-optical technique. This technique was initially used to understand the basic principles of vortex line motion under the Lorentz force ($\mathbf{j} \times \mathbf{B}$) due to a transport supercurrent $\mathbf{j}$ (ref. 11); it has been considerably developed and is now particularly successfully applied to the investigation of complicated material problems in high-temperature superconductors[12,13]. A recent development is the implementation of ferrimagnetic garnet films with in-plane anisotropy as the element sensitive to the magnetic induction B: such films are the most sensitive available to date and have the largest working range in temperature[14]. Thus, small samples of any superconductor material can be studied without special sample preparation, the only prerequisite being flat surfaces on which the garnet film can be placed. The induction perpendicular to the sample is observed using the Faraday rotation of the polarization direction of the incident light, induced in the garnet film.

The observations were made possible by the very low pinning of the $YBa_2Cu_3O_{7-\delta}$ single crystals used. The twinned single crystals were grown in new $BaZrO_3$ crucibles which do not contaminate the sample[15]. The crystal purity is the highest we have achieved to date; samples grown by this method also exhibit the 'vortex lattice melting' step in magnetization and the corresponding latent heat[16,17].

The experimental procedure is given in ref. 18. A magnetic field $H_{||}$ is applied in the plane of the flat rectangular $YBa_2Cu_3O_{7-\delta}$ crystal, parallel to the crystal's longer side. An in-plane vortex lattice is produced by cooling the crystal through its critical temperature T_c. Once the desired working temperature is reached, a magnetic field $H_\perp$ is applied perpendicular to the plane of the sample. This field induces an in-plane circulating screening current which flows parallel to the sample edges. Along the shorter crystal sides, the current is perpendicular to the vortices, so the latter start to move out of the crystal plane under the action of the Lorentz force. This out-of-plane motion is limited by flux pinning, and the well known critical state[1] is built up. Along the longer sample sides the current is parallel to the in-plane vortices. The Lorentz force is zero and vortices initially do not move. This 'force-free configuration' is the same as that in a current-carrying type-II superconducting wire in a parallel magnetic field. The anisotropy that the force-free configuration induces can also be studied using transverse a.c. susceptibility experiments, as shown in refs 19 and 20.

We observe that, although the Lorentz force on the vortices is nominally zero, and there is no reason to expect vortex motion, flux penetration from the long crystal sides starts when $H_\perp$ is increased above a threshold of ~200 G (Fig. 1a). (Motion of the force–free configuration was not observed in the previous study[18], probably because the higher vortex pinning prevented it in the $YBa_2Cu_3O_{7-\delta}$ crystals studied there.) The flux profile taken perpendicular to the long crystal sides, and associated with the novel motion (Fig. 1b), is characterized by a very steep moving front and is different from the standard critical-state model where the induction gradient is constant over the region of penetration[1]. The observed steep front is the signature of an additional critical current, which we associate with vortex-cutting processes occurring in the region of the front. To determine the density of this current from the flux profile observed at the sample surface is, however, very difficult. The flux front should have a curved structure between the sample surfaces, and all currents distributed throughout the sample thickness contribute to $B_\perp$.

A much more controllable situation can be realized by reversing

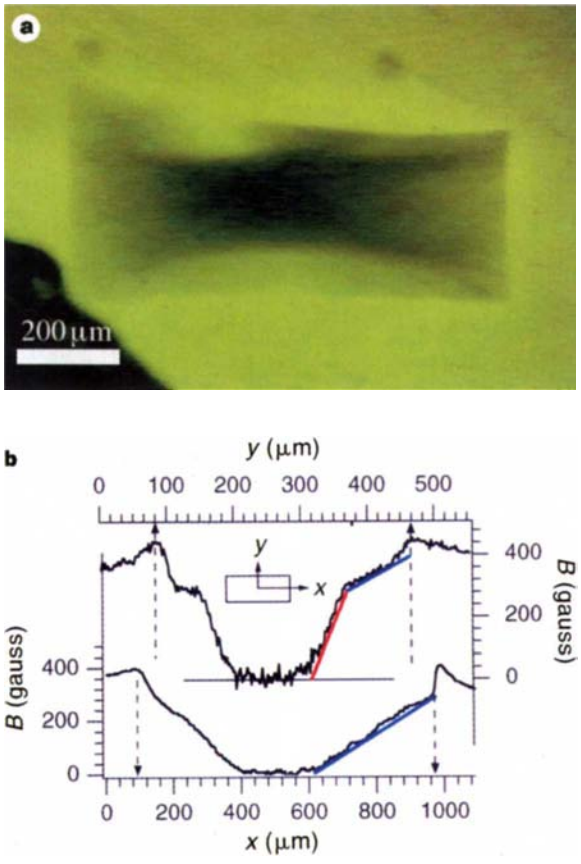

Figure 1 a, The penetration of perpendicular flux into a $YBa_2Cu_3O_{7-\delta}$ single crystal of thickness 24 μm in the presence of an in-plane magnetic field $H_{||} = 1{,}550$ G oriented parallel to the long crystal sides ($H_\perp = 355$ G, $T = 67$ K). The higher perpendicular induction $B_\perp$ corresponds to the brighter areas in the video frame. The crystal edges are revealed as the sharp straight boundaries between areas of higher $B_\perp$ outside the sample and areas of lower $B_\perp$ inside it. The screening current along the shorter left- and right-hand sides of the crystal is perpendicular to $H_{||}$; flux penetration there is gradual, with nearly constant critical induction gradient (the blue line near the lower curve in **b**). The flux penetration from the long sides, where current and flux are in a force-free configuration, has started later, and is characterized by a very steep front (the red line near the upper curve in **b**) corresponding to the extra current needed for vortex cutting. The critical slope behind the front is again determined by pinning (blue line). **b**, Flux profiles, taken through the centre of the image in the vertical (y) direction (top trace), and in the horizontal (x) direction (bottom trace). The vertical dashed lines correspond to the position of the crystal edges.

$H_\perp$ (Fig. 2). Vortex lines will now be rotated in the opposite direction, and a negative $B_\perp$ gradually replaces the trapped positive $B_\perp$. Again, the development of the flux profile along the short sample sides is described by the standard critical-state model. A completely different picture, with very sharp boundaries between regions of opposite polarity of $B_\perp$, is observed along the longer, 'force-free' sides of the crystal. Because of the finite sample thickness, electrodynamics requires that the B-lines turn around the boundary, and when superposed on the constant in-plane field, produce two flux-line helicoids of opposite chirality moving in from the long crystal sides. Around the flux step at $B_\perp = 0$, which is seen in Fig. 2 as a dark thin line, tens of thousands of vortices are twisted together in helicoidal trajectories constrained by the sample thickness, as schematically shown in Fig. 3. Although the precise way in which the whole process develops remains to be elucidated, we argue that in order for this novel macroscopic 'vortex twister' to move, vortices should be cut and interconnected everywhere inside

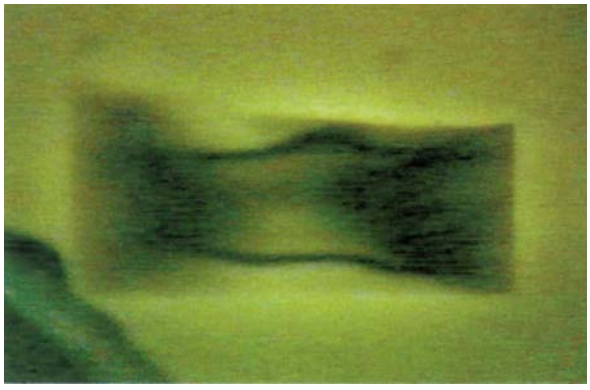

Figure 2 The perpendicular flux distribution in the single crystal after $H_\perp$ has been increased from 355 G (Fig. 1) to 443 G, then decreased to −305 G. The external magnetic field reversal twists vortices around two dark narrow lines of $B_\perp = 0$. The mutual cutting of vortex helices fully constrained into the crystal, as shown schematically in Fig. 3, determines the magnitude of the strong extra currents concentrated along these lines. The smooth contrast with wide dark areas near the (short) sample ends corresponds to the usual critical flux gradients controlled by the balance of pinning and Lorentz forces.

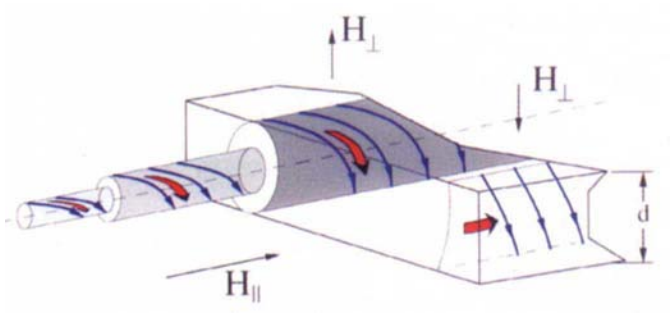

Figure 3 Scheme of the enclosed helicoidal vortex trajectories (blue arrows) and currents (red arrows) inside the 'vortex twister' shown in Fig. 2. Only current helices constrained within the thickness of the crystal can follow the magnetic field helicoids; currents outside the 'twister' flow straightforwardly and produce the Lorentz force.

it. Vortex cutting sustains a strong current which is additional to the low pinning critical current background. Its magnitude can be estimated from the observed flux distribution as ~1 A.

The 'vortex twister' is in fact a miniature reproduction of the experiments devised to study cross-flux flow in current-carrying cylindrical superconducting wires in an axially applied magnetic field[1–4]. These experiments showed that, in order to accomodate the field change induced by the current, outer vortices 'paramagnetically' compress those of lesser pitch on the inside of the helicoid, and thereby rotate the supercurrent along it. In this way a force-free supercurrent configuration is formed throughout. The additional longitudinal critical current density necessary for vortex cutting, $j_{||}$ in Clem's notation[5], can be estimated from the total extra current of the 'twister' as $j_{||} \approx 2 \times 10^9\ \mathrm{A\,m^{-2}}$. The background pinning current density, extracted from the field dependence of the flux penetration depth is only $j_\perp \approx 3 \times 10^8\ \mathrm{A\,m^{-2}}$. In spite of its relatively small value, $j_\perp$ plays an important role, as it prevents a completely trivial flux penetration from the short sample sides only. At the same time $j_\perp$ reduces the flux compression inside the 'twister', and the current configurations deviate from ideally force-free, as the supercurrent no longer precisely follows the helicoidal vortex paths[21].

The fact that the 'vortex twisters' are really strong macroscopic structures is clearly demonstrated by their behaviour under much higher-frequency a.c. excitation (Fig. 4). 'Twisters' of opposite chirality, successively generated by a periodic perpendicular magnetic field, carry currents of opposite polarity and thus repel each other electromagnetically; at the same time vortices of opposite helicity may annihilate. The interplay of these two effects produces a moving pattern of flux 'waves' slowly emanating from the crystal sides, asynchronously with respect to the applied a.c. magnetic field. An important general analogy to the 'twister' itself and the pattern of many 'twisters' is the work hardening of crystalline solids: during cyclic plastic deformation different interacting dislocations irreversibly produced in a crystal inhibit each other's motion and the material strength can rise to much higher values[22]. Similarly, we observe that the structure of 'twisters' generated by an a.c. magnetic field is very stable and remains in the sample for a long time (hours) after the a.c. excitation is switched off; in contrast at the same temperature, the ordinary critical-state profile without in-plane

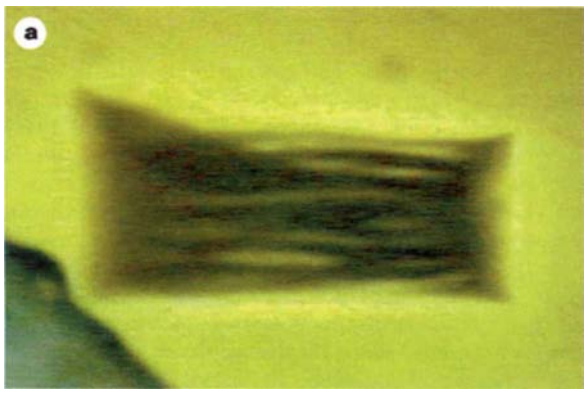

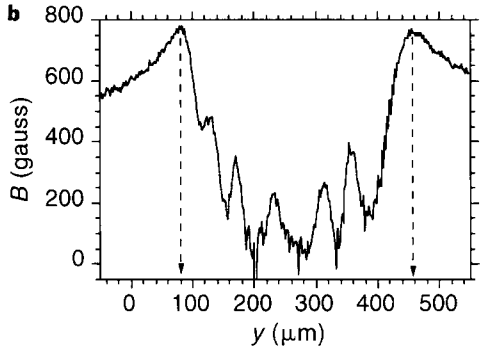

Figure 4 a, Pattern of flux waves emanating from the edges of the single crystal. The waves consist of asynchronously moving 'twisters' of opposite chirality, generated by successive cycles of the perpendicular a.c. magnetic field (frequency 46 Hz, amplitude 555 G). This pattern can be considered a macroscopical realization of vortex entanglement. **b**, Flux profile taken across the crystal in the y direction. Moving images of the moving 'twisters' are available at http://igahpse.epfl.ch/htc/twister.html).

magnetic field relaxes within seconds. The 'twisters' are a macroscopic realization of the microscopically entangled vortex state, and their stability shows that thermodynamic phases of entangled vortices could occupy a considerable area of the mixed-state phase diagram. □

Received 21 November 1996; accepted 10 January 1997.

1. Campbell, A. M. & Evetts, J. E. *Adv. Phys.* **21,** 199–428 (1972).
2. Timms, W. E. & Walmsley, D. G. *J. Phys. F* **5,** 287–306 (1975).
3. LeBlanc, M. A. R. *et al. Phys. Rev. Lett.* **14,** 704–707 (1965); **66,** 3309–3312 (1991); **71,** 3367–3370 (1993).
4. Fillion, G., Gauthier, R. & LeBlanc, M. A. R. *Phys. Rev. Lett.* **43,** 86–89 (1979).
5. Clem, J. R. *Phys. Rev. B* **26,** 2463–2473 (1982).
6. Brandt, E. H. *Rep. Prog. Phys.* **58,** 1456–1594 (1995).
7. Nelson, D. R. *Phys. Rev. Lett.* **60,** 1973–1977 (1988).
8. Fisher, M. P. A. *Phys. Rev. Lett.* **62,** 1415–1419 (1989).
9. Brandt, E. H. & Sudbø, A. *Phys. Rev. Lett.* **66,** 2278 (1991).
10. Obukhov, S. P. & Rubinstein, M. *Phys. Rev. Lett.* **66,** 2279 (1991).
11. DeSorbo, W. & Healy, W. A. *Cryogenics* **4,** 257–326 (1964).
12. Durán, C. A. *et al. Nature* **357,** 474–477 (1992).
13. Welp, U. *et al. Nature* **376,** 44–46 (1995).
14. Dorosinskii, L. A. *et al. Physica C* **203,** 149–156 (1992).
15. Erb, A., Walker, E. & Flükiger, R. *Physica C* **258,** 9–20 (1996).
16. Schilling, A. *et al. Nature* **382,** 791–793 (1996).
17. Roulin, M. *et al. J. Low. Temp. Phys.* **105,** 1099–1104 (1995).
18. Indenbom, M. V. *et al. Physica C* **226,** 325–332 (1994).
19. D'Anna, G. *et al. Europhys. Lett.* **25,** 225–230 (1994).
20. André, M.-O. *et al. Proc. 7th Int. Workshop on Critical Currents* (ed. Weber, H. W.) 276–279 (World Scientific, Singapore, 1994).
21. Meissner, H. *Phys. Rev. B* **97,** 1627–1633 (1955); **101,** 31–36 (1956).
22. Nabarro, F. R. N., Bazinski, Z. S. & Holt, D. B. *Adv. Phys.* **13,** 193–323 (1964).

Acknowledgements. We thank E. H. Brandt for many useful discussions. This work was supported by the Swiss National Science Foundation.

Correspondence and requests for materials should be addressed to G.D'A. (e-mail: supra@igahpse.epfl.ch).

Abrupt changes in early Holocene tropical sea surface temperature derived from coral records

J. Warren Beck*, Jacques Récy†, Fred Taylor‡, R. Lawrence Edwards§ & Guy Cabioch†

* *NSF Arizona AMS Facility, Department of Physics, University of Arizona, Tucson, Arizona 85721, USA*

† *ORSTOM (Institut Français de Recherche Scientifique pour le Développement en Coopération), Laboratoire de Géodynamique, Observatorie Océanographique, BP 48, 06230 Villefranche-sur-Mer, France*

‡ *Institute for Geophysics, University of Texas at Austin, Texas 78759, USA*

§ *Minnesota Isotope Laboratory, Department of Geology and Geophysics, University of Minnesota, Minneapolis, Minnesota 55455, USA*

For many high-latitude regions of the globe, it is now clear that the transition to modern climate following the Last Glacial Maximum was punctuated by a number of rapid and substantial climate oscillations[1,2]. In contrast, relatively little is known about how the tropics responded to the deglaciation, because few high-resolution records are available from lower latitudes. Corals have recently been shown to provide an important source of tropical climate records because they can be easily and accurately dated, using either ^{14}C or ^{230}Th, and because past sea surface temperatures can be recovered from the Sr/Ca ratios in coral skeletons. Here we use this technique to derive several early Holocene sea surface temperature records from a coral drill core recovered from Espiritu Santo, Vanuatu in the tropical southwest Pacific Ocean. These records indicate that sea surface temperatures in this region were depressed by as much as 6.5 °C below modern values at ~10,350 calendar years BP, but rose very abruptly during the following 1,500 years. This temperature increase lags the post-Younger Dryas increase observed in a coral record from the tropical Atlantic Ocean[3] by about 3,000 years, an unexpected phase-shift that may ultimately shed light on the mechanisms of deglacial climate change.

Our sea surface temperature (SST) data contrast markedly with the results of CLIMAP[4] published nearly two decades ago which advanced the view that tropical ocean SSTs varied little between the current interglacial period and the Last Glacial Maximum (LGM) at ~18–20 kyr ago. Although oxygen-isotope constraints from deep sea sediments[5,6] appear to corroborate the CLIMAP findings, CLIMAP is not in agreement with the records of alpine glacier snow lines[7–9] or the records of tropical glacier oxygen-isotope measurements[9] which suggest that tropical and subtropical SSTs may have been 4.2–8 °C cooler during the LGM than today. Likewise, the CLIMAP results are not compatible with some modelling results[10,11] of LGM conditions or with many terrestrial pollen assemblages[10,12] which suggest that tropical SSTs must have been of the order of 2–5 °C colder than at present. Calculations derived from the dissolved concentrations of rare gases in ice-age ground water[13] similarly indicate that LGM temperatures were 5 °C colder than today in tropical regions. This perspective of relatively cold ice-age tropics is further reinforced by the recent findings that Caribbean LGM SSTs appear to have been 5–6 °C colder than at present based on coral Sr/Ca thermometry results from Barbados[3]. These results compel us to take seriously the proposition that LGM tropical climate may have been significantly colder than at present.

We present evidence here that these cold tropical temperatures may have persisted until relatively late in the last deglaciation in parts of the tropics, or that the tropics experienced protracted cold episodes midway during the deglaciation. There are now many indications from high-latitude records that the transition from the LGM to the present interglacial conditions has not been a smooth gradual change, but rather has been punctuated by at least several periods of rapid climate change. The best known of these is the so-called Younger Dryas cold period (~12.9–11.5 kyr BP), although other periods of extremely rapid climate change are now known to have occurred during the last deglaciation[14]. According to the GISP II Greenland ice-core records, these climate oscillations may last for centuries to millennia, but the transitions between them may be extremely abrupt[1]. Understanding what causes such abrupt oscillations is a principal outstanding question in climatology.

One quantity that is known to be important in climate dynamics is SST. Because of the nonlinearity of the relationship between SST and heat transfer to the atmosphere[15,16], even small changes in tropical SST (0.5–1.0 °C) can have large effects on the patterns of rainfall, storm tracks and intensities, and indeed on the overall general atmospheric circulation[17–19]. For this reason, estimates of SST are an essential boundary condition used in general circulation models (GCMs) of past or future climate[20]. Obtaining high temporal-resolution records of SST has in the past, however, proved to be a daunting task. The reason for this is that bioturbation, combined with generally very slow ocean sediment accumulation rates, produces a pronounced averaging effect. In general, this limits the temporal resolution of deep sea sediment records to a resolution not higher than ~3–5 kyr. Corals, on the other hand, appear to offer a vehicle for obtaining very high resolution records of SST with monthly or even weekly time resolution. Thus corals may for the first time alow us to evaluate the details of past climate change.

Recent studies have shown that skeletal Sr/Ca ratios in corals are a proxy for SST, with a precision of the order of ±0.1 °C when measurements are made using thermal ionization mass spectrometry (TIMS)[21]. The very long residence times of Sr and Ca in ocean water initially led us to propose that this 'thermometer' might permit recovery of SST records with an accuracy of as great as 0.5 °C. Several other more recent calibration studies have verified the

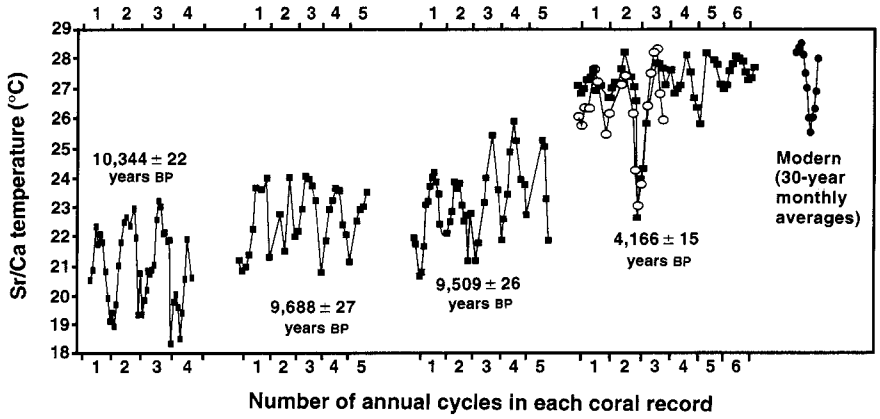

Figure 1 Coral Sr/Ca temperatures for four periods of time (filled rectangles). The dates listed are ^{230}Th ages determined by thermal ionization mass spectrometry (TIMS). Reported errors in age are 2σ. Each of the four samples shown here represents between four and six years of coral growth, as determined by X-radiography of the corals. Each symbol represents about one month of coral growth. Also shown for comparison are the modern instrumental records of 30-year average SST for this region[28] (filled circles), and oxygen-isotope temperatures for the ~4,166 yr BP record (open circles).

apparent robustness of this proxy thermometer, showing it to have an accuracy of between 0.5 and 1.0 °C (refs 22–24, 37). These additional studies have shown that coral vital effects and/or variations in the Sr/Ca ratio of sea water limit the overall accuracy of this thermometer to ~1 °C for most of the tropical oceans[23,24]. Even larger variability in ocean water Sr/Ca can be seen in upwelling zones, such as the eastern equatorial Pacific Ocean, where local artefacts of as large as 2.5 °C may be produced by upwelling of deep ocean water with an unusual Sr/Ca ratio[24]. Thus, this thermometer should be used with caution in such regions. However, the SST variations observed in the present study are considerably larger than the accuracy limitations of the Sr/Ca method.

The corals used here were collected far from any upwelling zone, from palaeo-reefs on the island of Espiritu Santo, Vanuatu, in the southwestern Pacific Ocean (15.5° S, 167° E). Collection was made using a land-based truck-mounted drilling rig, capable of recovering 2-inch drill cores from depths greater than 50 m. Because the drilling site has undergone rapid tectonic uplift at ~5–6 mm yr^{-1}, the depth from the surface to the LGM shoreline is shallow enough to make reefs of this age accessible using only a small drill system. Much of the coral encountered by the drill was in the form of relatively small fragments. Only a few of these were of the species *Porites lobata*, which is the sole species for which we have a verified temperature calibration based on modern corals.

These corals were dated using ^{230}Th dating techniques[25,26], whereas the annual cycles of growth for each individual coral head were determined by X-radiography which reveals the yearly density growth bands. Because of the small sample size requirements for Sr/Ca thermometry, we sampled these corals at a density of ~12 samples per recorded year. Coral Sr/Ca temperatures (°C) were derived using the equation $T = 167.8 \pm (16{,}013(\mathrm{Sr/Ca})_{\mathrm{atomic}})$; this equation differs from that given in Beck *et al.*[21], which contained a minor error[27].

Figure 1 shows several coral Sr/Ca temperature records obtained from cores recovered from Espiritu Santo. These records indicate that the SST in this region of the south Pacific averaged 4–6 °C colder than modern temperatures at ~10 kyr ago, but appears to have reached near modern values of 27.5 °C by ~4,200 calendar years BP. Seasonal fluctuations in temperature at ~10 kyr ago appear to have been slightly greater than those seen today.

An unusually large year-long negative temperature anomaly is seen in the coral SST record for ~4,166 ± 15(2σ)yr BP. Because large negative SST anomalies of this magnitude are very unusual in the modern instrumental records of SST from this region[28], we decided to evaluate independently the SST record for this coral using oxygen isotope thermometry[29,30]. Using the relationship between *Porites lobata* coral ^{18}O/^{16}O ratio and SST derived by McConnaughey[30], we find that the ^{18}O/^{16}O-based temperature record (open circles, Fig. 1) shows the same large negative temperature anomaly as indicated by the coral Sr/Ca ratio. Because it is unlikely that both tracers would respond to alteration of the coral in the same way, we cite this as independent evidence of a major year-long cold-event occurring at ~4,166 ± 15 yr BP. These data also strengthen the view that the Sr/Ca thermometer is well behaved on palaeo-corals of this age. The cause of this year-long 'cold snap' is unknown.

The observation of SSTs much colder than present in this region during the early Holocene is consistent with similar coral palaeo-SST data from New Guinea[22,31] (Fig. 2). High-resolution deep sea sediment records form this region are rare, but one such record[32] from ODP site 828A (which is very close to our coral collection site in Vanuatu) appears to corroborate our findings. This observed rise in SST is also broadly consistent with pollen-based climate reconstructions from Australia and New Guinea[33] which generally indicate that temperatures rose 2–6 °C between 12 and 5 kyr BP.

It might be argued that the low early Holocene SST and subsequent rapid rise observed in Vanuatu and New Guinea may be only a regional phenomena caused by local changes in ocean circulation. It is certainly true that the ~130-m eustatic sea-level rise since the LGM caused a dramatic reduction in the size of the emergent areas of continental shelf in the region surrounding Indonesia and adjacent to North Australia. The possibility exists that regional ocean circulation patterns may have reacted to these changes in sea level, and such changes may have caused regionally anomalous changes in SST[31]. On the other hand, there is evidence that the south tropical Atlantic Ocean also experienced anomalously cold SST at ~9 kyr BP, with mean February and August SSTs respectively 2.25 and 1.6 °C below present temperatures[34]. Likewise, oxygen isotope temperatures from glacial ice cores in the central Andes also appear to show unusually cold and rapidly rising (atmospheric) temperatures 10 and 8 kyr BP (ref. 9). Such results suggest that these Vanuatu corals may be truly representative of the tropics in recording a widespread temperature depression and rapid temperature rise during the early Holocene. At present there is insufficient data to determine whether tropical SSTs had remained cold since the LGM, or whether these low temperatures and rapid rise represent only a relatively short-term anomaly in the deglacial climate.

Not all records indicate that the tropics behaved uniformly during the deglaciation, however. In particular, although the Barbados

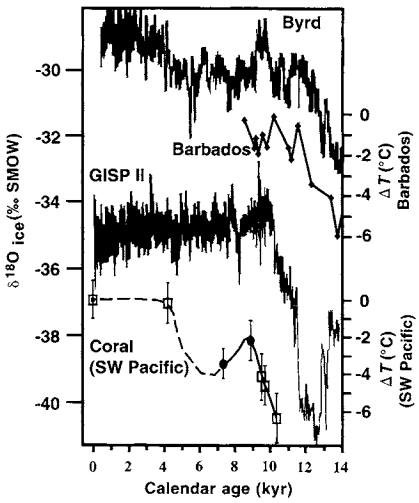

Figure 2 Comparison of the coral Sr/Ca SST records from the SW Pacific (Vanuatu, open rectangles; New Guinea[31], filled ovals) with that from Barbados[3] (filled diamonds), and the $\delta^{18}O_{ice}$ records from the Greenland GISP II[1] and Antarctic Byrd[35] high-latitude ice cores. Coral data are plotted as deviation of mean annual SST from modern values. Error bars indicate the 1 s.d. annual range in mean monthly temperature variations for each 4–6 year period sampled. Note the extremely abrupt and rapid rise in SST between ~10.4 and 8.9 kyr BP in the SW Pacific record. Using a conversion[36] between temperature and $\delta^{18}O_{ice}$ of ~0.6‰ per °C for the ice cores, the changes in high-latitude atmospheric temperature in this time frame are comparable to the changes in SST observed in the tropical records.

coral SST reconstruction[3] also indicates a rapid 6 °C SST rise in the western equatorial Atlantic during the late deglaciation, the timing appears to be phase-shifted with that seen in the southwest Pacific by nearly 3 kyr, with most of the Atlantic warming occurring between 14 and 11.5 kyr BP (Fig. 2). We note that a similar phase shift in high-latitude deglacial warming has also recently been determined[35] based on a comparison of the GISP II and Byrd polar ice cores (Fig. 2). In that case, however, the inter-hemispheric phasing is reversed, with warming in the Antarctic beginning ~3 kyr before the warm Bølling period in Greenland. As seen in Fig. 2, the large rise in SST observed in the southwest Pacific much more closely matches the timing of the post-Younger Dryas warming seen in the GISP II record than in the Antarctic Byrd ice-core record. Nevertheless, the Byrd $\delta^{18}O$ record appears to mimic the southwest Pacific coral SST data after ~9 kyr BP. Although it is somewhat premature to extrapolate the entire deglacial climate from these four sites, these records appear to reveal a very surprising bipolar structure to the deglacial climate and suggest that strong meridional temperature gradients were maintained during parts of the last deglaciation. □

Received 22 November 1996; accepted 6 January 1997.

1. Alley, R. B. *et al. Nature* **362,** 527–529 (1993).
2. Fairbanks, R. G. *Paleoceanography* **5,** 937–948 (1990).
3. Guilderson, T. P., Fairbanks, R. & Rubenstone, J. L. *Science* **263,** 663–665 (1994).
4. CLIMAP Project Members *Seasonal Reconstructions of the Earth's Surface at the Last Glacial Maximum* (Map and Chart Ser., MC-36, Geol. Soc. Am., 1981).
5. Shackleton, N. J. *Quat. Sci. Rev.* **6,** 183–190 (1987).
6. Broecker, W. S. *Quat. Res.* **26,** 121–134 (1986).
7. Hope, G. S., Peterson, J. A., Radok, U. & Allison, I. *The Equatorial Glaciers of New Guinea* (Balkerma, Rotterdam, 1976).
8. Broecker, W. & Denton, G. S. *Geochim. Cosmochim. Acta* **53,** 305–341 (1989).
9. Thompson, L. G. *et al. Science* **269,** 46–50 (1995).
10. Rind, D. & Peteet, D. *Quat. Res.* **24,** 1–22 (1985).
11. Manabe, S. & Broccoli, A. J. *J. Atmos. Sci.* **42,** 2643–2651 (1985).
12. Hope, G. S. *J. Ecol.* **64,** 627–664 (1976).
13. Stute, M. *et al. Eos* **75,** 381 (1994).
14. Wright, H. E. Jr in *The Geology of North America: An Overview* (eds Bally, A. W. & Palmer, A. R.) 513–536 (Geol. Soc. Am., Boulder, 1989).
15. Palmer, T. N. & Mansfield, D. A. *Nature* **333,** 367–369 (1984).
16. Bony, S., Duvel, J.-P. & Treut, H. L. *Clim. Dynam.* **11,** 307–320 (1995).
17. Rind, D. *Nature* **346,** 317–318 (1990).
18. Walser, D. E. & Grahm, N. E. *J. Geophys. Res.* **96,** 12881–12893 (1993).
19. Schneider, N., Barnett, T., Latif, M. & Stockdale, T. *J. Clim.* **9,** 219–239 (1996).
20. Kutzbach, J. E., Guetter, P. J., Behling, P. J. & Selin, R. in *Global Climates since the Last Glacial Maximum* (ed. Wright, H. E. Jr) 24–93 (Univ. Minnesota Press, Minneapolis, 1993).
21. Beck, J. W. *et al. Science* **257,** 644–647 (1992).
22. McCulloch, M. T., Gagan, M. K., Mortimer, G. E., Chivas, A. R. & Isdale, P. *Geochim. Cosmochim. Acta* **58,** 2747–2754 (1994).
23. Shen, C. C. *et al. Geochim. Cosmochim. Acta* **60,** 3849–3858 (1996).
24. de Villiers, S., Shen, G. T. & Nelson, B. K. *Geochim. Cosmochim. Acta* **58,** 197–208 (1994).
25. Edwards, R. L., Chen, J. H. & Wasserburg, G. J. *Earth Planet. Sci. Lett.* **81,** 175–192 (1987).
26. Edwards, R. L. *et al. Science* **260,** 962–968 (1993).
27. Beck, W. *Science* **264,** 891 (1994).
28. Halpert, M. S. & Ropelewski, C. F. (NOAA, US Dept of Commerce, Silver Spring, MD, 1989).
29. Weber, J. N. & Woodhead, M. J. *J. Geophys. Res.* **77,** 463–473 (1972).
30. McConnaughey, T. *Geochim. Cosmochim. Acta* **53,** 151–162 (1989).
31. McCulloch, M. T. *et al. Earth Planet. Sci. Lett.* **138,** 169–178 (1996).
32. Martinez, J. I. *Palaeogeogr. Palaeoclimatol. Palaeoecol.* **112,** 19–62 (1994).
33. Harrison, S. & Dodson, J. in *Global Climates since the Last Glacial Maximum* (ed. Wright, H. E. Jr) 265–293 (Univ. Minnesota Press, Minneapolis, 1992).
34. Ruddiman, W. F. & Mix, A. C. in *Global Climates since the Last Glacial Maximum* (ed. Wright, H. E. Jr) 94–124 (Univ. Minnesota Press, Minneapolis, 1993).
35. Sowers, T. & Bender, M. *Science* **269,** 210–214 (1995).
36. Stuiver, M., Grootes, P. M. & Braziunas, T. F. *Quat. Res.* **44,** 341–354 (1995).
37. Alibert, C. & McCulloch, M. T. *Paleoceanography* (in the press).

Acknowledgements. We thank Th. Delcroix, A. Dessier, Ch. Henin and P. Rual for providing instrumental records of climate from New Caledonia, and S. Gray for providing one of the U/Th coral dates quoted here. This work was supported by ORSTOM (Institut Franç de Recherche Scientifique pour le Développement en Coopération), the US NSF and NOAA.

Correspondence should be addressed to J.W.B. (e-mail: wbeck@physics.arizona.edu).

Interhemispheric synchrony of the last deglaciation inferred from alkenone palaeothermometry

Edouard Bard*†, Frauke Rostek* & Corinne Sonzogni*

* *CEREGE, Université d'Aix-Marseille III et CNRS-UMR 132, Europôle de l'Arbois, BP 80, 13545 Aix-en-Provence cedex 4, France*
† *Institut Universitaire de France*

The relative timings of the last deglacial warming in the Southern and Northern hemispheres are not well constrained, but are a crucial component in understanding the mechanisms of deglaciation[1]. A clearer picture of the degree of interhemispheric synchrony has been obscured by a dearth of high-resolution temperature records that can be tied to the absolute calendar timescale. Moreover, the quantification of tropical temperatures during the last glacial cycle is controversial[2–8]. Here we apply the alkenone method of sea surface temperature reconstruction[9,10] to several high-resolution sediment cores recovered from the tropical Indian Ocean between 20° N and 20° S. The inferred initial sea surface temperature warming ~15,000 calendar years ago at 20° S is in phase with Northern Hemisphere sea (this study) and air[11] temperature changes, but lags Antarctic warming[12–14] by several millennia. This finding, along with the results of recent modelling studies[15,16], provides strong support for the idea that changes in the ocean's global thermohaline circulation were not the only cause of interhemispheric climate teleconnection during the last deglaciation.

For high latitudes, the clearest palaeotemperature records are obtained from Greenland and Antarctica because amplitudes of climate variations were enhanced at high latitudes and because ice cores provide information at very high resolution for at least the last glacial cycle[11–14]. Although the exact relationship between atmospheric temperature and $\delta^{18}O$ in ice is still uncertain[17], there

is no doubt that very large temperature shifts of 6–10 °C were experienced in polar regions during the last glacial cycle.

For the low-latitude ocean, temperature variations during the last deglaciation have been evaluated by means of strontium measurements in corals[3]. However, the amplitude of the deglacial warming estimated from corals (5–6 °C) is in conflict with reconstructions based on micropalaeontological transfer functions which indicate almost no warming in the tropical belt between the Last Glacial Maximum (LGM) and the Holocene epoch[4]. Palaeotemperatures estimated by the transfer-function method are supported by the use of the modern analogue technique[5,6]. Small (<3 °C) temperature changes were also inferred from $\delta^{18}O$ measurements of planktonic foraminifera[7] (see also ref. 8 for recent work based on $\delta^{18}O$ analysis of single foraminifera).

The alkenone time series presented here are expressed in terms of $U^{K'}_{37}$ units, the simplified unsaturation index of C37 alkenones[10]. Gas chromatographic techniques used at CEREGE to quantify alkenones are described elsewhere[18]. Standard deviations better than 0.01 $U^{K'}_{37}$ units were obtained on replicated measurements of several deep sea sediment samples and an algal extract[18]. The $U^{K'}_{37}$ values have also been converted into sea surface temperature (SST) by applying a widely used calibration based on a coccolithophorids culture[19] (slope of 0.034 $U^{K'}_{37}$ units per °C). Although cultured prymnesiophyte strains display more than one response curve[20,21], several subsequent studies of natural samples (such as particulate, sediment-trap and core-top organic matter) have confirmed the usefulness of the original Prahl *et al.*[19] calibration for the SST range between 5 and 25 °C (refs 10, 18, 22, 23). In addition, recent work based on Indian Ocean core tops suggests that the slope of the $U^{K'}_{37}$ versus SST relationship could be smaller (0.023; ref. 18) above 24 °C than observed for the 5–25 °C range. Although a firm confirmation using cultures is needed, this possibility must be kept in mind when evaluating amplitudes of temperature changes.

Figure 1a and b presents the $\delta^{18}O$ and $U^{K'}_{37}$ time series obtained on cores MD85674 (3° 11′ N, 50° 26′ E, 4,875 m depth) and MD85668 (0° 01′ S, 46° 02′ E, 4,020 m depth). As can be clearly seen, the $\delta^{18}O$ records are unambiguous and there is little uncertainty on the assignments of isotope stages (see refs 24, 25 for MD85668 and 25, 26 for MD85674). Although the time resolution in core MD85674 is better than in core MD85668, the two alkenone records are highly similar and follow closely the $\delta^{18}O$ records measured in the two cores. The oxygen-isotope signal is mostly global in origin because the glacial/Holocene difference attributable to continental ice-volume changes is ~1.25‰, that is, 70–80% of the total $\delta^{18}O$ amplitude observed in the two cores. Moreover, there are striking similarities between the alkenone records and the isotopic temperatures from the Vostok site in Antarctica[27] (Fig. 1c). These facts clearly indicate that the last glacial cycle at the Indian Ocean Equator was dominated by global climate variations. In both deep sea cores, the maximum temperature is reached during isotopic substage 5e (the last interglacial period at ~125,000 calendar years before present, cal. yr BP) while cold minima correspond to isotopic stage 4 and stage 2 (LGM at ~20,000 cal. yr BP). The total amplitude change is of the order of 2.5–3 °C for the whole glacial cycle and only 1.5 °C for the transition between LGM and Holocene. The rather small deglacial warming observed for these two cores is typical of the equatorial-tropical zone of the Indian Ocean, as determined in 19 cores (Fig. 2) characterized by high sedimentation rates (usually >10 cm kyr^{-1}) and detailed $\delta^{18}O$ stratigraphies[26,28,29]. The mean deglacial warming based on the alkenone method is 1.7 °C ($1\sigma = 0.7$ °C) in broad agreement with previous work on foraminifera[5] (see Fig. 2) but significantly lower than the dramatic 5–6 °C deglacial warming inferred from the Sr/Ca ratio in tropical corals[3]. This conclusion remains valid (mean deglacial warming ~2.4 °C) when assuming a smaller slope of the $U^{K'}_{37}$ versus SST relationship for the high-temperature range (~0.023 instead of 0.034).

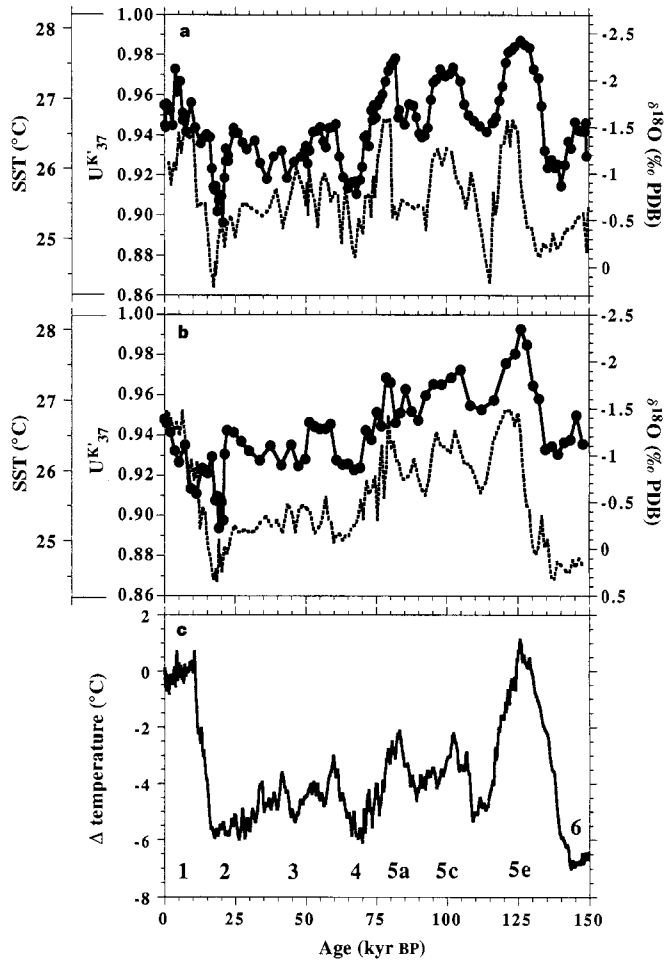

Figure 1 a, Solid line with dots, $U^{K'}_{37}$ record for core MD85674; dashed line, $\delta^{18}O$ record obtained on the bulk carbonate (data from ref. 26 and age-depth stratigraphy from ref. 25). **b**, Solid line with dots, $U^{K'}_{37}$ record for core MD85668; dashed line, $\delta^{18}O$ record obtained on the bulk carbonate (data and age-depth stratigraphy from ref. 24). The temperature calibration used to construct the SST *y*-axis is $U^{K'}_{37} = 0.034 \times SST + 0.039$ (ref. 19). The age-depth stratigraphies of the two cores are based on matching with the SPECMAP timescale with an average error of ~5 kyr. Nevertheless, the SST changes often lead by a few millennia the $\delta^{18}O$ variations observed in the same core. **c**, Smoothed temperature changes calculated for the Vostok site in Antarctica[27]. These relative temperature changes are calculated by assuming a deuterium/temperature gradient of 9‰ per °C after accounting for the isotopic change of sea water[27]. The record is corrected for the influence of the geographical position of the precipitation site[27] and the timescale is obtained by orbital tuning[38].

To describe in more detail the last deglaciation in the Southern Hemisphere, we show in Fig. 3a the complete alkenone record obtained for one core: MD79257, 20° 24′ S, 36° 20′ E, 1,260 m depth. This particular core has been precisely dated[29] by accelerator mass spectrometry ^{14}C, so it is then possible to study the last deglaciation on an absolute timescale through the use of ^{14}C calibration formulas[30]. The LGM/Holocene temperature contrast is of the order of 2.5 °C which is at the high end of the set of 19 cores. The last deglaciation is characterized by an abrupt 1.5 °C warming at ~15,100 cal. yr BP followed by a transitory pause until ~12,200 cal. yr BP and a small cooling until ~11,500 cal. yr BP (Fig. 3a and legend). The second part of the last deglaciation is more complex and less abrupt than the first, with a 1 °C warming between 11,000 and 7,000 cal. yr BP. Taking into account the dating uncertainties, the warming at ~15,100 cal. yr BP is in phase with that of

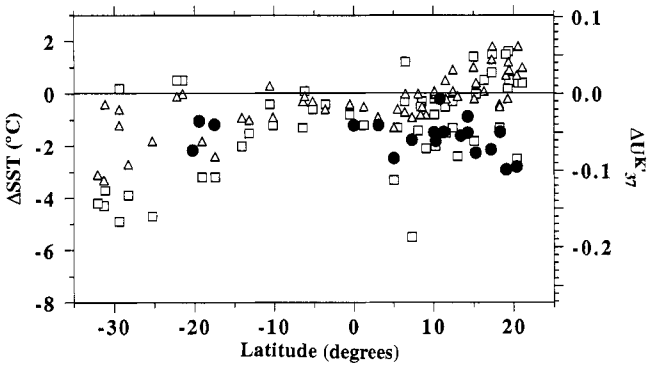

Figure 2 Mean SST and $U^{K'}_{37}$ differences between LGM and modern for Indian Ocean cores (calibration from ref. 19). Filled circles represent estimates based on the alkenone method applied to 19 high-sedimentation-rate cores from the Indian Ocean (usually >10 cm kyr^{-1}). Details will be published elsewhere (C.S. *et al.*, manuscript in preparation). Open squares have been calculated by the TF technique and open triangles by the MAT technique (see text; results described in ref. 5).

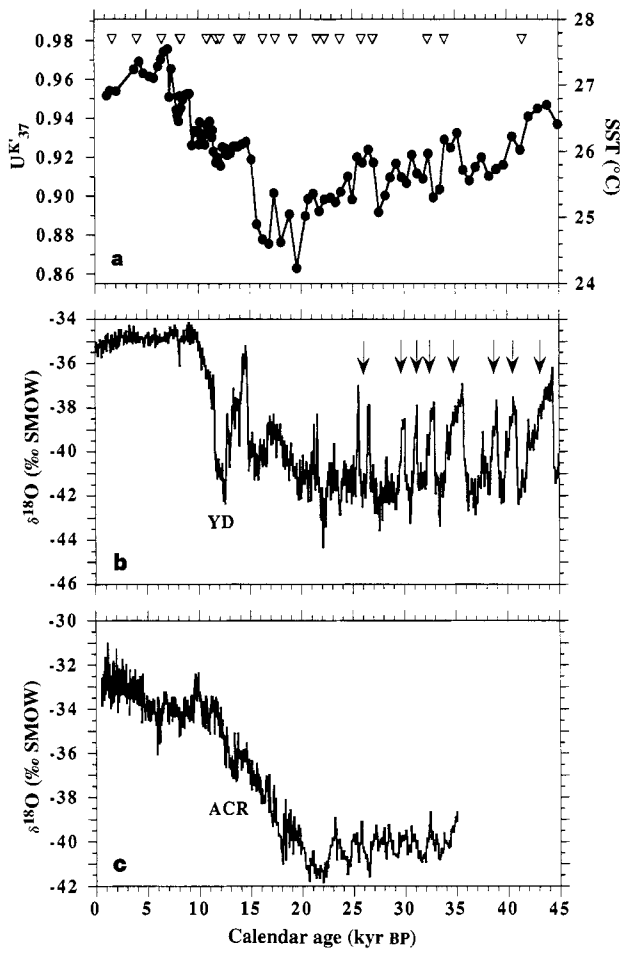

Figure 3 a, Alkenone record obtained for core MD79257. $U^{K'}_{37}$ axis is on the left while SST is provided on the right axis (calibration from ref. 19). Open triangles indicate the age control points which are based on AMS-^{14}C dating of *Globigerinoides ruber*[29]. For calibrating ^{14}C ages back to 42 kyr BP we use the following equation based on U-Th dating of corals[30]: age cal. yr BP = $-1{,}807 + 1.39 \times (^{14}\text{C age yr BP}) - 5.85 \times 10^{-6} \times (^{14}\text{C age yr BP})^2$. The calendar timescale for core MD79257 has been obtained by polynomial fitting (fifth-order) through the calibrated AMS-^{14}C ages. **b**, δ^{18}O of the GRIP ice core from Greenland[11] with an updated chronology[31]. The arrows indicate the midpoints of the interstadial maxima of atmospheric methane[32]. YD, Younger Dryas period. **c**, δ^{18}O record of the Byrd ice core[39] with an updated chronology[12,13]. ACR, Antarctic Cold Reversal. The midpoint of the 1.5 °C warming step on **a** occurs at the depth level 559 cm in core MD79257 (bracketed between $U^{K'}_{37}$ measurements at 554 and 564 cm). The nearest AMS-^{14}C ages are 11,900 ± 210 ^{14}C yr BP at 540 cm and 13,830 ± 230 ^{14}C yr BP at 580 cm (ref. 29) which translate into calendar estimates of ~13,900 and ~16,300 cal. yr BP, respectively (ref. 30). The midpoint of this climate warming is thus dated at ~15,100 cal. yr BP.

Greenland at ~14,900 cal. yr BP (ref. 31). There is also a clear synchrony between the transient feature between 12,200 and 11,500 cal. yr BP and the Younger Dryas cold period observed in the Northern Hemisphere (see, for example, ref. 11). The main difference is that the reversal in core MD79257 does not correspond to a return to full glacial conditions as is the case for the Greenland records (see Fig. 3b).

The temperature reversal at 20° S is similar in relative amplitude to that observed in climate records from Antarctica but the oceanic warming steps are distinctly younger (Fig. 3c). Indeed, the well dated[12,13] isotopic record of the Byrd ice core (West Antarctica) clearly shows that the deglacial warming started at ~20,000–19,000 cal. yr BP, which is much earlier (by ~5,000–4,000 yr) than in core MD79257. Moreover, the second warming which follows the Antarctic Cold Reversal[12–14] leads by ~2,000 yr the second SST increase at 20 °S in the Indian Ocean. Finally, the Holocene temperature optimum in Antarctica is reached at ~9,000–10,000 cal. yr BP, about 3,000 yr before the Holocene SST maximum in core MD79257.

For the time interval between 45,000 and 20,000 cal. yr BP, the $U^{K'}_{37}$ record of MD79257 exhibits a general cooling of ~2 °C. In addition, the $U^{K'}_{37}$ profile shows several warm transients superimposed on the cooling trend, although these are very close to the precision limit. It is tempting to correlate these wiggles with the interstadial warm events recorded in the GRIP ice core (Fig. 3b). These so-called Dansgaard–Oeschger events are of very large magnitude in Greenland (~10 °C with the new δ^{18}O-temperature calibration[17]) and their equivalents in MD79257 are severely attenuated by an order of magnitude. It should also be noted that the warm transients are concomitant with maxima of atmospheric methane concentration[32] measured in air bubbles enclosed in the GRIP ice core (arrows on Fig. 3b).

The recent studies based on terrestrial evidence of mountain glacier readvance in New Zealand[33] and Chile[34] also suggested a climatic synchrony between Southern and Northern hemispheres. Although the dating precision of the New Zealand study was recently criticized[35], our temperature record at 20° S clearly reinforces those previous works and suggests that the synchrony applied to the surface ocean. These observations may be used to discriminate between the climatic mechanisms invoked to explain the timing of the last deglaciation and the abruptness of Dansgaard–Oeschger events.

In particular, rapid variations of global sea level and associated changes of land albedo can be ruled out as explanations of the timing of the last deglaciation. Indeed, ~80% of the deglacial sea level change occurred after 14,200 cal. yr BP as reconstructed by U–Th dating of submerged corals[36]. It thus appears that global sea levels lag behind the deglacial warming observed at different latitudes.

Switching on and off the global thermohaline circulation has been called on to explain warming and cooling events observed in the Northern Hemisphere and, especially, in the North Atlantic area. Numerical modelling of the ocean–atmosphere coupled system suggests that Northern and Southern Hemisphere temperatures should have changed in opposite directions if oscillations of the thermohaline circulation did control the timing of the last deglaciation and Dansgaard–Oeschger events[15,16]. In particular, several models predict a warming for most of the Southern Hemisphere

when the thermohaline circulation is forced to diminish in order to simulate an intense Younger Dryas-type cold event in the North Atlantic area[15,16]. This scenario found some support in the timing of the last deglaciation: the Antarctic Cold Reversal is in phase with the Bølling–Allerød warm period and the second Antarctic warming step corresponds to the Younger Dryas cold event[12–14]. However, the terrestrial data on glacier readvance and our oceanic palaeotemperatures indicate interhemispheric synchrony, reinforcing doubts that the global ocean circulation is the direct and only cause of the climate teleconnection. In fact, as hypothesized recently by Broecker[1], the ocean circulation could have an indirect effect on the Southern Hemisphere by changing the dynamics of the low-latitude atmosphere which in turn would affect the atmospheric water vapour content and hence the strength of its greenhouse effect. The water vapour could act as the rapid vector of interhemispheric teleconnection because low-latitude moisture is redistributed rapidly by large-scale eddies and the mean meridional circulation of the atmosphere[37]. According to Broecker[1], this mechanism could also explain why the break in climate synchrony was at the Antarctic convergence instead of at the Equator. Furthermore, the apparent correlation between atmospheric methane levels and interstadial events would be a logical consequence of this mechanism because low-latitude moisture and temperature fluctuations play major roles in changes of the methane cycle. □

Received 2 September 1996; accepted 14 January 1997.

1. Broecker, W. S. *Geotimes* **41**(2), 40–41 (1996).
2. Webster, P. J. & Streten, N. A. *Quat. Res.* **10**, 279–309 (1978).
3. Guilderson, T. P., Fairbanks, R. G. & Rubenstone, J. L. *Science* **263**, 663–665 (1994).
4. CLIMAP Project Members *Map and Chart Ser. C36* (Geol. Soc. Am., Boulder, 1981).
5. Prell, W. L. *Tech. Rep. TRO25* (Dept of Energy, Washington DC, 1985).
6. Anderson, D. M., Prell, W. L. & Barratt, N. J. *Paleoceanography* **4**, 615–627 (1989).
7. Broecker, W. S. *Quat. Res.* **26**, 121–134 (1986).
8. Stott, L. D. & Tang, C. M. *Paleoceanography* **11**, 37–56 (1996).
9. Brassell, S. C., Eglinton, G., Marlowe, L. T., Pflaumann, U. & Sarnthein, M. *Nature* **320**, 129–133 (1986).
10. Prahl, F. G. & Wakeham, S. G. *Nature* **330**, 367–369 (1987).
11. Johnsen, S. J. *et al. Nature* **359**, 311–313 (1992).
12. Sowers, T. & Bender, M. *Science* **269**, 210–214 (1995).
13. Hammer, C. U., Clausen, H. B. & Langway, C. C. *Ann. Glaciol.* **20**, 115–120 (1994).
14. Jouzel, J. *et al. Clim. Dyn.* **11**, 151–161 (1995).
15. Mikolajewicz, U. *A Meltwater Induced Collapse of the 'Conveyor Belt'* 1–25 (Rep. 189, Max-Planck-Inst. für Meteorol., Hamburg, 1996).
16. Stocker, T. F. & Wright, D. G. *Paleoceanography* **11**, 773–795 (1996).
17. Johnsen, S. J., Dahl-Jensen, D., Dansgaard, W. & Gunderstrup, N. *Tellus* **47B**, 624–629 (1995).
18. Sonzogni, C. *et al. Quat. Res.* (in the press).
19. Prahl, F. G., Muehlhausen, L. A. & Zahnle, D. *Geochim. Cosmochim. Acta* **52**, 2303–2310 (1988).
20. Prahl, F. G., Pisias, N., Sparrow, M. A. & Sabin, A. *Paleoceanography* **10**, 763–773 (1995).
21. Volkman, J. K., Barrett, S. M., Blackburn, S. I. & Sikes, E. L. *Geochim. Cosmochim. Acta* **59**, 513–520 (1995).
22. Sikes, E. L., Farrington, J. W. & Keigwin, L. D. *Earth Planet. Sci. Lett.* **104**, 34–47 (1991).
23. Rosell-Melé, A., Eglinton, G., Pflaumann, U. & Sarthein, M. *Geochim. Cosmochim. Acta* **59**, 3099–3107 (1995).
24. Shackleton, N. J., Hall, M. A., Pate, D., Meynadier, L. & Valet, P. *Paleoceanography* **8**, 141–148 (1993).
25. Meynadier, L., Valet, J. P., Weeks, R., Shackleton, N. J. & Lee Hagee, V. *Earth Planet Sci. Lett.* **114**, 39–57 (1992).
26. Vergnaud Grazzini, C., Caulet, J. P. & Vénec-Peyré, M.-T. *Bull. Soc. Géol. Fr.* **166**, 259–270 (1995).
27. Jouzel, J. *et al. Nature* **364**, 407–412 (1993).
28. Duplessy, J. C., Bé, A. W. H. & Blanc, P. L. *Palaeogeogr. Palaeoclimatol. Palaeoecol.* **33**, 9–46 (1981).
29. Duplessy, J. C. *et al. Earth Planet. Sci. Lett.* **103**, 27–40 (1991).
30. Bard, E., Arnold, M., Fairbanks, R. G. & Hamelin, B. *Radiocarbon* **35**, 191–199 (1993).
31. Hammer, C. U. *et al. The Stratigraphic Dating of the GRIP Ice Core* (Rep. 1 Niels Bohr Inst., Copenhagen, in the press).
32. Chappellaz, J. *et al. Nature* **366**, 443–445 (1993).
33. Denton, G. H. & Hendy, C. H. *Science* **264**, 1434–1437 (1994).
34. Lowell, T. V. *et al. Science* **269**, 1541–1549 (1995).
35. Mabin, M. C. G. *Science* **271**, 668–670 (1996).
36. Bard, E. *et al. Nature* **382**, 241–244 (1996).
37. Del Genio, A., Lacis, A. A. & Ruedy, R. A. *Nature* **351**, 382–385 (1991).
38. Waelbroeck, C. *et al. Clim. Dyn.* **12**, 113–123 (1995).
39. Johnsen, S. J., Dansgaard, W., Clausen, H. B. & Langway, C. C. *Nature* **235**, 429–434 (1972).

Acknowledgements. We thank G. Eglinton, J. R. Maxwell, P. J. Müller, T. Rosell-Melé, L. Sikes and J. Volkman for showing us analytical procedures and/or providing alkenone calibration samples; J. P. Caulet, J. C. Duplessy, L. Labeyrie and Y. Lancelot for giving access to cores stored at MNHN in Paris, CFR at Gif-sur-Yvette, and CEREGE in Aix-en-Provence; S. J. Johnsen and J. Jouzel for providing the numerical isotopic data of GRIP, Byrd and Vostok ice cores; M. Arnold, M. Bender, T. Blunier, J. Chappellaz, C. U. Hammer, S. J. Johnsen, J. Jouzel and T. Sowers for comments and help to construct updated chronologies for MD79257, GRIP, Byrd and Vostok cores; L. Beaufort, J. O. Grimalt, G. Haddad, J. Jouzel, U. Mikolajewicz, T. Stocker and T. Webb for discussions and/or reviews of the manuscript; and F. Prahl for comments. This work was supported by MENESR (JE192 and IUF) and INSU (PNEDC).

Correspondence should be addressed to E.B. (e-mail: ebard@arbois.cerege.fr).

Direct observation of complete miscibility in the albite–H_2O system

Andy H. Shen* & Hans Keppler†

* *Department of Earth Sciences, University of Cambridge, Downing Street, Cambridge CB2 3EQ, UK*

† *Bayerisches Geoinstitut, Universität Bayreuth, 95440 Bayreuth, Germany*

There are essentially two main types of mobile phases in the Earth's crust and mantle: silicate melts and hydrous fluids. Near the surface of the Earth, the physical and chemical properties of these phases are fundamentally different. But with increasing pressure, the solubility of water in silicate melts and the solubility of silicate materials in hydrous fluids increase. This has led to the suggestion that, above a certain critical pressure, the compositions of the two phases in mutual equilibrium become indistinguishable[1–5]. Here we report the direct visual observation of this phenomenon in the albite–H_2O system using an externally heated diamond anvil cell. Our results suggest both that there should be complete miscibility between silicate melts and hydrous fluids in the deeper parts of the upper mantle and that, in the presence of a hydrous fluid, a melting temperature for this part of the mantle can no longer be defined.

In our experiments, we used a Bassett-type externally heated diamond anvil cell[6,7]. In this cell, the sample is contained in a 500-μm borehole in a rhenium gasket with an initial thickness of 250 μm. The gasket is compressed between two flat diamond surfaces of 1 mm diameter. Heating is achieved by electrical coils around the tungsten carbide seats below the diamond and temperature is measured by an external thermocouple touching the diamonds. It has been shown that after cycling the cell a few times through the temperature interval of interest, it behaves as an isochoric system[8]. If water is used as a pressure medium, the pressure at any temperature inside the cell may be determined from the equation of state of water, provided the bulk density of the fluid phase in the cell is known[8]. This can easily be determined by measuring the melting temperature of ice in the cell or the temperature at which a vapour bubble disappears in the cell on heating.

At the beginning of each experiment, we filled the cell with water to the desired bulk density and cycled it several times through the temperature interval of interest. We then opened the cell again and filled it with about equal amounts by weight of water and hydrous albite glass ($NaAlSi_3O_8$, containing 5 wt% of H_2O). On heating above the glass transformation temperature, a round drop of hydrous silicate melt forms which is surrounded by water, containing some dissolved silicate material (Fig. 1a). If the temperature and pressure inside the cell approaches a critical point, the compositions of the two phases converge. This results in a reduced optical contrast between the two phases and fading of the phase boundary (Fig. 1b and c). At the critical point, the phase boundary disappears entirely (Fig. 1d). Note that this critical behaviour is very different from the simple dissolution of a phase. If a phase dissolves, its composition remains constant but its volume decreases. In a system with critical behaviour, the compositions of the respective phases change, while their volumes remain approximately constant. When the homogeneous, supercritical phase in the diamond cell was cooled again to a temperature a few °C below the critical homogenization temperature observed on heating, it first turned milky and then separated into a fluid phase and a melt phase. During this process, vigorous turbulence was observed inside the sample chamber. The milky appearance of the sample just before phase separation is a typical

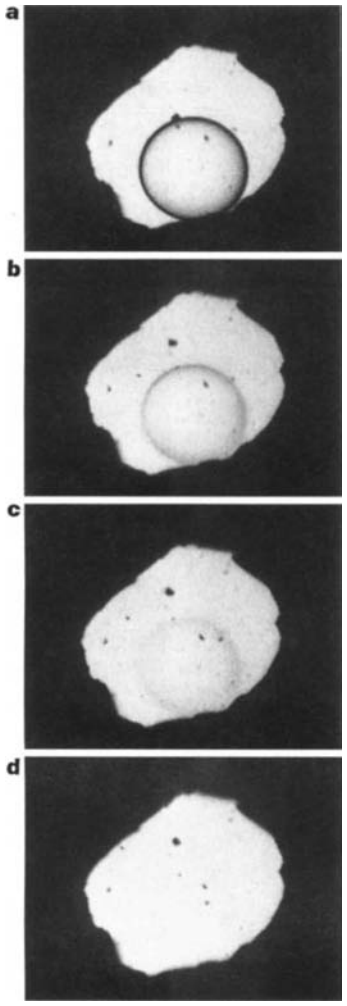

Figure 1 The system albite-H_2O as seen in a diamond cell under the following conditions: **a**, 763 °C and 14.5 kbar; **b**, 764 °C and 14.5 kbar; **c**, 765 °C and 14.5 kbar; **d**, 766 °C and 14.5 kbar. At 763 °C (**a**) a sphere of hydrous albite melt is surrounded by hydrous fluid. With increasing temperature, the compositions of the melt and fluid phase approach each other, resulting in reduced optical contrast and a fading of the boundary between the two phases (**b** and **c**). At 766 °C, the system reached a critical point and the phase boundary between melt and fluid disappeared.

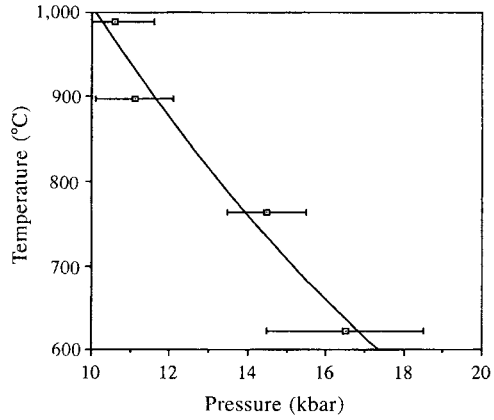

Figure 2 The critical curve in the system albite-H_2O. Temperature uncertainty is a few °C, about the size of the plotting symbols. In the experiment at the highest pressure, the uncertainty in pressure is relatively large due to difficulties in measuring the density of the fluid phase in this experiment.

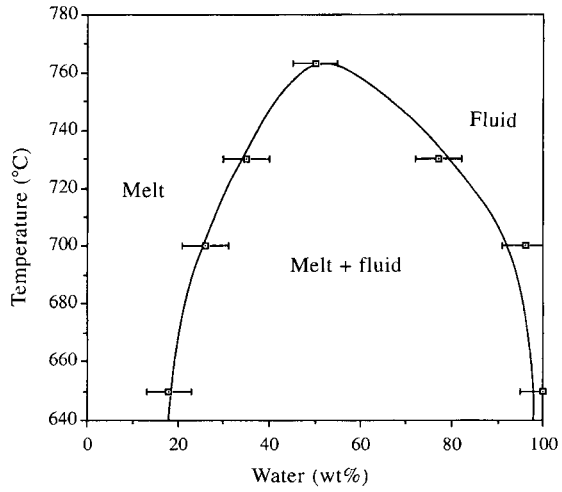

Figure 3 Compositions of coexisting fluid and melt phase in the system albite-H_2O. Data are derived from infrared spectra in an experiment with a bulk density of water loaded into the cell of 0.996 g cm^{-3}. This yields a pressure of 12.2 kbar at 650 °C and of 14.5 kbar at 763 °C, the critical temperature. Temperature uncertainty is a few °C, about the size of the symbols.

phenomenon of critical behaviour known as critical opalescence[9]. It is due to extreme density fluctuations occurring in the fluid close to the critical point.

By the kind of experiment described above, the critical temperature and pressure in the albite–H_2O system may be determined for a given bulk density. However, different bulk densities will generate different pressures inside the cell for a given temperature. As the solubility of H_2O in the melt and of silicate material in the fluid are both pressure-dependent, the critical points for different pressures will be at different temperatures. By varying the bulk density of the sample inside the diamond anvil cell, we therefore determined a series of critical points, which in a pressure–temperature diagram define a curve, the critical curve for the system albite–H_2O. This curve is shown in Fig. 2, where it may be seen that the critical temperature in the system albite–H_2O strongly decreases with pressure, from 989 °C at 10.6 kbar to 623 °C at 16.5 kbar.

To determine the composition of the coexisting phases close to the critical point, we measured their infrared spectra at high pressure and temperature. These measurements were carried out using a Bruker IFS 120 Fourier-transform infrared spectrometer together with the focusing optics of a Bruker infrared microscope. The latter instrument allowed focusing of the beam to pass through the fluid or melt phase only. Details of the experimental methods used have been described elsewhere[10,11]. From the infrared spectra, we estimated total water contents of the coexisting phases using the integral absorbance of the overtone band around 7,000 cm^{-1}, with an integral extinction coefficient of 137 l mol^{-1} cm^{-2}. This extinction coefficient was measured for liquid water at room temperature; we verified, by measuring spectra of pure water to 800 °C, that it does not vary significantly with temperature, provided the density remains constant. Moreover, this extinction coefficient is also similar to values reported for traces of water in silicate glasses[12], suggesting that reasonable estimates of water contents can be obtained over the entire range of compositions studied. Results for one experiment with a critical temperature of 763 °C and a critical pressure of 14.5 kbar are shown in Fig. 3. Only data above 650 °C are shown, because at lower temperature, chemical exchange between the phases involved becomes too sluggish to obtain

equilibrium compositions within a few minutes. At 650 °C and a pressure of 12.2 kbar, our measurements suggest a water solubility in albite melt of 18 wt%, in very good agreement with previous work[5]. The coexisting fluid phase under the same conditions appears to be almost pure water with only a few wt% of dissolved silicate component. This means that at least up to these conditions (which are rather close to the critical point), the equation of state of pure water probably describes the pressure–volume–temperature properties of the fluid fairly well and, therefore, our calculated pressures are probably rather accurate, with estimated errors of less than 1 kbar.

The system albite–H_2O is a simple model which is not directly applicable to phase relations in the upper mantle. Magmas generated by anhydrous partial melting of the upper mantle are usually silica-undersaturated and contain large amounts of MgO, whereas albite is silica-saturated and MgO-free. However, it is well established[13] that in the presence of water, partial melts in the upper mantle become strongly enriched in silica and depleted in magnesium. The compositions of experimentally produced partial melts of a hydrous peridotite are very similar to albite in SiO_2 and Al_2O_3 content. The only difference is that instead of just Na_2O, they contain a mixture of Na_2O, CaO and MgO as network-modifying cations. But because the chemical behaviour of alkali and alkali earth elements in silicate melts is similar, this is unlikely to affect the behaviour of the system in a fundamental way. As Mg and Ca are rather less soluble in hydrous solutions than Na, the critical curve could be shifted to somewhat higher pressure. Our experiments therefore suggest that, at least in the deeper part of the upper mantle, there will be complete miscibility between silicate melts and hydrous fluids. Direct evidence for complete miscibility between H_2O and silicate material in the mantle comes from inclusions in diamonds that contain water and silicate in comparable amounts[14]. Also, traces of silica- and volatile-rich melt inclusions found in some mantle xenoliths may in fact be remnants of silica-rich supercritical fluids[15,16].

The existence of complete miscibility between fluids and silicate melts has profound consequences for the phase relations in the mantle. At conditions below the critical point, a hydrous fluid phase can coexist with solid mantle minerals, until the water-saturated solidus is reached. At this temperature, a hydrous silicate melt forms which coexists with the hydrous fluid and mantle minerals. Beyond the critical point, however, fluid and melt can no longer coexist as two separate phases. Therefore, if a hydrous fluid coexists with solid mantle minerals, increasing temperature will result in the fluid dissolving more and more of the silicate material, until it becomes a hydrous melt: there will be no discrete melting event. If the conditions of critical behaviour are approached, the water content in the melt increases rapidly with pressure and temperature (Fig. 3). As this dramatically enhances the melting point depression, the solidus temperatures of a system would be expected to drop down drastically once a critical point is approached. This is exactly what has been observed in the system albite–water: Goldsmith and Jenkins[17] found that the slope of the solidus changes suddenly above ~14 kbar and drops from 680 to 600 °C at 18 kbar. This is in excellent agreement with the critical curve shown in Fig. 2. Supercritical behaviour in fluid–melt systems may also influence trace-element enrichment patterns observed in subduction-zone volcanics. Although such enrichment patterns can usually be related to a hydrous, chloride-rich fluid[18], it appears that in very deep parts of the subduction zone the nature of the metasomatizing fluid is changing. The enrichment pattern observed in volcanics overlying very deep parts of the subduction zone appears to suggest mass transport by a more silica-rich medium[19], with properties between a hydrous fluid and a silicate melt. □

Received 18 September 1996; accepted 3 January 1997.

1. Kennedy, G. C., Wasserburg, G. J., Heard, H. C. & Newton, R. C. *Am. J. Sci.* **260,** 501–521 (1962).
2. Boettcher, A. L. & Wyllie, P. J. *Am. J. Sci.* **267,** 875–909 (1969).
3. McMillan, P. F. & Holloway, J. R. *Contrib. Mineral. Petrol.* **97,** 320–332 (1987).
4. McMillan, P. F. *Rev. Mineral.* **30,** 131–156 (1994).
5. Paillat, O., Elphick, S. C. & Brown, W. L. *Contrib. Mineral. Petrol.* **112,** 490–500 (1992).
6. Bassett, W. A., Shen, A. H., Bucknum, M. & Chou, I-Ming *Rev. Scient. Instrum.* **64,** 487–495 (1993).
7. Bassett, W. A., Shen, A. H., Bucknum, M. & Chou, I-Ming *Pur. Appl. Geophys.* **141,** 487–495 (1993).
8. Shen, A. H., Bassett, W. A. & Chou, I-Ming in *High-Pressure Research: Applications to Earth and Planetary Sciences* (eds Syono, Y. & Manghnani, M. H.) 61–68 (Am. Geophys. Union, Washington DC, 1992).
9. Stanley, H. E. *Introduction to Phase Transitions and Critical Phenomena* (Oxford Univ. Press, 1971).
10. Keppler, H. & Bagdassarov, N. S. *Am. Mineral.* **78,** 1324–1327 (1993).
11. Shen, A. H. & Keppler, H. *Am. Mineral.* **80,** 1335–1338 (1995).
12. Stolper, E. *Contrib. Mineral. Petrol.* **81,** 1–17 (1982).
13. Hess, P. C. *Origins of Igneous Rocks* (Harvard Univ. Press, 1989).
14. Navon, O., Hutcheon, I. D., Rossman, G. R. & Wasserburg, G. J. *Nature* **335,** 784–789 (1988).
15. Schiano, P. & Clocchiatti, R. *Nature* **368,** 621–624 (1994).
16. Wulff-Pedersen, E., Neumann, E.-R. & Jensen, B. B. *Contrib. Mineral. Petrol* **125,** 113–139 (1996).
17. Goldsmith, J. R. & Jenkins, D. M. *Am. Mineral.* **70,** 924–933 (1985).
18. Keppler, H. *Nature* **380,** 237–240 (1996).
19. Ryan, J. G., Morris, J., Tera, F., Leeman, W. P. & Tsvetkov, A. *Science* **270,** 625–627 (1995).

Acknowledgements. We thank F. Spera for pointing out some omissions from the original manuscript. This work was supported by German Science Foundation (DFG). A.H.S. was supported at Bayerisches Geoinstut by the European Union Human Capital and Mobility—Access to Large-Scale Facility Programme.

Correspondence and requests for materials should be addressed to A.H.S. (e-mail: ahs26@esc.cam.ac.uk).

Multituberculate and other mammal hair recovered from Palaeogene excreta

Jin Meng* & André R. Wyss†

* *Department of Biology and Graduate Program in Organismic and Evolutionary Biology, University of Massachusetts, Amherst, Massachusetts 01003, USA*
† *Department of Geology, University of California, Santa Barbara, California 93106, USA*

Evidence of hair from several extinct mammals has been recovered from a rich accumulation of fossil excrement from the Late Palaeocene beds of Inner Mongolia, China. This highly unusual and previously undocumented depositional occurrence consists of hundreds of mammalian carnivore coprolites (fossil faeces) and a lesser number of probably raptorial bird regurgitalites[1] (fossil pellets). The fossil hair occurs as impressions and natural casts in the extremely fine-grained, calcareous matrix that cements the skeletal remains within these faecal structures and preserves even the cuticular scale pattern on individual hair. Hair from at least four mammalian taxa, most notably the multituberculate *Lambdopsalis bulla*[2], has been identified. This record constitutes the first tangible evidence that, along with monotremes and therian mammals, multituberculates were hirsuite, and lends support for the presence of this mammalian feature in the most recent common ancestor of these three groups.

Mammalian faeces and bird pellets are usually rare, isolated occurrences in the pre-Pleistocene palaeontological record[3,4], as is the preservation of soft tissue such as hair[5]. We have examined a rich accumulation of hair-containing coprolites and regurgitalites (Fig. 1), an unprecedented datum in Palaeogene strata anywhere. This material was recovered from a small area (~400 m^2) of the late Palaeocene Nomogen Formation at the locality Bayan Ulan[6], Inner Mongolia. Sediments producing these structures and the associated Bayan Ulan fauna[7] are fine-grained, reddish clays, representing a low-energy depositional setting, possibly a pond margin.

We have identified two types of coprolites from Bayan Ulan on the basis of size, general morphology, and biogenic content (Fig. 1a). The unmistakable fusiform shape and high proportion of contained skeletal material indicates the faecal nature of these structures. The larger coprolites (~3–5 cm in length) usually have a smooth surface and consist mainly of white chalky matrix containing small bone fragments and isolated teeth. The smaller ones (~1–2 cm in length) have a rougher exterior and generally

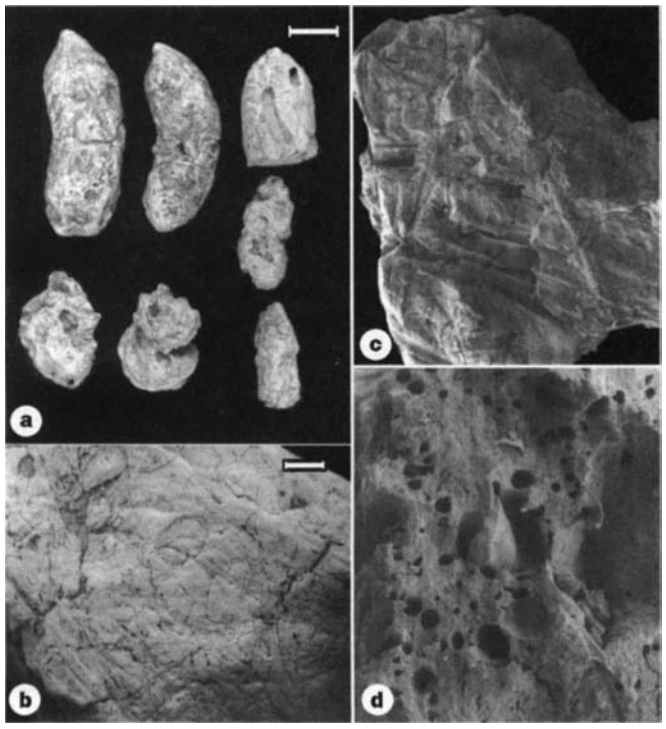

Figure 1 a, Large (top three) and small (two in bottom right) coprolites, and probable bird pellets (two in bottom left). The broken large coprolite in the top right bears grooves and burrows, presumably made by dung beetles. The bird pellets are irregular in shape, but are roughly oval and flat. **b**, Hair impressions on the surface of a coprolite. **c**, A small piece broken from a coprolite, containing intercrossed hair impressions and casts. **d**, A freshly broken piece of coprolite showing cross-sections of hair moulds, with casts dissolved. All specimens were collected from the ~55 Myr Nomogen Formation at Bayan Ulan of Inner Mongolia, China. Scale bars: **a**, 10 mm; **b**, 500 μm; **c**, 200 μm; **d**, 50 μm.

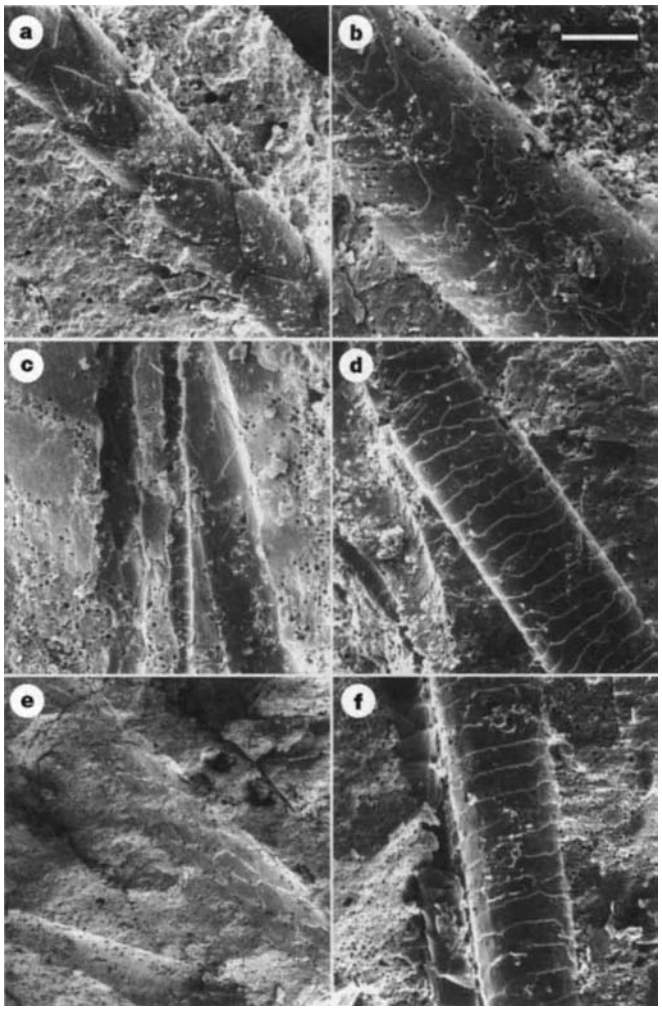

Figure 2 a, **b**, Proximal (cast) and distal (impression) segments of hair associated with skeletal remains of the multituberculate *Lambdopsalis*. The proximal cuticular scales form diamond-shaped shingles, the free tips pointing towards the apex of the hair; distally the margins of the scales are jagged. **c**, **d**, Hair scale patterns (impressions) of an as yet unnamed 'eurymylid' (a distant rodent ally); note the flattened, asymmetric, diamond-shaped scales on the proximal regions (**c**) and the more rectangular scales with straighter margins on the distal region. **d**, **e**, Two hair segments of *Palaeostylops* (a herbivorous mammal questionably related to South American notoungulates), of which the lower one (impression) displays an irregular wavy cuticular pattern, whereas the cuticle arrangement in the upper one (cast) resembles narrowly diamond-shaped shingles. **f**, Two segments of hair from *Tribosphenomys* (the nearest outgroup of rodents). The left one (a broken cast of a proximal segment) has a simple coronal scale pattern, and on the right one (impression of a distal segment) it is irregularly waved. All scanning electron micrographs are taken on coated freshly broken samples untreated by acid. Scale bars: **a**–**d**, **f**, 20 μm; **e**, 40 μm.

contain more complete skeletal material and a higher percentage of bone (more than 80% by weight of the nodule). We attribute these coprolites to carnivorous mammals rather than to crododilians because the enamel on the teeth they contain is in pristine condition; enamel is usually highly eroded during digestion in crocodilians[8]. This is consistent with the absence of crocodilian fossils at Bayan Ulan and the occurrence of several carnivorous mammals in the coprolite-yielding beds, including a possible viverravid, a creodont and two mesonychids[7].

Nodules here identified as bird regurgitalites are irregularly ovoid and flat (Fig. 1a), with many having a textured surface, probably as a result of the original pellets being enveloped by hair. In contrast to pellets produced by most extant raptorial birds, these nodules are relatively small and do not contain intact skulls. However, articulated postcranial skeletal elements, for example nearly complete limbs, as well as nearly complete jaws of exceedingly small mammals, are not uncommon in these structures.

Our analysis was restricted to coprolites containing skeletal remains of a single species, generally of a single individual, allowing secure identification of the hair. We have recovered hair casts and impressions of at least four mammalian taxa: *Palaeostylops iturus*[9] (a 'hoofed' mammal of disputed affinity to South American notoungulates[10]), *Tribosphenomys minutus*[11] (the nearest outgroup of rodents[12]), an undescribed 'eurymylid' (a more distant rodent ally), and the taeniolabidoid multituberculate *Lambdopsalis bulla*[2]. The preservational quality of these hair casts and impressions depends not only on the grain size of the matrix but also on the degree of bacterial decomposition at the time of burial. Where little decomposition has taken place, the matrix is dense and of a sufficiently fine consistency to record cuticular surfaces of hair in microscopic detail (Fig. 2). As decomposition advances, the matrix becomes more porous and hair degrades to varying degrees, resulting in poor preservation of the scale pattern or its obliteration altogether by fossil bacteria, which are themselves fossilized (Fig. 3).

Securely identified *Lambdopsalis* remains have been recovered from only the larger Bayan Ulan coprolites, in which much less hair is preserved than in the smaller ones. Hair attributable to this taxon has been obtained from five coprolites: three containing teeth, one the palate, and one the squamosal portion of the zygoma; each includes only *Lambdopsalis* skeletal remains. As it is impossible to excavate a single hair in its entirety, hundreds of hair segments were

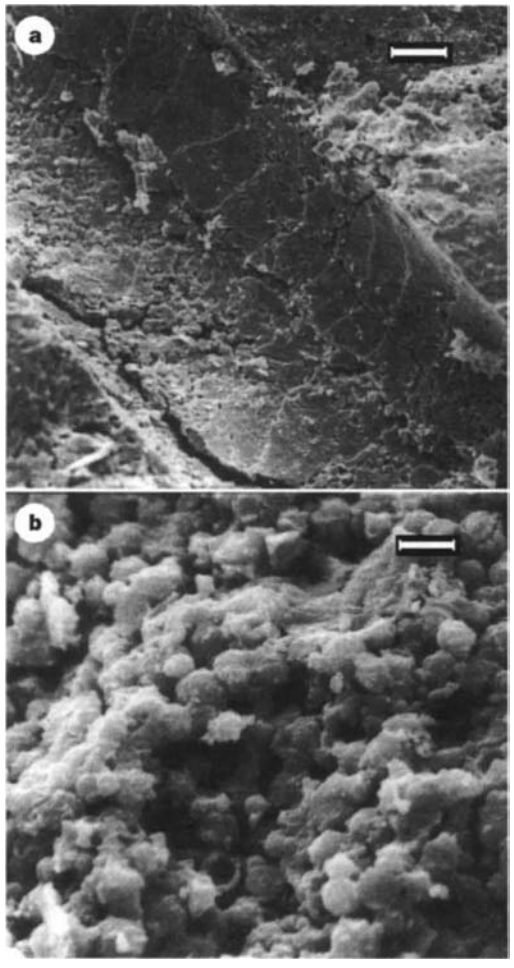

Figure 3 a, A hair impression with scales partly destroyed by bacterial degradation. Compared with the hair casts and impressions shown in Fig. 2, the scale pattern is largely disrupted. **b**, A close-up view of the surface of a hair impression, where the scale pattern is entirely replaced by cocci-shaped bacteria. The bacteria, ranging from 1 to 2 μm in diameter, closely resemble those reported from the Middle Eocene Messel deposit[5]. Scale bars: **a**, 10 μm; **b**, 2 μm.

examined and recorded by scanning electron microscopy; this method allows the cuticular scale variation along the length of a single hair to be determined. Scale patterns vary consistently for hair within a given coprolite, and between coprolites containing skeletal remains of the same taxon. As in many living mammals[13,14], the proximal portion of *Lambdopsalis* hair is usually thin and bears diamond-shaped cuticular scales (Fig. 2a). Scales surround the hair shaft in an alternating shingle-like arrangement, with the free end of each scale directed distally. Hair increases in diameter distally (from ~20 to ~60 μm in sampled specimens), and the margins of scales become jagged, producing an irregular pattern of waves (Fig. 2b).

Hair from the other three taxa has been sampled from the smaller coprolites and the regurgitalites using the same method. The dominant faunal element contained in these nodules is *Palaeostylops*, the cuticular pattern of which consists of narrow diamond-shaped scales (Fig. 2e). Cuticular scales in the 'eurymylid' are flattened and asymmetric on proximal portions of the hair, with gently undulating smooth margins on distal portions (Fig. 2c, d). A similar pattern occurs on distal segments of the hair in *Palaeostylops* and *Tribosphenomys*. *Tribosphenomys* hair is characterized by a simple coronal scale pattern proximally (Fig. 2f). *Lambdopsalis* hair has a greater diameter than that of other taxa, particularly *Tribosphenomys* and the 'eurymylid', probably because of its greater body size.

Hair is commonly regarded as a unique mammalian feature[15], probably related to endothermy as insulation of the body surface[16]. Although multituberculates are usually considered to have had hair[17–19], current debate over whether multituberculates are members of the mammalian crown clade obscures the phylogenetic basis of this inference[18–21]. The fundamental resemblance between the hair of *Lambdopsalis* and that of living mammals suggests that hair is conservative evolutionarily, and argues for its occurrence in the most recent common ancestor of multituberculates, monotremes and therians. Regardless of whether multituberculates are members of the clade stemming from the most recent common ancestor of monotremes and therians ('Mammalia' *sensu* ref. 20) or an outgroup to this clade[18,19,21], the hair from *Lambdopsalis* provides the first material evidence for the great antiquity of this anatomical hallmark, suggesting that its origin antedates the Late Triassic to Early Jurassic (about 210 Myr ago), the earliest multituberculate record[22]. Phylogenetic implications of the details of hair from *Lambdopsalis* and other Bayan Ulan taxa are uncertain, as too little is currently known about hair in early mammals to polarize available characters.

As well as representing an important new source of early Cenozoic micromammals, many representing taxa previously unknown at relatively high taxonomic levels[7,11], the Bayan Ulan coprolites and pellets also have significance for several palaeoecological and taphonomic issues. Several coprolites are burrowed (Fig. 1a), indicating use of the original faeces by insets, an uncommon occurrence in the fossil record[3]. Material from Bayan Ulan demonstrates that both carnivore scat[23] and bird pellets[24] may contribute importantly to the formation of microvertebrate fossil assemblages. Also, the coexistence of at least three gliriform eutherians and two multituberculates in the Bayan Ulan fauna, and the fact that members of both groups were prey items, must be taken into account in future causal explanations of multituberculate extinction[25–27]. Finally, we hope that this study of the unusual source of hair and microvertebrate remains will stimulate a search for potential coprolites containing, or generated by, early mammals (and near outgroups) in more ancient deposits. □

Received 15 October; accepted 11 December 1996.

1. Hunt, A. P. *New Mex. Bur. Mines Miner. Resour. Bull.* **138,** 221–229 (1992).
2. Chow, M. & Qi, T. *Vertebrata PalAsiatica.* **16,** 77–85 (1978).
3. Hunt, A. P., Chin, K. & Lockley, M. G. in *The Palaeobiology of Trace Fossils* (ed. Donovan, S. K.) 221–240 (The Johns Hopkins Univ. Press, Baltimore, 1994).
4. Edwards, P. & Yatkola, D. *Contrib. Geol. Univ. Wyoming* **13,** 67–73 (1974).
5. Schaal, S. & Ziegler, W. *Messel—an Insight into the History of Life and of the Earth* (Clarendon, Oxford, 1992).
6. Russell, D. E. & Zhai, R. *Mem. Mus. Natl Hist. Nat. (Paris)* C**52,** 1–488 (1987).
7. Meng, J., Zhai, R. & Wyss, A. R. *Bull. Carnegie Mus.* (in the press).
8. Fisher, D. C. *Contrib. Mus. Paleontol., Univ. Michigan* **25,** 259–275 (1981).
9. Matthew, W. D. & Granger, W. *Am. Mus. Novit.* **189,** 1–12 (1925).
10. Cifelli, R. L., Schaff, C. R. & McKenna, M. C. *Bull. Mus. Comp. Zool.* **152,** 1–44 (1989).
11. Meng, J., Wyss, A. R., Dawson, M. R. & Zhai, R. *Nature* **370,** 134–136 (1994).
12. Meng, J. & Wyss, A. R. *J. Mamm. Evol.* **2,** 185–203 (1994).
13. Brunner, H. & Coman, B. *The Identification of Mammalian Hair* (Inkata, Melbourne, 1974).
14. Debrot, S., Fivaz, G., Mermod, C. & Weber, J.-M. *Atlas des Poils de Mammifères d'Europe* (Imprimerie de l'Ouest S. A., Peseux, 1982).
15. Vaughan, T. A. *Mammalogy* (W. B. Saunders, Philadelphia, 1986).
16. Kemp, T. S. *Mammal-like Reptiles and the Origin of Mammals* (Academic, London, 1982).
17. Jenkins, F. A. Jr & Krause, D. W. *Science* **220,** 712–715 (1983).
18. Miao, D. *Contrib. Geol. Univ. Myoming, Spec. Pap.* **4,** 1–106 (1988).
19. Kielan-Jaworowska, Z. & Gambaryan, P. P. *Fossils Strata* **36,** 1–92 (1994).
20. Rowe, T. *J. Vert. Paleontol.* **8,** 241–264 (1988).
21. Hopson, J. A. in *Short Courses in Paleontology* Vol. 7, *Major Features of Vertebrate Evolution* (ed. Spencer, R. S.) 190–219 (The Paleontological Soceity, 1994).
22. Hahn, G., Sigogneau-Russell, D. & Wouters, G. *Bull. Soc. Bel. Géol.* **96,** 39–47 (1987).
23. Mellett, J. S. *Science* **185,** 349–350 (1974).
24. Andrews, P. & Nesbitt-Evans, E. M. *Paleobiology* **9,** 289–307 (1983).
25. Landry, S. O. *Syst. Zool.* **16,** 172–173 (1967).
26. Ostrander, G. *Nebraska Acad. Sci. Trans.* **12,** 71–80 (1984).
27. Krause, D. W. *Contrib. Geol. Univ. Wyoming, Spec. Pap.* **3,** 95–117 (1986).

Acknowledgements. We thank R. Zhai, A. Weil, N. B. Simmons and S. K. Bell for discussions and comments; J. A. Hopson and R. Presley for criticism; and P. F. Melville for scanning electron micrographs. This work was supported by the Institute of Vertebrate Paleontology and Paleoanthropology of Beijing, Erlian Museum, American Museum of Natural History, the University of California, Santa Barbara, the University of Massachusetts, the Margaret E. and Howard E. Bigelow Gift to the University of Massachusetts, the National Geographic Society, and NSF.

Correspondence and requests for materials should be addressed to J.M. (e-mail: jmeng@bio.umass.edu).

Haramiyids and Triassic mammalian evolution

Farish A. Jenkins Jr*, Stephen M. Gatesy†, Neil H. Shubin‡ & William W. Amaral*

* *Department of Organismic and Evolutionary Biology, and Museum of Comparative Zoology, Harvard University, Cambridge, Massachusetts 02138, USA*
† *Department of Ecology and Evolutionary Biology, Brown University, Providence, Rhode Island 02912, USA*
‡ *Department of Biology, University of Pennsylvania, Philadelphia, Pennsylvania 19104, USA*

Isolated teeth referred to the family Haramiyidae are among the earliest known fossil evidence of mammals. First discovered in European Late Triassic deposits a century and a half ago[1], haramiyids have been interpreted as related to multituberculates[2–7], a diverse and widespread lineage that occupied a rodent-like niche from the Late Jurassic to the Early Tertiary. Nonetheless, haramiyid relationships have remained enigmatic[8,9] because the orientation and position of the teeth in the upper or lower jaw could not be determined with certainty; even their mammalian status has been questioned[10]. The discovery of haramiyid dentaries, a maxilla and other skeletal remains in the Upper Triassic of East Greenland reveals haramiyids as highly specialized mammals with a novel pattern of puncture-crushing occlusion that differs dramatically from the grinding or shearing mechanisms of other Early Mesozoic mammals.

Class Mammalia
Order Haramiyida Hahn, 1973
Family Haramiyidae Simpson, 1947
Haramiyavia clemmenseni gen. et sp. nov.

Etymology. Combining *Haramiya*, Arabic (fem.)[11] for 'trickster, petty thief' with *avia*, Latin for grandmother; *clemmenseni*, as acknowledgement to Lars B. Clemmensen, whose geological studies led to the discovery of the Fleming Fjord fauna[12].
Holotype. Museum of Comparative Zoology (MCZ) 7/G95 (Figs 1b, c, e, 2), associated dentaries, premaxilla and other cranial elements, and a disarticulated, partial postcranial skeleton including vertebrae and limb bones.
Referred material. MCZ 10/G95 (Fig. 1a, d), partial maxilla with three molariform teeth.
Horizon. Tait Bjerg Beds, Ørsted Dal Member of the Fleming Fjord Formation.
Locality. N 71° 32.958′, W 22° 55.188′, altitude ~670 m, north side of Ærenprisdal at the intersection with Pingel Dal, Jameson Land, East Greenland.
Age. Late Triassic (?Norian–Rhaetic)[12].
Diagnosis. Derived features shared with other mammals: differentiated teeth (I_4 C_1 P_4 M_3; Figs 1c and 2) and multirooted molariforms. The first and second molariforms in both the upper and lower dentitions are of comparable size, and are larger than the third molariform (Fig. 3). Derived features shared with the haramiyid *Thomasia*[8]: basined lower molariform teeth with two mesiodistally aligned rows of cusps; the lingual row (row A; refs 6, 10, 13) bears the highest cusp (A1; Figs 1c, e and 2) mesially, with cusps of successively decreasing heights distally. The mesial cusp (B1; Fig. 1e) on the buccal side (row B; refs 6, 10, 13) is variable in height, but not as high as A1; cusps B2–B5 progressively decrease in height. A low crest on M_1 or a cusp (B5; Fig. 1e) on M_3 joins the two rows distally and encloses a 'basin'. Distinguished from *Thomasia antiqua* and *T. anglica* by the presence of four, rather than three, cusps in the lingual row. Derived features shared with *Haramiya*[8,11]: basined upper molariform teeth with two mesiodistally aligned rows of cusps; three cusps in the buccal row (row A; refs 6, 10, 13) of subequal height, the mesial of which (A3) is the lowest. The lingual row (row B; refs 6, 10, 13) bears a large distal cusp, preceded by a series of four progressively smaller cusps. On M^1, the four smaller lingual cusps are more or less aligned, thus comparable to the four minor lingual cusps of *Haramiya moorei*[8], whereas on M^{2-3}, the most mesial cusp (B5; Fig. 1d) is positioned more centrally and encloses the central basin as in *H. fissurae*[8]. Differs from *H. moorei* and *H. fissurae* in the presence of two buccal cuspules (C1, 2; Fig. 1d); a shelf-like cingulum occurs between the cuspules on M^{2-3}, but is absent on M^1 where C2 is very small. The specimens are registered in the Geological Museum, University of Copenhagen, as MGUH VP 3351 (MCZ 7/G95) and MGUH VP 3352 (MCZ 10/G95).

Before the discovery of *Haramiyavia clemmenseni*, haramiyids were known on the basis of several hundred isolated teeth, principally from English and continental European deposits of either Rhaetic or 'Rhaeto–Liassic' age[10,13,14]. The two genera *Haramiya* and *Thomasia*, diagnosed from features of the tooth crown[8], can now be definitively recognized as representing upper and lower teeth, respectively, confirming suppositions advanced by Parrington[15], Crompton[16], Sigogneau-Russell[14] and Butler and MacIntyre[10]. Morphological variation along the tooth row in *H. clemmenseni* supports the probability that the various species of *Haramiya* and *Thomasia* may be different teeth from the same dentition. Although the taxonomic status and diversity of European haramiyids cannot be resolved on the basis of available material, the anatomical orientation of their teeth can be confidently determined relative to those in *Haramiyavia clemmenseni*. Lower teeth ('*Thomasia*' spp.) have a basin that is more or less open mesially, in agreement with conventional designations[6,8]. The row with the highest mesial cusp (row A) is lingual, verifying the interpretation of Hahn[6]. For upper teeth ('*Haramiya*' spp.), the end conventionally designated as mesial[8,13,15] is in fact distal; thus, the enclosed end of the central basin is mesial, and the row of three cusps (row A; ref. 13) is buccal. The hypotheses advanced by Sigogneau-Russell[14] and by Butler and MacIntyre[10] concerning the orientations of upper and lower teeth are correct.

Earlier workers interpreted haramiyids as multituberculates[2–4,17], but others [8,9,18] expressed uncertainty because of the paucity of data. Hahn's[5,6] comparison of teeth of *Thomasia antiqua* with those of *Paulchoffatia delgadoi* and *Kuehneodon simpsoni*, paulchoffatiid multituberculates from the Late Jurassic (Kimmeridgian) of Portugal, represents the most detailed analysis supporting haramiyid–multituberculate affinities, but the systematic value of the evidence has been questioned[10,19]. Hahn's assessment was based primarily on a tooth of *Thomasia antiqua* that he compared to upper left teeth of *Kuehneodon* sp. The dentition of *Haramiyavia clemmenseni* demonstrates that the haramiyid tooth illustrated by Hahn is in fact a lower left molariform.

Several features that have been proposed to be shared by haramiyids and primitive multituberculates can now be re-examined. From the distribution of wear facets and their relative wear, Hahn[6] correctly deduced (as did Parrington[15]) that the upper and lower teeth were offset to provide interlocking occlusion of rows and basins. Hahn also concluded from the relative wear on the facets that the lower of the two cusp rows on both upper and lower teeth (row B) made occlusal contact with the opposing basin. Although the teeth of *Haramiyavia clemmenseni* are only slightly worn, this occlusal pattern (Fig. 4) is verified as a feature common to haramiyids and the earliest known true multituberculates. The Greenlandic haramiyid's procumbent incisors and substantial diastema are the only other derived dental features shared with multituberculates.

Despite these superficial similarities, important differences in jaw and dental structure, as well as occlusal movements, distinguish

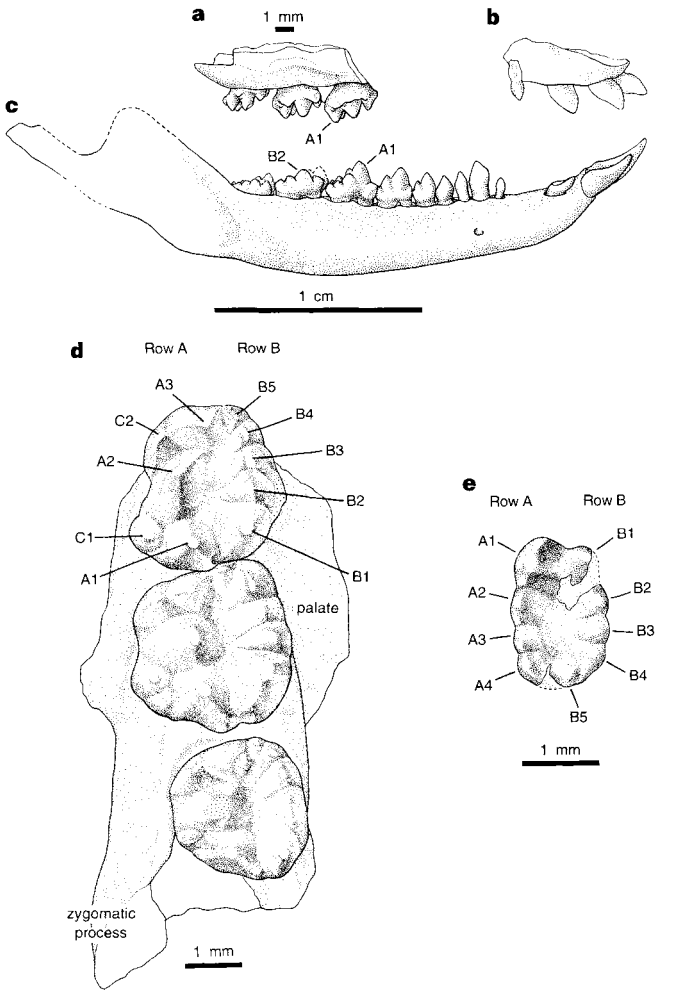

Figure 1 The dentition of *Haramiyavia clemmenseni*, gen. et sp. nov. **a**, Right maxilla (MCZ 10/G95) in lateral view. **b**, Left premaxilla (MCZ 7/G95, reversed) in lateral view (same scale as **c**). I^{1-3} are broad, blunt and procumbent, and are separated by a short diastema from a small, lanceolate I^4. **c**, Reconstruction of the right dentary in lateral view, based on the right and left dentaries of MCZ 7/G95. I_{1-2} are large, procumbent incisors with upwardly inflected apices; the elongate occlusal (dorsal) surface of each tooth is bordered mesially and distally by sharp margins that extend from the base of the crown nearly to the apex. The smaller I_3 is also procumbent; the occlusal surface, which is buccolingually narrow and diamond-shaped in outline, bears slight eminences on the mesiolabial and distolingual margins. I_4 is a very small, slender tooth with an elongate root (in length about 5× the height of the crown); in the present state of preservation the crown appears to have been in the form of a bulbous nubbin. The lower canine is a simple, blade-like tooth with an obtuse apex. The crowns of P_1 and P_2 are lanceolate with a single apical cusp and mesial and distal crests. P_1 is present only in the left dentary. On the right dentary there is a short diastema between the canine and P_2 with no indication of an alveolus. P_3, slightly higher than P_2, is enlarged by the presence of a secondary cusp on the distal crest and a slight distal cingulum that bears a small cuspule distolingually. P_4 is substantially larger and, unlike other premolars, is double-rooted. In addition to the secondary cusp on the distal crest, a third cusp is borne on the distal cingulum. All three molars are double-rooted. M_1 is longitudinally fractured and only the buccal row and buccal side of the lingual row of cusps are preserved. The mesial cusp of the lingual row is highest (and appears to be the highest cusp of the lower dentition), followed by three cusps of decreasing height. The buccal row on M_1 bears four cusps. The largest cusp (B2) is distinctly bulbous and is joined to the mesial cusp (A1) of the lingual row by a prominent ridge that thus defines the mesial end of the basin; mesial to B2 is an extensive shelf separating it from a small cuspule (B1) on the mesiobuccal margin of the crown. M_2 is also longitudinally fractured. The buccal cusp row of M_2 differs in possessing a prominent mesial cusp (B1) and in lacking any shelf; the distal two cusps are missing but have been restored from a natural mould. An impression of the lingual cusp row of M_2 on the counterpart block reveals a row of four cusps, the mesial two of which are tallest. A fragment of M_2 from the right dentary preserves part of a cuspule on a crest that joins the two cusp rows along the distal margin of the crown and thus contributes to forming a central basin. **d**, Right maxilla (MCZ 10/G95) in occlusal view. Two mesiodistally aligned rows of cusps flank elongate central basins. Distally, the basin narrows to a V-shaped embrasure between the relatively closely set cusps A1 and B1. On M^{2-3}, crests passing from apex to base on the distal side of cusps A1 and B1 bear a tiny cuspule near the base; on M^1, a crest and cuspule are developed only on A1. On the buccal side of row A are two small accessory cusps; the mesial cusp (C2) is borne on a crest descending from the apex of A3, whereas the distal cusp (C1) is distinctly separated from A1 and A2 by shallow intercuspal notches. On the M^3 a shelf-like cingulum extends the buccal margin of the crown between these accessory cusps; the cingulum is only slightly developed on M^2, and is absent on M^1. **e**, Right M_3 (MCZ 7/G95) in occlusal view. M_3 is smaller than M_{1-2}, and bears four cusps in the lingual row; the mesial cusp (A1) is highest and is followed by three cusps of decreasing height and smaller size. In the buccal row the mesial two cusps (B1, 2) are largest and subequal in height. The last cusp in this series (B5) is more centrally positioned and encloses the basin distally.

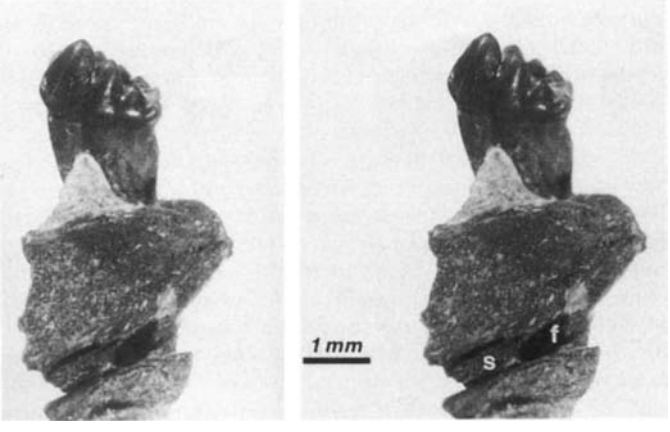

Figure 2 Stereoscopic photographs of the right M_3 of *Haramiyavia clemmenseni*, gen. et sp. nov., MCZ 7/G95, in lingual view. The tooth was displaced post mortem almost completely out of the alveolus. The associated dentary fragment preserves the inferior alveolar foramen (f) and a large sulcus (s) for post-dentary bones.

haramiyids and paulchoffatiids. The slender dentary of *Haramiyavia clemmenseni* (Fig. 1c), in which the condylar process is protracted posterodorsally, differs from the short, robust dentaries of primitive multituberculates, in which the condylar processes are ventrally positioned[20]. Although the lower molariform teeth of both groups exhibit a gradient of cusp heights from front to back, the cusp pattern in upper molariforms is different: in haramiyids the largest cusps are distal, whereas in paulchoffatiids the largest cusps are mesial. In paulchoffatiids, a U-shaped central basin is formed by two cusp rows that are joined by a crest along the distal margin of the crown; both upper and lower basins are thus open mesially[6]. In haramiyids, the U-shaped basins are reversed between upper and lower teeth; the crest that links the cusp rows is mesial on upper teeth and distal on lower teeth. Additionally, there is no evidence in *H. clemmenseni* of a lingual offset of the last upper molar that characterizes multituberculates[21]. Even more significant are differences in molar occlusion. In typical multituberculates, molar crowns are aligned to produce linear rows of cusps and basins, thus forming a continuous occlusal surface suited for palinal movement[22]. In haramiyids, striations have been cited as evidence of longitudinal movement[10,14], but certain wear facets 'cannot be

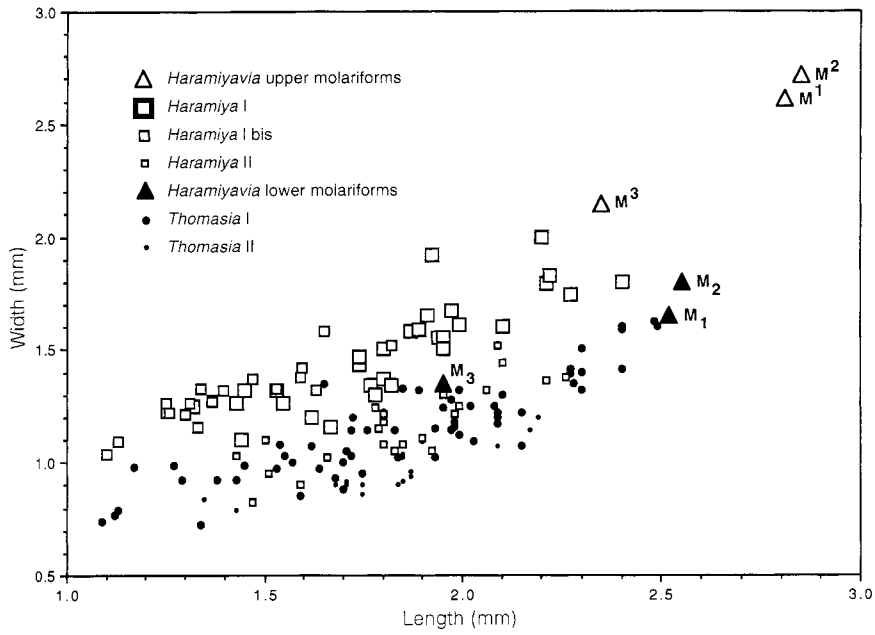

Figure 3 Tooth dimensions of *Thomasia* and *Haramiya* spp.[14] compared with those of *Haramiyavia clemmensensi*, gen. et sp. nov. The widths of M_1 and M_2 of *H. clemmenseni* are estimated. Although the upper molariform teeth (MCZ 10/G95) appear to be from a larger individual than that representing the lower dentition (MCZ 7/G95), conspecific status of the two specimens is indicated by a reconstruction of occlusal relations (Fig. 4).

produced by horizontal movement'[10]. Interpretations of masticatory movements in haramiyids have varied from 'a power stroke with a transverse component'[16] to 'longitudinal'[23], 'non-propalinal'[13] (that is, orthal), 'essentially rotary, with an orthal component, a longitudinal component, and some transverse laxity'[14] and 'palinal'[10]. Several features of *H. clemmenseni*, which are not apparent in the isolated teeth of Anglo-European haramiyids, confirm that occlusion was orthal in this species. The crowns of upper molariform teeth are set en echelon (Fig. 1a); this step-like pattern is also reflected in the inclination of the basins of lower molariforms in which the basin floors are lower distally and higher mesially. This geometry necessitates a 1:1 relation between upper and lower teeth, and obviates the possibility of palinal movement of a lower molariform across two upper molariforms. The complex interlocking of cusp rows engendered by the dentition of *H. clemmenseni* would permit only a predominantly orthal movement (Fig. 4), which thus differs from the palinal stroke of multituberculates. If other features of *Haramiyavia clemmenseni* are found to support an affinity with multituberculates, a profound transformation occurred in mandibular and dental structure, as well as in occlusal relations, during the 50 million years between the Late Triassic and Late Jurassic (Kimmeridgian). Available evidence, however, does not indicate a close relationship between the two groups.

The postcranial skeleton of *Haramiyavia clemmenseni*, although disarticulated and incomplete, possesses various features (a bicondylar distal humerus, well developed olecranon process, asymmetry of the femoral condyles, atlas arch structure) comparable to those of morganucodontids, the only other early mammalian group for which postcranials are known[24]. However, *H. clemmenseni* appears to have been larger and more gracile than its contemporaries. The dentary is about 33% and 85% longer than that in *Morganucodon* and *Kuehneotherium*, respectively. In limb proportions, the radius of *H. clemmenseni* is almost equal to the humerus in length (~97%), whereas the radius is shorter than the humerus in *Morganucodon* (~75%). A relatively elongate distal limb may also be reflected by the fact that the longest metapodial element preserved with *H. clemmenseni* is ~40% of humeral length, whereas the longest

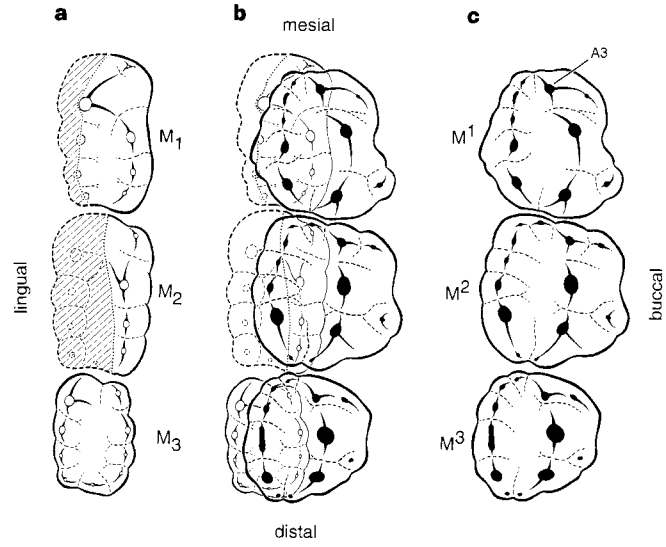

Figure 4 Cusp diagrams of *Haramiyavia clemmensensi* molariform teeth illustrating reconstructed occlusal relations. **a**, Right lower molariforms; cross-hatched parts of M_1 and M_2 are reconstructed on the basis of impressions. **b**, Occlusion involved the interdigitation of upper and lower cusp rows with the central basins in an essentially orthal movement. The buccal row of lower molariforms meets the central basins of upper molariforms, and the lingual row of upper molariforms meets the central basins of lower molariforms. Although Parrington's hypothesis[15] that the open (non-enclosed) end of the basins faced in opposite directions on upper and lower teeth is essentially correct, important differences in cusp size and occlusal pattern characterize tooth pairs which may account for the substantial variability of wear facets observed on isolated haramiyid molariforms[10]. On M^{2-3}, cusp A3 occludes on the buccal side of the most mesial cusp in the lower buccal cusp row; on M^1, however, the position of A3 is shifted lingually to occlude in the large embrasure within the buccal cusp row of M_1, obviating the possibility of mesiodistal jaw movements during occlusion. **c**, Diagram of right upper molariforms, reversed for occlusal comparison.

metapodial of *Morganucodon* is only ~30%. Comparison of diaphysial diameter/bone length ratios confirms the impression that the long bones of the new haramiyid are more gracile than those of *Morganucodon*.

Among the earliest known mammals (of Late Triassic or 'Rhaeto–Liassic' age), representatives of two families, Morganucodontidae and Kuehneotheriidae, are the best known in terms of their dental apparatus. These taxa share a suite of features, including premolar–molar differentiation, multirooted post-canines (with the exception of the mesial premolars), molars with three primary cusps, slender dentaries, small dentary condyles, and unilateral, shearing occlusion[16,25,26]. *Haramiyavia clemmenseni* is comparable in the degree of premolar–molar and post-canine root differentiation. Although the condylar region of *H. clemmenseni* is not preserved, the overall shape of the slender dentary is similar to that in morganucodontids and *Kuehneotherium*; a small dentary condyle is likely to have been present. Yet significant differences separate *H. clemmenseni* from contemporaneous mammals. In *H. clemmenseni*, the sulcus anterior to the inferior alveolar foramen (Fig. 2) is proportionately wider than that in *Morganucodon* and *Kuehneotherium*, indicating that post-dentary bones were retained at a relatively more primitive, less reduced size. Furthermore, the orthal and probably bilateral occlusion produced a puncture-crushing effect that differs from the shearing mechanisms of morganucodontids and *Kuehneotherium* and the grinding dentitions of multituberculates. Thus haramiyids retain features of the jaw and post-dentary apparatus that would place them in a basal position among mammals, but at the same time they exhibit a highly specialized dentition. The dramatic dental differences exhibited by the new haramiyid in comparison to those of other Late Triassic mammals further increases the likelihood of a much earlier—possibly Middle Triassic—diversification of the earliest mammals[13]. □

Received 9 October; accepted 11 December 1996.

1. von Plieninger, W. H. T. *Jh. Ver. vaterl. Naturk. Württ.* 164–167 (1847).
2. Marsh, O. C. *Am. J. Sci.* **33,** 327–348 (1887).
3. Osborn, H. F. *J. Acad. Nat. Sci. Philad.* **9,** 186–265 (1888).
4. Gregory, W. K. *Bull. Am. Mus. Nat. Hist.* **27,** 1–524 (1910).
5. Hahn, G. *Palaeontographica A* **133,** 1–100 (1969).
6. Hahn, G. *Palaeontographica A* **142,** 1–15 (1973).
7. Sigogneau-Russell, D. & Hahn, G. in *In the Shadow of the Dinosaurs: Early Mesozoic Tetrapods* (eds Fraser, N. C. & Sues, H.-D.) 197–213 (Cambridge University Press, Cambridge, 1994).
8. Simpson, G. G. *A Catalogue of the Mesozoic Mammalia in the Geological Department of the British Museum* (Oxford University Press, London, 1928).
9. Clemens, W. A. & Kielan-Jaworowska, Z. in *Mesozoic Mammals, the First Two-thirds of Mammalian History* (eds Lillegraven, J. A., Kielan-Jaworowska, Z. & Clemens, W. A.) 99–149 (University of California Press, Berkeley, 1979).
10. Butler, P. M. & MacIntyre, G. T. *Phil. Trans. R. Soc. B* **345,** 433–458 (1994).
11. Simpson, G. G. *J. Paleont.* **21,** 497 (1947).
12. Jenkins, F. A. Jr *et al. Meddr. Grønland, Geoscience* **32,** 1–25 (1994).
13. Clemens, W. A. *Zitteliana* **5,** 51–92 (1980).
14. Sigogneau-Russell, D. *Palaeontographica A* **206,** 137–198 (1989).
15. Parrington, F. R. *Proc. Zool. Soc. Lond.* **116,** 707–728 (1947).
16. Crompton, A. W. *Bull. Br. Mus. Nat. Hist.* **24,** 397–437 (1974).
17. Hennig, E. *N. Jahrb. Min., Geol., Paläont.* **46,** 181–267 (1922).
18. Mills, J. R. E. in *Early Mammals* (eds Kermack, D. M. & Kermack, K. A.) 29–63 (Academic, London, 1971).
19. Simmons, N. B. in *Mammal Phylogeny: Mesozoic Differentiation, Multituberculates, Monotremes, Early Therians, and Marsupials* (eds Szalay, F. S., Novacek, M. J. & McKenna, M. C.) 146–164 (Springer, New York, 1993).
20. Hahn, G. *Geol. Palaeontol.* **12,** 177–212 (1978).
21. Krause, D. W. & Hahn, G. *J. Paleont.* **64,** 1051–1054 (1990).
22. Krause, D. W. *Paleobiology* **8,** 265–281 (1982).
23. Hahn, G., Sigogneau-Russell, D. & Wouters, G. *Geol. Palaeontol.* **23,** 205–215 (1989).
24. Jenkins, F. A. Jr & Parrington, F. R. *Phil. Trans. R. Soc. B* **273,** 387–431 (1976).
25. Kermack, D. M., Kermack, K. A. & Mussett, F. *Zool. J. Linn. Soc.* **47,** 407–423 (1968).
26. Crompton, A. W. in *Functional Morphology in Vertebrate Paleontology* (ed. Thomason, J.) 55–75 (Cambridge University Press, Cambridge, 1995).

Acknowledgements. We thank L. L. Meszoly for rendering Figs 1 and 4, A. H. Coleman for stereophotography, T. I. H. Andersson (Danish Polar Center), L. B. Clemmensen, W. R. Downs, H. E. Jenkins II, D. V. Kent, D. C. Roberts, C. R. Schaff and M. D. Shapiro for field work, and P. M. Butler, W. A. Clemens, A. W. Crompton, J. A. Hopson, D. W. Krause, G. Hahn, M. J. Novacek, D. Sigogneau-Russell and H.-D. Sues for critical advice. Supported by grants from the NSF, the Carlsberg Foundation, and the Putnam Expeditionary Fund of the Museum of Comparative Zoology.

Correspondence should be addressed to F.A.J.

Airborne signalling by methyl salicylate in plant pathogen resistance

Vladimir Shulaev, Paul Silverman* & Ilya Raskin

AgBiotech Center, Cook College, Rutgers University, PO Box 231, New Brunswick, New Jersey 08903-0231, USA

Methyl salicylate, a volatile liquid, also known as oil of wintergreen, is made by a number of plants[1–9]. Here we show that methyl salicylate is a major volatile compound produced by tobacco plants inoculated with tobacco mosaic virus. Methyl salicylate is synthesized from salicylic acid, a non-volatile chemical signal required for the establishment of acquired resistance[10] and local and systemic induction of antimicrobial pathogenesis-related proteins[11]. Methyl salicylate acts by being converted back to salicyclic acid. We conclude that methyl salicylate may function as an airborne signal which acitvates disease resistance and the expression of defence-related genes in neighbouring plants and in the healthy tissues of the infected plant.

Resistance to tobacco mosaic virus (TMV) in tobacco plants (*Nicotiana tabacum* cv. Xanthi-nc) carrying the *N* gene is associated with a hypersensitive response at sites of viral inoculation. While investigating the movement and distribution of salicylic acid (SA) in TMV-inoculated tobacco plants, we discovered that these plants produced gaseous methyl salicylic acid (MeSA) (Fig. 1). No MeSA was volatilized from healthy, mock-inoculated or mechanically wounded tobacco plants. MeSA evolution from a 5-week-old tobacco plant inoculated with TMV on two middle leaves was first observed 48 h post-inoculation and reached a maximum of 22 ng per hour per plant 84 h post-inoculation, when MeSA became one of the most abundant volatile products emitted. Increased MeSA evolution paralleled the appearance of hypersensitive lesions, which in turn coincided with the induction of SA biosynthesis[12,13]. The identification of plant-produced MeSA was confirmed by mass spectral analysis (Fig. 1c, d).

Incubation of TMV-inoculated tobacco plants at 32 °C blocks the development of the hypersensitive-resistance response and leads to systemic infection[14] without accumulation of SA or of pathogenesis-related (PR) proteins. Infected tobacco plants shifted from 32 to 24 °C undergo systemic necrosis and a massive increase in tissue SA[15]. No MeSA was detected when TMV-inoculated plants were kept at 32 °C for 48 h (Fig. 1b). When TMV-inoculated plants were shifted to 24 °C, MeSA production reached 283 ng per hour per plant 60 h after the temperature shift.

To understand the role of MeSA in the defence response, tobacco plants were preincubated for 6 days in gas-tight chambers containing air supplemented with different concentrations of MeSA. At the end of the incubation, plants were analysed for their SA content, PR-protein induction, and resistance to TMV. Incubation of tobacco plants with gaseous MeSA resulted in a dramatic accumulation of SA in the leaves (Fig. 2a). Even at 2.5 $\mu g\,l^{-1}$, MeSA increased endogenous SA content 1.4-fold compared to the untreated control, whereas 250 $\mu g\,l^{-1}$ MeSA increased SA levels 298-fold to 29.9 μg per g fresh weight. Enhanced TMV resistance, measured as reduced lesion size, was directly proportional to MeSA concentration (Fig. 2b). The mean lesion diameter was reduced by 25% by preincubation with 6.25 $\mu g\,l^{-1}$ MeSA, whereas 250 $\mu g\,l^{-1}$ of MeSA gave a 75% reduction in mean lesion diameter. Increases in tissue SA and

* Present address: Abbott Agricultural Research Center, Plant Science Department, Long Grove, Illinois, 60067, USA.

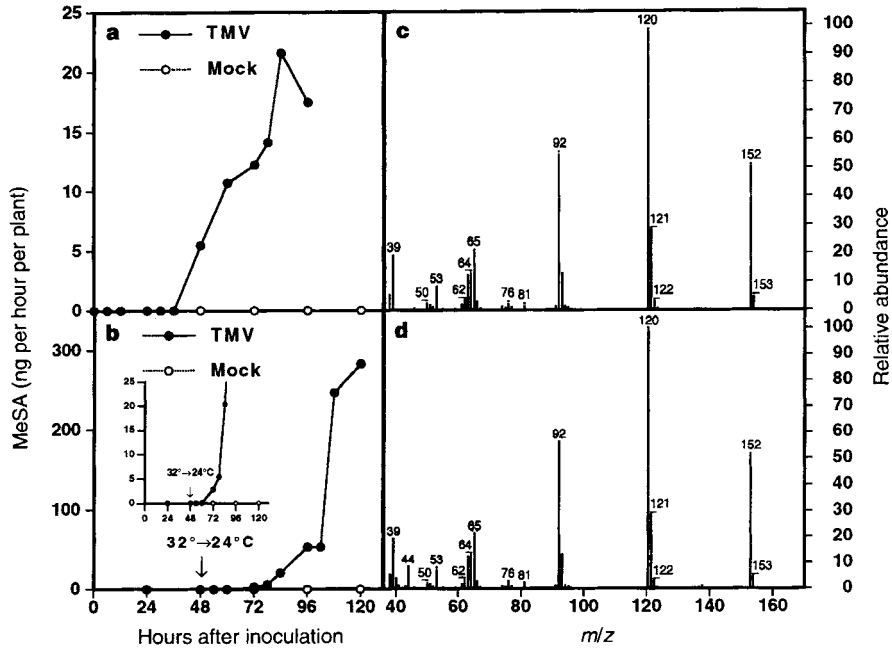

Figure 1 MeSA evolution by TMV-inoculated tobacco plants, kept at 24 °C (**a**) or incubated at 32 °C for 48 h and shifted to 24 °C at the times indicated (**b**); **b**, inset, fine scale on *y*-axis shows that no MeSA was detected in inoculated plants kept at 32 °C. Mass spectra of **c**, authentic MeSA standard, and **d**, of the putative MeSA produced by inoculated plants kept at 24 °C. The experiment was repeated three times with similar results. Note the difference in the scale of the *y*-axis in **a** and **b**.

TMV resistance following MeSA treatment was accompanied by large increases in expression of the *PR-1* gene, a molecular marker for acquired resistance (Fig. 3c). The large amounts of MeSA produced by inoculated leaves and its efficacy in inducing resistance make MeSA a likely candidate for an airborne signal which affects healthy tissues located close to the site of infection.

To establish whether the amounts of MeSA released by TMV-inoculated tobacco plants are sufficient to induce resistance in adjacent healthy plants, we constructed eight two-compartment flow-through systems (Fig. 3a). Each system consisted of a gas-tight glass chamber containing eight TMV- or mock-inoculated donor plants (D) connected to another glass chamber containing one non-inoculated recipient plant (R). Air was pumped at 30 ml min^{-1} from the donor plant chamber to the recipient plant chamber; this air passed from the donor chamber to the recipient chamber either directly (−) or through a column packed with Tenax-TA resin (+). This Tenax-TA column, which was replaced every 6 to 12 h, trapped airborne MeSA and other volatile hydrocarbons containing more than five carbon atoms[16–18]. TMV-inoculated plants were put inside the donor chamber 24 h after inoculation and maintained for 3 days. A second group of inoculated plants was then placed inside the donor chamber for another three days. A single non-inoculated plant was kept in the recipient chamber for the duration of the experiment (6 days). At the end of the experiment, total RNA was extracted from the TMV-inoculated leaves of donor plants (second group) and from healthy middle leaves of a recipient plant, and analysed by northern blotting for *PR-1* expression (Fig. 3b). In another, similar experiment eight TMV-inoculated plants kept at

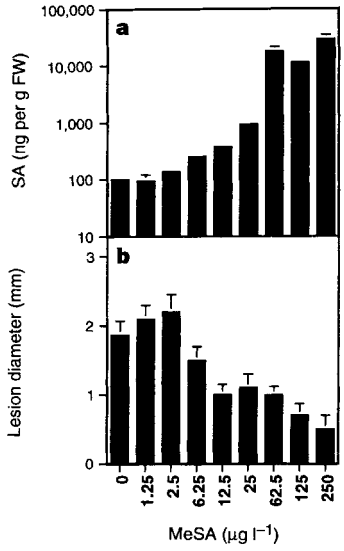

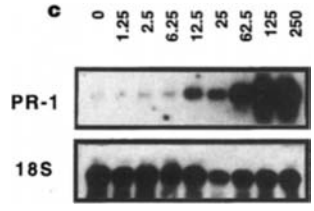

Figure 2 Effect of MeSA on **a**, total SA levels, **b**, TMV resistance, and **c**, PR-1 gene expression; FW, fresh weight. Five-week-old tobacco plants were enclosed for 6 d in 4-l gas-tight glass chambers. Different amounts of liquid MeSA were applied to the tip of a cotton swab placed inside the chamber and were allowed to evaporate. The air with MeSA was replaced every 24 h. At the end of the incubation period, one middle leaf was removed from each plant and analysed for total SA content and expression of PR genes. Plants were then inoculated with TMV on two other middle leaves, and the diameter of the TMV-induced lesions measured 4 days post-inoculation. Numbers above lanes indicate dosage of MeSA. The experiment was repeated twice with similar results.

32 °C for 3 days and then shifted to 24 °C were used as donors (Fig. 3b). Because of the longer preincubation at 32 °C, these plants showed greater necrosis and produced substantially more MeSA than plants analysed in Fig. 1b. The amount of MeSA produced by donor plants during this experiment was estimated as 184 μg (calculated by multiplying an average measured rate of MeSA production of 23 μg over 6 days by each plant, by 8—the number of donor plants). This amount of MeSA should be sufficient to activate a defence response in recipient plants (compare with Fig. 2). The temperature-shifted TMV-inoculated donor plants triggered the greatest *PR-1* expression in recipient plants. No induction of *PR-1* was detected in recipient plants when donors were mock-inoculated or when the air from TMV-inoculated plants was passed through a MeSA trap. In addition, plants receiving MeSA-containing air from TMV-inoculated plants showed a moderate increase in TMV resistance (Fig. 3c), manifesting as a statistically significant 28% reduction in lesion diameter, when compared to plants receiving air directly from mock-inoculated plants. We verified that most of the MeSA produced by donor plants was retained in the trap. No MeSA was detected in Tenax-TA traps when mock-inoculated plants were used as donors. We also verified that ethylene, a gaseous plant hormone capable of inducing some defence responses[19], is not trapped by Tenax-TA resin (data not shown). Moreover, replacing the Tenax-TA trap with a trap containing the ethylene scrubber Purafil did not prevent induction of *PR-1* in the recipient plant exposed to air from TMV-inoculated plants (data not shown).

The dependence of MeSA production on tissue SA levels, as well as the structural similarity of these compounds, indicates that MeSA in tobacco plants may be derived from SA. To investigate whether tobacco plants convert SA to MeSA, two fully expanded middle leaves of a healthy five-week-old tobacco plant were infiltrated with 1 ml of 0.5 mM ^{14}C-SA (56 mCi mmol^{-1}) and placed inside a 4-l air-tight glass chamber. Air was filtered through activated charcoal, passed through the chamber at 40 ml min^{-1}, and the volatiles collected for 12 h one day after infiltration. MeSA was trapped on a Tenax-TA column and analysed by gas chromatography and mass spectrometry (GC-MS). The mass spectrum of MeSA produced by the ^{14}C-SA-infiltrated plant showed that 99% of MeSA emitted by the infiltrated plant was derived from ^{14}C-SA (Table 1).

To determine the metabolic fate of gaseous MeSA in the tobacco leaf, a tobacco plant was incubated in air containing ^{14}C-MeSA for 48 h. The initial concentration of ^{14}C-MeSA in the 4-l air-tight glass chamber containing a single 5-week-old plant was 50 μg l^{-1}. The appearance of the molecular ion (*m/z* 140) of ^{14}C-SA in leaf extracts from ^{14}C-MeSA-treated leaves was confirmed by high-pressure liquid chromatography and liquid chromotography with mass spectrometry (LC-MS). We calculated that 93% of the SA extracted from tobacco leaves was made from gaseous ^{14}C-MeSA (Table 1).

Table 1 Methyl salicylate biosynthesis and metabolism in tobacco

Treatment	^{14}C atom % excess	Plant product	^{14}C atom % excess	Conversion (%)
^{14}C-SA (leaf infiltration)	91.67	MeSA	90.99	99.25
^{14}C-MeSA (as gas)	91.67	SA	85.51	93.28

Tobacco plants were either infiltrated into two leaves with ^{14}C-SA or gassed with ^{14}C-MeSA. ^{14}C-MeSA was prepared from 7-^{14}C SA (56 mCi mmol^{-1}; Du Pont-NEN) by methylation with diazomethane[21]. ^{14}C-labelled products (MeSA and SA) were quantified by mass spectrometry. The experiment was repeated twice with similar results.

Our data indicate that TMV-inoculated tobacco plants evolve sufficient amounts of gaseous MeSA to induce expression of PR proteins and TMV resistance in nearby healthy plants. It is known that systemic acquired resistance, in which pathogen-free parts of an infected plant become resistant to pathogen attack, depends on the systemic accumulation and possible phloem transport of SA[20,21]. We suggest that volatilization of MeSA, facilitated by tissue desiccation during necrosis, produces an airborne signal which functions as a vehicle for long-distance transport of SA within and between plants. In addition, the vascular translocation of MeSA, which is a liquid at room temperature, and benzoic acid, an immediate biosynthetic precursor of SA[21,22], may serve as back-up systems to ensure systemic accumulation of SA in the infected plant. We have observed an accumulation of large amounts of non-gaseous MeSA in TMV-inoculated leaves (data not shown). Thus, as suggested earlier[23,24], infected plants may produce other systemic signals in addition to SA. However, these signals may act by being converted to SA in target tissues. The aerial movement of MeSA also helps to explain the fact that systemic acquired resistance is observed in the leaves above and below the inoculated leaf[25].

To our knowledge, MeSA is the first airborne signal to be shown to be involved in communication between infected and healthy

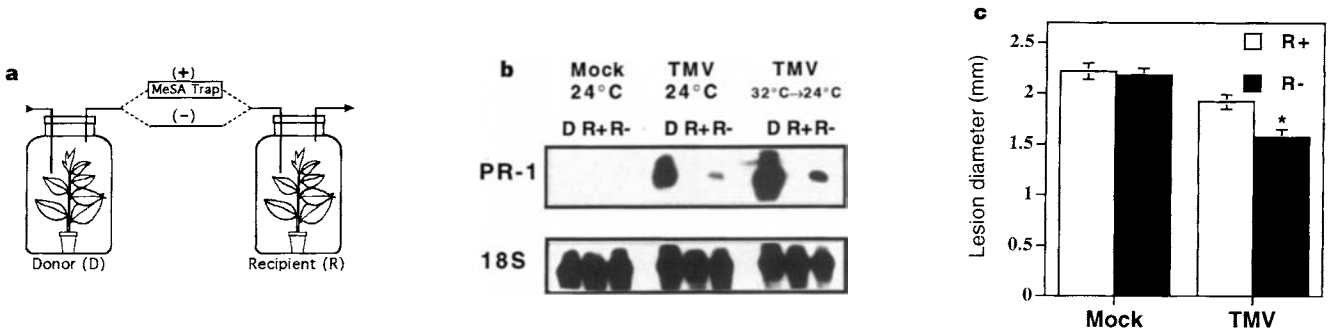

Figure 3 Induction of PR-1 gene expression and TMV resistance in healthy tobacco plants by gaseous products produced by TMV-inoculated plants. **a**, The two-compartment flow-through system. **b**, Northern blot analysis of PR-1 gene expression. Total RNA used for hybridization with a radioactive PR-1 cDNA probe was isolated from TMV- or mock-inoculated donor plants (D) and healthy recipient plants (R). **c**, Diameter of TMV-induced lesions on recipient plants 4 days after inoculation. After six days of exposure to air from donor plants, three recipient plants were inoculated on four middle leaves with TMV. The mean diameter of all lesions ± s.e. from 3 replicate recipient plants ($n = 3$) is shown. 'mock' and 'TMV' refer to the inoculation status of the donor plant; 32° → 24 °C, donor plants inoculated at 32 °C and shifted to 24 °C; + or − refers to the presence or absence of Tenax-TA trap between two chambers; asterisk indicates a statistically significant change compared with all other treatments (Student's *t*-test at $P = 0.01$). Mean lesion size in TMV (R+) treatment was not significantly different at $P = 0.01$ confidence level from either of two mock-inoculated treatments. The experiment was repeated twice with similar results.

plants. Although the significance of MeSA-mediated communication among field grown-plants is unknown, MeSA may accumulate inside dense canopies and exert a physiological effect. □

Methods

Extraction and quantification of SA. Tobacco (*Nicotiana tabacum* cv Xanthinc) seeds were germinated and grown as described[20]. Total SA (sum of free and glucosylsalicylic acid) was measured following the hydrolysis of leaf (0.5 g fresh weight) extracts with almond β-glucosidase (Sigma)[26]. SA concentrations in hydrolysed extract were determined by spectrofluorescence using HPLC[15]. All data were corrected for SA recovery.

Quantification of MeSA. Five-week-old tobacco plants were inoculated on two middle leaves with the U1 strain of TMV[20] and placed into a 1-l Wheaton purge-and-trap apparatus (Wheaton). Air filtered through activated charcoal was passed through the apparatus (40 ml per min flow rate) and volatiles were collected in a silylated glass-lined stainless-steel desorption tube (3.0 mm i.d. × 10 mm length; Scientific Instrument Services) packed with 100 mg of Tenax-TA resin (60/80 mesh; Scientific Instrument Services). D8-naphthalene was added to the absorbent traps as an internal standard. Trapped volatiles were analysed using a short-path thermal desorption system[27] (Scientific Instrument Services) connected to the injection port of a Varian 3040 gas chromatograph equipped with DB-5MS capillary column connected by a heated transfer line maintained at 280 °C to the ion source of a Finnigan-MAT 8230 high-resolution double-focusing magnetic sector mass spectrometer[21].

Liquid chromatography and mass spectrometry. LC-MS analysis was done on a Micromass Platform II LC-MS (Micromass, Altringham, UK) using negative ion atmosphere pressure chemical ionization (APCI). Cone voltage was 15 V and there was little or no fragmentation of molecular anions; source temperature was 150 °C and the APCI probe temperature was 350 °C. Data were analysed using Masslinx v.2.0 software.

RNA isolation and blot hybridization analysis. Tobacco PR-1 mRNA was detected with a radioactive probe prepared from the PR-1 cDNA by random priming (gift from E. Ward). Total leaf RNA (30 μg) was loaded in each lane and PR-1 transcripts were detected with tobacco PR-1 cDNA. As a loading control, blots were stripped and rehybridized with a probe for 18S rRNA (gift from R. Mittler).

Received 23 September; accepted 12 December 1996.

1. Buttery, R. G., Ling, L. C. & Wellso, S. G. *J. Agr. Food Chem.* **30,** 791–792 (1982).
2. Buttery, R. G., Kamm, J. A. & Ling, L. C. *J. Agr. Food Chem.* **32,** 254–256 (1984).
3. Buttery, R. G., Flath, R. A., Mon, T. R. & Ling, L. C. *J. Agr. Food Chem.* **34,** 820–822 (1986).
4. Kobayashi, A., Kubota, K. & Yano, M. in *Bioactive Volatile Compounds from Plants* (eds Teranishi, R., Buttery, R. G. & Sugisawa, H.) 49–56 (Am. Chem. Soc., Washington, 1993).
5. Buttery, R. G. & Ling, C. in *Bioactive Volatile Compounds from Plants* (eds Teranishi, R., Buttery, R. G. & Sugisawa, H.) 23–34 (Am. Chem. Soc., Washington, 1993).
6. Anderson, R. A. *et al. J. Agr. Food Chem.* **36,** 295–299 (1988).
7. Hill, N. G., Williams, N. H. & Dodson, C. H. *Biotropica* **4,** 61–68 (1972).
8. Dicke, M. *et al. J. Chem. Ecol.* **16,** 381–396 (1990).
9. Dicke, M., Sabelis, M. W., Takabayashi, J., Bruin, J. & Posthumus, M. A. *J. Chem. Ecol.* **16,** 3091–3118 (1990).
10. Ryals, J., Uknes, S. & Ward, E. *Plant Physiol.* **104,** 1109–1112 (1994).
11. Carr, J. P. & Klessig, D. F. in *Genetic Engineering, Principles and Methods* Vol. 11 (ed. Setlov, J. K.) 65–109 (Plenum, New York and London, 1989).
12. Malamy, J., Carr, J. P., Klessig, D. F. & Raskin, I. *Science* **250,** 1002–1004 (1990).
13. Malamy, J., Hennig, J. & Klessig, D. F. *Plant Cell* **4,** 359–366 (1992).
14. Kassanis, B. *Ann. Appl. Biol.* **39,** 358–369 (1952).
15. Leon, J., Yalpani, N., Raskin, I. & Lawton, M. A. *Plant Physiol.* **103,** 323–328 (1993).
16. Hamilton-Kemp, T. R. *et al. J. Chem. Ecol.* **14,** 789–796 (1988).
17. Robertson, G. W., Griffiths, D. W., MacFarlane Smith, W. & Batcher, R. D. *Phytochem. Anal.* **4,** 152–157 (1993).
18. Muller, S., Efer, J. & Engewald, W. *Chromatographia* **38,** 694–700 (1994).
19. Enyedi, A. J., Yalpani, N., Silverman, P. & Raskin, I. *Cell* **70,** 879–886 (1992).
20. Yalpani, N., Silverman, P., Wilson, T. M. A., Kleier, D. A. & Raskin, I. *Plant Cell* **3,** 809–818 (1991).
21. Shulaev, V., Leon, J. & Raskin, I. *Plant Physiol.* **103,** 315–321 (1993).
22. Yalpani, N., Leon, J., Lawton, M. A. & Raskin, I. *Plant Physiol.* **103,** 315–321 (1993).
23. Rasmussen, J. B., Hammerschmidt, R. & Zook, M. N. *Plant Physiol.* **97,** 1342–1347 (1991).
24. Ryals, J., Uknes, S. & Ward, E. *Plant Physiol.* **104,** 1109–1112 (1994).
25. Guedes, M. E. M., Richmond, S. & Kuc, J. *Physiol. Plant Path.* **17,** 229–233 (1980).
26. Enyedi, A. J., Yalpani, N., Silverman, P. & Raskin, I. *Proc. Natl Acad. Sci. USA* **89,** 2480–2484 (1992).
27. Hartman, T. G. *et al.* in *Flavor Measurements* (eds Ho, C.-T. & Manley, C. H.) 37–60 (Dekker, New York, Basel and Hong Kong, 1993).

Acknowledgements. We thank E. Ward for the PR-1 cDNA clone, R. Mittler for the 18S rRNA probe, and I. Chet, P. Day, M. A. Lawton, R. Mittler, M. Moynihan and R. Smith for discussion.

Correspondence and requests for materials should be addressed to I.R. (e-mail: raskin@aesop.rutgers.edu).

DNA antisense therapy for asthma in an animal model

Jonathan W. Nyce*† & W. James Metzger‡

* *Department of Molecular Pharmacology and Therapeutics, EpiGenesis Pharmaceuticals, Greenville, North Carolina 27834, USA*
‡ *Department of Medicine, Section of Allergy, Asthma and Immunology, and*
† *Department of Pharmacology, School of Medicine, East Carolina University, Greenville, North Carolina 27858, USA*

Asthma is an inflammatory disease characterized by bronchial hyper-responsiveness that can proceed to life-threatening airway obstruction. It is one of the most common diseases in industrialized countries, and in the United States accounts for about 1% of all healthcare costs[1]. Asthma prevalence and mortality have increased dramatically over the past decade[2], and occupational asthma is predicted to be the pre-eminent occupational lung disease in the next decade[3]. Increasing evidence suggests that adenosine, an endogenous purine that is involved in normal physiological processes, may be an important mediator of bronchial asthma[4–15]. In contrast to normal individuals, asthmatic individuals respond to adenosine challenge with marked airway obstruction[6,7], and concentrations of adenosine are elevated in the bronchoalveolar lavage fluid of asthma patients[9]. We performed a randomized crossover study using the dust mite-conditioned allergic rabbit model of human asthma. Administration of an aerosolized phosphorothioate antisense oligodeoxynucleotide targeting the adenosine A_1 receptor desensitized the animals to subsequent challenge with either adenosine or dust-mite allergen.

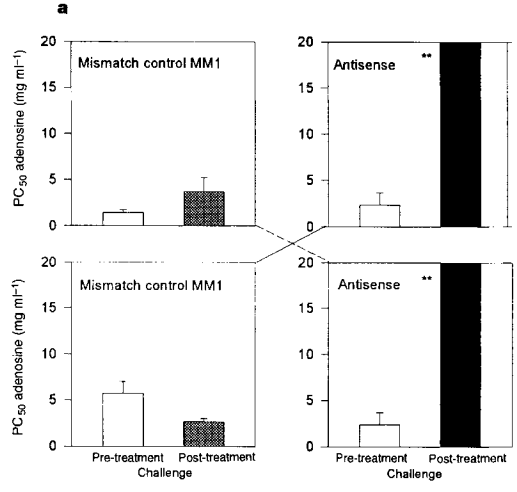

b

A_1 MM Control		PC50 Adenosine A_1 MM2 control		A_1AS	
Pre ODN	Post ODN	Pre ODN	Post ODN	Pre ODN	Post ODN
3.56 ± 1.02	3.25 ± 0.34	2.46 ± 0.50	2.81 ± 0.70	2.36 ± 0.68	>19.5 ±0.34**

Figure 1 a, Effects of adenosine A_1 receptor antisense ODN upon PC_{50} values in asthmatic rabbits. PC_{50} adenosine values were determined before and after intratracheal administration of aerosolized A_1AS or A_1MM to allergic rabbits. After a two-week rest period between parts of the experiment, rabbits were then crossed over, with those that had received A_1AS in the first part now receiving A_1MM, and those that had received A_1MM in the first part now receiving A_1AS. A_1MM2-treated animals were a separate group. **b**, Data summary. Results are presented as the mean ± s.e.m. Significance was determined by repeated-measures ANOVA and Tukey's protected *t*-test. Asterisks indicate a significant difference from all other groups, $P < 0.01$.

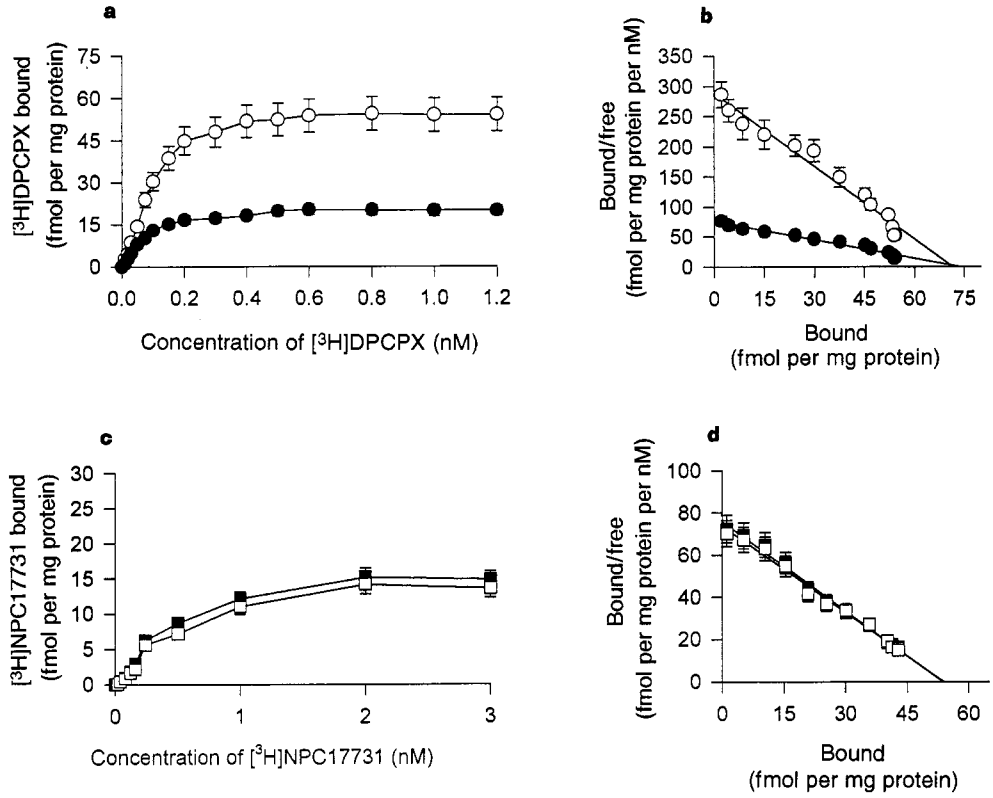

Figure 2 Specificity of action of adenosine A_1 receptor antisense ODN A_1AS. Airway smooth muscle tissue was dissected from rabbits administered a total of 20 mg A_1AS or A_1MM in four divided doses over 48 h. Plasma-membrane fractions were prepared. **a**, Saturation isotherm of [^{3}H]DPCPX binding to allergic rabbit lung plasma membrane from A_1AS- (filled circles) and A_1MM-treated (open circles) allergic rabbits showing an approximate 75% decrease in adenosine A_1 receptor number in airway smooth muscle from A_1AS-treated animals. **b**, Scatchard plot of saturation isotherm from **a** indicating a single class of binding sites; A_1AS (filled circles), A_1MM (open circles). **c**, Saturation isotherm of [^{3}H] NPC17731 binding to allergic rabbit lung plasma membrane from A_1AS- (open squares) and A_1MM-treated (filled squares) allergic rabbits showing no change in bradykinin B_2 receptor number in airway smooth muscle of A_1AS-treated animals. **d**, Scatchard plot of saturation isotherm from **c** indicating a single class of binding sites. A_1AS (open squares), A_1MM (filled squares). Error bars represent s.e.m.

Antisense oligodeoxynucleotides (ODNs) induce functional gene ablation by degenerating the template activity of specific target mRNAs[16,17]. We considered the lung to represent an excellent potential target for aerosolized antisense ODNs, for several reasons. The lung can be approached non-invasively and relatively specifically by inhaled aerosolized ODNs; it has a very large absorption surface (150 m^2 in the human); and it is lined with surfactant, a material that could potentially facilitate the pulmonary distribution and intracellular uptake of respired ODNs. In this regard, cationic lipids have been used to enhance cellular uptake of antisense ODNs[18,19], and dipalmitoylphosphatidylcholine, a major constituent of surfactant, is a zwitterionic lipid that can act as a weak cation at physiological pH. Indeed, a surfactant-based delivery system for transfection of airway cells with DNA has been described[20]. Other aspects of the physiology of surfactant, for example its high rate of recycling between the alveolar surface and the pulmonary epithelium[21], might also potentially facilitate pulmonary distribution and uptake of respired ODNs. We considered bronchial hyperresponsiveness in the allergic rabbit model of human asthma to be an excellent endpoint for antisense application because the tissues involved in this response lie near the point of contact with aerosolized ODNs, and the model closely simulates an important human disease. Furthermore, a serendipitous homology between the human and rabbit adenosine A_1 receptors centring on the initiation codon allowed us to use in the allergic rabbit model an antisense ODN (A_1AS) designed to target the human adenosine A_1 receptor mRNA.

In the first part of the experiment, four randomly selected allergic rabbits were administered A_1AS, and four were administered a mismatched control, A_1MM. On the morning of the third day, PC_{50} values (the concentration of aerosolized adenosine required to reduce the dynamic compliance of the bronchial airway 50% from the baseline value) were obtained and compared with PC_{50} values obtained for these animals before exposure to ODN. The experiment was repeated two weeks later in crossover fashion, with the animals previously treated with A_1AS now receiving the mismatched control A_1MM, and the animals previously treated with A_1MM now receiving A_1AS. Another group of four animals was administered a second mismatch control, A_1MM2. The results of this experiment are shown in Fig. 1. In both parts of the experiment, animals receiving the antisense ODN showed an increase of at least an order of magnitude in the dose of aerosolized adenosine required to reduce dynamic compliance of the lung by 50%. No effect of the mismatched control ODNs upon PC_{50} values was observed. A_1AS desensitized allergic rabbits to adenosine in a dose-dependent fashion over a range of 0.2, 2.0 and 20.0 mg total dose, and A_1MM was without effect over this same dose range.

When the crossover experiment was completed, airway smooth muscle was surgically dissected from all of the rabbits and processed for quantitative assessment of adenosine A_1 receptors. As a control for specificity of the antisense ODN, adenosine A_2 receptors and bradykinin B_2 receptors were also quantified. Rabbits treated with A_1AS in the crossover experiment had a nearly 75% decrease in A_1

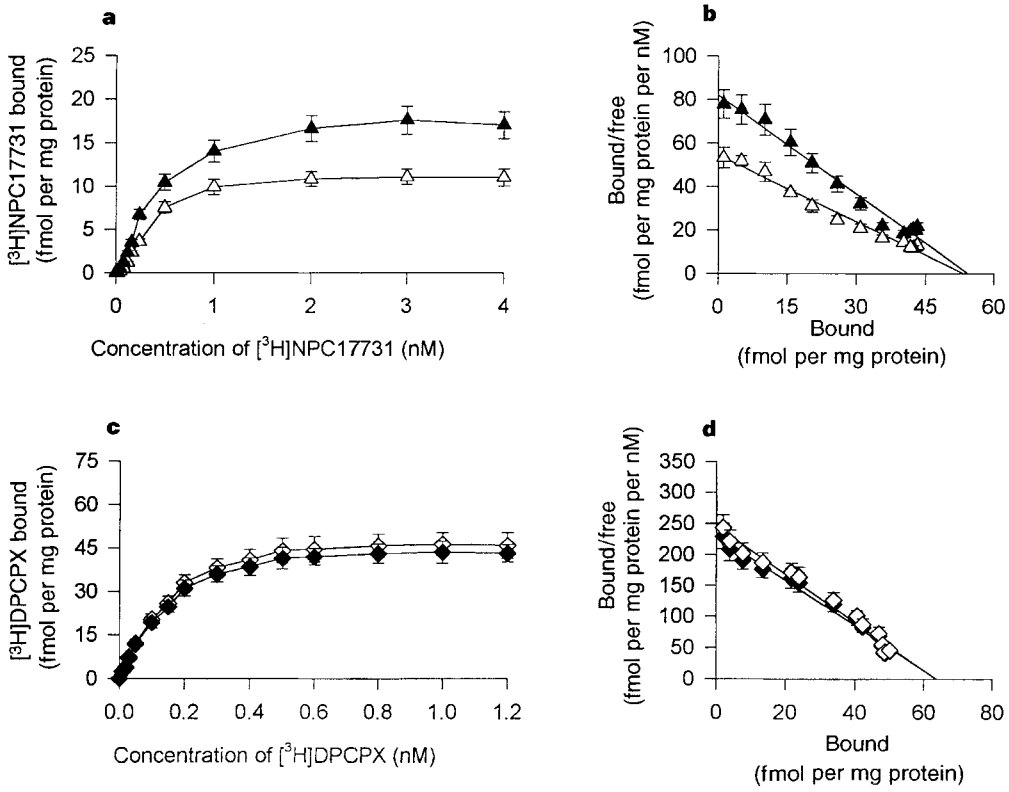

Figure 3 Specificity of action of bradykinin B_2 receptor antisense ODN B_2AS. Airway smooth muscle tissue was dissected from rabbits administered 20 mg B_2AS or B_2MM in four divided doses over 48 h. Plasma-membrane fractions were prepared. **a**, Saturation isotherm of [^{3}H]NPC17731 binding to allergic rabbit lung plasma membrane from B_2AS- (open triangles) and B_2MM-treated (filled triangles) allergic rabbits showing an approximate 40% decrease in bradykinin B_2 receptor number in airway smooth muscle from B_2AS-treated animals. **b**, Scatchard plot of saturation isotherm from **a** indicating a single class of binding sites; B_2AS (open triangles), B_2MM (filled triangles). **c**, Saturation isotherm of [^{3}H]DPCPX binding to allergic rabbit lung plasma membrane from B_2AS- (open diamonds) and B_2MM-treated (filled diamonds) allergic rabbits showing no change in adenosine A_1 receptor number. **d**, Scatchard plot of saturation isotherm from **c** indicating a single class of binding sites; B_2AS (open diamonds), B_2MM (filled diamonds).

receptor density compared with controls (Fig. 2), as assayed by specific binding of [^{3}H]-DPCPX. This effect occurred in a dose-dependent fashion over the range 0.2, 2.0 and 20.0 mg total dose. There was no change in adenosine A_2 receptor density, as assayed by specific binding of the A_2 receptor-specific ligand 2-[-p(2-carboxyethyl) - phenethylamino] - 5′- (N - ethylcarboxamido) adenosine (CGS-21680), or in bradykinin B_2 receptor density, as assayed by specific binding of the bradykinin B_2 receptor-specific ligand NPC17731, over this same dose range of A_1AS. Scatchard analysis of the binding isotherm of [^{3}H]-DPCPX to membranes prepared from bronchial smooth muscle isolated from allergic rabbits treated with 20 mg A_1AS yielded K_d and B_{max} values of 0.36 nM and 19 fmol mg^{-1} protein, respectively, compared with values of 0.34 nM and 52 fmol mg^{-1} protein, respectively, for rabbits treated with control A_1MM ODN (Fig. 2). This confirms that there is effective and selective attenuation by A_1AS of a single class of adenosine receptors of the A_1 type.

As a further control to demonstrate gene-specific effects in this model system, an antisense ODN targeting the bradykinin B_2 receptor (B_2AS) was administered as an aerosol to allergic rabbits under the same conditions as for A_1AS. Like adenosine, bradykinin is a potent bronchoconstrictor agent in asthmatic airways[22], and this effect is thought to be mediated through the B_2 receptor[23,24]. Aerosolized B_2AS specifically downregulated B_2 receptor binding by the B_2 receptor-specific ligand [^{3}H]-NPC17731 in airway smooth muscle of allergic rabbits (Fig. 3a, b). Neither adenosine A_1 nor A_2 receptor binding by their specific ligands was affected by B_2AS over the dose range 0.2, 2.0 and 20.0 mg. A minimally mismatched control molecule, B_2MM, was without effect on any receptor over this same dose range. Scatchard analysis of the binding isotherm of [H^3]-NPC17731 to membranes prepared from bronchial smooth muscle isolated from allergic rabbits treated with 20 mg B_2AS yielded K_d and B_{max} values of 0.38 nM and 8.7 fmol mg^{-1} protein, respectively, compared with values of 0.41 nM and 14.0 fmol mg^{-1} protein, respectively, for rabbits treated with control B_2MM ODN (Fig. 3). This confirms that there is specific attenuation by B_2AS of a single class of receptors of the B_2 type.

These results show that aerosolized A_1AS reached airway smooth muscle; reduced adenosine A_1 receptor number in this tissue in a dose-dependent manner; had no effect on either the adenosine A_2 or bradykinin B_2 receptors; and attenuated the bronchoconstrictor response to adenosine challenge in allergic rabbits. B_2AS provided further evidence of selective attenuation of target gene expression in this system, as it reduced bradykinin B_2 receptor number in airway smooth muscle in a dose-dependent manner, and was without effect on adenosine A_1 or A_2 receptors. Furthermore, all three mismatch control molecules (A_1MM, A_1MM2 and B_2MM), each minimally different from their corresponding antisense molecules, were completely without effect at any receptor at every dose tested. These results provide a clear demonstration of gene-specific antisense effects by aerosolized ODNs in the asthmatic rabbit lung (Table 1).

To assess further the role of the adenosine A_1 receptor in

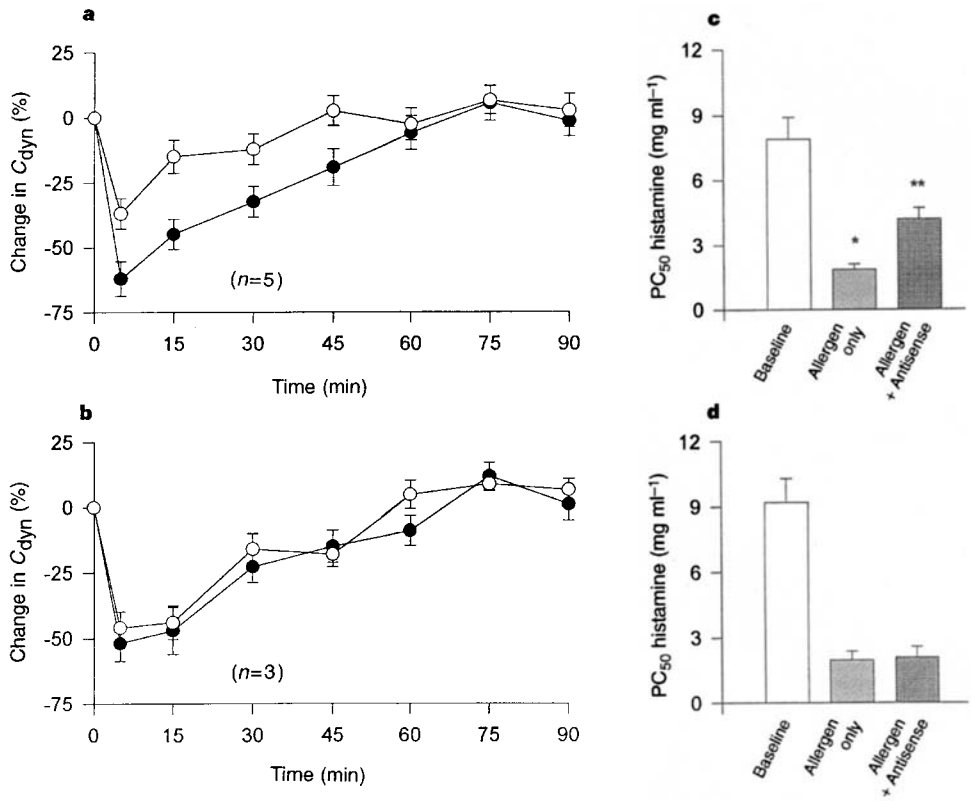

Figure 4 The effect of antisense and mismatch ODNs on allergen-induced airway obstruction and bronchial hyperresponsiveness in allergic rabbits. **a**, Effect of A_1AS antisense ODN on allergen-induced airway obstruction. Allergen only (filled circles); allergen + antisense (open circles). As calculated from the area under the curve, A_1AS significantly inhibited allergen-induced airway obstruction (55%, $P < 0.05$; repeated measures ANOVA and Tukey's *t*-test. **b**, Lack of effect of mismatch control A_1MM on allergen-induced airway obstruction. Allergen only (filled circles); allergen + antisense (open circles). **c**, Effect of A_1AS antisense ODN on allergen-induced bronchial hyperresponsiveness. As calculated from the PC_{50} histamine, A_1AS significantly inhibited allergen-induced bronchial hyperresponsiveness in allergic rabbits (61%, $P < 0.05$; repeated measures ANOVA and Tukey's *t*-test). **d**, Lack of effect of A_1MM mismatch control on allergen-induced bronchial hyperresponsiveness. Dynamic compliance (C_{dyn}) is the change in the volume of the lungs divided by the change in the alveolar-distending pressure during the course of a breath.

Table 1 Binding characteristics

Treatment	A_1 receptor		B_2 receptor	
A_1AS (mg)	K_d (nM)	B_{max} (fmol)	K_d (nM)	B_{max} (fmol)
20	0.36 ± 0.029	19 ± 1.52*	0.39 ± 0.031	14.8 ± 0.99
2	0.38 ± 0.030	32 ± 2.56*	0.41 ± 0.028	15.5 ± 1.08
0.2	0.37 ± 0.030	49 ± 3.43	0.34 ± 0.024	15.0 ± 1.06
A_1MM (mg)				
20	0.34 ± 0.027	52.0 ± 3.64	0.35 ± 0.024	14.0 ± 1.0
2	0.37 ± 0.033	51.8 ± 3.88	0.38 ± 0.028	14.6 ± 1.02
0.2	0.39 ± 0.027	48.3 ± 2.92	0.40 ± 0.032	15.7 ± 1.35
B_2AS (mg)				
20	0.36 ± 0.028	45.0 ± 3.15	0.38 ± 0.027	8.7 ± 0.62*
2	0.39 ± 0.035	44.3 ± 2.90	0.34 ± 0.024	11.9 ± 0.76**
0.2	0.40 ± 0.028	47.0 ± 3.76	0.35 ± 0.028	15.1 ± 1.05
B_2MM (mg)				
20	0.39 ± 0.031	42.0 ± 2.94	0.41 ± 0.029	14.0 ± 0.98
2	0.41 ± 0.035	40.0 ± 3.20	0.37 ± 0.030	14.8 ± 0.99
0.2	0.37 ± 0.029	43.0 ± 3.14	0.36 ± 0.025	15.1 ± 1.35
Saline control	0.37 ± 0.041	46.0 ± 5.21	0.39 ± 0.047	14.2 ± 1.35

Binding characteristics of the adenosine A_1-selective ligand [^{3}H]DPCPX and the bradykinin B_2-selective ligand [^{3}H]NPC 17731 in membranes isolated from airway smooth muscle of A_1 adenosine receptor and B_2 bradykinin receptor antisense- and mismatch-treated allergic rabbits. Treatment values refer to total ODN administered in four equivalently divided doses over a 48-h period. Significance was determined by repeated-measures ANOVA and Tukey's protected *t*-test; $N = 4$–6 for all groups. All assays were performed in triplicate.
* Significantly different from mismatch control- and saline-treated groups, $P < 0.001$.
** Significantly different from mismatch control- and saline-treated groups, $P < 0.05$.

mediating airway obstruction and bronchial hyperresponsiveness, allergic rabbits were administered A_1AS or control A_1MM followed by bronchoprovocation with house dust mite allergen (*Dermatophagoides farinae*). In the antisense ODN-treated allergic rabbits there was a 55% improvement in dynamic compliance and a 61% reduction in bronchial hyperresponsiveness in response to histamine challenge (Fig. 4).

These findings suggest that adenosine is an important mediator of both airway obstruction and inflammation, and that some portion of these effects are mediated through the pulmonary adenosine A_1 receptor in the asthmatic lung. They further indicate that the lung may have great potential as a target for antisense ODN-based disease intervention in asthma and related lung pathologies. □

Methods

Preparation of allergic rabbits. Neonatal New Zealand white Pasturella-free rabbit littermates were immunized intraperitoneally within 24 h of birth with 312 antigen units per 0.5 ml house dust mite (*D. farinae*) extract (Berkeley Biologicals) mixed with 10% kaolin[23,26]. Immunizations were repeated weekly for the first month and then every 2 weeks for the next 3 months. At 4 months of age, sensitized rabbits were prepared for aerosol administration[25].

Synthesis and design of antisense ODNs. Phosphorothioate ODNs were synthesized on an Applied Biosystems model 396 oligonucleotide synthesizer using tetraethylthiuram in acetonitrile as sulphurizing agent. Crude ODNs (trityl on) were purified using NENSORB chromatography (DuPont). The

sequence of A1AS was: 5′-GATGGAGGGCGGCATGGCGGG-3′. Two different mismatched ODNs were used as controls and had the sequences: A_1MM 5′-GTAGGTGGCGGGCAAGGCGGG-3′, and A_1MM2 5′-GATGGAGGCGGG-CATGGCGGG-3′. Sequence of B_2AS: 5′-GGTGATGTTGAGCATTTCGGC-3′; sequence of B_2MM: 5′-GGTGAT TTGAGGATTTCGGC-3′.

Administration of aerosolized antisense ODNs and assessment of pulmonary function. Aerosols of either adenosine (0–20 mg ml^{-1}) or antisense or mismatch ODNs (5 mg ml^{-1}) were generated by an ultrasonic nebulizer (Model 646, DeVilbiliss, Somerset, PA), producing aerosol droplets of which 80% were less than 5 μm in diameter. Aerosols were administered directly to the lungs through an intratracheal tube. Rabbits were selected at random, and on day 1 pretreatment values for PC_{50} were obtained for aerosolized adenosine challenge. Animals were subsequently administered aerosolized antisense or mismatch ODN through the intratracheal tube (5 mg in a volume of 1.0 ml), for 2 min, twice daily for 2 days (total dose, 20 mg). On the morning of the third day, post-treatment PC_{50} values were recorded (post-treatment challenge). For Fig. 1, $N = 7$ for mismatch control A_1MM; $N = 4$ for mismatch control A_1MM2; and $N = 8$ for A_1AS antisense ODN. A_1MM2 ODN-treated animals ($N = 4$) were analysed separately and were not part of the crossover experiment. In 6 of the 8 animals treated with antisense ODN and reported in Fig. 1, a PC_{50} value for adenosine could not be obtained up to the limit of solubility of adenosine, 20 mg ml^{-1}. For the purpose of calculation, PC_{50} values for these animals were set at 20 mg ml^{-1}. The values given therefore represent a minimum figure for antisense effectiveness; actual effectiveness was higher. Other groups of allergic rabbits ($N = 4$–6 for each group) were administered doses of 0.5 or 0.05 mg A_1AS or A_1MM in the manner and according to the schedule described above (total doses of 2.0 or 0.2 mg). A_1AS reduced sensitivity to applied adenosine in a dose-dependent manner over the dose range of 0.2 mg total dose (PC_{50} adenosine, 8.32 ± 7.2 mg), 2.0 mg total dose (PC_{50} adenosine 14.0 ± 2.7 mg), and 20 mg total dose (PC_{50} adenosine, 19.5 ± 0.34 mg). No change in PC_{50} adenosine values occurred in rabbits treated with A_1MM control ODN over the same dose range (PC_{50} adenosine, 2.51 ± 0.46 mg at 0.2 mg A_1MM; 3.13 ± 0.71 mg at 2.0 mg A_1MM; and 3.25 ± 0.34 mg at 20 mg A_1MM). Assessment of bronchial hyperresponsiveness using histamine aerosol (Fig. 4) was performed as previously described[25].

Receptor binding. Airway smooth-muscle tissue from tertiary bronchi of rabbits ($N = 4$–6 per group) administered 0.2, 2.0 or 20 mg A_1AS, A_1MM, B_2AS or B_2MM in four divided doses over 48 h was assessed for receptor content[12,26,27]. Protein content was determined as described[28]. No significant inter- or intra-group difference in adenosine A_2 receptor-specific [^{3}H]CGS-21680 binding was observed in airway smooth-muscle plasma membranes isolated from A_1AS-treated animals (specific binding of 2,125 ± 371 c.p.m. per mg protein at 0.2 mg A_1AS; 1,925 ± 370 c.p.m. per mg protein at 0.2 mg A_1AS; and 1,861 ± 281 c.p.m. per mg protein at 0.2 mg A_1AS); from A_1MM-treated animals (specific binding of 2,210 ± 395 c.p.m. per mg protein at 0.2 mg A_1MM; 2,010 ± 390 c.p.m. per mg protein at 0.2 mg A_1MM; and 1,731 ± 276 c.p.m. per mg protein at 0.2 mg A_1MM); from B_2AS-treated animals (specific binding of 2,015 ± 225 c.p.m. per mg protein at 0.2 mg B_2AS; 1,910 ± 342 c.p.m. per mg protein at 0.2 mg B_2AS; and 1,776 ± 349 c.p.m. per mg protein at 0.2 mg B_2AS); or from B_2MM-treated animals (specific binding of 1,914 ± 192 c.p.m. per mg protein at 0.2 mg B_2MM; 1,875 ± 316 c.p.m. per mg protein at 0.2 mg B_2MM; and 1,805 ± 327 c.p.m. per mg protein at 0.2 mg B_2MM). Statistical significance was assessed by repeated measures analysis of variance (ANOVA), and Tukey's *t*-test.

Received 28 October; accepted 17 December 1996.

1. Weiss, K. B., Gergen, P. J. & Hodgson, T. A. *New Engl. J. Med.* **326,** 862–866 (1992).
2. *MMWR-Morbidity and Mortality Weekly Report* **41,** 733–735 (1992).
3. Chan-Yeung, M. & Malo, J. L. *Eur. Respir. J.* **7,** 346–371 (1994).
4. Pauwels, R. A., Kips, J. C. & Joos, G. F. *Clin. Exp. Allergy* **21** (suppl.), 48–55 (1991).
5. Bjorck, T., Gustafsson, L. E. & Dahlen, S. E. *Am. Rev. Respir. Dis.* **145,** 1087–1091 (1992).
6. Church, M. K. & Holgate, S. T. *Trends Pharmacol. Sci.* **7,** 49–50 (1986).
7. Cushley, M. J., Tattersfield, A. E. & Holgate, S. T. *Br. J. Clin. Pharmacol.* **15,** 161–165 (1983).
8. Holgate, S. T., Church, M. K. & Polosa, R. *Ann. NY Acad. Sci.* **629,** 227–236 (1991).
9. Driver, A. G., Kukoly, C. A., Ali, S. & Mustafa, S. J. *Am. Rev. Respir. Dis.* **148,** 91–97 (1993).
10. Pauwels, R. A. & Joos, G. F. *Arch. Int. Pharmacodyn. Ther.* **329,** 151–160 (1995).
11. Ali, S., Mustafa, S. J. & Metzger, W. J. *Agents Actions* **37,** 165–176 (1992).
12. Ali, S., Mustafa, S. J. & Metzger, W. J. *J. Pharmacol. Exp. Ther.* **268,** 1328–1334 (1994).
13. Ali, S., Mustafa, S. J. & Metzger, W. J. *Am. J. Physiol.* **266,** L271–L277 (1994).
14. Cushley, M. J., Tattersfield, A. E. & Holgate, S. T. *Am. Rev. Respir. Dis.* **129,** 380–384 (1984).
15. Mann, J. S. & Holgate, S. T. *Br. J. Clin. Pharmacol.* **19,** 685–692 (1985).
16. Wagner, R. W. *Nature* **372,** 333–335 (1994).
17. Stein, C. A. & Narayanan, R. *Curr. Opin. Oncol.* **6,** 587–594 (1994).
18. Bennett, C. F., Chiang, M. Y., Chan, H., Shoemaker, J. E. & Mirabelli, C. K. *Mol. Pharmacol.* **41,** 1023–1033 (1992).
19. Saijo, Y., Perlaky, L., Wang, H. & Busch, H. *Oncol. Res.* **6,** 243–249 (1994).
20. Ross, G. F. *et al. Hum. Gene Ther.* **6,** 31–40 (1995).
21. Pison, U., Neuendank, M. A., Weissbach, S. & Pietschmann, S. *Eur. J. Clin. Invest.* **24,** 586–599 (1994).
22. Hulsmann, A. R., Raatgeep, H. R., Saxena, P. R., Kerrebijn, K. F. & de Tongate, J. C. M. *J. Respir. Crit. Care Med.* **150,** 1012–1018 (1994).
23. Tsukagoshi, H., Haddad, E. B., Barnes, P. J. & Chung, G. F. *J. Pharmacol. Exp. Ther.* **273,** 1257–1263 (1995).
24. Feletou, M. *et al. Eur. J. Pharmacol.* **274,** 57–64 (1995).
25. Metzger, W. J. in *Late Phase Allergic Reactions* (ed. Dorsch, W.) 347–362 (CRC Press, Boca Raton, FL, 1990).
26. Jarvis, M. F. *et al. J. Pharmacol. Exp. Ther.* **251,** 888–893 (1989).
27. Trifilieff, A., DaSilva, A., Landry, Y. & Gles, J. P. *J. Pharmacol. Exp. Ther.* **263,** 1377–1382 (1992).
28. Bradford, M. M. *Anal. Biochem.* **72,** 240–254 (1976).

Acknowledgements. We thank C. Welch, L. Gregg, C. Knox, S. Police, S. A. Leonard and V. A. Best for technical assistance.

Correspondence and requests for materials should be addressed to J.W.N. (e-mail: 104130.440@compuserve.com).

Mechanism of odorant adaptation in the olfactory receptor cell

Takashi Kurahashi* & Anna Menini†

* *National Institute for Physiological Sciences, Myodaiji, Okazaki 444, Japan, and Department of Biology, Osaka University, Toyonaka 560, Japan*
† *Istituto di Cibernetica e Biofisica, Consiglio Nazionale delle Ricerche, 16149 Genova, Italy*

Adaptation to odorants begins at the level of sensory receptor cells[1–5], presumably through modulation of their transduction machinery. The olfactory signal transduction involves the activation of the adenylyl cyclase/cyclic AMP second messenger system which leads to the sequential opening of cAMP-gated channels and Ca^{2+}-activated chloride ion channels[4–7]. Several reports of results obtained from *in vitro* preparations describe the possible molecular mechanisms involved in odorant adaptation; namely, ordorant receptor phosphorylation[8,9], activation of phosphodiesterase[10], and ion channel regulation[11–14]. However, it is still unknown whether these putative mechanisms work in the intact olfactory receptor cell. Here we investigate the nature of the adaptational mechanism in intact olfactory cells by using a combination of odorant stimulation and caged cAMP photolysis[15] which produces current responses that bypass the early stages of signal transduction (involving the receptor, G protein and adenylyl cyclase). Odorant- and cAMP-induced responses showed the same adaptation in a Ca^{2+}-dependent manner, indicating that adaptation occurs entirely downstream of the cyclase. Moreover, we show that phosphodiesterase activity remains constant during adaptation and that an affinity change of the cAMP-gated channel for ligands accounts well for our results. We conclude that the principal mechanism underlying odorant adaptation is actually a modulation of the cAMP-gated channel by Ca^{2+} feedback.

We investigated adaptation to odorant stimuli in single, dissociated olfactory receptor cells using whole-cell recording. An odorant pulse was applied to the cell and followed by a second pulse of the same intensity and duration (Fig. 1a). As reported previously[2], the peak amplitude of the response to the second pulse was small for short interpulse intervals but recovered as the interpulse interval increased.

When double-pulse experiments were repeated at +100 mV, or in a solution of low Ca^{2+} concentration at −50 mV, there was no significant difference between the first and second response to odorants (data not shown), indicating that Ca^{2+} entering the cell

was responsible for the current reduction, which is consistent with previous experiments[2] in which external Ca^{2+} removal almost completely abolished the response decay during a long odorant step (see also ref. 16).

Sensory adaptation is defined as a shift of the dynamic response range due to the conditioning or background stimuli (see ref. 7 for example), which allows the cell to work over a broad range of stimulus intensities. This property might be especially important in olfactory cells because the dynamic range of single olfactory cells under control conditions is extremely narrow, spanning only about 1.2 log units of stimulus intensity[17]. We therefore examined whether the current reduction observed in double-pulse experiments is actually a change of the dynamic range or a reduction of the maximum current (I_{max}). In the presence of a conditioning pulse, a higher dose of odorant was necessary to induce a response of the same size as the control response (Fig. 1b, c) and there was little difference in I_{max}. The shift of the dose–response relation induced by the conditioning pulse is shown in Fig. 1d. Comparing data from various cells, we found that, as previously shown[3,17], different olfactory cells are variable in their dose–response curves, with $K_{1/2}$ values (the concentration of cAMP producing half-maximal current) differing by as much as an order of magnitude. However, by comparing dose–response relations obtained in the same cell, we consistently found that the dose–response curve in the adapted state was always shifted towards a higher odorant dose with respect to that in the control state (3 cells).

To investigate whether the response reduction in the adapted state was due to a reduction in the cAMP production by the odorant-induced enzymatic cascade or to some other mechanism, we first performed the experiments shown in Fig. 2, using a pulse of odorant followed by photolysis of caged cAMP. The current induced by an odorant pulse was measured (Fig. 2a) and the intensity and duration of an ultraviolet-light-photolysing caged cAMP loaded in the ciliary cytoplasm (see 7Methods) was adjusted to produce a current of similar magnitude and time course as that caused by the odorant stimulus (Fig. 2a). The odorant pulse was then applied to the cell, followed shortly afterwards by ultraviolet light (Fig. 2b) which causes the photolysis of caged cAMP to produce rapid and repeatable increments in cAMP concentration. Therefore if the adaptation shown in Fig. 1 was due to a reduction in cAMP production, a current reduction would not be expected in the photolysis response. If, on the other hand, the molecular target for adaptation is located at a downstream point in the transduction cascade, the current reduction should be similar to that in experiments with double pulses of odorant. As shown in Fig. 2b, the caged cAMP response was reduced to about the same level as in the second odorant response. It has been shown that in the olfactory cell the total current induced by photolysis of caged cAMP, due to the sequential opening of cAMP-gated channels and Ca^{2+}-activated Cl^- channels, is highly cooperative[18] (see 7Methods). Through this strong nonlinear amplification, even a small change in cAMP concentration will produce a large change in the current response. Therefore the similarities observed in the experiments shown in Fig. 2b strongly indicate that odorant-induced cyclase activity was not significantly affected in the adapted state. To obtain more quantitative information about adaptation, experiments like those in Fig. 1 were repeated by stimulating the cell previously loaded with caged cAMP, with double flashes of ultraviolet light instead of odorants

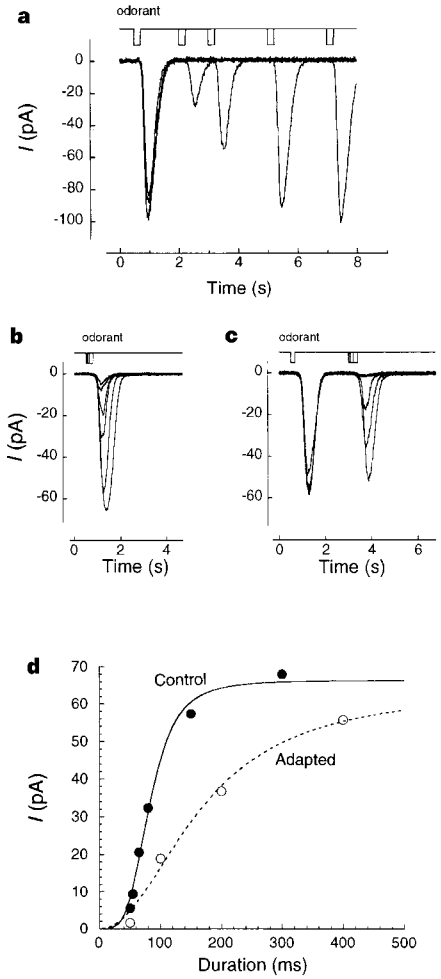

Figure 1 Odorant adaptation observed in a solitary olfactory receptor cell. **a**, Response reductions by a conditioning pulse and their recovery. Pulses of the odorant amyl acetate at the same concentration and duration were applied to the cell at intervals of 1.5, 2.5, 4.5 and 6.5 s. Membrane potential (V_h), −50 mV. **b**, Dose dependence of the odorant-induced current. Stimulus duration was changed while the odorant concentration was kept constant; $V_h = -50$ mV. **c**, Dose dependence of the odorant-induced current during adaptation. Conditioning odorant pulse was kept constant while the second pulse was changed in duration and applied 2.5 s after the first pulse; the cell was the same as in **b**. **d**, Relations between stimulus and response of an isolated olfactory receptor cell under control (filled circles) and adapted (open circles) conditions. Peak currents for the traces shown in **b** and **c** were plotted versus duration of the odorant stimulus. Data were fitted by the Hill equation ($I = I_{max}t^n/(t^n + K_{1/2}^n)$) with the following parameters: $I_{max} = 66$ pA, $n = 3.9$, $K_{1/2} = 82$ ms in control, and $I_{max} = 64$ pA, $n = 2.1$, $K_{1/2} = 167$ ms in the adapted state.

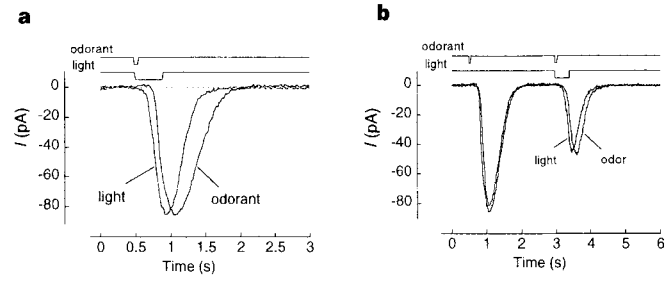

Figure 2 Reduction of current induced by photolysis of caged cAMP by an odorant-conditioning pulse. Caged cAMP was included in the recording pipette. $V_h = -50$ mV. **a**, Responses to odorant stimulation and photolysis of caged cAMP in the same cell. Current traces were superimposed by adjusting both stimuli to the same starting points; UV intensity was saturating. Odorant response had a delay of ~200 ms, probably owing to the enzymatic cascade (see also ref. 18). **b**, Reduction of photolysis and odorant responses by a conditioning odorant pulse. Note that the current induced by photolysis of caged cAMP is reduced by the same amount as the odorant response.

(Fig. 3). In these experiments, cAMP production is entirely controlled by the intensity and duration of the ultraviolet flash both during the first and second stimulus. The response reduction in double-flash experiments (Fig. 3) was very similar to that measured with double-odorant pulses (Fig. 1), again confirming that adaptation is regulated downstream of the cyclase. The reduced current recovered with increasing interstimulus intervals (Fig. 3a). Responses to flashes of the same intensity and duration in the same cell were highly reproducible, as shown by the almost perfect superimposition of photolysis responses on the left of Fig. 3a (3 responses) and Fig. 3c (6 responses). Dose–response relations were obtained by measuring the peak current as a function of flash duration both in control and adapted conditions (Fig. 3b–d). It can be seen that the olfactory cell is less sensitive in the adapted state because a longer ultraviolet flash was necessary to elicit the same peak response as the control response (Fig. 3c, d). Even under adaptation, however, it was possible to reach the same I_{max} value. Different cells tested in the same conditions showed variability in the $K_{1/2}$ of their dose–response relations, as previously shown[18]. However, dose–response relations in the adapted state were always shifted towards longer ultraviolet flashes compared to the control state. The relative shift for each curve was measured as the ratio between $K_{1/2}$ in the adapted and in the control state and the mean value was 2.1 ± 0.7 (mean ± s.d.; 3 cells). Mean values for Hill coefficients were 4.4 ± 1.6 and 3.6 ± 0.7 for control and adapted state, respectively. Thus the general properties of odorant adaptation

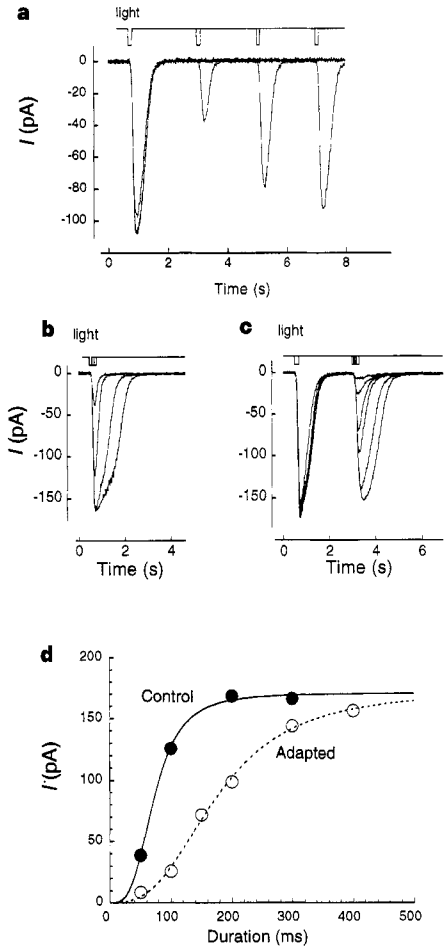

Figure 3 a, Reduction of photolysis responses by a conditioning UV flash and its recovery time course. Two identical saturating UV flashes were applied to the cilia at intervals of 3, 5 and 7 s. $V_h = -50$ mV. Caged cGMP was included in the recording pipette. **b**, Change in the relation between stimulus and response. The duration of the light stimulation was changed while the intensity was fixed to a saturating intensity; the cell was different from that in **a**. Caged cAMP was in the patch pipette and V_h was -50 mV. **c**, Duration dependence of the photolysis response in the presence of a conditioning UV flash. The cell and the protocol were as in **b**, except that the light conditioning pulse was applied 2.5 s before the test flashes. $V_h = -50$ mV. **d**, Peak currents were plotted as a function of flash duration from the experiments shown in **b** and **c**. Filled circles, control condition; open circles, adapted conditions. The best fit of the Hill equation to the data gave the following values: $I_{max} = 171$ pA, $n = 3.3$, $K_{1/2} = 73$ ms in the control; $I_{max} = 173$ pA, $n = 2.8$, $K_{1/2} = 175$ ms in the adapted state.

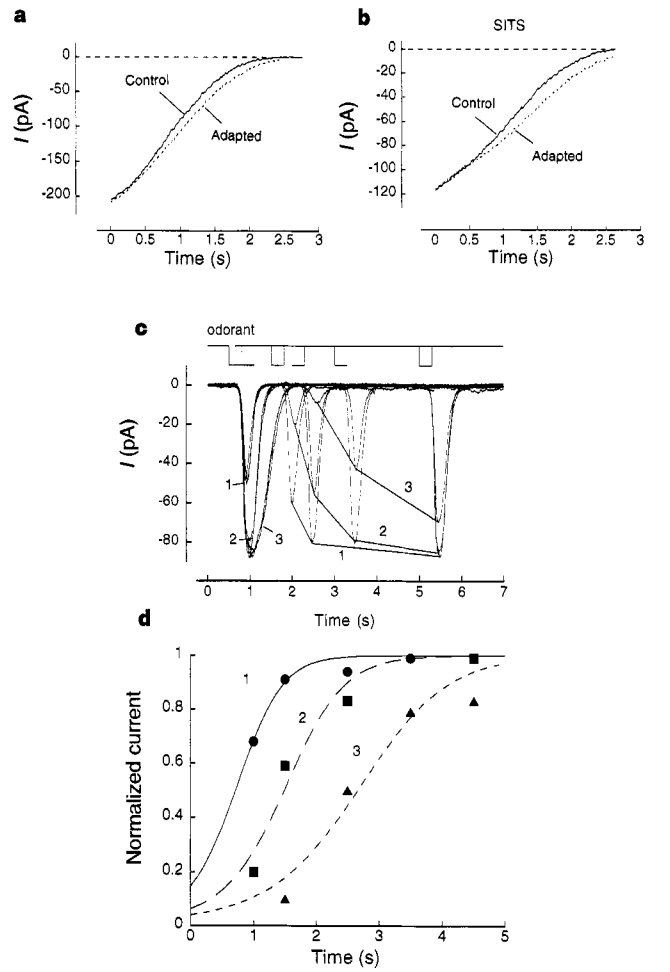

Figure 4 a, Change of the falling phase from the saturating light-induced response under the control and adapted state (caged cGMP). A double sequential flash was applied to a cell with different light duration. Each duration was chosen to induce a saturating current with the shortest exposure; $V_h = -80$ mV. **b**, Same experiments as in **a**, in the presence of 3 mM SITS and using the same cell. **c**, Response reduction and recovery after three different doses of odorant conditioning pulses were measured in the same cell; $V_h = -50$ mV. The odorant concentration and duration (300 ms) of the second pulse were kept constant. Peak amplitude of the adapted responses induced after a conditioning pulse of the same duration, 150, 300 or 600 ms, are connected by lines numbered 1, 2 and 3, respectively. **d**, Fitting of current recovery by using the Ca^{2+}-calmodulin effect on the cAMP-gated channel (see Methods). Normalized peak amplitude of the responses was plotted against the time after the conditioning pulses. Continuous lines were obtained from the best fit of equation (3) to the data using the following parameters: Ca_{in} 4.9, 5.9, 6.6 μM, and τ_{Ca} 2.4, 3.1, 4.6 s for traces 1, 2 and 3 respectively. This is the same cell as in **c**, with some additional data points.

(Fig. 1) and of photolysis adaptation (Fig. 3) are very similar, suggesting that the underlying mechanisms are the same.

The results shown in Figs 1–3 demonstrate that the principal mechanisms for odorant adaptation are localized downstream of the cyclase. As cAMP directly gates a cationic channel, other possible mechanisms of olfactory adaptation could involve an enhanced activity of the phosphodiesterase (PDE) that hydrolyses cAMP or an altered ligand affinity of cAMP-gated channels. To discriminate between these two possibilities, we first examined the falling phase of saturating current responses after the cessation of light stimuli. When the production of cAMP is stopped by the termination of the ultraviolet flash, cytoplasmic cAMP concentration will be reduced with time by the action of cytoplasmic PDE, and the current decay can be used to test the state of PDE activation. If enhancement of PDE activity is the major mechanism for adaptation, the reduction in cAMP concentration will be faster in the adapted state compared to that in the control state. If, on the other hand, PDE activity is not significantly changed during the adapted state and a decrease in channel affinity for cAMP is the major mechanism for adaptation, the falling phase in the adapted state will be similar, or even delayed, with respect to that in the control condition. Figure 4a shows that the latter is the case because the falling phase in the adapted state was slightly delayed compared to that in the control state. Several cells showed an even longer delay. The delay was measured as the difference between the time at which the adapted and control response decayed to 50% of the peak current. The time shift had a mean of 204 ± 126 ms (± s.d.; 13 measurements in 7 cells). To rule out the possibility that the Ca^{2+}-activated Cl^- current could be responsible for the different falling phase, the same experiment was repeated in the presence of the Cl^- channel blocker 4-acetamido-4′-isothiocyanato-stilbene-2,2′-disulphonic acid (SITS). Figure 4b shows that the falling phase of the current in the adapted state was also slightly prolonged in the presence of SITS.

A different type of experiment was also done to investigate further the role of PDE in adaptation. It has been shown[19] that the introduction of cAMP into the cell by free diffusion from the patch pipette causes an inward current. In these experiments, at 0.5 mM cAMP the current reached a peak and then decayed, reaching a sustained value that was about 4% of the peak current with a half-decay time of 2.3 ± 1.4 s (6 cells)[19]. It has been thought that this decaying time course represents adaptation of the cell. We repeated the same type of experiment with a non-hydrolysable analogue of cAMP, 8Br-cAMP. When 8Br-cAMP diffused into the cell from the patch pipette, a current was induced with a very similar time course to that induced by cAMP introduction. The current in 0.5 mM 8Br-cAMP decayed to 10 ± 8% (3 cells) of its peak value, with a half-decay time of 3.2 ± 1.1 s. These results also confirm that the contribution of PDE to odorant adaptation is likely to be small, and therefore the main mechanism of adaptation is likely to be located at the channel level.

It has been reported[13] that Ca^{2+}-calmodulin changes the apparent affinity of the cAMP-gated channel for ligands. We therefore investigated whether known parameters for the effect of Ca^{2+}-calmodulin can quantitatively describe the measured properties of odorant adaptation. In the hypothesis that olfactory adaptation is entirely regulated by Ca^{2+}-calmodulin modulation of the cAMP-gated channel, the recovery of the adapted peak current as a function of time could be described by equation (3) (see 7Methods) with only two free parameters: Ca_{ini}, the cytoplasmic Ca^{2+}-calmodulin concentration determined by the conditioning pulse, and τ_{Ca}, the time constant for exponential Ca^{2+} decay. From double-odorant pulse experiments like those shown in Fig. 1a, the peak current of the adapted responses was measured and normalized, then plotted against the interpulse time interval; data from several individual cells were fitted by equation (3). Mean values of the free parameters obtained for the best fit were: 5.1 ± 1.0 μM for Ca_{ini} and 6.8 ± 4.1 s for τ_{Ca} (± s.d.; 7 measurements in 5 cells). Figure 4c shows double-odorant pulse experiments obtained from a cell which was exceptionally stable for a long time, allowing direct quantitative comparison of adaptation properties using different odorant doses in the first pulse to change Ca^{2+} concentrations in the cell. The second odorant pulse was kept constant in all the experiments. The recovery of the peak current as a function of time was faster when the odorant dose of the first pulse was smaller (Fig. 4d). From the best fit of equation (3) to the data, Ca_{ini} due to the first pulse was estimated to increase in this cell from 4.9 to 6.6 μM as the odorant dose increased. All results fitted well with the theoretical curve, the physiological parameters strongly supporting the idea that the principal means of adaptation to odorants is by modulation of the cAMP-gated channel.

Vertebrate photoreceptors use a similar enzymatic cascade for light transduction (for reviews, see refs 7, 20). The cGMP-gated channel could also be modulated by Ca^{2+}-calmodulin[21], but its contribution to light adaptation appears to be negligible, with the predominant molecular mechanisms being the modulation by Ca^{2+} of guanylyl cyclase and phosphodiesterase (for review, see ref. 22). It has been shown that PDE modulation requires, at least in part, proteins that inhibit receptor phosphorylation, which are different in rods (S-modulin or recoverin)[23,24] and cones (visinin)[25,26]. As olfactory transduction involves hundreds or even thousands of receptor proteins[27], a mechanism similar to that of visual adaptation may need many different proteins to regulate receptor phosphorylation. If odorant adaptation is mainly regulated at the channel level, the same effect will be present in cells expressing different receptor proteins. Moreover, the high amplification caused by cAMP-gated and Ca^{2+}-activated Cl^- channels and the large Ca^{2+}-calmodulin modulation makes regulation at the channel level a very sensitive control mechanism. □

Methods

Electrophysiological recordings. Solitary receptor cells were enzymatically dissociated from the olfactory epithelium of the newt *Cynops pyrrhogaster*, and currents were recorded in the whole-cell voltage-clamp mode as described[28]. The intracellular pipette solution contained (in mM): 103, CsCl; 5, EGTA; 10, HEPES (pH adjusted to 7.4 with CsOH). Cells were bathed in Ringer solution. All experiments were performed at room temperature (23–25 °C). For odorant stimuli, amylacetate (1 μl ml^{-1}) was dissolved in Ringer solution, included into a puffer pipette and applied using pressure ejection in a pressure-regulation system developed in our laboratory. The timings of the pressure pulses are shown above the current traces in the figures. Results were reproducible in more than three different preparations.

Photolysis of caged cyclic nucleotides. Caged cAMP or caged cGMP (Dojin, Japan) was dissolved in dimethylsulphozide (DMSO) at 100 mM and stored frozen at − 20 °C. The stock solution was diluted in the pipette solution to a final concentration of 100 μM–1 mM. UV flashes were applied to the cell through an epifluorescent system. A 100 W mercury or 100 W xenon lamp was used to induce photolysis. We could detect little difference in current responses induced by these light sources. The timing and duration were regulated by a mechanical shutter and the light intensity was specified by a wedge filter under computer control. The light source was mechanically isolated from the inverted microscope to avoid transmission of vibrations. Flashes were always applied to cover only the ciliary region. There was no difference in results between caged cAMP and caged cGMP, except for a slightly higher sensitivity to cGMP. A higher sensitivity of olfactory cyclic-nucleotide-gated channels to cGMP compared with cAMP has been found in inside-out membrane patch preparations[29,30]. The timing of the UV flashes is shown above the current traces in the figures. In double-flash experiments, the possibility of caged cAMP depletion in the cilia during the second flash was excluded, because at +100 mV photolysis responses showed exactly the same waveform and peak amplitude in the control and in the adapted state. Also, the possibility that the current reduction was due to Cl^- depletion in the cilia was excluded, because even in the adapted state (see, for example Fig. 3d) it was possible to reach the same maximum current as in the control response, which contains a significant

fraction of Cl^-. Moreover, current reductions with similar properties were observed in the presence of a selective Cl^{-1} channel blocker (3 mM SITS).

Theory. The whole-cell current induced by photolysis of caged cAMP can be described by the Hill equation[18], with an apparent cooperativity of the cAMP-induced current that is much higher than that measured in excised patches. This higher cooperativity is due to the Cl^- component of the whole-cell current. We obtained an average Hill coefficient of 4.6 ± 1.6 in our preparation (7 cells). Therefore the total whole-cell current is described by the Hill equation $I = I_{max}c^n/(c^n + K_{1/2}^n)$, where I is the current, I_{max} is the maximal current, c is the cAMP concentration, n is the Hill coefficient, and $K_{1/2}$ is the concentration of cAMP producing half of the maximal current. Moreover, Chen and Yau[13] have shown that Ca^{2+}-calmodulin directly modulates the olfactory cAMP-gated channel to produce a maximal 20-fold increase in $K_{1/2}$. This effect is described by the following equation:

$$K_{1/2} = K_{max}\frac{Ca^m}{Ca^m + K_{d_{Ca}}^m} \quad (1)$$

where K_{max} is the maximal value for $K_{1/2}$, Ca is the activity of Ca^{2+} available for calmodulin, m is the Hill coefficient, and $K_{d_{Ca}}$ is the Ca^{2+} concentration producing a half-maximal increase in $K_{1/2}$.

In the intact cell, the cytoplasmic Ca^{2+}-calmodulin concentration in the cilia is unknown, and it is assumed to decay exponentially:

$$Ca = Ca_{ini}\,e^{-t/\tau_{Ca}} \quad (2)$$

where τ_{Ca} is the time constant, and Ca_{ini} is the cytoplasmic Ca^{2+}-calmodulin concentration determined by the conditioning pulse.

The amplitude of the adapted odorant responses can be described by substituting equations (1) and (2) into the Hill equation:

$$\frac{I}{I_{max}} = \frac{c^n}{c^n + \left[K_{max}\frac{(Ca_{ini}e^{-t/\tau_{Ca}})^m}{(Ca_{ini}e^{-t/\tau_{Ca}})^m + K_{d_{Ca}}^m}\right]^n} \quad (3)$$

For our calculations, we adopt $n = 4.6$ as explained above (see also ref. 18); $K_{max} = 64\ \mu M$, $K_{d_{Ca}} = 7.1\ \mu M$, $m = 1.8$ (from ref. 13) and $c = 15\ \mu M$ as the concentration of cAMP estimated to produce 90% of the maximal current (from ref. 13; see also ref. 29). Ca_{ini} and τ_{Ca} are unknown parameters determined from the best fit of equation (3) to the data (see legend to Fig. 4d).

Received 14 October; accepted 18 December 1996.

1. Getchell, T. V. & Shepherd, G. M. *J. Physiol. (Lond.)* **282,** 541–560 (1978).
2. Kurahashi, T. & Shibuya, T. *Brain Res.* **515,** 261–268 (1990).
3. Firestein, S., Shepherd, G. M. & Werblin, F. S. *J. Physiol. (Lond.)* **430,** 135–158 (1990).
4. Reed, R. R. *Neuron* **8,** 205–209 (1992).
5. Breer, H. *et al.* in *Sensory Transduction* (eds Corey, D. P. & Roper, S. D.) 93–108 (Rockefeller Univ. Press, New York, 1992).
6. Kurahashi, T. & Yau, K.-W. *Curr. Biol.* **4,** 256–258 (1994).
7. Torre, V., Ashmore, J. F., Lamb, T. D. & Menini, A. *J. Neurosci.* **15,** 7757–7768 (1995).
8. Boekhoff, I. & Breer, H. *Proc. Natl Acad. Sci. USA* **89,** 471–474 (1992).
9. Boekhoff, I., Schleicher, S., Strotmann, J. & Breer, H. *Proc. Natl Acad. Sci. USA* **89,** 11983–11987 (1992).
10. Borisy, F. F. *et al. J. Neurosci.* **12,** 915–923 (1992).
11. Kramer, R. H. & Siegelbaum, S. A. *Neuron* **9,** 897–906 (1992).
12. Lynch, J. W. & Lindemann, B. *J. Gen. Physiol.* **103,** 87–106 (1994).
13. Chen, T.-Y. & Yau, K. W. *Nature* **368,** 545–548 (1994).
14. Balasubramanian, S., Lynch, J. W. & Barry, P. H. *J. Membr. Biol.* **152,** 13–23 (1996).
15. Nerbonne, J. M., Richard, S., Nargeot, J. & Lester, H. *Nature* **310,** 74–76 (1984).
16. Zufall, F., Shepherd, G. M. & Firestein, S. *Proc. R. Soc. Lond. B* **246,** 225–230 (1991).
17. Firestein, S., Picco, C. & Menini, A. *J. Physiol. (Lond.)* **468,** 1–10 (1993).
18. Lowe, G. & Gold, G. H. *Nature* **366,** 283–286 (1993).
19. Kurahashi, T. *J. Physiol. (Lond.)* **430,** 355–371 (1990).
20. Lamb, T. D. & Pugh, E. N. *Trends Neurosci.* **15,** 291–298 (1992).
21. Hsu, Y.-T. & Molday, R. S. *Nature* **361,** 76–79 (1993).
22. Koutalos, Y. & Yau, K.-W. *Trends Neurosci.* **19,** 73–81 (1996).
23. Kawamura, S. & Murakami, M. *Nature* **349,** 420–423 (1991).
24. Kawamura, S. *Nature* **362,** 855–857 (1993).
25. Yamagata, K., Goto, K., Kuo, C.-H., Kondo, H. & Miki, N. *Neuron* **2,** 469–476 (1990).
26. Kawamura, S. *et al. J. Biol. Chem.* **271,** 21359–21364 (1996).
27. Buck, L. & Axel, R. *Cell* **65,** 175–187 (1991).
28. Kurahashi, T. *J. Physiol. (Lond.)* **419,** 177–192 (1989).
29. Nakamura, T. & Gold, G. H. *Nature* **325,** 442–444 (1987).
30. Kurahashi, T. & Kaneko, A. *NeuroReport* **2,** 5–8 (1991).

Acknowledgements. We thank S. Firestein, G. H. Gold, A. Kaneko, Y. Koutalos, T. D. Lamb and V. Torre for comments on the manuscript; R. Isogai for secretarial assistance; and Y. Ito, K. Kato, H. Maebashi, J. Ohashi and N. Yamaguchi for technical support. This work was partially supported by a Fellowship from the Japan Society for Promotion of Science and research grants from the European Community, from the Human Frontier Science Program and from the Japanese Ministry of Education.

Correspondence and requests for materials should be addressed to T.K. (e-mail: kurahasi@nips.ac.jp).

A metalloproteinase disintegrin that releases tumour-necrosis factor-α from cells

Roy A. Black, Charles T. Rauch, Carl J. Kozlosky, Jacques J. Peschon, Jennifer L. Slack, Martin F. Wolfson, Beverly J. Castner, Kim L. Stocking, Pranitha Reddy, Subhashini Srinivasan, Nicole Nelson, Norman Boiani, Kenneth A. Schooley, Mary Gerhart, Raymond Davis, Jeffrey N. Fitzner, Richard S. Johnson, Raymond J. Paxton, Carl J. March & Douglas Pat Cerretti

Immunex Corporation, 51 University Street, Seattle, Washington 98101, USA

Mammalian cells proteolytically release (shed) the extracellular domains of many cell-surface proteins[1]. Modification of the cell surface in this way can alter the cell's responsiveness to its environment[2] and release potent soluble regulatory factors[3]. The release of soluble tumour-necrosis factor-α (TNF-α) from its membrane-bound precursor[4,5] is one of the most intensively studied shedding events because this inflammatory cytokine is so physiologically important[6,7]. The inhibition of TNF-α release (and many other shedding phenomena) by hydroxamic acid-based inhibitors indicates that one or more metalloproteinases is involved[3,8,9]. We have now purified and cloned a metalloproteinase that specifically cleaves precursor TNF-α. Inactivation of the gene in mouse cells caused a marked decrease in soluble TNF-α production. This enzyme (called the TNF-α-converting enzyme, or TACE) is a new member of the family of mammalian adamalysins (or ADAMs)[10], for which no physiological catalytic function has previously been identified. Our results should facilitate the development of therapeutically useful inhibitors of TNF-α release, and they indicate that an important function of adamalysins may be to shed cell-surface proteins.

Soluble TNF-α is released by cleavage of the precursor at the Ala76-Val77 bond, and we have previously shown that TACE cleaves a 12-residue peptide spanning this site with the same specificity[3,11]. The enzyme was purified by following its activity with an assay for cleavage of this processing-site peptide. Five peptides derived from the purified protein had amino-acid sequences that we were unable to find in any data base (underlined in Fig. 1). Peptide 32 contained a zinc-binding domain similar to those found in several metalloproteinases, and the aspartic acid residue following the third conserved histidine (Asp 416; Fig. 1) indicated that TACE belongs to the adamalysin family of the metzincin metalloproteinases[12]. Peptide 30 was found to be homologous (56% identity) to a region of a bovine adamalysin called MADM[13].

This information provided the basis for a two-step cloning strategy using the polymerase chain reaction (PCR). In the first step, single-strand complementary DNA was generated with reverse transcriptase from the messenger RNA of lipopolysaccharide(LPS)-stimulated THP-1 cells for use as a template[14]. For primers, two pools of oligonucleotides (accounting for the degeneracy of the genetic code) were designed, encoding the first six amino acids of peptide 30 and the sequence EECDCG, found in MADM and conserved in other adamalysins. The PCR procedure yielded a product of 182 base pairs (bp), encoding 61 amino acids, including all of peptide 30. In the second step, oligonucleotide primers based on this partial TACE cDNA were used with various phage cDNA libraries as templates. The expected PCR product of 144 bp was generated from several libraries, including a λ library from the KB human epithelial cell line (ATCC CCL 17). This library was

```
        Signal sequence  |  Pro-domain
  1  MRQSLLFLTS VVPFVLAPRP PDDPGFGPHQ RLEKLDSLLS DYDILSLSNI

 51  QQHSVRKRDL QTSTHVETLL TFSALKRHFK LYLTSSTERF SQNFKVVVVD

101  GKNESEYTVK WQDFFTGHVV GEPDSRVLAH IRDDDVIIRI NTDGAEYNIE

151  PLWRFVNDTK DKRMLVYKSE DIKNVSRLQS PKVCGYLKVD NEELLPKGLV

                      |  Metalloprotease domain
201  DREPPEELVH RVKRRADPDP MKNTCKLLVV ADHRFYRYMG RGEESTTTNY

251  LIELIDRVDD IYRNTSWDNA GFKGYGIQIE QIRILKSPQE VKPGEKHYNM

301  AKSYPNEEKD AWDVKMLLEQ FSFDIAEEAS KVCLAHLFTY QDFDMGTLGL

351  AYVGSPRANS HGGVCPKAYY SPVGKKNIYL NSGLTSTKNY GKTILTKEAD
                        17         27                 13   32

401  LVTTHELGHN FGAEHDPDGL AECAPNEDQG GKYVMYPIAV SGDHENNKMF
                                          30
                                 |  Disintegrin domain
451  SNCSKQSIYK TIESKAQECF QERSNKVCGN SRVDEGEECD PGIMYLNNDT

501  CCNSDCTLKE GVQCSDRNSP CCKNCQFETA QKKCQEAINA TCKGVSYCTG

                                 |  EGF-like domain
551  NSSECPPPGN AEDDTVCLDL GKCKDGKCIP FCEREQQLES CACNETDNSC

     |  Crambin-like domain
601  KVCCRDLSGR CVPYVDAEQK NLFLRKGKPC TVGFCDMNGK CEKRVQDVIE

                                 |  Transmembrane domain  |
651  RFWDFIDQLS INTFGKFLAD NIVGSVLVFS LIFWIPFSIL VHCVDKKLDK

     Cytoplasmic domain
701  QYESLSLFHP SNVEMLSSMD SASVRIIKPF PAPQTPGRLQ PAPVIPSAPA

751  APKLDHQRMD TIQEDPSTDS HMDEDGFEKD PFPNSSTAAK SFEDLTDHPV

801  TRSEKAASFK LQRQNRVDSK ETEC
```

Figure 1 Amino-acid sequence of TACE, deduced from the sequence of cDNA clone λ6-1. The significance of the underlined sequences is explained in the text. Numbers correspond to the approximate time of elution, in minutes, from the C18 column. Potential *N*-linked glycosylation sites are indicated in bold. The first six residues of peptide 32 (beginning with Glu 398) were ambiguous owing to the presence of a contaminating peptide.

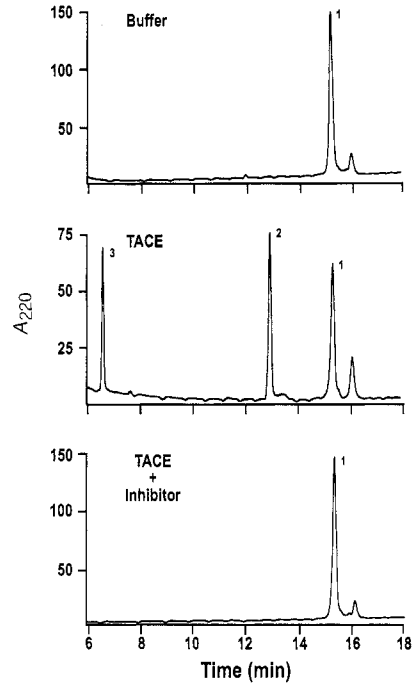

Figure 2 Enzymatic activity of recombinant TACE. The TNF-α cleavage-site peptide was incubated with the indicated components, and the samples analysed by HPLC. The composition of the peaks was determined by mass spectrometry: 1, substrate peptide; 2, Ac-SPLAQA; 3, VRSSSR-NH_2. The small peak eluting after peak 1 is an unidentified buffer component.

screened with a probe based on the partial TACE cDNA, and 24 hybridizing clones were isolated. Clone λ6-1 has a cDNA insert of 3,014 bp and an open reading frame of 824 amino acids (Fig. 1), starting with an initiator methionine codon at nucleotide 115 and ending with a termination codon at nucleotide 2,589. An in-frame termination codon precedes the initiator methionine codon at nucleotide 13. The amino-acid sequences of the five peptides derived from the purified TACE are encoded by the cDNA (underlined amino acids in Fig. 1), confirming the identity of this cDNA clone.

As predicted from the amino-acid sequence of peptide 32, TACE is a member of the adamalysin family of zinc-binding metalloproteinases. It contains a signal sequence followed by a pro-domain with a probable cysteine switch[15] at Cys 184, a catalytic domain preceded by a potential furin cleavage site[16] (residues 211–214 in Fig. 1), and a disintegrin domain. Unlike other mammalian adamalysins, which then have a cysteine-rich domain and an EGF-like domain, the TACE disintegrin domain is followed by an EGF-like domain and a crambin-like domain[17]. TACE also differs from other family members in having a proline in place of the second cysteine in the consensus EECDCG sequence (residues 487–492 in Fig. 1). The protein ends with an apparent transmembrane domain and cytoplasmic tail (Fig. 1). There are six potential *N*-linked glycosylation sites in the extracellular domain, excluding the pro-domain. Comparison with other family members indicated that TACE is most similar to bovine MADM[13], with 29% amino-acid identity. It is less similar to other mammalian adamalysins (for example, fertilin-α[18], Ms2 (ref. 19), metargidin[20], meltrin-α[21], and MDC9 (ref. 22)), which are 15–18% identical to TACE.

To confirm that the cloned cDNA encodes a proteinase with the specificity of the TNF-α-processing enzyme, DNA encoding the apparent extracellular domain of TACE (amino acids 1–670 in Fig. 1) was placed in a mammalian expression vector and transfected into 293/EBNA cells[23]. Conditioned medium from these cells contained a processing-site peptide-cleaving activity not present in medium from cells transfected with an empty vector (data not shown). The enzyme responsible for this activity was partially purified by Q-Sepharose and hydroxyapatite chromatography and was found to generate only two products from the cleavage-site peptide (Fig. 2). Mass spectrometry confirmed that these products resulted from the predicted cleavage between residues representing Ala 76 and Val 77. This activity was inhibited by a peptide hydroxamate (Immunex compound 3), similar to one known to block TNF-α processing[3].

To determine whether recombinant TACE correctly cleaves the natural substrate, precursor TNF-α was expressed in COS cells and extracted with detergent[11]. The extract was incubated for 15 min with the partially purified 293/EBNA-produced TACE extracellular domain, and the amino terminus of the resulting product was determined with an automated sequencer following purification on an anti-TNF-α antibody-affinity column. A single sequence was detected, Val-Arg-Ser-Ser-Ser-Arg-Thr-Pro-Ser, which corresponds with the amino terminus of correctly processed TNF-α. (Only a small proportion of the precursor TNF-α prepared under these conditions is converted to the 17K form in the absence of the added TACE.)

We next determined whether TACE's pattern of tissue expression and its subcellular localization are consistent with a role in TNF-α

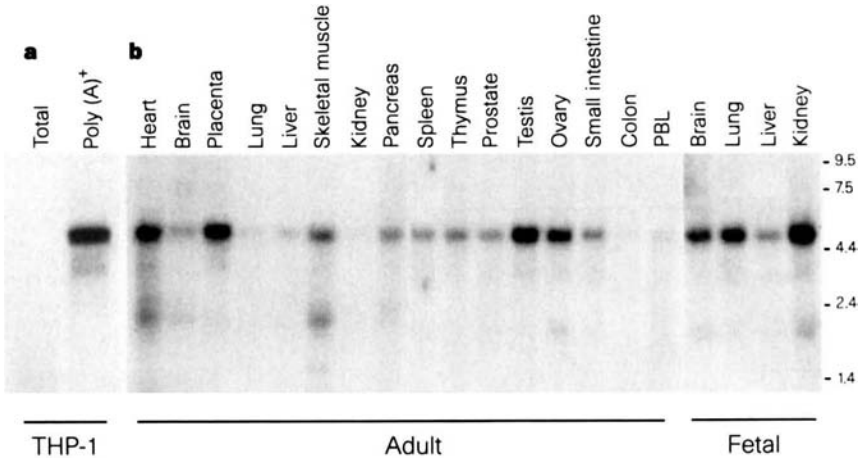

Figure 3 Northern blot analysis of TACE RNA. **a**, THP-1 total (left) and poly(A)$^+$ (right) RNA. **b**, Poly(A)$^+$ RNA from human adult and fetal tissues.

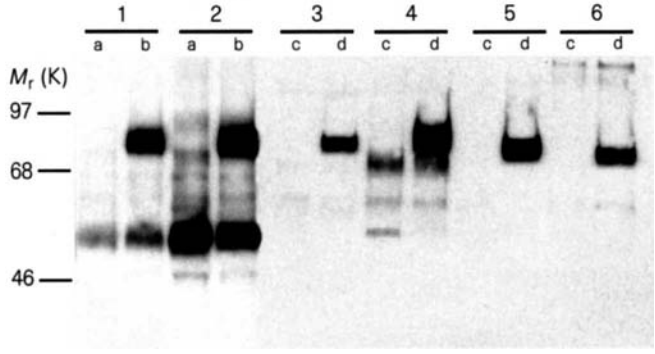

Figure 4 Cell-surface expression of TACE. Cell-surface proteins were biotinylated and solubilized, then immunoprecipitated with a control antiserum (**a**), the anti-TACE antiserum described in the text (**b**), a control monoclonal antibody (**c**), or M220 monoclonal antibody (**d**). Immunoprecipitated proteins were subjected to SDS–PAGE (8% acrylamide), transferred to nitrocellulose, and detected by HRP–streptavidin staining. Lanes: 1, monocytes; 2, monocytes exposed to LPS (2 μg ml^{-1}) for 1.5 h before biotinylation; 3, peripheral blood T cells; 4, neutrophils; 5, endothelial cells; 6, smooth-muscle cells.

processing, which occurs in many cell types. Northern blot analysis detected a TACE RNA species of ~5 kilobases(kb) in THP-1 cells and in all human tissues examined (Fig. 3). The highest levels were seen in adult heart, placenta, skeletal muscle, pancreas, spleen, thymus, prostate, testes, ovary and small intestine, and in fetal brain, lung, liver and kidney.

To determine whether TACE protein is also widely expressed, and whether it resides on the cell surface, proteins on the surface of various cells were biotinylated with a reagent that does not penetrate the membrane. Cells were then lysed with detergent and protein immunoprecipitated with serum from a rabbit immunized with a peptide representing the amino terminus of the metalloproteinase domain (residues 215–225 in Fig. 1), with monoclonal antibody M220 (derived from mice immunized with the TACE recombinant extracellular domain), or with appropriate control antibodies. SDS–PAGE of the precipitates, followed by transfer to nitrocellulose and staining with horseradish peroxidase(HRP)–streptavidin, showed that in all cell types tested (monocytes, peripheral blood T cells, neutrophils, endothelial and smooth muscle cells) a protein of M_r ~85K specifically precipitated, consistent with the relative molecular mass of purified TACE (Fig. 4). The slight variation in M_r may be due to differential glycosylation. There was no evidence of the putative TACE pro-enzyme. Moreover, neither the amount nor the size of the protein changed significantly upon stimulation of these cells with various reagents; the result obtained with monocytes and LPS stimulation is shown in Fig. 4.

To test whether TACE is required for the release of TNF-α, mouse cells genetically deficient in the zinc-binding domain of the enzyme were generated by homologous recombination. 129-derived embryonic stem (ES) cells were transfected with a G418-selectable targeting vector (Fig. 5). Clones carrying a disrupted TACE allele were selected by culturing in the presence of G418 and then identified by PCR and genomic Southern blot analysis as described[24]. ES cells homozygous for the mutation (TACE$^{-/-}$) were isolated by selection in elevated concentrations of G418 (ref. 25) and identified by genomic Southern blot analysis. Independently derived TACE$^{-/-}$ ES cell clones were injected into C57BL/6 blastocysts to generate chimaeric mice composed of both wild-type and TACE$^{-/-}$ cell types.

TACE$^{-/-}$ T-cells (129-derived, ly9.1$^+$) and TACE$^{+/+}$ T-cells (C57BL/6-derived, ly9.1$^-$) from the chimaeric mice were separated by flow cytometry and tested for their ability to release TNF-α (Fig. 6a). TACE$^{-/-}$ cells showed an 80–90% reduction in TNF-α release and an increase in surface TNF-α expression compared with the wild-type cells from the chimaera and compared with normal 129 T cells. The residual TNF-α release by the TACE$^{-/-}$ T cells was not inhibited by Immunex compound 3, which substantially blocked the release of TNF-α from wild-type cells as expected. Secretion of interferon-γ was unaffected by the TACE mutation (data not shown), demonstrating that TACE-deficient T cells remain responsive to activation and are not generally deficient in protein secretion. The expression of wild-type and mutant TACE alleles in the ly9.1$^-$ and ly9.1$^+$ T-cell fractions, respectively, was confirmed by PCR analysis with reverse transcription (RT-PCR) using primers flanking the mutation (Fig. 6b). We also found that TACE$^{-/-}$ myeloid cells, derived from chimaeric bone marrow Dexter cultures[26] selected in G418, released 80–90% less TNF-α than a comparable population of wild-type cells (data not shown).

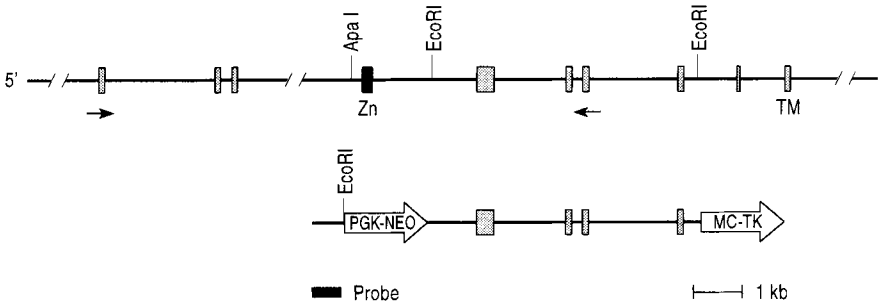

Figure 5 Targeted disruption of the TACE gene. Exons are depicted as boxes. Arrows represent PCR primers used for RT-PCR. The indicated probe was used for analysis of genomic Southern blots.

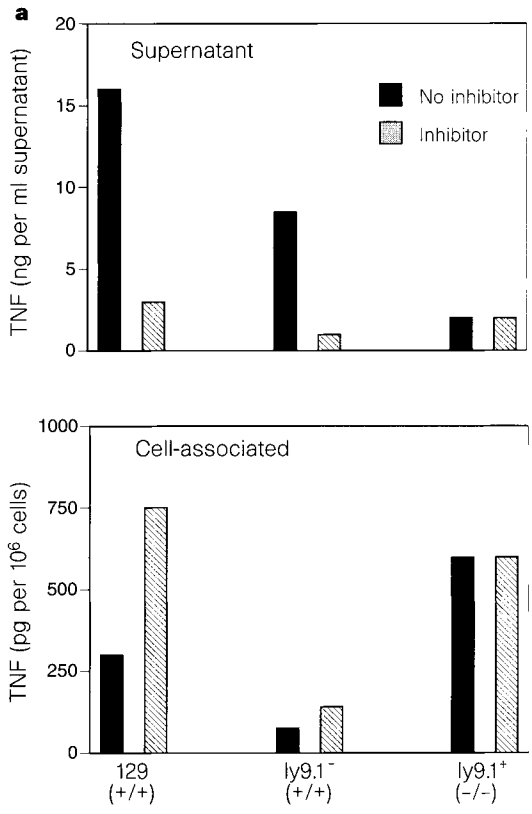

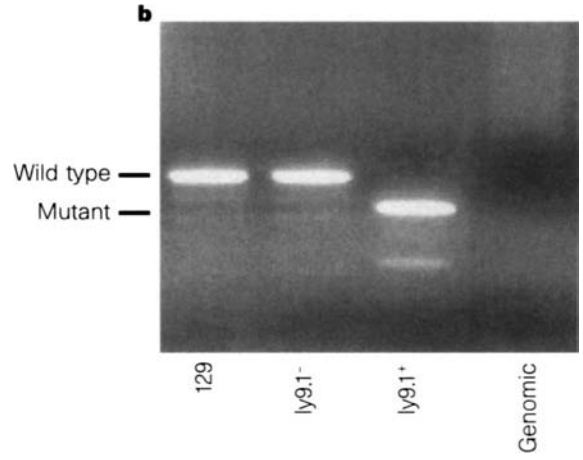

Figure 6 TNF-α production by TACE$^{-/-}$ and TACE$^{+/-}$ T cells. **a**, TNF-α levels in the medium (top) and lysates (bottom) from stimulated cultures of the indicated cells. **b**, RT-PCR analysis of RNA from the indicated cell populations, as well as a genomic DNA control, using the primers shown in Fig. 5.

Our findings indicate that a single enzyme generates most of the TNF-α released by T cells and myeloid cells under the conditions tested. Studies with TACE-deficient animals will be required to determine the extent to which TACE accounts for the production of soluble TNF-α *in vivo*. Whether or not there are other substrates of TACE can also be investigated with such animals. The disintegrin domain in some mammalian adamalysins mediates cell–cell fusion[21,27], but the corresponding region in TACE shows little sequence similarity beyond the conserved cysteines. Its function and that of the cytoplasmic domain remain to be determined. □

Methods

Purification of TACE. Membranes from the human monocytic cell line THP-1 were prepared from ~1.2×10^{11} stimulated cells and protein was solubilized with detergent as described[3]. Phospholipids were removed by acetone extraction. Protein was fractionated on DEAE–Sephacel and wheat-germ agglutinin–agarose[3]; specific activity was increased further by chromatography on Mono-Q, hydroxyapatite, SEC-400 and Red120–agarose. SDS–PAGE of the active Red120–agarose fractions followed by silver staining gave a broad band between 80K and 90K which correlated with activity.

Active fractions were pooled, acidified, and then applied to a C4 column. Proteins were eluted with an increasing gradient of acetonitrile, and a protein of about 85K was eluted with 70% acetonitrile. After evaporation of the solvent, this material was incubated with endo-LYS-C to generate peptides for sequencing. The peptides were separated by capillary C18 chromatography and then sequenced with an automated sequencer.

Determination of peptide-cleaving activity. The TNF-α cleavage-site peptide Ac-SPLAQAVRSSSR-NH_2 was incubated with the buffer in which the recombinant TACE had been prepared, with recombinant TACE, or with recombinant TACE that had been pretreated with 10 μM Immunex compound 3 (a peptide hydroxamate identical to Immunex compound 2 (ref. 3), except that the naphthylalanine side chain of compound 2 is replaced by a *t*-butyl group). Reactions were stopped by addition of HCl and samples were analysed by HPLC as described[11].

Northern blots. Isolation of RNA and northern blot analysis were done as described[14], using an antisense riboprobe encoding amino acids 1 to 473 (Fig. 1). Blots contained ~2 μg RNA per lane. Blots in Fig. 3b were purchased (catalogue numbers 7759-1, 7760-1 and 7761-1) from Clonetech (Palo Alto, California).

Cell-surface biotinylation. Human leukocytes were prepared by standard procedures. Endothelial cells[28] and smooth-muscle cells[29] were provided by P. Libby. Surface proteins were biotinylated and detected as described[30].

Targeted disruption of the TACE gene. Mouse TACE genomic clones encoding a portion of the TACE gene were isolated from a 129 genomic library (Stratagene) using a human TACE cDNA probe, and were mapped by a combination of restriction and Southern blot analyses. A gene-targeting vector

was constructed by replacing a 1.2-kb *Apa*I–*Eco*RI fragment encoding the zinc-binding domain with a PGK-neo cassette.

Separation and stimulation of TACE$^{-/-}$ and TACE$^{+/+}$ T cells. T cells from chimaeric spleens and mesenteric lymph nodes were sorted by flow cytometry using FITC-conjugated αly9.1 and PE-conjugated anti-CD3ε (PharMingen) and cultured on irradiated DBA/2 spleen cells in media containing 10 ng ml^{-1} each hulL-7 and mulL-2. T cells were activated by culturing on anti-CD3ε-coated plates at 10^6 cells ml^{-1} in the presence or absence of 50 μM Immunex compound 3. After 24 h, supernatants and cell pellets were assayed for TNF-α and interferon-γ by ELISA (Genzyme). T cells isolated from control 129 mice were similarly analysed as a control for strain variation. Data are representative of several experiments using chimaeras generated from independently derived TACE$^{-/-}$ ES cell clones.

Received 21 October; accepted 23 December 1996.

1. Rose-John, S. & Heinrich, P. C. Soluble receptors for cytokines and growth factors: generation and biological function. *Biochem. J.* **300**, 281–290 (1994).
2. Walcheck, B. *et al.* Neutrophil rolling altered by inhibition of L-selectin shedding *in vitro*. *Nature* **380**, 720–723 (1996).
3. Mohler, K. M. *et al.* Protection against a lethal dose of endotoxin by an inhibitor of tumour necrosis factor processing. *Nature* **370**, 218–220 (1994).
4. Decker, T., Lohmann-Matthes, M. L. & Gifford, G. E. Cell-associated tumour necrosis factor (TNF) as a killing mechanism of activated cytotoxic macrophages. *J. Immunol.* **138**, 957–962 (1987).
5. Kriegler, M., Perez, C., De Fay, K., Albert, I. & Lu, S. D. A novel form of TNF/cachectin is a cell surface cytotoxic transmembrane protein: ramifications for the complex physiology of TNF. *Cell* **53**, 45–53 (1988).
6. Bazzoni, F. & Beutler, B. The tumor necrosis factor ligand and receptor families. *N. Engl. J. Med.* **334**, 1717–1725 (1996).
7. Sherry, B. & Cerami, A. Cachectin/tumor necrosis factor exerts endocrine, paracrine, and autocrine control of inflammatory responses. *J. Cell Biol.* **107**, 1269–1277 (1988).
8. McGeehan, G. M. *et al.* Regulation of tumour-necrosis factor-α processing by a metalloproteinase inhibitor. *Nature* **370**, 558–561 (1994).
9. Gearing, A. J. *et al.* Processing of tumour-necrosis factor-α precursor by metalloproteinases. *Nature* **370**, 555–557 (1994).
10. Wolfsberg, T. G. & White, J. M. ADAMs in fertilization and development. *Dev. Biol.* **180**, 389–401 (1996).
11. Black, R. A. *et al.* Relaxed specificity of matrix metalloproteinases (MMPs) and TIMP-insensitivity of tumor necrosis factor-α (TNF-α) production suggest the major TNF-α converting enzyme is not an MMP. *Biochem. Biophys. Res. Commun.* **225**, 400–405 (1996).
12. Stocker, W. *et al.* The metzincins—topological and sequential relations between the astacins, adamalysins, serralysins, and matrixins (collagenases) define a superfamily of zinc-peptidases. *Protein Sci.* **4**, 823–840 (1995).
13. Howard, L., Lu, X., Mitchell, S., Griffiths, S. & Glynn, P. Molecular cloning of MADM: a catalytically active mammalian disintegrin-metalloprotease expressed in various cell types. *Biochem. J.* **317**, 45–50 (1996).
14. Cerretti, D. P. *et al.* Molecular cloning of the interleukin-1β converting enzyme. *Science* **256**, 97–100 (1992).
15. Woessner, J. F. Jr Matrix metalloproteinases and their inhibitors in connective tissue remodeling. *FASEB J.* **5**, 2145–2154 (1991).
16. Barr, P. J. Mammalian subtilisins: the long-sought dibasic processing endoproteases. *Cell* **66**, 1–3 (1991).
17. Teeter, M. M., Roe, S. M. & Heo, N. H. Atomic resolution (0.83 A) crystal structure of the hydrophobic protein crambin at 130K. *J. Mol. Biol.* **230**, 292–311 (1993).
18. Wolfsberg, T. G. *et al.* The precursor region of a protein active in sperm-egg fusion contains a metalloprotease and a disintegrin domain: structural, functional, and evolutionary implications. *Proc. Natl Acad. Sci. USA* **90**, 10783–10787 (1993).
19. Yoshida, S., Setoguchi, M., Higuchi, Y., Akizuki, S. & Yamamoto, S. Molecular cloning of cDNA encoding MS2 antigen, a novel cell surface antigen strongly expressed in murine monocytic lineage. *Int. Immunol.* **2**, 585–591 (1990).
20. Krätzschmar, J., Lum, L. & Blobel, C. P. Metargidin, a membrane-anchored metalloprotease-disintegrin protein with an RGD integrin binding sequence. *J. Biol. Chem.* **271**, 4593–4596 (1996).
21. Yagami-Hiromasa, T. *et al.* A metalloprotease-disintegrin participating in myoblast fusion. *Nature* **377**, 652–656 (1995).
22. Weskamp, G., Krätzschmar, J., Reid, M. S. & Blobel, C. P. MDC9, a widely expressed cellular disintegrin containing cytoplasmic SH3 ligand domains. *J. Cell. Biol.* **132**, 717–726 (1996).
23. McMahan, C. J. *et al.* A novel IL-1 receptor, cloned from B cells by mammalian expression, is expressed in many cell types. *EMBO J.* **10**, 2821–2832 (1991).
24. Peschon, J. J. *et al.* Early lymphocyte expansion is severely impaired in interleukin 7 receptor-deficient mice. *J. Exp. Med.* **180**, 1955–1960 (1994).
25. Mortensen, R. M., Conner, D. A., Chao, S., Geisterfer-Lowrance, A. A. & Seidman, J. G. Production of homozygous mutant ES cells with a single targeting construct. *Mol. Cell. Biol.* **12**, 2391–2395 (1992).
26. Dexter, T. M., Allen, T. D. & Lajtha, L. G. Conditions controlling the proliferation of haemopoietic stem cells *in vitro*. *J. Cell. Physiol.* **91**, 335–344 (1976).
27. Snell, W. J. & White, J. M. The molecules of mammalian fertilization. *Cell* **85**, 629–637 (1996).
28. Libby, P., Alroy, J. & Pereira, M. E. A neuraminidase from *Trypanosoma cruzi* removes sialic acid from the surface of mammalian myocardial and endothelial cells. *J. Clin. Invest.* **77**, 127–135 (1986).
29. Warner, S. J. & Libby, P. Human vascular smooth muscle cells. Target for and source of tumor necrosis factor. *J. Immunol.* **142**, 100–109 (1989).
30. Meier, T., Arni, S., Malarakannan, S., Poincelet, M. & Hoessli, D. Immunodetection of biotinylated lymphocyte-surface proteins by enhanced chemiluminescence: a nonradioactive method for cell-surface protein analysis. *Anal. Biochem.* **204**, 220–226 (1992).

Acknowledgements. We thank K. Brasel, A. Alpert, S. Braddy, D. Hirschstein, C. Otten, F. Wagener, M. Timour, Q.-P. Tran, T. Greenstreet and the Immunex Bioservices Group for technical assistance, M. Hall for preparing the figures, and D. Williams and D. Cosman for critically reviewing the manuscript.

Correspondence and requests for materials should be addressed to R.A.B. (e-mail: rblack@immunex.com). The DNA sequence has been submitted to GenBank under accession number U69611.

Cloning of a disintegrin metalloproteinase that processes precursor tumour-necrosis factor-α

Marcia L. Moss*, S.-L. Catherine Jin†, Marcos E. Milla‡, William Burkhart§, H. Luke Carter‖, Wen-Ji Chen‖, William C. Clay‖, John R. Didsbury¶, Daniel Hassler*, Christine R. Hoffman‖, Thomas A. Kost‖, Millard H. Lambert#, M. Anthony Leesnitzer*, Philip McCauley‖, Gerard McGeehan☆, Justin Mitchell*, Mary Moyer§, Gregory Pahel‖, Warren Rocque‖, Laurie K. Overton, Frank Schoenen, Theresa Seaton††, Jui-Lan Su‖, Janet Warner*, Derril Willard‖ & J. David Becherer***

*Departments of * Molecular Biochemistry, ** Diversity Sciences, ‖ Molecular Sciences, § Analytical Chemistry, # Structural Chemistry, ¶ Molecular Pharmacology, Glaxo Wellcome Research and Development Inc., 5 Moore Drive Research Triangle Park, North Carolina 27709, USA*

Tumour-necrosis factor-α (TNF-α) is a cytokine that contributes to a variety of inflammatory disease states[1]. The protein exists as a membrane-bound precursor[2,3] of relative molecular mass 26K which can be processed by a TNF-α-converting enzyme (TACE), to generate secreted 17K mature TNF-α. We have purified TACE and cloned its complementary DNA. TACE is a membrane-bound disintegrin metalloproteinase. Structural comparisons with other disintegrin-containing enzymes indicate that TACE is unique, with noteable sequence identity to MADM[4], an enzyme implicated in myelin degradation, and to KUZ[5], a *Drosophila* homologue of MADM important for neuronal development. The expression of recombinant TACE (rTACE) results in the production of functional enzyme that correctly processes precursor TNF-α to the mature form. The rTACE provides a readily available source of enzyme to help in the search for new anti-inflammatory agents that target the final processing stage of TNF-α production.

Previous studies demonstrated that potent broad-spectrum inhibitors of the matrix metalloproteinases (MMPs) can prevent TNF-α release from monocytic cell lines[6–8]. These results provided evidence that the target of the inhibitors was TACE. We purified TACE from porcine spleen because this tissue has an abundance of immunocompetent cells and because of the similarities between the porcine and human TNF-α cleavage sequences. The purification included detergent solubilization of membrane preparations containing TACE activity, followed by concanavalin A chromatography. After elution and a subsequent concentration step, the material was affinity-purified using the biotinylated inhibitor GW9277 described in Fig. 1 legend. GW9277 is an analogue of GW9471[8], a potent inhibitor of TNF-α release. Table 1 summarizes the purification results. The procedure provided a 400,000-fold increase in specific activity with an overall yield of 10%. After the affinity step, sodium dodecyl sulphate–polyacrylamide get electrophoresis (SDS–PAGE) revealed a predominant band at 85K. Further purification of the eluate by sedimentation through a glycerol density gradient and analysis of gradient fractions indicated that converting enzyme activity correlated with the appearance of the 85K protein on SDS–PAGE (Fig. 2a, b). In addition, data from a similar purification of TACE from the human monocytic cell line Mono Mac 6, provided results comparable to porcine spleen (data not shown).

Present addresses: †† Dow Corning Corporation, Midland, Michigan 48686-0994; ☆ RPR, 600 Arcola Road, Collegeville, Pennsylvania 19426; † Stanford University School of Medicine, Division of Reproductive Biology, Department of Gynecology and Obstetrics, Stanford, California 94305, USA.

Table 1 Protein purification table for TACE

Fraction	(mg ml⁻¹)	Total (mg)	Total activity	Specific activity	Purification factor
Homogenate	9	250,000	26,000	0.1	1
Pellet	100	102,000	22,000	0.2	2
Pellet after wash	3	160,000	36,000	0.2	2
Solubilized	12	140,000	56,000	0.4	4
Con A/Q fast	6	2,400	38,000	16	100
Affinity	0.1	0.1	5,200	44,000	400,000

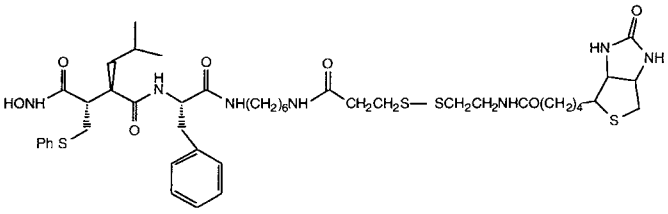

Figure 1 Structure of GW9277, a biotinylated derivative of GW9471 used as an affinity reagent in the purification of TACE.

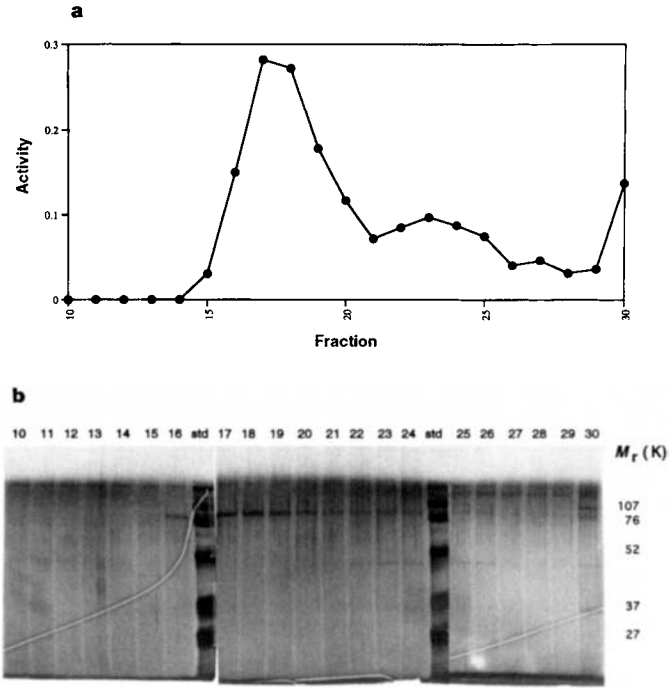

Figure 2 Sedimentation profiles of the affinity-purified material from human porcine spleens through an 8–28% glycerol gradient. **a**, Plot of activity versus fraction number. **b**, SDS–PAGE analysis of the same fractions.

After Lys-C endoprotease digestion, amino-terminal sequence analysis of the 85K protein from porcine spleen yielded a stretch of 41 amino acids. Homology searches of the GenBank and EMBL databases showed this sequence to be unique. Degenerate polymerase chain reaction (PCR) primers were synthesized and reverse transcription (RT)-PCR performed using porcine spleen poly(A)$^+$ RNA. The predicted 89-base-pair (bp) PCR product was obtained and used as a probe to screen a λgt10 porcine spleen cDNA library. The series of overlapping clones isolated spanned 2,914 bp but lacked sequence encoding the N terminus of the converting enzyme.

DNA fragments from the porcine clones were used to screen about 2.5×10^5 clones each from human leukocyte and monocyte cDNA libraries. Sequence analysis of eight positive cones revealed a continuous 2,307-bp open reading frame highly homologous to the porcine cDNA. Because this sequence also lacked the 5′ sequence corresponding to the N terminus of TACE, 5′-rapid amplification of cloned ends (RACE) was carried out using poly(A)$^+$ RNA isolated from human monocytic THP-1 cells. This yielded the missing 5′ sequence, which was confirmed by screening a monocyte library with a 330-bp fragment corresponding to the 5′ end of the original sequence. Ligation of restriction fragments from four overlapping primary clones resulted in a full-length clone that was further modified by PCR to engineer appropriate restriction sites for subsequent subcloning and expression. Figure 3a shows the deduced amino-acid sequence of full-length human TACE and Fig. 3b depicts the structural domains of the enzyme.

Examination of TACE using FastA searches of GenBank, EMBL and SwissProt identified a number of similar sequences that all belonged to the disintegrin family of metalloproteinases. The most closely related were a metalloproteinase of unknown function from *Caenorhabditis elegans* (GenBank accession number U70844), MADM, a metalloproteinase isolated from bovine brain[4] and KUZ, a closely related *Drosophila* metalloproteinase involved in neuronal development[5]. Other disintegrin family members[9] showed significant but lower similarity.

The X-ray crystal structure of adamalysin II[10] previously revealed the overall structure of a disintegrin metalloproteinase catalytic domain. An alignment with adamalysin identified the rough endpoints of the catalytic domain in TACE, shown in red in Fig. 3a, and indicated that the overall structure was generally conserved, except possibly for helix-C. In MMPs, the pro domain contains a conserved sequence, PRCGVPD (single-letter amino-acid code), called a cysteine switch. The sulphydryl group of the cysteine binds to the active-site zinc, thereby inhibiting the enzyme[11]. The PKVCGYL sequence in TACE can be aligned with the presumed cysteine switch sequences[12] of several other disintegrin metalloproteinases (not shown). This suggests that, like the matrix metalloproteinases, TACE is synthesized in an inactive pro form, and subsequently cleaved between the cysteine switch and the catalytic domain to generate the mature, active enzyme.

Although sequence alignment indicates that the cysteine-rich/disintegrin region is relatively well conserved, its function is not obvious. Some snake venom disintegrin metalloproteases can degrade type IV collagen[13], and the disintegrin domain probably serves as a recognition motif for this matrix[14]. The disintegrin domain of TACE may serve an analogous function by recognizing precursor TNF-α. Alternatively, the domain might interact with integrins on cellular surfaces. Disintegrins containing the RGD sequence, for example, bind with high affinity to gp IIb/IIIa, thereby interfering with platelet aggregation[15].

The cytoplasmic tail of TACE is proline rich and contains a potential tyrosine phosphorylation site, KKLDKQYESL, and a site that potentially binds to the *Src*-homology 3 domain (SH3), PAPQTPGR. Another disintegrin metalloprotease, MDC9, has

Table 2 Substrate specificity constants for TACE

Enzyme	Dnp-SPLAQAVRSSSRNH$_2$	N-Flag-tagged precursor TNF-α
Microsomal	2.8×10^5 M^{-1} s^{-1}	2.0×10^4 M^{-1} s^{-1}
M^1–R^{861}	1.8×10^5 M^{-1} s^{-1}	1.0×10^4 M^{-1} s^{-1}

Human Mono Mac 6 cells[24] were used to purify a source of human TACE. Specificity constants for the microsomal enzyme using either Dnp-SPLAQAVRSSSRNH$_2$ or N-Flag-tagged precursor TNF-α were taken from M. Moss *et al.* manuscript in preparation. Standard errors were less than 30%.

a

```
  1 MRQSLLFLTS VVPFVLAPRP PDDPGFGPHQ RLEKLDSLLS DYDILSLSNI
 51 QQHSVRKRDL QTSTHVETLL TFSALKRHFK LYLTSSTERF SQNFKVVVVD
101 GKNESEYTVK WQDFFTGHVV GEPDSRVLAH IRDDDVIIRI NTDGAEYNIE
151 PLWRFVNDTK DKRMLVYKSE DIKNVSRLQS PKVCGYLKVD NEELLPKGLV
201 DREPPEELVH RVKRRADPDP MKNTCKLLVV ADHRFYRYMG RGEESTTTNY
251 LIELIDRVDD IYRNTSWDNA GFKGYGIQIE QIRILKSPQE VKPGEKHYNM
301 AKSYPNEEKD AWDVKMLLEQ FSFDIAEEAS KVCLAHLFTY QDFDMGTLGL
351 AYVGSPRANS HGGVCPKAYY SPVGKKNIYL NSGLTSTKNY GKTILTKEAD
401 LVTTHELGHN FGAEHDPDGL AECAPNEDQG GKYVMYPIAV SGDHENNKMF
451 SNCSKQSIYK TIESKAQECF QERSNKVCGN SRVDEGEECD PGIMYLNNDT
501 CCNSDCTLKE GVQCSDRNSP CCKNCQFETA QKKCQEAINA TCKGVSYCTG
551 NSSECPPPGN AEDDTVCLDL GKCKDGKCIP FCEREQQLES CACNETDNSC
601 KVCCRDLSGR CVPYVDAEQK NLFLRKGKPC TVGFCDMNGK CEKRVQDVIE
651 RFWDFIDQLS INTFGKFLAD NIVGSVLVFS LIFWIPFSIL VHCVDKKLDK
701 QYESLSLFHP SNVEMLSSMD SASVRIIKPF PAPQTPGRLQ PAPVIPSAPA
751 APKLDHQRMD TIQEDPSTDS HMDEDGFEKD PFPNSSTAAK SFEDLTDHPV
801 TRSEKAASFK LQRQNRVDSK ETEC
```

b

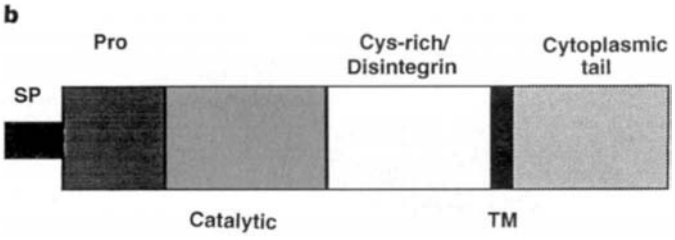

Figure 3 a, Deduced amino-acid sequence of human TACE. The domains are coloured as follows: signal peptide in dark red; pro domain in green, with cysteine switch underlined and furin-like cleavage site double underlined; catalytic domain in red with zinc motif underlined and met-turn double underlined; disintegrin domain in blue with specificity loop underlined; cysteine-rich domain in dark yellow; transmembrane segment in black; cytosolic tail in purple with potential phosphorylation site underlined, and potential SH3-binding site double underlined. The dotted underline identifies the location in the human TACE sequence of the 41-residue peptide sequenced from the purified porcine enzyme. **b**, Domain structure of TACE. The structure of TACE includes a signal peptide (SP), pro domain, catalytic domain, cysteine (cys) rich/disintegrin domain, transmembrane region (TM) and cytoplasmic tail.

been shown to bind the Src SH3 domain[16]. Therefore, the cytoplasmic region may have signalling functions or could be important for subcellular localization of the enzyme.

A recombinant form of the enzyme was generated that contained the signal peptide and pro domain but lacked the transmembrane region and cytoplasmic tail. Subcloning of the cDNA corresponding to amino acids Met 1 to Arg 651 into pFastBac1 produced a recombinant baculovirus. Infection of BTI-Tn-5B1-4 cells with the virus produced TACE activity in the culture medium. Analysis by SDS–PAGE and western blotting identified a predominant 70K band and a minor 90K band (Fig. 4a b).

Purification of the enzyme activity to homogeneity demonstrated that the TACE activity corresponded to the 70K form. Activity assays of the purified enzyme verified that the rTACE activity was comparable to that found in microsomal preparations obtained from Mono Mac 6 cells. The recombinant enzyme processed N-Flag tagged precursor TNF-α between Ala 76 and Val 77 to generate the 17K mature form (data not shown). In addition, cleavage of a peptide substrate that spans the cleavage sequence of precursor TNF-α, dinitrophenyl (Dnp)-SPLAQAVRSSSRNH$_2$, occurred at the correct site (Ala-Val; data not shown). The specificity constants (k_{cat}/K_m) for both cleavage reactions were comparable for the recombinant and microsomal enzymes (Table 2). Finally, the rank order of potency for five different metalloproteinase inhibitors and their inhibition constants against the recombinant and native converting enzymes were similar (Table 3).

The recombinant 70K form of the enzyme was further characterized by carboxy- and amino-terminal sequencing. The C terminus

Table 3 Comparison of inhibition constants between microsomal and recombinant (M^1-R^{651}) TACE

Inhibitor	Microsomal inhibition constant (nM)	M^1-R^{651} inhibition constant (nM)
GW9471*	5.7	13
GW9277†	43	86
BB94‡	4.5	11
TAPI§	8.1	8.8
CGS27023‖	59	54

Errors were less than 30%. Samples were run in triplicate.
* GW9471 is a broad spectrum MMP inhibitor that also inhibits TNF-α release[8].
† See Fig. 1.
‡ BB94 is a British Biotech compound also known as Batismastat[25].
§ TAPI is described in ref. 7.
‖ CGS 27023 is described in ref. 26.

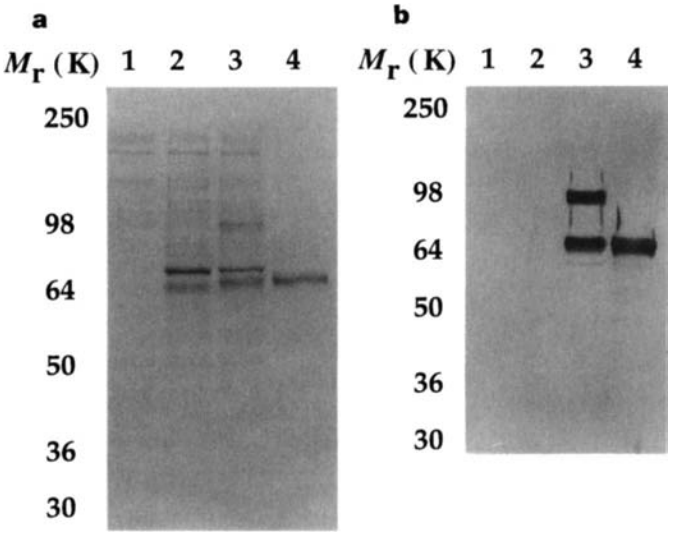

Figure 4 Expression and purification of truncated human recombinant TACE (rTACE). **a**, SDS-PAGE analysis of media samples and purified rTACE. Lane 1, Medium from uninfected BTI-Tn-5BI-4 cells. Lane 2, Medium from BTI-Tn-5BI-4 cells infected with wild-type baculovirus. Lane 3, Medium from BTI-Tn-5BI-4 cells infected with rTACE baculovirus. Lane 4, rTACE after purification. **b**, Western blot analysis using the TACE specific monoclonal antibody Tc3-7.49. The antibody was generated using the catalytic domain of *E. coli*-expressed rTACE as an antigen. Lane 1, Medium from uninfected BTI-Tn-5BI-4 cells. Lane 2, Medium from BTI-Tn-5BI-4 infected with wild-type baculovirus. Lane 3, Medium from BTI-Tn-5BI-4 cells infected with rTACE baculovirus. Lane 4, Purified rTACE.

ended with Arg 651, as predicted, whereas the N terminus began with Arg 215. Therefore the pro domain was removed by cleavage on the carboxyl side of the sequence ....RVKR[214]. Presumably, a furin-like enzyme present in the recombinant baculovirus-infected insect cells processes rTACE. Whether TACE is processed at the furin-like site in mammalian cells is unknown. Interestingly, the presence of a furin-like cleavage sequence in the pro domain may explain previous results indicating that serine-protease inhibitors can prevent TNF-α release[17].

The similarities in structural features of TACE in relation to the known disintegrin metalloproteinases raise intriguing questions as to the role of this converting enzyme in cell–cell and cell–matrix interactions. In addition, many of the disintegrin metalloproteinases, such as MDC9 and MADM, have unknown physiological substrates. Whether these metalloproteinases are responsible for the hydroxamate-sensitive shedding of L-selectin[18], interleukin-6 receptor[19], transforming-growth-factor-α[20] and tumour-necrosis-factor receptors[21] from cellular surfaces remains to be determined. □

Methods

TACE assays. Reactions were performed at 37 °C and pH 7.5 in 10 mM HEPES containing 0.00075% Brij. The peptide substrate Dnp-SPLAQAVRSSSRNH$_2$ was used in the determination of specificity constants. Substrate and product peaks were detected by absorbance at 350 nM after separation by reverse-phase HPLC (M. Moss *et al.*, manuscript in preparation). Assays to determine inhibition constants were run in a 96-well plate using a biotinylated and tritiated peptide substrate based on the cleavage sequence surrounding precursor TNF-α. Depletion of substrate was followed using a scintillation proximity assay (SPA).

Purification of porcine spleen TACE. Approximately 3–7 kg of porcine spleens were homogenized in cold grind buffer (10 mM HEPES, pH 7.5, 0.25 M sucrose, 2 mM $MgCl_2$, and a protease inhibitor cocktail). Three volumes of buffer were used for every gram of spleen tissue. The ground tissue was then passed through a fibreglass screen and the filtered material was centrifuged for 10 min at 2,000*g*. The supernatant was removed, $CaCl_2$ was added with stirring to a final concentration of 8 mM, and centrifuged for 20 min at 10,000*g*. The pellets were resuspended in 1/6th of the volume of the supernatant in 10 mM HEPES, pH 7.5, 0.25 M sucrose, and protease inhibitors, then frozen for future use or directly washed in buffer containing 0.05% Nonidet P-40, 20 mM HEPES, pH 7.5 and 200 mM NaCl and a protease-inhibitor cocktail (buffer B). The washed pellet was combined with 6 l of buffer C (buffer B with the exception that the detergent concentration was 1% Nonidet P-40) for every l of initial membrane suspension. The solution was allowed to stir for 30 min in the cold followed by centrifugation for 1 h at 38,700*g* (TFA 20.250 rotor, Sorvall). The supernatant was loaded onto a 1-l concanavalin A (Pharmacia) column equilibrated in buffer C. The converting enzyme activity was eluted with 10 mM HEPES, pH 7.5 containing 250 mM methyl mannopyranoside. The eluant was loaded directly onto a 500 ml Q fast-flow column (Pharmacia). The activity was eluted with 10 mM HEPES, pH 7.5, containing 200 mM NaCl and a protease inhibitor cocktail. The eluted protein was dialysed against 10 mM HEPES, pH 7.5 overnight and then concentrated on a 2 ml Poros HQ column. Elutions were carried out with 10 mM HEPES, pH 7.5, containing 500 mM NaCl and protease inhibitors. Fractions containing converting enzyme activity were incubated with GW9277 (Fig. 1) to a final concentration of 1 μM. then after 10–30 min in the cold, NeutrAvidin Plus beads (PIERCE) were added (0.4 ml of slurry per 1 ml of enzyme). After an additional 10 min with rocking, the slurry was pelleted by centrifugation in a microfuge. The beads were washed and the enzyme was eluted from the beads by rocking overnight in 0.4 ml buffer containing 10 mM HEPES, pH 7.5, and a protease inhibitor cocktail. The affinity-purified enzyme, 0.2 ml, was loaded onto a 12-ml centrifuge tube containing an 8–28% linear glycerol gradient in 10 mM HEPES, pH 7.5 and 0.05% Nonidet P-40 (buffer S). The gradient was centrifuged for 48 h at 4 °C at 272,000*g* in a TH-641 rotor (Sorvall). After centrifugation, 0.35-ml fractions were collected from top (fraction 1) to bottom. Samples from each fraction were assayed for converting enzyme activity and the protein profile was analysed by SDS–PAGE (silver staining).

Sequencing of TACE. Lys-C proteolytic fragments of TACE were sequenced as described in ref. 22.

Cloning, overexpression and purification of truncated human rTACE. A reverse cloning approach was used based on peptide microsequencing information as described in the results section. Library construction and screening, as well as 5′-RACE were done following standard techniques. rTACE was prepared for expression by PCR from the full-length clone using the 5′ primer 5′-GTCGTCGTCGTCGTCGTCCATATGAGGCAGTCTCTCCTATTC CTGACCAGCGTG-3′ and the 3′ primer 5′-CGCGCGCGCGGGATCCCTAT CGTTCAATACATCCTGTACTCGTTTCTC-3′. The PCR product was subcloned into pFastBac1 and recombinant baculovirus generated using the Bac-to-Bac system (Gibco, BRL). BTI-Tn-5BI-4 cells[23] were infected with virus and culture media collected after 48 h. Media was concentrated 10-fold and desalted followed by ion exchange chromatography on a Poros 50 HQ column. Elution was accomplished using a linear NaCl gradient. Fractions containing TACE activity were pooled and loaded onto a concanavalin A Sepharose column and eluted with 250 mM methyl-α-D-mannopyranoside. The eluted material was concentrated and subjected to gel filtration on a prep grade Superdex 75 column. Peak fractions were pooled to yield the final purified rTACE.

Received 4 November 1996; accepted 20 January 1997.

1. Vassalli, P. The pathophysiology of tumour necrosis factors. *Annu. Rev. Immunol.* **10,** 411–452 (1992).
2. Decker, T., Lohmann-Matthes, M. L., & Gifford, G. E. Cell-associated tumor necrosis factor (TNF) as a killing mechanism of activated cytotoxic macrophages. *J. mmuno.* **138,** 957–962 (1987).
3. Kriegler, M., Perez, C., DeFay, K., Albert, I. & Lu, S. D. A novel form of TNF/cachectin is a cell surface cytotoxic transmembrane protein: ramifications for the complex physiology of TNF. *Cell* **53,** 45–53 (1996).
4. Howard, L., Lu, X., Mitchell, S., Griffiths, S. & Glynn, P. Molecular cloning of MADM: a catalytically active mammalian disintegrin-metalloprotease expressed in various cell types. *Biochem. J.* **317,** 45–50 (1996).
5. Rooke, J., Pan, D., Xu, T. & Rubin, G. M. KUZ, a conserved metalloprotease-disintegrin protein with two roles in Drosophila neurogenesis. *Science* **273,** 1227–1231 (1996).
6. Mohler, K. M. *et al.* Protection against a lethal dose of endotoxin by an inhibitor of tumor necrosis factor processing. *Nature* **370,** 218–220 (1994).
7. Gearing, A. *et al.* Processing of tumor necrosis factor-α precursor by metalloproteases. *Nature* **370,** 558–561 (1994).
9. Wolfsberg, T. G. & White, J. M. ADAMs in fertilization and development. *Dev. Biol.* **180,** 389–401 (1996).
10. Gomis-Reuth, F. X. *et al.* Refined 2.0 angstrom x-ray crystal structure of the snake venom zinc-endopeptidase adamalysin II. Primary and tertiary structure determination, refinement, molecular structure and comparison with astacin, collagenase and thermolysin. *J. Mol. Biol.* **239,** 513–544 (1994).
11. Van Wart, H. E. & Birkedal-Hansen, B. The cysteine switch: a principle of regulation of metalloprotease activity with potential applicability to the entire matrix metalloprotease gene family. *Proc. Natl Acad. Sci. USA* **87,** 5578–5581 (1990).
12. Grams, F., Huber, R., Kress, L. F., Moroder, L. & Bode, W. Activation of snake venom metalloproteases by a cysteine switch-like mechanism. *FEBS Lett.* **335,** 76–80 (1993).
13. Shannon, J. D., Baramova, E. N., Bjarnason, J. B. & Fox, J. W. Amino acid sequence of a Crotalus atrox venom metalloprotease which cleaves type IV collagen and gelatin. *J. Biol. Chem.* **264,** 11575–11583 (1989).
14. Zhou, Q., Dangelmaier, C. & Smith, J. B. The hemorrhagin catrocollastatin inhibits collagen-induced platelet aggregatin by binding to collagen via its disintegrin-like domain. *Biochem. Biophys. Res. Commun.* **219,** 720–726 (1996).
15. Gould, R. J. *et al.* Disintegrins: a family of integrin inhibitory proteins from viper venoms. *Proc. Soc. Exp. Biol. Med.* **195,** 168–171 (1990).
16. Weskamp, G., Kratzschmar, J., Reid, M. S. & Blobel, C. P. MDC0, a widely expressed cellular disintegrin containing cytoplasmic SH3 ligand domains. *J. Cell Biol.* **132,** 717–726 (1996).
17. Suffys, P., Beyaert, R., Van Roy, F. & Fiers, W. Involvement of a serine protease in tumor necrosis factor-mediated cytotoxicity. *Eur. J. Biochem.* **178,** 257–265 (1988).
18. Bennett, T. A., Lynam, E. B., Sklar, L. A. & Rogelj, S. Hydroxamate-based metalloprotease inhibitor blocks shedding of L-selectin adhesion molecule from leukocytes. Functional consequences for neutrophil aggregation. *J. Immunol.* **156,** 3093–3097 (1996).
19. Mullberg, J. *et al.* A metalloprotease inhibitor blocks shedding of the IL-6 receptor and te p60 TNF receptor. *J. Immunol.* **155,** 5198–5205 (1995).
20. Arribas, J. *et al.* Diverse cell surface protein ectodomains are shed by a system sensitive to metalloprotease inhibitors. *J. Biol. Chem.* **271,** 11376–11382 (1996).
21. Crowe, P. D. *et al.* A metalloprotease inhibitor blocks shedding of the 80-kD TNF receptor and TNF processing in T lymphocytes. *J. Exp. Med.* **181,** 1205–1208 (1995).
22. Moyer, M., Rose, D. & Burkhart, W. Elutin of proteins from polyacrylamide gels onto the HP sequencing column. in *Techniques in Protein Chemistry* (ed. Crabb, J.) 195–204 (Academic, San Diego, 1994).
23. Granados, R. R., Guoxun, L., Derksen, A. C. G. & McKenna, K. A. A new cell line from *Trichoplusia ni (BTI-Tn-5BI-4)* susceptible to *Trichoplusia* single enveloped nuclear polyhedrosis virus. *J. Invert. Path.* **64,** 260–266 (1994).
24. Ziegler-Heitbrook, *et al.* Establishment of a human cell line (Mono Mac 6) with characteristics of mature monocytes. *Int. J. Cander* **41,** 456–461 (1988).
25. Morris, S. A. *et al.* Inhibition of organ invasion by the matrix metalloprotease inhibitor batimastat (BB-94) in two human colon carcinoma metastasis models. *Cancer Res.* **55,** 3629–3633 (1995).
26. O'Byren, E. M. *et al.* Oral administration of a matrix metalloprotease inhibitor, CGS 27023A, protects the cartilage proteoglycan matrix in a partial meniscectomy model of osteoarthritis in rabbits. *Inflam. Res.* **44** (suppl. 2), S117–S118 (1995).

Acknowledgements. We thank G. Barrett for technical assistance.

Correspondence and requests for reprints should be addressed to M.L.M. Genbank accession number is U86755.

Editing of ubiquitin conjugates by an isopeptidase in the 26S proteasome

Y. Amy Lam*, Wei Xu*, George N. DeMartino† & Robert E. Cohen*

* *Department of Biochemistry, University of Iowa, Iowa City, Iowa 52242, USA*
† *Department of Physiology, University of Texas Southwestern Medical Center, Dallas, Texas 75235, USA*

In eukaryotes, ubiquitin (Ub)-dependent proteolysis is essential for bulk protein turnover as well as diverse processes including cell-cycle control, differentiation, antigen presentation, and the stress response[1–3]. Generally, multiple ubiquitins are added onto a substrate to form an isopeptide-linked 'polyubiquitin' chain, which targets substrates for degradation by the 26S proteasome[4–7]. The specificity of Ub-dependent degradation was thought to depend primarily on the selection of targets for ubiquitination, but recently we have reported evidence[8] for a second level of specificity in which (poly)Ub-protein conjugates are partitioned among two fates: degradation of the protein substrate by the 26S proteasome; and disassembly by Ub isopeptidase(s) to regenerate the protein substrate. Potentially, an isopeptidase could influence degradation by 'editing' (poly)Ub-protein conjugates according to the extent of ubiquitination rather than the structure of the ubiquitination target itself. Here we describe a bovine isopeptidase that is well suited to such an editing function because of its unique localization and specificity. This enzyme is an intrinsic subunit of PA700, the 19S regulatory complex of the 26S proteasome. By disassembling the degradation signal from only the distal end of (poly)Ub chains, this isopeptidase can selectively rescue poorly ubiquitinated or slowly degraded Ub-protein conjugates from proteolysis.

The 26S proteasome is assembled from two different multisubunit complexes[2,3,9–11]. The proteolytic sites are contained within a 20S proteasome core that, in the presence of ATP, can associate with PA700, a 19S complex that confers the ability to bind and process ubiquitinated substrates. There are ~18 different polypeptides in PA700, including the S5a polyUb-binding protein and multiple ATPase subunits[9–12]. PA700 also seemed to be a likely site for an editing Ub isopeptidase. A candidate for this activity in purified PA700 from bovine red blood cells was suggested initially by the use of K48-linked diubiquitin as a substrate (Fig. 1a). The activity could be blocked completely by the isopeptidase inhibitor Ub-aldehyde (Ubal)[13,14] and was not affected by ATP. These characteristics distinguish the PA700 isopeptidase from an ATP-stimulated and Ubal-insensitive isopeptidase found in 26S proteasomes from rabbit reticulocytes[15]. Incorporation of PA700 into 26S proteasomes also did not affect the isopeptidase. We found that k_{cat}/K_m for PA700 with unlabelled Ub_2 is $1.31 \pm 0.35\ min^{-1}\ \mu M^{-1}$; this value was not changed significantly when PA700 was preincubated with 20S in a 2:1 ratio to form functional 26S proteasomes. In addition to cleaving Ub–Ub linkages, the PA700 isopeptidase can also remove Ub conjugated directly to lysozyme and α-globin (data not shown). No isopeptidase activity was found in the purified 20S proteasomes.

Co-sedimentation of ^{125}I-Ubal with PA700 suggested that the isopeptidase was tightly bound to the complex (Fig. 1b). Additional

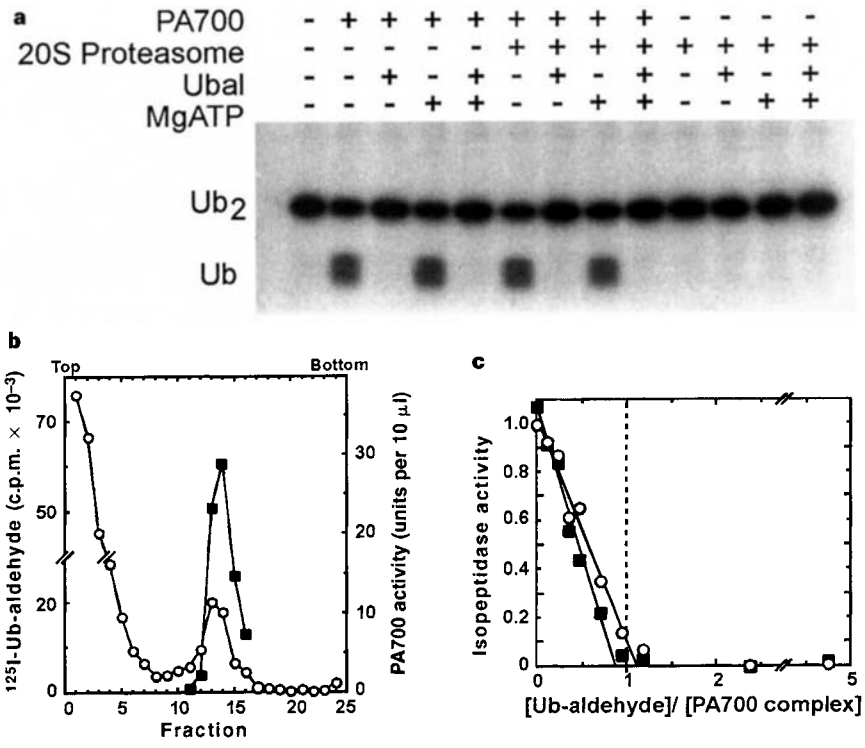

Figure 1 An intrinsic Ub isopeptidase activity in the PA700 complex. **a**, Isopeptidase activity assays used ^{125}I-labelled Ub_2 as the substrate and, where indicated, 43 nM PA700, 0.6 μM Ubal, 60 μM ATP, 14 nM 20S proteasomes, or 26S proteasomes assembled by preincubation of the PA700 and 20S complexes. The products were analysed by SDS–PAGE and autoradiography. **b**, The association of the isopeptidase with the PA700 complex was revealed by its co-sedimentation with Ubal. A mixture of PA700 and ^{125}I-Ubal was centrifuged at 4 °C through a 10–40% glycerol gradient. Fractions of 0.2 ml were collected and ^{125}I-radioactivity (open circles) and PA700 activity (filled squares) were measured. **c**, For active-site titrations, PA700 (0.21 μM) was preincubated at 37 °C for 5 min in reaction buffer with 0–1 μM Ubal, and isopeptidase activity was assayed with 3.1 μM ^{125}I-Ub_2. The results, shown for titrations of two independent preparations of PA700, indicate that there is one isopeptidase per PA700 complex.

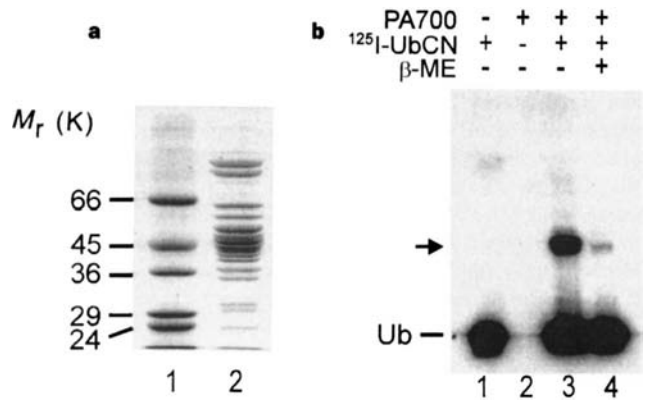

Figure 2 Affinity-labelling of the PA700 isopeptidase by ^{125}I-UbCN. **a**, PA700 polypeptides were separated by SDS-PAGE (10% acrylamide) and stained with Coomassie blue (lane 2); molecular weight standards are in lane 1. **b**, Equimolar PA700 and ^{125}I-UbCN were incubated at pH 7 for 5 min at 37 °C; after acidification to promote thiolester formation (see 7Methods), samples mixed with SDS-PAGE loading buffer ±5% β-mercaptoethanol (β-ME) were analysed by SDS-PAGE and autoradiography. Lane 3 shows that ~10% of the ^{125}I-UbCN formed an adduct of M_r~45K (arrow) with a component of PA700; reversal of adduct formation by addition of excess thiol (lane 4) is consistent with an ^{125}I-Ub-isopeptidase thiolester having been formed.

evidence that the isopeptidase is an intrinsic subunit of PA700 was obtained from active-site titrations with Ubal (Fig. 1c). For two independent preparations of PA700, the titrations demonstrated that a single isopeptidase is present in each PA700 complex of M_r 700K. Although the yeast Doa4p isopeptidase[16] co-purifies with the 26S proteasome, unlike the PA700-isopeptidase its association appears to be weak, and it may not be a stoichiometric component of the complex (M. Hochstrasser, personal communication).

Attempts to identify the PA700-isopeptidase polypeptide by chemical crosslinking to Ubal were unsuccessful, so we sought an alternative inhibitor for use as an affinity label. All known Ub isopeptidases are thiol proteases[17] and, in analogy with the inhibition by peptidyl-nitriles of other thiol proteases such as papain[18–20], we expected that the PA700-isopeptidase could be inhibited by a carboxy-terminal nitrile derivative of Ub. Ub-nitrile (UbCN) was synthesized and found to be a potent isopeptidase inhibitor ($K_i < 1\ \mu$M). In the isopeptidase–UbCN complex, reversible attack by the active-site cysteine thiolate on the nitrile carbon is likely to generate a thioimidate ester. Based on studies of model thioimidates[21], we postulated that acidification could convert the enzyme-bound Ub-thioimidate irreversibly to a thiolester. By this treatment an ^{125}I-labelled 45K covalent adduct was made from ^{125}I-UbCN and PA700 (Fig. 2). The lability of this new species to β-mercaptoethanol is evidence of a thiolester linkage.

That a single new ^{125}I-labelled adduct was formed from ^{125}I-UbCN confirms our determination by active-site titration of one isopeptidase per PA700. Moreover, this result significantly limits the possible candidates for the isopeptidase. After subtraction of the molecular mass contributed by Ub (M_r 8.5K), the isopeptidase component of the adduct has an apparent M_r of ~37K. This eliminates most PA700 polypeptides including the polyUb binding protein S5a (M_r 50K)[22] and all known ATPases ($M_r > 44$K)[3,10] as candidates for the isopeptidase. Of the ~18 different polypeptides resolved from the PA700 complex, only two (designated p35 and p37) are in this molecular weight range. A bovine analogue of the Doa4p or tre-2 isopeptidases, which we expect to have $M_r > 100$K by analogy with the yeast and human proteins[16], has not been detected in our preparations of PA700 (unpublished results).

Because the 26S proteasome preferentially degrades polyubiquitinated substrates, we investigated polyUb chain disassembly by the

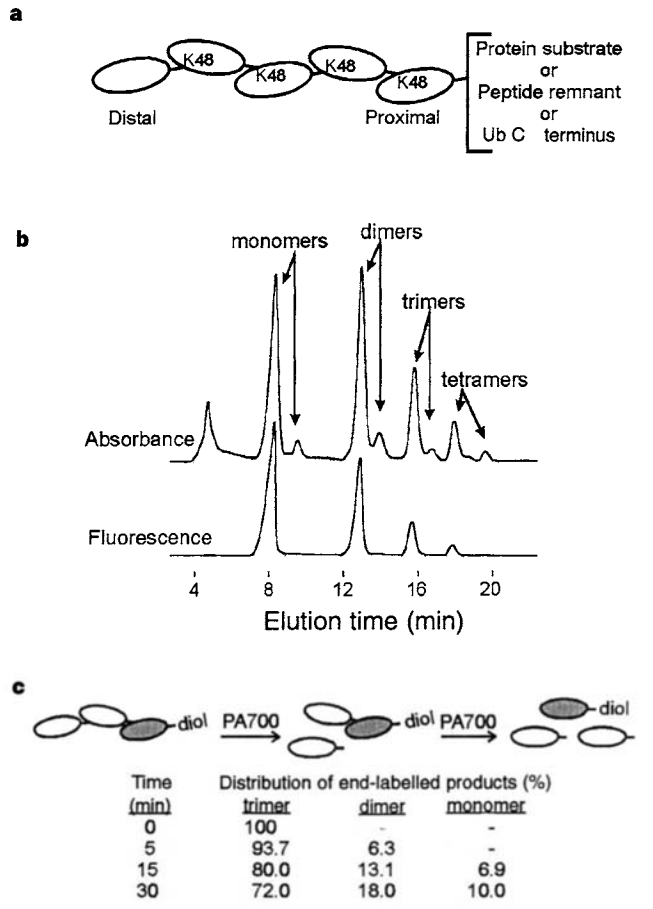

Time (min)	Distribution of end-labelled products (%) trimer	dimer	monomer
0	100	-	-
5	93.7	6.3	-
15	80.0	13.1	6.9
30	72.0	18.0	10.0

Figure 3 Distal-end specificity of the PA700 isopeptidase. **a**, PolyUb chains are linked by an isopeptide bond between the C-terminal carboxyl group of one Ub and the ε-amino group of a lysine on another Ub; typically, the linkage is to K48. The proximal Ub is defined as the Ub whose C terminus is either free or linked to a protein substrate (or fragment thereof); the distal Ub is at the opposite end of the chain. **b**, K48-linked polyUb oligomers with a Lucifer yellow-labelled proximal Ub were synthesized and resolved from each other and unlabelled chains by cation-exchange HPLC. **c**, Ub-Ub-Ub(T66C-Lucifer yellow)-diol trimers (1 μM) and PA700 (8 nM) were incubated at 37 °C for the indicated times and the Lucifer yellow-labelled products were separated by HPLC and quantified by their fluorescence (see 7Methods). The results show that the PA700-isopeptidase releases products progressively from the distal ends of Ub_n oligomers, as is illustrated here schematically for the end-labelled trimer.

PA700 isopeptidase. As potential substrates, fluorescent K48-linked Ub_n oligomers were synthesized with the label on the proximal Ub (see Fig. 3a, b). With fluorescently labelled Ub_3, the products generated early in the reactions were labelled dimer and unlabelled monomer; fluorescently labelled monomer appeared only as the reaction progressed further (Fig. 3c). This indicates that the PA700-isopeptidase exclusively removed one Ub at a time from the distal end of the chain. In other assays, wild-type Ub at the proximal position did not alter this distal-end specificity, and the rates of disassembly of tetra-, tri- and di-ubiquitins were similar (data not shown). Taken together, these results demonstrate that the PA700 isopeptidase removes Ub from K48-linked polyUb only from the distal end of the chain and without regard to its length.

It had been speculated that conjugate disassembly may serve as a correction mechanism for ATP-dependent proteolysis[23,31], and we postulate that the PA700 isopeptidase could have this function. By processing only from the distal end of a polyUb chain, the PA700-isopeptidase may edit all or most of the (poly)Ub degradation signal from a poorly ubiquitinated conjugate, thereby precluding its

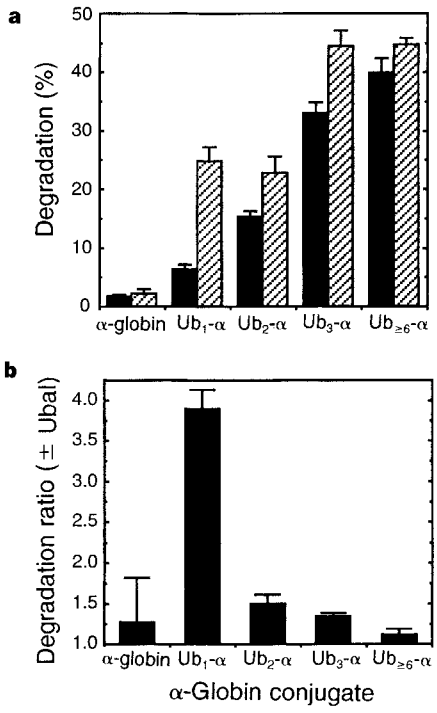

Figure 4 Selectivity of Ub-dependent protein degradation conferred by the PA700 isopeptidase. **a**, 26S proteasomes were assembled from the bovine 20S proteasome and PA700 regulatory complex and, where indicated, were supplemented with Ubal. Degradation reactions were initiated by the addition of ^{125}I-α-globin or Ub$_n$-^{125}I-α-globin (see 7Methods). Substrate degradation was determined after 1 h at 37 °C; degradation levels in mixtures without ATP, typically <1%, have been subtracted. The means and standard deviations of the results from 3 experiments (or, for ^{125}I-α-globin, 2 experiments) are indicated for reactions without Ubal (filled bars) and with 2 μM Ubal (hatched bars). **b**, The data in **a** are represented for each substrate as the ratio of its degradation in the presence of 2 μM Ubal divided by the degradation without Ubal.

degradation. Consequently, this enzyme has the potential to bias protein degradation by the 26S proteasome towards highly ubiquitinated substrates. To test this possibility, 26S proteasomes and radiolabelled Ub$_n$-α-globin (where $n = 0$, 1, 2, 3 or ≥6) were incubated with and without Ubal to assess the effect of the PA700 isopeptidase upon degradation (Fig. 4). The dependence on Ub of these reactions is evident from the very low level of degradation observed with free α-globin. In mixtures without Ubal, the most extensively ubiquitinated α-globin conjugates were, as expected, degraded most rapidly. With Ubal to inhibit the isopeptidase, degradation of the lower-order conjugates, and Ub$_1$-α-globin in particular, was enhanced markedly, whereas the degradation of Ub$_{\geq 6}$-α-globin was relatively unchanged.

The editing ability of the PA700 isopeptidase is not determined by an inherent preference for the length of the polyUb chain or by recognition of the degradation substrate. Rather, by progressively cutting the (poly)Ub moiety of a conjugate from its distal end, a poorly ubiquitinated substrate bound to the proteasome can be deubiquitinated and released before its degradation ensues. Thus PA700 provides two different mechanisms that promote the specificity of Ub-dependent degradation. In the first, highly polyubiquitinated conjugates are bound preferentially (for example, through the S5a subunit[22]). In the second, conjugate disassembly by the isopeptidase is a final safeguard against the proteolysis of poorly, and perhaps erroneously, ubiquitinated proteins.

The isopeptidase activity within the PA700 complex may serve other important functions for Ub-dependent proteolysis. Localization of the proteasome's catalytic sites to the interior of a central channel suggests that ubiquitinated proteins initially bound to PA700 must be translocated to those sites; shortening of polyUb chains might facilitate this process. Furthermore, because the 13-Å opening of the channel can probably accommodate only a single unfolded polypeptide[9–11], deubiquitination may be essential for the complete degradation of a substrate. The PA700 isopeptidase may also promote the release of partly degraded proteins from the 26S proteasome, such as in the case of the limited proteolysis required for activation of the NF-κB precursor p105 (ref. 24). □

Methods

Ub isopeptidase activity assays. Assay mixtures (10 μl) contained reaction buffer (50 mM Tris-HCl, pH 8 at 37 °C, 10 mM $MgCl_2$ and 5 mM DTT) and either PA700, Ubal, ATP or 20S proteasomes. 26S proteasomes were assembled by preincubation of bovine PA700 and 20S proteasomes with 60 μM ATP[25]; when Ubal was included, the preincubation was continued for 5 min after its addition. Assays were initiated by the addition of substrate. With ^{125}I-Ub$_2$ (1.6 μM; 2×10^4 c.p.m. pmol^{-1}), the products after 30 min at 37 °C were analysed by SDS–PAGE (16% acrylamide) and autoradiography, and radioactivity was quantified with a Packard InstantImager. Assays with non-radioactive Ub$_2$ were analysed by cation-exchange HPLC (TSK SP-NPR column eluted at 1.25 mL min^{-1} with 0.05–0.45 M NaCl in 25 mM NH_4OAc, pH 4.5) with detection at 235 nm.

Glycerol gradient centrifugation. PA700 (0.71 μM) and ^{125}I-Ubal (0.59 μM) in reaction buffer were incubated at room temperature for 10 min and then applied onto a 4.55 ml gradient of 10–40% glycerol in 20 mM Tris-HCl, pH 7.6, and 1 mM DTT. After centrifugation at 4 °C (ref. 26), 0.2 ml fractions were collected. ^{125}I-radioactivity was measured by γ-counting, and PA700 by its activation of the 20S proteasome peptidase[25].

Synthesis of isopeptidase inhibitors and Ub derivatives. Ubal was synthesized essentially by a previous method[27] modified in that the Ub-diol intermediate was made by carboxypeptidase Y-catalysed exchange of (±)-3-amino-1,2-propanediol for Gly 76 of Ub. UbCN was prepared similarly by the exchange of aminoacetonitrile for Gly 76 (R. E. Cohen *et al.*, manuscript in preparation). The fluorescent dye Lucifer yellow was incorporated by reaction of the iodoacetamide derivative (Molecular Probes) with Ub(T66C)-diol, a mutant form of Ub with a single Cys residue[28] and whose C terminus was converted to a diol as described above. All Ub derivatives were purified by cation-exchange chromatography with a POROS HS/H column.

Affinity labelling of the PA700 isopeptidase by ^{125}I-UbCN. UbCN was radioiodinated with carrier-free Na^{125}I and chloramine T to 1.6×10^3 c.p.m. pmol^{-1} and was used within 10 days of preparation. PA700 and ^{125}I-UbCN, each 1.1 μM, were incubated at pH 7 in 20 mM Tris-HCl, 20 mM NaCl, 1 mM EDTA, 5 mM β-mercaptoethanol, and 10% glycerol for 5 min at 37 °C; SDS in 0.1 M HCl then was added to make the mixture 1% SDS, pH 2.2. After 90 min at 30 °C, SDS–PAGE loading buffer with or without 5% β-mercaptoethanol was added and the proteins were analysed by SDS–PAGE and autoradiography. In assays with Ub$_2$ as the substrate, inhibition by UbCN of the PA700-isopeptidase indicated a K_i of <1 μM (S. Mikesell, Y. A. Lam and R. E. Cohen, unpublished results).

Fluorescently labelled polyubiquitin chains. Synthesis of K48-linked polyUb chains was done with a 1:1 mixture of Ub(T66C-Lucifer yellow)diol and wild-type Ub and purified Ub-activating (E1) and conjugating (E2$_{25K}$) enzymes essentially as described[29]. Labelled and unlabelled oligomers were resolved by cation-exchange HPLC (POROS HS/H column eluted at 4 ml min^{-1} with 0.05–0.85 M NaCl in 25 mM NH_4OAc, pH 4.5); protein absorbance (235 nm) and Lucifer yellow fluorescence (ex. 426 nm, em. 530 nm) were monitored. For disassembly reactions, mixtures (10 μl) containing 1 μM

Ub-Ub-Ub(T66C-Lucifer yellow)diol trimers, 8 nM PA700, and reaction buffer were incubated at 37 °C, stopped by the addition of 90 μl of 1 M acetic acid, and the products labelled with Lucifer yellow were separated by cation-exchange HPLC (TSK SP-NPR column eluted at 1.25 ml min^{-1} with 0.05–0.45 M NaCl in 25 mM NH_4OAc, pH 4.5) and quantified by their fluorescence (ex. 426 nm, em. 530 nm).

Degradation of Ub_n-α-globin conjugates. Gel-purified ^{125}I–α-globin and Ub_n–^{125}I-α-globin conjugates were prepared[30]. 26S proteasomes were assembled[25] by preincubation at 37 °C of 20S proteasomes (12 μg ml^{-1}) and PA700 (40 μg ml^{-1}) in 0.1 M Tris-HCl, pH 7.25, with 10 mM DTT, 40 μg ml^{-1} bovine serum albumin, 10 mM $MgCl_2$, and 60 μM ATP; after 40 min, some mixtures were supplemented with 4 μM Ubal, and the preincubation was continued for a further 5 min. Degradation reactions were initiated by mixing 10 μl of ^{125}I-labelled conjugates in 2 mM ATP with 10 μl of the 26S proteasomes; the final reaction mixtures contained 2–4 nM (~10^3 c.p.m.) of a conjugate. After incubation at 37 °C, substrate degradation was assayed as the fraction of ^{125}I-radioactivity that was soluble in cold 10% trichloracetic acid[8].

Received 15 October; accepted 19 December 1996.

1. Ciechanover, A. *Cell* **79,** 13–21 (1994).
2. Hochstrasser, M. *Curr. Opin. Cell Biol.* **7,** 215–223 (1995).
3. Hilt, W. & Wolf, D. H. *Trends Biochem. Sci.* **21,** 96–102 (1996).
4. Hershko, A. & Heller, H. *Biochem. Biophys. Res. Commun.* **128,** 1079–1086 (1985).
5. Chau, V. *et al. Science* **243,** 1576–1583 (1989).
6. Hochstrasser, M., Ellison, M. J., Chau, V. & Varshavsky, A. *Proc. Natl Acad. Sci. USA* **88,** 4606–4610 (1991).
7. Finley, D. *et al. Mol. Cell. Biol.* **14,** 5501–5509 (1994).
8. Shaeffer, J. R. & Cohen, R. E. *Biochemistry* **35,** 10886–10893 (1996).
9. Rubin, D. M. & Finley, D. *Curr. Biol.* **5,** 854–858 (1995).
10. Coux, O., Tanaka, K. & Goldberg, A. L. *Annu. Rev. Biochem.* **65,** 801–847 (1996).
11. Stock, D. *et al. Curr. Opin. Biotechnol.* **7,** 376–385 (1996).
12. DeMartino, G. N. *et al. J. Biol. Chem.* **269,** 20878–20884 (1994).
13. Pickart, C. M. & Rose, I. A. *J. Biol. Chem.* **261,** 10210–10217 (1986).
14. Hershko, A. & Rose, I. A. *Proc. Natl Acad. Sci. USA* **84,** 1829–1833 (1987).
15. Eytan, E., Armon, T., Heller, H., Beck, S. & Hershko, A. *J. Biol. Chem.* **268,** 4668–4674 (1993).
16. Papa, F. R. & Hochstrasser, M. *Nature* **366,** 313–319 (1993).
17. Larsen, C. N., Price, I. S. & Wilkinson, K. D. *Biochemistry* **35,** 6735–6744 (1996).
18. Moon, J. B., Coleman, R. S. & Hanzlik, R. P. *J. Am. Chem. Soc.* **108,** 1350–1351 (1986).
19. Liang, T.-C. & Abeles, R. H. *Arch. Biochem. Biophys.* **252,** 626–634 (1987).
20. Dufour, E., Storer, A. C. & Menard, R. *Biochemistry* **34,** 9136–9143 (1995).
21. Chaturvedi, R. K., MacMahon, A. E. & Schmir, G. L. *J. Am. Chem. Soc.* **80,** 6984–6993 (1967).
22. Deveraux, Q., Ustrell, V., Pickart, C. & Rechsteiner, M. *J. Biol. Chem.* **269,** 7059–7061 (1994).
23. Hershko, A., Ciechanover, A., Heller, H., Haas, A. L. & Rose, I. A. *Proc. Natl Acad. Sci. USA* **77,** 1783–1786 (1980).
24. Palombella, V. J., Rando, O. J., Goldberg, A. L. & Maniatis, T. *Cell* **78,** 773–785 (1994).
25. Ma, C.-P., Vu, J. H., Proske, R. J., Slaughter, C. A. & DeMartino, G. N. *J. Biol. Chem.* **269,** 3539–3547 (1994).
26. Ma, C.-P., Slaughter, C. A. & DeMartino, G. N. *J. Biol. Chem.* **267,** 10515–10523 (1992).
27. Dunten, R. L. & Cohen, R. E. *J. Biol. Chem.* **264,** 16739–16747 (1989).
28. Ecker, D. J. *et al. J. Biol. Chem.* **264,** 1887–1893 (1989).
29. Beal, R., Deveraux, Q., Xia, G., Rechsteiner, M. & Pickart, C. *Proc. Natl Acad. Sci. USA* **93,** 861–866 (1996).
30. Shaeffer, J. R. & Kania, M. A. *Biochemistry* **34,** 4015–4021 (1995).
31. Ellison, M.J. & Hochstrasser, M. *J. Biol. Chem.* **226,** 21150–21157 (1991).

Acknowledgements. We thank J. Schaeffer for guidance in the production of the α-globin derivatives; S. Mikesell for the preparation of UbCN; C. Pickart for diubiquitin and $E2_{25K}$; D. Price for help with figure preparation; and M. Hochstrasser, C. Pickart and A. Robertson for discussions and comments on the manuscript. This work is in partial fulfillment of the Ph.D. in Biochemistry to Y.A.L. from the University of California at Los Angeles, and was supported by NIH grants to R.E.C. and G.N.D.

Correspondence and requests for materials should be addressed to R.E.C.

Control of telomere length by the human telomeric protein TRF1

Bas van Steensel & Titia de Lange

The Rockefeller University, 1230 York Avenue, New York, New York 10021, USA

Human telomeres, the nucleoprotein complexes at chromosome ends, consist of tandem arrays of TTAGGG repeats bound to specific proteins. In normal human cells, telomeres shorten with successive cell divisions[1,2], probably due to the terminal sequence loss that accompanies DNA replication. In tumours and immortalized cells, this decline is halted through the activation of telomerase[3–5], a reverse transcriptase that extends the telomeric TTAGGG-repeat arrays[6–7]. Telomere length is stable in several immortal human-cell lines[3], suggesting that a regulatory mechanism exists for limiting telomere elongation by telomerase. Here we show that the human telomeric-repeat binding factor TRF1 (ref. 8) is involved in this regulation. Long-term overexpression of TRF1 in the telomerase-positive tumour-cell line HT1080 resulted in a gradual and progressive telomere shortening. Conversely, telomere elongation was induced by expression of a dominant-negative TRF1 mutant that inhibited binding of endogenous TRF1 to telomeres. Our results identify TRF1 as a suppressor of telomere elongation and indicate that TRF1 is involved in the negative feedback mechanism that stabilizes telomere length. As TRF1 does not detectably affect the expression of telomerase, we propose that the binding of TRF1 controls telomere length *in cis* by inhibiting the action of telomerase at the ends of individual telomeres.

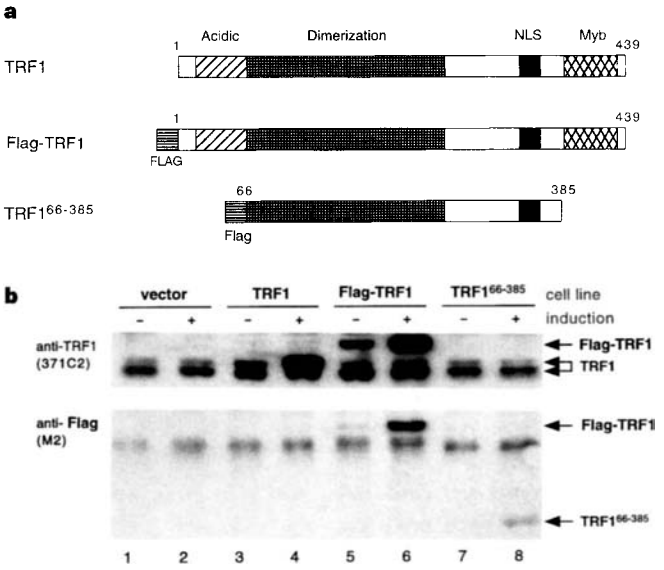

Figure 1 Tetracyclin-regulated expression of TRF1 proteins in HT1080 cells. **a**, Domain structure of TRF1 proteins used in this study. NLS, putative nuclear localization signal. **b**, Western analysis of inducible TRF1 expression in HTC75 clones. Whole-cell extracts from induced and uninduced cells were analysed using anti-TRF1 antibody 371C2 or anti-Flag monoclonal antibody M2. Endogenous TRF1 is represented by a doublet: the top band co-migrates with the transfected full-length protein (lane 4). The bottom band of the doublet probably represents an alternatively spliced form of TRF1 that lacks 20 amino acids in the non-conserved region of the protein (J. Karlseder and T.d.L., unpublished observations).

Mammalian telomeres show a species-specific length setting[9] which suggests that a regulatory mechanism exists to control telomere length in the germ line. Telomere-length control is also evident from the stability of telomeres in telomerase-expressing cell lines[3] and from the observation that newly formed telomeres acquire a length appropriate for the host cell[10,11]. The latter observation suggests that cells monitor and modulate the length of individual telomeres, a process that is likely to involve a protein that binds to the duplex telomeric repeat region at mammalian chromosome ends. A candidate for this function is TRF1, a duplex telomeric TTAGGG-repeat binding protein that is associated with human and mouse telomeres in interphase and in mitosis[8,12–15].

To investigate the role of TRF1 in the regulation of telomere length, we studied the effects of long-term overexpression of wild-type TRF1 and of a dominant-negative mutant on telomere length in a telomerase-positive human tumour-cell line with stable telo-

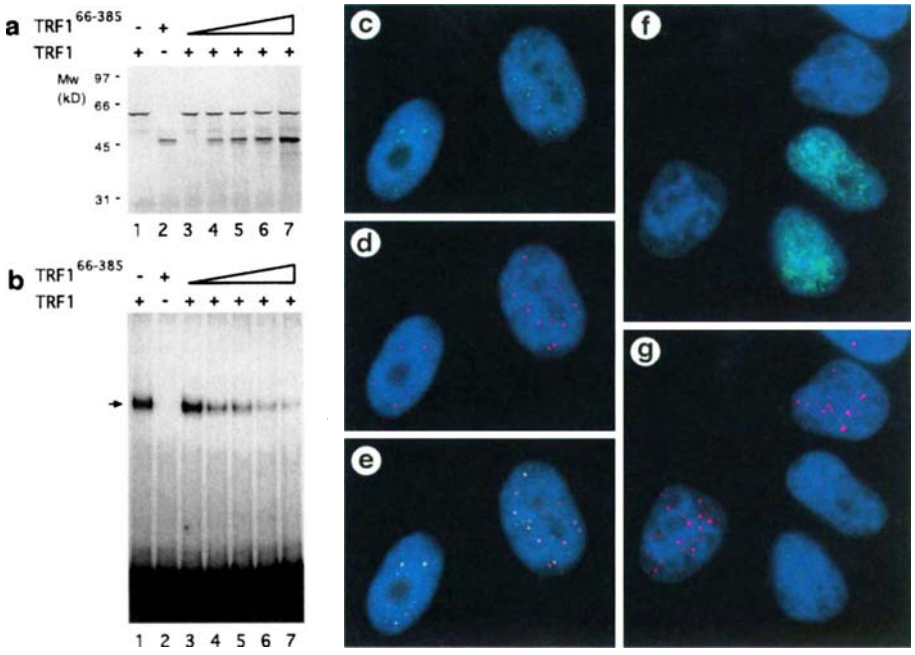

Figure 2 Characterization of the dominant interfering activity of TRF1$^{66-385}$. **a**, ^{35}S-Met-labelled translation of full-length TRF1 *in vitro* with increasing amounts of TRF1$^{66-385}$. **b**, TTAGGG-repeat binding activity (arrow) obtained with unlabelled proteins synthesized in parallel with **a**. **c–e**, Co-localization of endogenous TRF1 with telomeric DNA in HeLa interphase nuclei. **c**, TRF1 detected with antibody 371C2 (green); **d**, telomeric DNA visualized in the same nuclei with a $[CCCUAA]_{27}$ RNA probe (red); and **e**, superimposition of **c** and **d**. **f**, **g**, Overexpression of TRF1$^{66-385}$ inhibits binding of endogenous TRF1 to telomeres. HeLa cells transiently co-transfected with the tTA expression construct[16] and the TRF1$^{66-385}$ construct were stained in **f** for TRF1$^{66-385}$ using the Flag tag antibody (M2) (green) and in **g** for endogenous TRF1 with antibody 371C2 (red). DNA was stained with DAPI (4,6-diamidino-2-phenylindole) (blue).

meres. We established a tetracycline-controlled gene-expression system[16] in the human fibrosarcoma cell line HT1080 (resulting in cell line HTC75) and used it for inducible expression of full-length TRF1, a TRF1 protein containing an N-terminal Flag epitope (Flag-TRF1) and a TRF1-deletion mutant encompassing amino acids 66–385 (TRF1$^{66-385}$) (Fig. 1a). Analysis by western blotting showed that doxycyclin controlled expression of each of these TRF1 proteins in clonal HTC75 cell lines transfected with the constructs (Fig. 1b). Induced overexpression of full-length TRF1 and of Flag-TRF1 also resulted in a 10–30-fold increase in the TTAGGG-repeat binding activity[12] (data not shown). Expression of TRF1$^{66-385}$ protein was consistently low compared with other TRF1 proteins (Fig. 1b, and data not shown). Expression of wild-type or mutant TRF1 proteins did not affect the viability or growth rate of the cells (data not shown).

Based on the architecture of TRF1, the deletion mutant TRF1$^{66-385}$ was expected to act as a dominant-negative mutant. TRF1 binds telomeric DNA *in vitro* as a homodimer, using a large dimerization domain to position two identical Myb-related DNA-binding motifs on its telomeric recognition site[17]. TRF1$^{66-385}$ contains the dimerization domain and putative nuclear localization sequences, but lacks the DNA-binding motif (Fig. 1a), suggesting that it might inhibit wild-type TRF1 by forming an inactive heterodimer. We tested the ability of TRF1$^{66-385}$ to inhibit DNA binding of wild-type TRF1 in a gel-shift assay with *in vitro* translated proteins. As expected, wild-type TRF1 formed a complex with telomeric DNA, whereas TRF1$^{66-385}$ showed no DNA-binding activity (Fig. 2b, lanes 1 and 2). Co-translation of TRF1 and TRF1$^{66-385}$ (Fig. 2a, lanes 3–7) under conditions that allow dimerization[17] showed that TRF1$^{66-385}$ caused a dose-dependent inhibition of the DNA-binding activity of TRF1 (Fig. 2b, lanes 3–7), indicating that TRF1$^{66-385}$ is a dominant-negative mutant.

Evidence was obtained that this dominant-negative effect on DNA binding resulted in loss of TRF1 from telomeres *in vivo*. Immunofluorescent labelling using a rabbit polyclonal antibody affinity-purified against the acidic domain of TRF1 (antibody 371C2; see 7Methods), combined with fluorescent *in situ* hybridization (FISH) using a telomere-specific probe, showed that endogenous TRF1 in HeLa cells was distributed in a speckled pattern which coincided with telomeric repeat DNA (Fig. 2c–e). This indicated that endogenous TRF1 was primarily located at telomeres in interphase nuclei. In contrast, immunolocalization of transiently transfected TRF1$^{66-385}$ in HeLa cells using a mouse monoclonal anti-Flag antibody revealed that this protein was distributed throughout the nucleus, regardless of its level of expression (Fig. 2f, and data not shown). Thus, as expected from the deletion of the Myb-homology region, TRF1$^{66-385}$ did not accumulate at telomeres. To test whether the mutant protein affected the localization of the endogenous TRF1 to telomeres, we carried out dual-labelling immunofluorescence with antibody 371C2 to detect endogenous wild-type TRF1 and with an anti-Flag monoclonal antibody to detect TRF1$^{66-385}$. The distribution of endogenous TRF1 was drastically altered in cells that expressed TRF1$^{66-385}$ (Fig. 2f, g). In transfected cells expressing large amounts of TRF1$^{66-385}$, the endogenous TRF1 protein did not show a punctate pattern, indicating that TRF1 was dislodged from the telomeres (Fig. 2g). In general, we observed an inverse correlation between the expression level of TRF1$^{66-385}$ and the staining intensity of endogenous TRF1 on telomeres (data not shown). We presume that displaced TRF1 was present throughout the nucleus, but in amounts too low to reveal a dispersed pattern of immunostaining. These results demonstrated that expression of TRF1$^{66-385}$ reduced the amount of TRF1 detectable on telomeres *in vivo*. Conversely, overexpression of full-length TRF1 in HeLa cells increased TRF1 detectable on the telomeres (data not shown).

Changes in the level of TRF1 expression affected telomere length in HTC75 cells. A control HTC75 cell line transfected with the vector had stable telomeres over 124 population doublings and

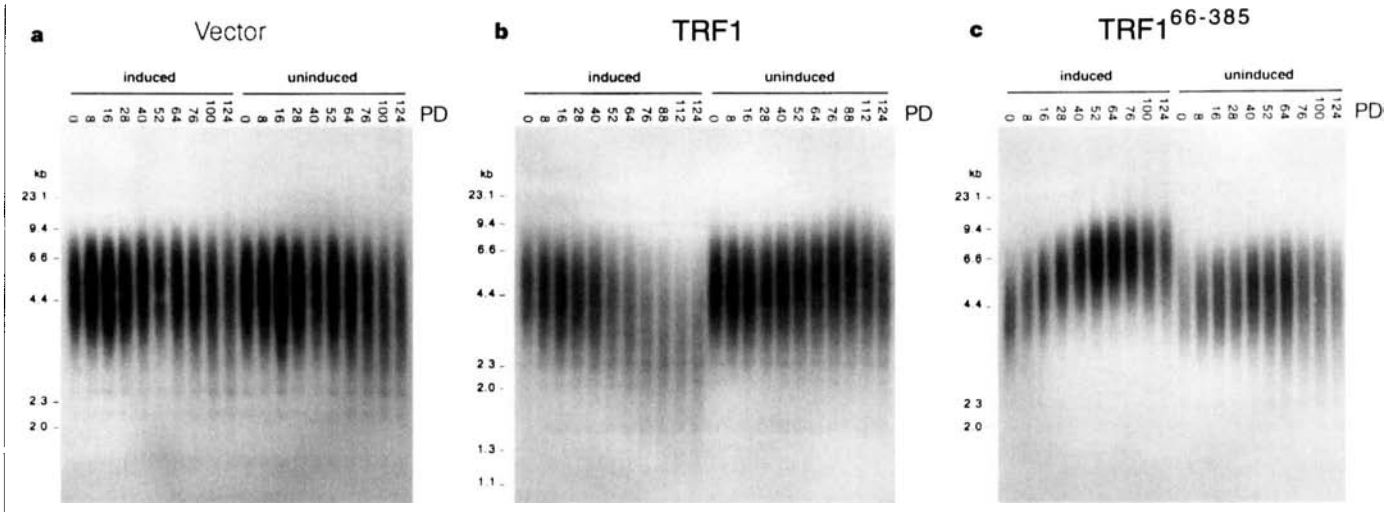

Figure 3 Telomere length changes in response to TRF1. **a–c**, Southern blots of *Hin*fI/*Rsa*I-digested genomic DNA from three clonal HTC75 cell lines (**a**, B6; **b**, D4; **c**, K10) expressing the indicated TRF1 genes. Each cell line was passaged for 124 PD in the presence (uninduced) or absence (induced) of doxycyclin and DNA samples were analysed at the indicated PDs. Blots were probed with a TTAGGG-repeat probe to detect telomeric restriction fragments.

there was no effect of doxycyclin on telomere length (Fig. 3a and Table 1). In contrast, cells overexpressing TRF1 showed gradual and progressive telomeric decline when grown under inducing conditions (Fig. 3b). The loss of telomeric sequences was evident from the shortening of the terminal restriction fragments and from a reduction in the TTAGGG repeat signal. Telomeres shortened in 4 out of 5 cell lines overexpressing either full-length or Flag-tagged TRF1 (Table 1). In three clones (D4, D16, and C20), the decline was strongly dependent on the absence of doxycyclin. One clone (C14), which expressed Flag-tagged TRF1 in considerable amounts and independently of induction (data not shown), showed a moderate loss of telomeric DNA both in the induced and non-induced state. These results implicated TRF1 in the regulation of telomere length. The rate of telomere shortening varied in the different cell lines from 3 to 11 base pairs (bp) per population doubling (Table 1).

In contrast, HTC75 cells expressing the dominant-negative mutant $TRF1^{66-385}$ showed a gradual increase in telomere length. In the K10 clone (Fig. 3c), telomeres showed progressive elongation over ~80 population doublings at a rate of ~35 bp per population doubling. Eventually the telomeres stabilized, suggesting that a feedback mechanism was operating, like that in budding yeast[18–20]. At this stage in the K10 culture, telomere length remained under the control of the dominant-negative form of TRF1 because repression of the gene at PD104 with doxycyclin induced a gradual shortening of the telomeres (data not shown).

Telomere elongation was also induced in four additional independent HTC75 clones expressing $TRF1^{66-385}$ (Table 1). In each case, telomere elongation was enhanced in the absence of doxycyclin, indicating that the effect is due to expression of the $TRF1^{66-385}$ protein. The altered dynamics appeared to affect all telomeres to about the same degree, leading to a gradual uniform elongation. After extensive growth of the cell lines (88 population doublings), the telomeres had elongated by 0.5–2.9 kilobases (kb) (Table 1). We estimated that the terminal restriction fragments visualized by genomic blotting (Fig. 3) harboured ~1.5 kb of subtelomeric DNA (see 7Methods). On the basis of this estimate, we infer that the telomere alterations in the $TRF1^{66-385}$-expressing cell lines represent a 20–105% increase in the length of the telomeric repeat array. There was a commensurate increase in the TTAGGG repeat signal (Fig. 3c, and data not shown).

Telomere length in human cell lines can be maintained in two ways: either by telomerase-mediated elongation[6,7] or in a telomerase-independent pathway that may involve recombination (known as alternative lengthening of telomeres, or ALT[21]). The gradual, rather than sudden, elongation of telomeres in cells expressing $TRF1^{66-385}$ is consistent with telomerase-mediated telomere maintenance. Furthermore, whereas the ALT pathway results in telomeres that are heterogeneous in length, often extending over a range of 30 kb, telomeres in the $TRF1^{66-385}$-expressing cell lines maintain roughly the same length heterogeneity as the starting population (Fig. 3c). These results suggest that TRF1 regulates the telomerase-dependent pathway of telomere-length maintenance.

We investigated whether TRF1 controls the expression of telomerase by using a polymerase chain reaction(PCR)-based TRAP assay[5,22]. In this assay, soluble telomerase in cell extracts extends a non-telomeric single-stranded substrate with arrays of TTAGGG repeats. As TRF1 only binds to duplex telomeric DNA[12], neither the TRAP-assay substrate nor the telomerase products will be associated with TRF1. The TRAP assay data therefore represent an approximation of the soluble telomerase present in the cell and do not reflect any interaction between telomerase and TRF1 at telomeres. Similar telomerase activity was detected in each of the cell lines shown in Table 1 and no difference was found between cells grown in the presence or absence of doxycyclin (data not shown). These results eliminated the possibility that TRF1 modulates telomere dynamics through a major effect on either the expression of telomerase or its activity in the TRAP assay.

Taken together, our findings showed that one function of TRF1 is to control telomere length, revealing an interesting parallel with the yeast telomeric proteins Rap1 and Taz1 (refs 23–26). The proposed role of Rap1 is to regulate telomere-length in budding yeast[23,25,27,28], and TRF1 likewise is inferred to have a negative effect on telomere-length maintenance by telomerase. As TRF1 affected telomere length without altering telomerase activity in cell extracts, we propose that the TRF1 provides a negative feedback signal to telomerase at individual telomeres. Although TRF1 may function less directly, we favour the possibility that TRF1 controls telomere maintenance by binding to telomeres. Such a *cis*-acting mechanism can explain how cells can monitor and regulate the length of individual telomeres[10,11]. According to this view, longer telomeres (elongated by telomerase) would recruit more of the telomerase

Table 1 Telomere-length control by TRF1

HTC75 clone	TRF1 construct	Δ Telomere length at PD88	
		+Dox	− Dox
B6	Vector	− 0.1 kb	0.0 kb
D4	Full-length TRF1	+0.2 kb	− 1.0 kb
D16	Full-length TRF1	− 0.1 kb	− 0.6 kb
D20	Full-length TRF1	+0.2 kb	+0.7 kb
C14	Flag-TRF1	− 0.3 kb	− 0.3 kb
C20	Flag-TRF1	+0.2 kb	− 0.6 kb
K4	$TRF1^{66-385}$	− 0.8 kb	+0.5 kb
K10	$TRF1^{66-385}$	+0.1 kb	+2.4 kb
K15	$TRF1^{66-385}$	+0.1 kb	+2.8 kb
K16	$TRF1^{66-385}$	+0.7 kb	+2.9 kb
K17	$TRF1^{66-385}$	+0.1 kb	+1.0 kb

PD, population doubling; Dox, doxycyclin.

inhibitor TRF1 than shorter telomeres would, causing elongated telomeres to exert a stronger negative feedback on telomerase and inhibit the enzyme. Such telomeres will shorten with successive rounds of replication until they no longer bind sufficient TRF1 to inhibit telomerase. The resulting telomere length homeostasis is a dynamic process governed by the amount of TRF1 on the telomere and the activity of telomerase. However, it is not excluded that TRF1 modulates telomere length by altering the rate at which telomeres are shortened. As telomere dynamics have been implicated in human ageing and cancer[2–5,29,30], it will be interesting to see how TRF1 contributes to changes in the length of human telomeres in normal, ageing and malignant cells. □

Methods

Inducible gene expression system. HT1080 cells were stably co-transfected with the tetracyclin-controlled transactivator (tTA) expression vector pUHD15-1 (ref. 16) and plasmid pBPGKHyg containing the hygromycin-resistance gene expressed from the PGK (phosphoglycerol kinase) promoter. About 50 hygromycin-resistant clones were expanded and tested for expression of transiently transfected luciferase reporter plasmid pUHC13-1 (ref. 16) in the absence or presence of doxycyclin (100 ng ml^{-1}). Clone HTC75 showed a ~100-fold increase in luciferase expression upon withdrawal of doxycyclin. Next, HTC75 cells were stably co-transfected with the neomycin-resistance plasmid pSXneo[11] and TRF1, Flag-TRF1 or $TRF1^{66-385}$ cloned into the tTA-regulated expression vector pUHD10-3 (ref. 16). For each construct, about 25 G418-resistant clones were expanded in the presence of doxycyclin and tested for inducible expression of the appropriate protein by immunofluorescence microscopy and western blotting using anti-Flag antibody M2 (Eastman–Kodak) and gel-shift analysis of whole-cell extracts using a telomeric-repeat probe[12].

Long-term cell culture. Cells were grown in DMEM supplemented with 10% bovine calf serum (Irving Science). Clones indicated in the text were passaged 1:16 when ~80% confluent (typically every 3 days). All clones were grown in parallel with or without doxycyclin (Sigma; 100 ng ml^{-1}). Addition of hygromycin (90 μg ml^{-1}) or G418 (150 μg ml^{-1}) to culture media was alternated every two weeks.

Antibodies. Antibody 371C2 against the acidic domain of TRF1 was affinity-purified in two steps from a rabbit polyclonal serum raised against baculovirus-expressed TRF1 protein (bacTRF1)[17]. The antiserum was purified against bacTRF1 coupled to CNBr-activated agarose and subsequently purified against a bacterially expressed fusion protein consisting of glutathione-S-transferase and residues 19–71 of TRF1. Antibody 371C2 did not crossreact with other parts of TRF1 (M. Schäfer, B.v.S. and T.d.L., unpublished observations). The following secondary antibodies were used in the experiments shown in Fig. 2: TRF1 detection with 371C2 was achieved with FITC-conjugated donkey anti-rabbit antibody (Fig. 2c), or with a Cy3-conjugated donkey anti-rabbit antibody (Fig. 2g). For FISH, digoxigenin-labelled RNA[8] was detected with a sheep anti-digoxigenin antibody (Boehringer) and a TRITC-conjugated donkey anti-sheep IgG. The Flag-tagged protein was detected with a monoclonal M2 (Kodak), followed by FITC-labelled donkey anti-mouse. All fluorochrome-conjugated antibodies (Jackson ImmunoResearch Labs) were multilabelling grade. Control experiments indicated that there was no cross-reactivity between antibodies.

Whole-cell extracts. Cells grown to ~80% confluence in 10-cm dishes were collected by scraping in PBS, then pelleted and incubated for 30 min at 4 °C in 250 μl buffer C[8] with 0.2% Nonidet P-40. After centrifugation (10 min at 14,000*g*) the supernatant was dialysed against buffer D[8] and stored at − 70 °C until use in gel-shift assays, western blotting and TRAP assays. Protein was determined by the Bradford assay (BioRad).

Genomic blotting and telomere-length estimation. Genomic DNA was isolated from cells at the indicated population doublings (PDs), digested to the completion with *Hin*fI and *Rsa*I and quantified by fluorometry using Hoechst 33258 dye. Genomic blots were prepared as described[13]. The median telomeric restriction-fragment length was determined by PhosphorImager analysis using ImageQuant software and not corrected for the dependence of signal strength on telomere length. The length of the subtelomeric DNA on the *Hin*fI/*Rsa*I fragments was estimated[3] to be ~1.5 kb.

Received 4 December; accepted 31 December 1996.

1. Cooke, H. J. & Smith, B. A. Variability at the telomeres of the human X/Y pseudoautosomal region. *Cold Spring Harbor Symp. Quant. Biol.* **L1**, 213–219 (1986).
2. Harley, C. B., Futcher, A. B. & Greider, C. W. Telomeres shorten during ageing of human fibroblasts. *Nature* **345**, 458–460 (1990).
3. Counter, C. M. *et al.* Telomere shortening associated with chromosome instability is arrested in immortal cells which express telomerase activity. *EMBO J.* **11**, 1921–1929 (1992).
4. Counter, C. M., Hirte, H. W., Bacchetti, S. & Harley, C. Telomerase activity in human ovarian carcinoma. *Proc. Natl Acad. Sci. USA* **91**, 2900–2904 (1994).
5. Kim, N. W. *et al.* Specific association of human telomerase activity with immortal cells and cancer. *Science* **266**, 2011–2015 (1994).
6. Morin, G. B. The human telomere terminal transferase enzyme is a ribonucleoprotein that synthesizes TTAGGG repeats. *Cell* **59**, 521–529 (1989).
7. Feng, J. *et al.* The RNA component of human telomerase. *Science* **269**, 1236–1241 (1995).
8. Chong, L. *et al.* A human telomeric protein. *Science* **270**, 1663–1667 (1995).
9. Kipling, D. & Cooke, H. J. Hypervariable ultra-long telomeres in mice. *Nature* **347**, 347–402 (1990).
10. Barnett, M. *et al.* Telomere directed fragmentation of mammalian chromosomes. *Nucleic Acids Res.* **21**, 27–36 (1993).
11. Hanish, J. P., Yanowitz, J. & de Lange, T. Stringent sequence requirements for telomere formation in human cells. *Proc. Natl Acad. Sci. USA* **91**, 8861–8865 (1994).
12. Zhong, Z., Shiue, L., Kaplan, S. & de Lange, T. A mammalian factor that binds telomeric TTAGGG repeats *in vitro*. *Mol. Cell. Biol.* **13**, 4834–4843 (1992).
13. Ludérus, M. E. E. *et al.* Structure, subnuclear distribution, and nuclear matrix association of the mammalian telomeric complex. *J. Cell. Biol.* **135**, 867–883 (1996).
14. Broccoli, D. *et al.* Comparison of the human and mouse genes encoding the telomeric protein, TRF1: chromosomal localization, expression, and conserved protein domains. *Hum. Mol. Genet.* **6**, 69–76 (1997).
15. Smith, S. & de Lange, T. TRF1, a mammalian telomeric protein. *Trends Genet.* **13**, 21–26 (1997).
16. Gossen, M. & Bujard, H. Tight control of gene expression in mammalian cells by tetracyclin-responsive promoters. *Proc. Natl Acad. Sci. USA* **89**, 5547–5551 (1992).
17. Bianchi, A., Smith, S., Chong, L., Elias, P. & de Lange, T. TRF1 is a dimer and bends telomeric DNA. *EMBO J.* (in the press).
18. Carson, M. J. & Hartwell, L. CDC17: An essential gene that prevents telomere elongation in yeast. *Cell* **42**, 249–257 (1985).
19. Lustig, A. J. & Petes, T. D. Identification of yeast mutants with altered telomere structure. *Proc. Natl Acad. Sci. USA* **83**, 1398–1402 (1986).
20. Shampay, J. & Blackburn, E. H. Generation of telomere-length heterogeneity in Saccharomyces cerevisiae. *Proc. Natl Acad. Sci. USA* **85**, 534–538 (1988).
21. Bryan, T. M. & Reddel, R. R. Telomere dynamics and telomerase activity in *in vitro*-immortalised human cells. *Eur. J. Cancer* (in the press).
22. Broccoli, D., Young, J. W. & de Lange, T. Telomerase activity in normal and malignant hematopoietic cells. *Proc. Natl Acad. Sci. USA* **92**, 9082–9086 (1995).
23. Conrad, M. N., Wright, J. H., Wolf, A. J. & Zakian, V. A. RAP1 protein interacts with yeast telomeres *in vivo*: Overproduction alters telomere structure and decreases chromosome stability. *Cell* **63**, 739–750 (1990).
24. Lustig, A. J., Kurtz, S. & Shore, D. Involvement of the silencer and UAS binding protein RAP1 in regulation of telomere length. *Science* **250**, 549–553 (1990).
25. Krauskopf, A. & Blackburn, E. H. Control of telomere growth by interactions of RAP1 with the most distal telomeric repeats. *Nature* **383**, 354–357 (1996).
26. Cooper, J., Nimmo, E., Allshire, R. & Cech, T. *Nature* (this issue).
27. McEachern, M. J. & Blackburn, E. H. Runaway telomere elongation caused by telomerase RNA gene mutations. *Nature* **376**, 403–409 (1995).
28. Marcand, S., Gilson, E. & Shore, D. A protein-counting mechanism for telomere length regulation in yeast. *Science* (in the press).
29. Hastie, N. D. *et al.* Telomere reduction in human colorectal carcinoma and with ageing. *Nature* **346**, 866–868 (1990).
30. de Lange, T. *et al.* Structure and variability of human chromosome ends. *Mol. Cell. Biol.* **10**, 518–527 (1990).

Acknowledgements. We thank M. Schäfer for isolation and characterization of the 371C2 TRF1 antibody, H. Bujard for tetracyclin system plasmids, and A. Lustig, R. Lang and members of our laboratory for criticism of this manuscript. This work was supported by grants from the NIH, the Rita Allen Foundation, and the Irma T. Hirschl Foundation (to T.d.L.). B.v.S. is the recipient of a Human Frontier Science Program postdoctoral fellowship.

Correspondence and requests for materials should be addressed to T.d.L. (e-mail: delange@rockvax.rockefeller.edu).

Regulation of telomere length and function by a Myb-domain protein in fission yeast

Julia Promisel Cooper*†, Elaine R. Nimmo‡, Robin C. Allshire‡ & Thomas R. Cech*

* *Howard Hughes Medical Institute, Department of Chemistry and Biochemistry, University of Colorado, Boulder, Colorado 80309, USA*
‡ *MRC Human Genetics Unit, Western General Hospital, Crewe Road, Edinburgh EH4 2XU, UK*
† *Present address: Imperial Cancer Research Fund, Lincoln's Inn Fields, London WC2A 3PX, UK.*

Telomeres, the specialized nucleoprotein structures that comprise the ends of eukaryotic chromosomes[1,2], are essential for complete replication[3–5], and regulation of their length has been a focus of research on tumorigenesis[6–8]. In the budding yeast *Saccharomyces cerevisiae*, the protein Rap1p binds to telomeric DNA and functions in the regulation of telomere length[9–12]. A human telomere protein, hTRF (human TTAGGG repeat factor) binds the telomere sequence *in vitro*[13] and localizes to telomeres cytologically[14], but its functions are not yet known. Here we use a genetic screen to identify a telomere protein in fission yeast, Taz1p (telomere-associated in *Schizosaccharomyces pombe*), that shares homology to the Myb proto-oncogene DNA-binding domain with hTRF. Disruption or deletion of the *taz1*$^+$ gene causes a massive increase in telomere length. Taz1p is required for the repression of telomere-adjacent gene expression and for normal meiosis or sporulation. It may be a negative regulator of the telomere-replicating enzyme, telomerase[1,3], or may protect against activation of telomerase-independent pathways of telomere elongation[8].

S. pombe, like the budding yeasts, is amenable to genetic analysis, and yet the fission and budding yeasts are sufficiently distant evolutionarily that features present in both genera should be widely conserved in eukaryotes[15]. Furthermore, certain properties of *S. pombe* chromosomes, such as centromere structure and chromosome segregation, are more similar to those of larger eukaryotes[16,17].

To explore the telomere structure of fission yeast, a one-hybrid screen[18] was used to identify proteins that bind specifically to the *S. pombe* telomere DNA sequence (Fig. 1a). This screen had two components: an expression library of *S. pombe* cDNAs, each fused to DNA encoding the *S. cerevisiae* GAL4 activation domain, and a *S. cerevisiae* reporter strain containing a target sequence (a 32-mer of *S. pombe* telomeric sequence[19]; Fig. 1b) located adjacent to the GAL4-activatable promoter of a *lacZ* gene. *S. pombe* proteins that bind to the telomeric target sequence recruit the GAL4 activation-domain fusion to the promoter, thereby activating transcription of the *lacZ* reporter gene and yielding a blue colony upon exposure to X-gal.

Of over a million colonies screened, four blue colonies were identified; these harboured distinct cDNAs, but all four contained the gene *taz1*$^+$. The Taz1 fusion protein did not activate *lacZ* transcription when a scrambled version of the telomeric sequence was used as a target (Fig. 1b), indicating the specificity of Taz1p for telomeric repeats.

To determine more precisely the sequence requirements for Taz1–GAL4 activation, strains with smaller tracts of telomeric sequence placed upstream of the *lacZ* reporter were transformed with the *taz1*$^+$–*GAL4* fusion plasmid (Fig. 1b). Three of the four targets resulted in activation by the Taz1p fusion. The only distinguishing feature of the unactivated, presumably unbound, target was the relative deficit of guanine stretches in the sequence; it contains only two G_2 tracts, whereas the activatable sequences have at least one G_3 tract and a G_4 or two G_2 tracts.

DNA sequencing of *taz1*$^+$ revealed its potential to encode a protein of 663 amino acids with a predicted relative molecular

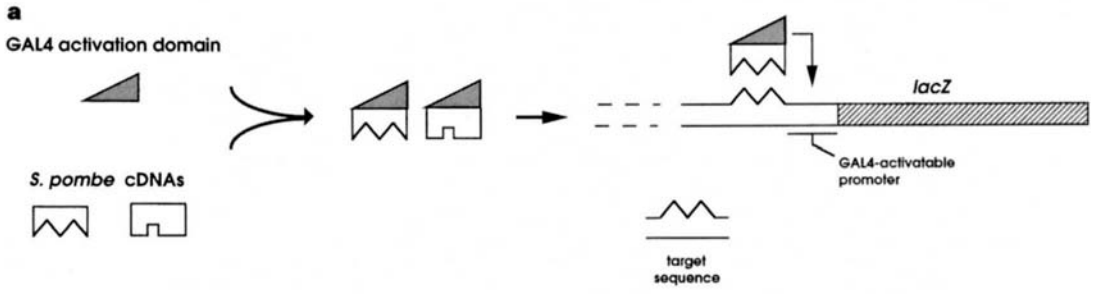

b

Sequence	Colony colour
gatc GGGTTACAAGGTTACGTGGTTACACGGTTACA gatc	blue
gatc GCTATGAATGCAGTAGTCGCGTAGTGTATCGA gatc	white
gatc GGGTTACAAGGTTACG gatc	blue
gatc TGGTTACACGGTTACA gatc	white
gatc GGTTACAGGTTACAGG gatc	blue
gatc GGGTTACAGGGGTTAC gatc	blue

Figure 1 Identification of *taz1*$^+$. **a**, One-hybrid screen for proteins that bind to the telomeric sequence of fission yeast. **b**, Target sequences used in one-hybrid experiments. Underlined are blocks of 5′-GGTTAC-3′, the most frequently occurring repeating unit in *S. pombe* telomeres (most telomere repeats in *S. pombe* conform to the consensus 5′GGTTACA$_{0-1}$C$_{0-1}$G$_{0-6}$-3′; ref. 19). The top sequence is a portion of the telomeric sequence[19] used for the one-hybrid screen. The second line is a randomized version of the first sequence. The colours are for colonies containing the given target sequence when transformed with a *taz1-GAL4* fusion plasmid.

a

```
  1  misvQSTETI QKVLENEGDQ QFDKEVVQNS DSNIETGQIS DSLTKAVEER
 51  AETESSSNLS NFTTSESESS KPAYCFNSHS QNMAEGSISI PVISHSMNVE
101  NEVSTAEGQD SRTGESENDQ NAMIVRSIWD IEKASLLVND CQNIANMAEQ
151  KVMMVSAIFS ESSKDIVNPE SFSERLGKET VKDLYEFNEQ LTTKYGLEFR
201  TIFFSYIRKY DAYWCLFEDL EKPLKSIQFF TGLIDLLDNT NKHLTLRSIV
251  LDALLSADEE DSFYGDALVL FEELVIRYFG TDSNPSIDAS EFILSCLPYT
301  SLDALNVVCG QVWKSQKICD FLKSTIGNTS NSPLQLRASF PAFVNAVIHF
351  LLEFKNVRRL ERKDLSVKGM LYDSDSQQIL NRLRERVSGS TAQSADEASG
401  HESDASEDTF SERTLGLNSI DNTEISEVVS LGLVSSALDK ITGLLSADNL
451  SETVSQARDF SHTLSKSLKS RAKSLSQKEA ANRSKLIAKR GDNLRREASL
501  SSEQDDLSED FPPVRESDEQ ESRSGGRSSA MRVSIERSAA RSGTRRSQGN
551  PYEGYRTRRK WTDEEENELY EMISQHGCCW SKIIHIQKLE NGPLKTFGPT
601  QIKDKARLIK ARFMKQNRLQ ELYSKSLNWK NVTVGQAYCE LHKIPYIEAT
651  PPLLREELVN YQS
```

b

```
                 Helix 1      Helix 2 ..........  Helix 3
Taz1p   RTRRKWTDEEENELYEMISQHG-CCWSKIIHIQKLENG---PLKTFGPTQIKDKARLIKAR
Tbf1p   KAKRTWSKEEEEALVEGLKEVG-PSWSKILDLYGPGGKITENLKNRTQVQLKDKARNWKLQ
hTRF    RKRQAWLWEEDKNLRSGVRKYGEGNWSKILLHY--------KFNNRTSVMLKDRWRTMKKL
```

Figure 2 Sequence and Myb homology of Taz1p. **a**, Sequence of Taz1p. Amino acids deduced from sequences of cDNAs identified in the one-hybrid screen (upper case). The first four amino acids (lower case) were not present in any of the Taz1-Gal4 fusion proteins and were subsequently identified by matching the deduced sequence with portions of the *S. pombe* genome sequenced by the Sanger Centre sequencing project (found on the *S. pombe* blast server; the gene is encompassed by cosmid c16A10D; ref. 30). Amino acids 112–663 were present in all of the Taz1-Gal4 fusions identified in the one-hybrid screen. The region with homology to Myb DNA binding domains is boxed. The arrow indicates the region of the Taz1p coding sequence that is missing in the *taz1*$^-$ disruption strains. **b**, Alignment of Taz1 protein sequence to the Myb-related (telobox) domains of the human TRF protein[14] and *S. cerevisiae* Tbf1p[20]. Amino acids in Taz1p that show identity to at least one of the other two sequences are indicated by bold type. The α-helices 1, 2 and 3 are proposed on the basis of a recent structure-sequence alignment of Myb domain, homeodomain and telomere-binding proteins by D. Rhodes (manuscript in preparation); helix ends are uncertain. The dashed line between helices 2 and 3 denotes a region of length variability[20].

mass of 74,600 (M_r 74.6K) (Fig. 2a). The carboxy-terminal region of the protein contains a 57 amino-acid region of homology with the Myb-related DNA-binding domain from the human telomere protein hTRF (Fig. 2b). This presumed helix–turn–helix motif is also known as the 'telobox' (ref. 20) because it is present in other proteins that bind telomere-like sequences *in vitro*, including the *S. cerevisiae* protein Tbf1p (refs 20–22). These proteins, including Taz1p, contain a single Myb-related domain near their C termini, which distinguishes them from several transcription factors containing multiple Myb domains[20]. The crystal structure of the *S. cerevisiae* Rap1 protein reveals two regions of structural homology to the Myb DNA-binding domain, despite it having only limited sequence homology[23]. Outside the Myb-related domain, Taz1p is acidic and has only slightly more homology with hTRF and Tbf1p (21–22% identity) than with randomly chosen proteins.

To explore the functions of Taz1p *in vivo*, a disruption of *taz1*$^+$ was made in which two-thirds of the gene was deleted (Fig. 2a) and replaced with a selectable marker, the *ura4* gene. Dissection of tetrads derived from the resulting heterozygous *taz1*$^+$/*taz1*$^-$ diploids showed that the two *ura4*$^+$ *taz1*$^-$ spores were viable and that *taz1*$^-$ haploids grow vegetatively at the same rate as cells containing wild-type *taz1*$^+$. A complete deletion of *taz1*$^+$ was also constructed and found not to affect viability.

Telomere length increased dramatically when *taz1*$^+$ was disrupted (Fig. 3) or deleted (data not shown). Two of the three *S. pombe* chromosomes contain *ApaI* restriction sites just centromere-proximal to their telomeric repeats[19]. Digestion of wild-type DNA with *ApaI* gave a broad distribution of telomeric fragments centred around 300 base pairs. In DNA from cells carrying the *taz1* disruption, the telomere band was shifted to a smear of ~2.5–4.5 kilobases. This striking increase in the abundance of telomeric DNA is further underscored by the greater intensity of telomeric hybridization relative to the signal for wild-type telomeric DNA. A similar increase in the intensity of hybridization to the rDNA-adjacent telomeres on chromosome III, which do not contain telomere-proximal *ApaI* sites, was also observed (Fig. 3); an increase in length of fragments as large as the rDNA telomeric fragments may not be detectable with the gel system used. Despite the continual presence

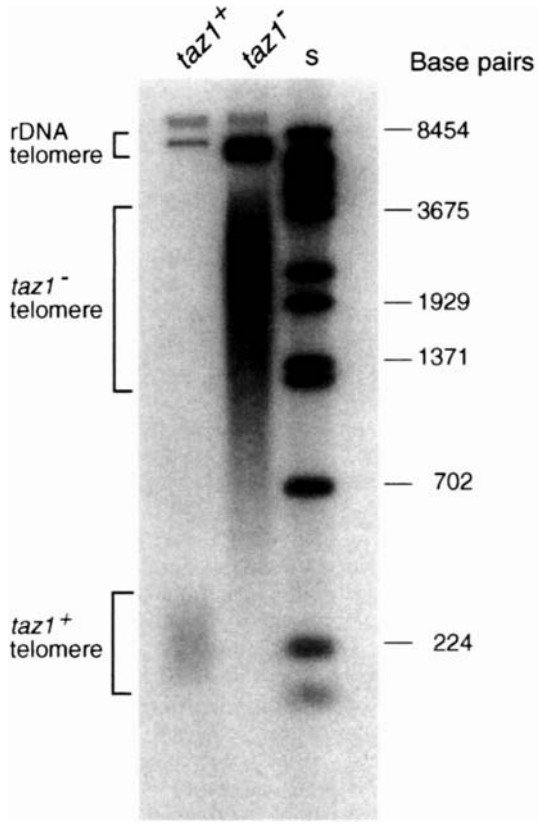

Figure 3 Elongated telomeres in *taz1*$^-$ strains. Southern blot of genomic DNA digested with *ApaI*; *taz1*$^+$ denotes strain CF11 containing the intact *taz1*$^+$ gene; *taz1*$^-$ denotes a strain of the same genotype as CF11 with the exception of the *taz1*$^-$ disruption. Ethidium bromide staining confirmed that approximately equal quantities of DNA were loaded in these two lanes. S, *Bst*EII digest of bacteriophage lambda DNA. Identical results were obtained when *taz1*$^+$ was disrupted or deleted in other strains.

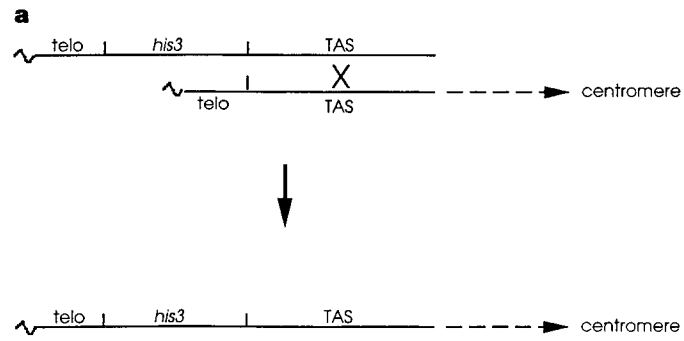

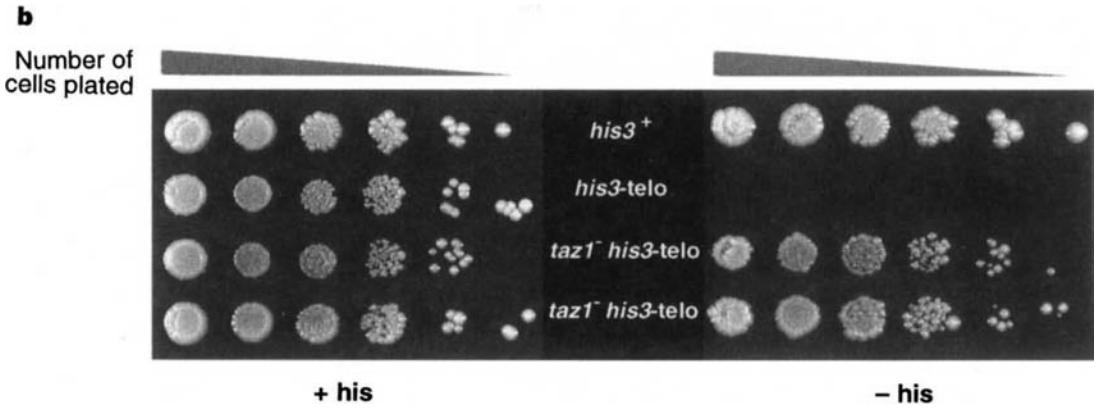

Figure 4 Alleviation of the telomere position effect in *taz1*$^-$ cells. **a**, Construction of the *his3*-telo reporter strain. A fragment containing the *his3*$^+$ gene cloned between TAS and telomere repeat sequences was transformed into a *his3*$^-$ *lot1*$^-$ strain; *lot1*$^-$ allows expression of telomere-adjacent genes (E.R.N. and R.C.A., unpublished data). Chromosome breakage in the TAS region generated the *his3*-telo strain, which was verified by Southern blot analysis and pulsed-field gel electrophoresis (data not shown). **b**, Derepression of expression of the telomeric *his3* gene upon *taz1* disruption. Tenfold serial dilutions of overnight cultures of the strains indicated were spotted onto plates either containing (+ his) or lacking (− his) histidine.

of longer telomeres, *taz1*$^-$ cells thrive for many generations, even after extensive subculturing.

The large and immediate increase in the number of telomeric DNA repeats when *taz1*$^+$ was disrupted or deleted suggests possible functions for the protein. (1) Taz1p might act as a negative regulator of telomerase. For example, Taz1p might bind directly or indirectly to the telomerase enzyme to inhibit its processivity, or it might limit the accessibility of telomerase to telomeric DNA. In support of this latter possibility, we have characterized a discrete non-nucleosomal chromatin structure at the telomeres of fission yeast, and observed the disruption of this structure in *taz1*$^-$ cells (J.P.C. and T.R.C., manuscript in preparation). (2) All *taz1*$^-$ cells might immediately activate some telomerase-independent, recombination-based mechanism of telomere repeat synthesis; such pathways have previously been observed as rare events in populations of yeast undergoing senescence[24].

In *S. cerevisiae* and *S. pombe*, genes that are transcriptionally active when located internally become subject to reversible transcriptional repression when placed adjacent to a telomere[25,26]. To test the involvement of Taz1p in telomeric repression, we used *S. pombe* strain FY1778, in which the endogenous *his3*$^+$ gene was deleted and cloned adjacent to a chromosomal telomere (Fig. 4a). The *his3*$^+$ gene in the resulting *his3*-telo strain is repressed to the extent that it gives an ~200,000-fold reduction in the number of colonies that grow on plates lacking histidine (Fig. 4b). In marked contrast, *his3*-telo cells in which *taz1*$^+$ has been disrupted grow equally well on plates containing or lacking histidine. Thus disruption of *taz1*$^+$ in *his3*-telo cells leads to nearly complete derepression of the telomeric *his3* gene.

The reduction in telomeric repression seen in *taz1*$^-$ cells could result from either the absence of *taz1*$^+$ or the increased length of *taz1*$^-$ telomeres, which might be expected to widen the distance between a telomere-adjacent gene and the protein complex that would repress its transcription. In support of the former, disruption of telomeric chromatin structure in *taz1* mutants (J.P.C. and T.R.C., manuscript in preparation) suggests that such repressive telomeric complexes may be absent or defective. In addition, when *taz1*$^+$ and *taz1*$^-$ haploids mate, telomeres remain longer than normal (~800 bp) for many (>130) generations, although the telomere position effect is quickly restored. Thus we think it likely that Taz1p is involved in establishing or maintaining a telosome structure that is required for telomere position effect.

The effect of *taz1* disruption on transcription appears to be analogous to that observed for a mutant of the *S. cerevisiae* Rap1 protein (*rap1-17*) in that *rap1*-17 cells exhibit both telomere lengthening and derepression of telomere-adjacent transcription[27].

Although vegetative growth of *taz1*$^-$ cells is normal, sexual reproduction is aberrant. Mating mixtures of homothallic *taz1*$^+$ cells (Fig. 5, left) contained normal haploid and diploid cells, as well as numerous asci in which meiosis and sporulation had occurred (filled arrows in Fig. 5, left); these asci usually contained four clearly visible, round spores. In contrast, mating mixtures in which *taz1* had been disrupted (*taz1::ura4* × *taz1::ura4*) or deleted were markedly deficient in healthy-looking asci. Most *taz1*$^-$ asci contained fewer than four distinct spores (open arrows in Fig. 5, right), which were often shaped aberrantly. Occasionally, *taz1*$^-$ asci contained four spores of normal appearance (filled arrow in Fig. 5, right), and some cells in the *taz1*$^+$ mixture may have corresponded to aberrant asci. Of the spores that did form in *taz1*$^-$ homozygous crosses, spore viability was only ~5% of that measured for *taz1*$^+$ crosses. Thus Taz1p is required for either efficient meiosis or sporulation. Telomeres may be important for meiotic processes, as telomeres mediate the attachment of chromosomes to spindle pole bodies and lead chromosome movement during the premiotic phase in *S. pombe*[28]. It is tempting to speculate that Taz1p may be involved in the interactions between chromosomes and spindle proteins, and that disruption of these interactions leads to defective meiosis.

The sequence specificity displayed by Taz1p in one-hybrid experiments and the presence of a known telomere DNA-binding motif,

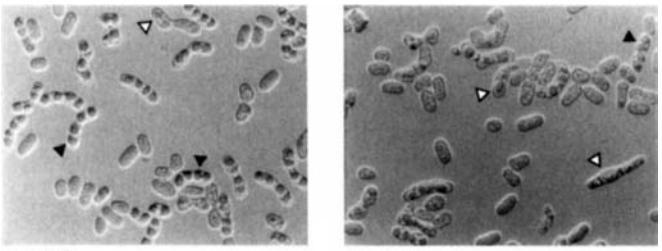

Figure 5 Meiosis/sporulation defect in *taz1*⁻ cells. The *taz1*⁺ gene was disrupted in strain FY1778, which is of the h^{90} homothallic (switchable) mating type. Nomarski images of homozygous *taz1*⁺ and *taz1*⁻ crosses after 3 days of incubation at 30 °C on malt-extract plates. Filled arrowheads indicate asci containing four distinct spores; open arrowheads indicate aberrant asci.

the Myb domain, suggest that Taz1p is recruited to telomeres by direct DNA binding. The many roles of Taz1p may be mediated either by modulating the conformation of telomeric DNA and its accessibility to other proteins, or by recruiting additional proteins to telomeres. For example, the striking increase in telomere length seen in *taz1*⁻ cells could be explained if Taz1p normally limits the accessibility of telomerase to its DNA substrate. The existence of such inhibitory regulation of telomerase has been predicted from studies of the budding yeast *Kluyveromyces lactis*[29]. The Rap1 protein is a likely candidate for such an inhibitory protein in budding yeasts. The functional homology between Rap1p and Taz1p also extends to their effects on telomere-adjacent transcriptional repression. This conservation of function between proteins that do not share sequence homology, and that come from two evolutionarily distant organisms, suggests that proteins with similar functional repertoires will be found in other eukaryotes.

The homology displayed by Taz1p to the Myb DNA-binding domain of the human TRF protein suggests that these proteins are also related. The relative ease with which functions can be dissected in *S. pombe* may help illuminate the functions of this whole class of proteins. If hTRF plays a role similar to that of Taz1p in telomere-length regulation, it may provide one of the missing links in the interplay between telomerase activity, telomere length and tumorigenesis. □

Methods

S. pombe strains and manipulations. The strains CF11 (h^- *ade6-M210 leu1-32 ura4-D18*), CF14 (h^+ *ade-M216 leu1-32 ura4-D18*) and FY1778 (h^{90} *ura4-D18 his3-D1 ade6-M210 leu1-32 his3-telo*) were grown in YES or EMMG media[15] with required supplements. The construct for *taz1* gene disruption was made by ligating polymerase chain reaction (PCR) fragments corresponding to base pairs 43–768 and 1151–2143 of *taz1*⁺ to either side of the *ura4*-containing *Eco*RI–*Bam*HI fragment of pSPORT-URA (provided by R. West). The construct for complete *taz1* deletion used a PCR fragment corresponding to base pairs −942 to +9 of the *taz1*⁺ open reading frame as the upstream complementary sequence. Disruption and deletion of *taz1* were performed in CF11 × CD14 diploids and confirmed by PCR. Details of construction of the FY1778 *his*-telo strain will be described elsewhere (E.R.N. and R.C.A., unpublished data). Disruption of *taz1*⁺ in FY1778 was as described above. Spore viability was measured by random spore analysis[15].

One-hybrid screen. A 32-mer of telomeric sequence (Fig. 1b, top sequence) was cloned into the unique *Bgl*II site of pB*gl-lacZ*[18], the resulting plasmid was linearized by digestion with *Stu*I and transformed into *S. cerevisiae* GGY1 (*MATalpha Δgal4 Δgal80 ura3 leu2 his3 ade2 tyr25*) to generate the reporter strain (both pB*gl-lacZ* and strain GGY1 were provided by J. Li). The *S. pombe* matchmaker cDNA library (Clontech; 1.3×10^7 independent clones with 90% containing inserts, average insert size 1.3 kb) was amplified on Luria broth plates and transformed into the reporter strain. All *S. cerevisiae* transformations were by dimethyl sulphoxide-enhanced whole-cell yeast transformation. After 3–4 days of growth on SC-leu plates, X-gal colony filter assays were performed as described in the Clontech manual. Dideoxy sequencing was performed according to standard procedures.

Measurements of telomere length. Genomic *S. pombe* DNA was prepared by a glass-bead lysis method, digested with *Apa*I, resolved on 1% agarose gels, transferred to nylon (Duralon) membranes and hybridized at 45°C to ^{32}P end-labelled telomeric oligonucleotides (Fig. 1b).

Received 28 August 1996; accepted 23 January 1997

1. Blackburn, E. H. & Greider, C. W. *Telomeres* (Cold Spring Harbor Laboratory Press, New York, 1995).
2. Zakian, V. A. *Science* **270,** 1601–1607 (1995).
3. Greider, C. W. & Blackburn, E. H. *Cell* **43,** 405–413 (1985).
4. Singer, M. S. & Gottschling, D. E. *Science* **266,** 404–409 (1994).
5. Lingner, J., Cooper, J. P. & Cech, T. R. *Science* **269,** 1533–1534 (1995).
6. Kim, N. W. *et al. Science* **266,** 2011–2015 (1994).
7. Broccoli, D., Young, J. W. & de Lange, T. *Proc. Natl Acad. Sci. USA* **92,** 9082–9086 (1995).
8. Bryan, T. M., Englezou, A., Gupta, J., Bacchetti, S. & Reddel, R. R. *EMBO J.* **14,** 4240–4248 (1995).
9. Conrad, M. N., Wright, J. H., Wolf, A. J. & Zakian, V. A. *Cell* **63,** 739–750 (1990).
10. Lustig, A. J., Kurtz, S. & Shore, D. *Science* **250,** 549–553 (1990).
11. Sussel, L. & Shore, D. *Proc. Natl Acad. Sci. USA* **88,** 7749–7753 (1991).
12. Kyrion, G., Boakye, K. A. & Lustig, A. J. *Mol. Cell. Biol.* **12,** 5159–5173 (1992).
13. Zhong, Z., Shiue, L., Kaplan, S. & de Lange, T. *Mol. Cell. Biol.* **12,** 4834–4843 (1992).
14. Chong, L. *et al. Science* **270,** 1663–1667 (1995).
15. Moreno, S., Klar, A. J. S. & Nurse, P. *Methods Enzymol.* **194,** 795–823 (1991).
16. Clarke, L. *Trends Genet.* **6,** 150–154 (1990).
17. Allshire, R. C. *Semin. Cell Biol.* **6,** 55–64 (1995).
18. Li, J. J. & Herskowitz, I. *Science* **262,** 1870–1874 (1993).
19. Sugawara, N. *thesis,* Harvard Univ. (1989).
20. Bilaud, T. *et al. Nucleic Acids Res.* **24,** 1294–1303 (1996).
21. Liu, Z. & Tye, B. K. *Genes Dev.* **5,** 49–59 (1990).
22. Louis, E. J., Naumova, E. S., Lee, A., Naumov, G. & Haber, J. E. *Genetics* **136,** 789–802 (1994).
23. König, P., Giraldo, R., Chapman, L. & Rhodes, D. *Cell* **85,** 125–136 (1996).
24. Lundblad, V. & Blackburn, E. H. *Cell* **73,** 347–360 (1993).
25. Gottschling, D. E., Aparicio, O. M., Billington, B. L. & Zakian, V. A. *Cell* **63,** 751–762 (1990).
26. Nimmo, E. R., Cranston, G. & Allshire, R. C. *EMBO J.* **13,** 3801–3811 (1994).
27. Kyrion, G., Liu, K., Liu, C. & Lustig, A. J. *Genes Dev.* **7,** 1146–1159 (1993).
28. Chikashige, Y. *et al. Science* **264,** 270–273 (1994).
29. McEachern, M. J. & Blackburn, E. H. *Nature* **376,** 403–409 (1995).
30. Hoheisel, J. D. *et al. Cell* **73,** 109–120 (1993).

Acknowledgements. We thank J. Lingner for suggestions, including the use of a one-hybrid screen; and T. Nakamura for discussions and help with protein sequence analysis; C. Chapon, G. Fang, J. Hayles, J. Mata, L. Pillus, E. Stone, Y. Watanabe and R. West for discussions; P. Nurse for advice on making gene disruptions; J. Li, N. Sugawara and R. West for plasmids and strains; and B. Boswell for help with microscopy. J.P.C. is grateful for the initial stimulus provided by T. Chappell, P. Young and the 1994 Cold Spring Harbor Fission Yeast Course. Research on fission yeast telomeres at the MRC HGU is supported by a grant from the Cancer Research Campaign to R.C.A. J.P.C. was an associate and T.R.C. is an investigator of the Howard Hughes Medical Institute.

Correspondence and requests for materials should be addressed to T.R.C. (e-mail: thomas.cech@colorado.edu). The sequence for *taz1* has been deposited in the EMBL database, accession no Y09406.

Notes for contributors

Nature is a weekly international journal covering all the sciences. Its readership is interdisciplinary, so manuscripts should be written clearly and simply, authors remembering that English is not the first language of many readers. Competition for *Nature*'s limited space is severe, so brevity is essential. *Nature*'s main formats for original research are Articles and Letters to Nature. Lengths of these contributions are specified in terms of numbers of pages they take up. An uninterrupted page of text contains about 1,300 words, so a typical Letter to Nature, occupying 2 1/2 pages, can contain about 1,500 words of text and four modest-sized display items (figures and/or tables) with brief legends. There are no formal limits on the number of display items, but extra items must be accompanied by commensurate reductions in the length of the text. Length limits can, however, be varied at the editors' discretion.

Articles are reports of original scientific research whose conclusions represent a substantial advance in understanding of an important problem and are of broad general interest. They do not generally exceed 5 pages of *Nature* and have no more than 50 references. They have a 'heading' of up to 80 words, often rewritten by *Nature*'s editors, which advertises the content of the paper in general terms and which should not contain numbers, abbreviations or measurements unless central to the message of the paper. The first three or four paragraphs of the main text should introduce and summarize the findings. Articles have a few subheadings of not more than 45 characters each.

Letters to Nature are short reports of original research focused on an outstanding finding with implications of interest to nonspecialists. They should not generally exceed 2 1/2 pages of *Nature*. They have a bold first paragraph of fewer than 180 words summarizing the background, rationale, conclusion and main implication of the work, aimed particularly at nonspecialist readers. Letters should have no more than 30 references.

Preparation of Articles and Letters

All manuscripts should be in English, typed double-spaced on one side of the paper only. Manuscripts (and revised manuscripts) should not be submitted in electronic form.

Manuscripts should be accompanied by two copies of a brief covering letter from the corresponding author, containing a full postal address, telephone and fax numbers, and e-mail address. Articles and Letters contain a statement at the end of the text: "Correspondence and requests for materials to xxxxx", with an e-mail address if desired, followed by the accession numbers or Web site address for supporting datasets. The designated author need not be the senior author, but *Nature* will expect this author to handle matters arising from the published contribution.

Five copies of manuscripts (and revised manuscripts) and figures are required. Each copy of a revised manuscript should be accompanied by a copy of the author's response to referees' and editors' comments on the earlier version. Two copies of relevant papers by any of the authors submitted or in press elsewhere (including papers submitted elsewhere while the *Nature* manuscript is under consideration) should also be enclosed, clearly marked as such; failure to do so may prejudice consideration of the manuscript.

Titles should not exceed three lines of 28 characters each (including spaces), and should avoid numerical values, acronyms, abbreviations and punctuation wherever possible.

References should be numbered sequentially as they appear in the text, tables and figure legends. Titles of all cited articles should be provided. Only papers that have been published or submitted to a named journal should be in the reference list: manuscripts in preparation and personal communications should be mentioned in the text with a list of authors. Published conference abstracts may be included in the reference list, but text, footnotes, grant details and acknowledgements may not.

Acknowledgements must be brief and appear after the reference list. *Nature* does not publish grant or contribution numbers.

Tables should each be presented on a separate sheet of paper. Symbols and abbreviations should be defined immediately below the table, followed by essential descriptive material, all in double-spaced text.

Figures should not be larger than 22 by 28 cm unless unavoidable, and should not contain more than one panel unless the assembled parts are logically connected. Each copy should be marked with the corresponding author's name and, when known, the manuscript reference number. One photocopy of original figures should be provided. All original figures are returned when *Nature* cannot offer to publish a manuscript, but one copy of the manuscript and the photocopy of the figures are kept in confidential files. Colour figures are welcome, but a contribution towards the cost of reproduction is requested. Inability to pay this charge will not prevent *Nature* from publishing figures for which colour is essential. Once a paper is accepted for publication, electronic versions of figures are preferred.

Methods. Brief details of materials and methods can be given in the text. Otherwise, they should be described at the end of the text in a section entitled "Methods", subdivided by short, bold headings referring to the methods used. This section should not exceed 800 words and ideally should be shorter. In contributions with methods sections, figure legends should not exceed 100 words each, and should be confined to a description of the figure and the symbols used.

Materials. As a condition of publication, authors are required to make materials and methods used freely available to academic researchers for their own use. Supporting datasets must be made available by the authors both directly and by posting on *Nature*'s Web site, by deposition in the appropriate public database or by distribution on the Internet.

Submissions. Manuscripts can be submitted to the Editor at *Nature*, Porters South, 4 Crinan St, London N1 9XW or at *Nature*, 968 National Press Building, Washington, DC 20045-1938. Proofs should be returned by express mail to London. Fax numbers and e-mail addresses for all editorial offices are on *Nature*'s information page.

Presubmission enquiries for Articles and Letters should be made by e-mail to nature@nature.com, clearly labelled as such. They should include a fully referenced summary paragraph in *Nature* format, and be accompanied by a paragraph stating briefly why the submission will be of interest to a broad general scientific readership. Authors will usually receive a response within two working days of receipt.

Material submitted to *Nature* must not be discussed with the media. Accepted contributions may be discussed with the media a week before the publication date under *Nature*'s embargo conditions.(See *Nature* **383**, 745; 1996 for further explanation.)

Other contributions

Nature publishes other contributed material as follows:

Correspondence contributions are short comments on topical issues, anecdotal material or reactions of readers to non-technical material published in *Nature*. All are unsolicited; submissions by e-mail to corres@nature.com are preferred (accents should be clearly indicated).

Commentary articles are informal editorials on topical issues of public interest that have some bearing on scientific research. They are often controversial. Unsolicited manuscripts are considered, but proposals can be made to the Commentary Editor by e-mail (nature@nature.com).

News and Views articles inform nonspecialist readers about new scientific advances, as reported either in published papers or at scientific meetings. Most are commissioned, but proposals can be made to the News and Views Editor before the paper is published or the meeting takes place. Detailed guidelines are available on request.

Scientific Correspondence contributions are brief reports of general interest, and are usually peer-reviewed. Priority is given to contributions of fewer than 500 words. Detailed guidelines are available on request. Presubmission enquiries are not considered: contributions for Scientific Correspondence should be submitted by mail, not e-mail.

Review Articles survey recent developments in a topical area of research. They should not generally occupy more than 6 pages of *Nature*.

Progress articles are shorter reviews of particularly topical and fast-moving fields. They do not exceed 4 pages of *Nature*.

Contributors wishing to submit a Review Article or Progress should first send an enquiry or a brief synopsis to the Reviews Coordinator, from whom guidelines are available on request.

According to the code

New programs and updates for this software roundup include those that can simulate clinical drug trials, perform computational chemistry functions, image analysis and processing, as well as check scientific spelling.

A visual research tool for custom visual displays

The VSG2/3 visual stimulus generator

From Cambridge Research Systems

A system that creates a variety of both standard and customized visual displays, and drives a variety of monitors

This software controls the VSG2/3, which provides a suite of high-level routines designed specifically for vision science applications and is available for C, Pascal, Delphi and Basic. Turnkey solutions include the company's Psycho contrast sensitivity test, the Cambridge colour test, and Optima, a system for VEP and ERG recording from colour pattern stimuli. These systems run under MS Windows for ease of use and compatibility with analysis and report writing packages. The software is designed to make it as simple as possible to produce commonly used visual stimuli while retaining total flexibility to customize these stimuli and to create entirely new ones. It uses a library of over 200 high-level functions, and in addition to the usual drawing routines supplied with general purpose graphics cards, extra functions are provided for stimuli, such as chessboard and gratings. There are also routines to complement the special hardware features of the VSG2/3, and to handle transparently procedures such as colour–space translations and gamma correction. The company can provide support for well-known commercial PC languages: C, C++, Pascal, Basic, Visual Basic and Delphi. Many stimuli can be displayed using very simple programs, and for extra flexibility, the company can supply full source code so that functions can be added, customized, optimized or even re-compiled. Full Windows DLL support is provided, so a VSG2/3 application can be as simple or sophisticated as needed.

Reader Enquiry No. 100

ACSL BioMed

From MGA Software

Software that is designed to simulate clinical drug trials

Today, researchers are faced with about a stated 50 per cent failure rate of all clinical trials. These failures add to a product's already long time-to-market and high development costs. As a simulation tool that enables the user to design, pre-test and modify study parameters before conducting actual live trials, ACSL BioMed should prove useful for increasing the likelihood of successful trials, and ultimately bring better products to market faster. This program is designed for modelling both small- and large-scale clinical trials, and is said to be powerful enough to simulate any trial design and its proposed PK/PD. The use of an icon format allows the user to drag study parameters into an empty work space using a mouse. The user can then enter parameters into the computer code to set variables, such as sampling method or dosing plan. A pharmacodynamic or pharmacokinetics model can then be chosen to identify the relationship of the drug to the body. The program simulates clinical trials one patient at a time, producing data that would be generated by an actual clinical trial. Statistical analysis is performed on the simulated data, including calculation of power and survival statistics. It also contains a direct link to S-Plus and SAS statistics packages, enabling clinicians to perform exploratory data analysis, generate charts, and graph data.

Reader Enquiry No. 101

Molecular motif

BioCatalysis database software

From Synopsis

A new upgrade to this biomolecular database of catalysts for organic synthesis

Designed to provide up-to-date information on the use of biomolecules as catalysts in organic synthesis, this update includes the release of some 16,500 reactions — with the remaining backlogged data to be released next month. The company has designed this product to maximize information content, while minimizing the overlap and redundancy so often evident in such data collections. It is configured for a number of popular reaction searching systems, including REACCS, ORAC and ISIS. Enhancements for this release include full compatibility with third-party databases in global searches using MDL's IRDAS or RXL-Browser applications. A standalone Accord version of the database is also scheduled for release this year.

Reader Enquiry No. 102

Power Vamp and Power Amber

From Oxford Molecular

Computational chemistry software optimized for Silicon Graphics MIPS R8000 microprocessors

Power Vamp is designed to perform semi-empirical quantum mechanics, allowing scientists to perform more rigorous and computationally intensive calculations than available in previous versions of the software. With this program, it is stated that large molecules can be studied in greater detail and with improved efficiency. This optimized system is based on the R8000 processor and includes a new method for calculating partial charges from the electrostatic potential, an improved solvent model, which takes into account the effect of environmental solvent molecules during the calculation, and a neural networks algorithm for the prediction of ^{13}C shifts. In addition, a mixed quantum mechanics/molecular mechanics model is also available in Vamp, allowing a mixed model to be used in the study of drug molecule–protein binding interactions. Power Amber is also available and is designed to take advantage of the floating point speed of the R8000 CPU and the system's shared memory capacity.

Reader Enquiry No. 103

4D-Draw Professional

From Autoscribe

An advanced drawing program with a module that understands IUPAC nomenclature rules

This program interprets chemical names and automatically creates quality structures in three styles: shorthand, Kekulé and semi-structural formula. It provides a full set of easy-to-use tools for drawing, text editing and labelling. It can be used to create chemistry graphics (structures, reaction schemes, text labels, flow charts and annotations) for reports, papers and presentations. Also supporting a wide range of object transformations, the colour of any objects can be changed and molecules can be rotated interactively in three dimensions. It exports pictures to word-processing programs and supports copyback for editing. The Windows version of the program supports OLE-2 where pictures are dynamically linked. All features of the standard version are included in release 2.1, which can

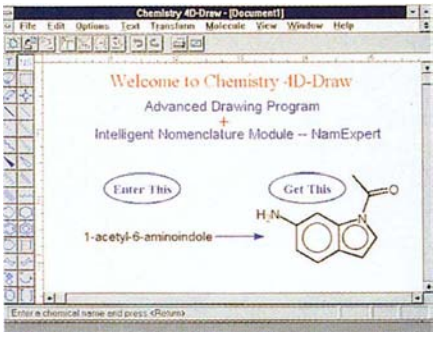

Autoscribe's 4-D Professional Draw program

exchange chemical information with other drawing or molecular modelling programs via MDL's MOL files. It comes with a 'smart' mass calculator that can compute the mass of a selected molecule or an entered formula and allows users to choose isotopes of elements. Users can also export pictures by dragging and dropping.
Reader Enquiry No. 104

WebLab Gene Explorer

From Molecular Simulations

A new computational environment for analysing DNA, protein sequences and protein structures

From restriction analysis to virtual, site-directed mutagenesis, WebLab Gene Explorer is designed to address the computational needs of molecular biology research in a single environment. This software was constructed to benefit biology researchers looking into the function and mechanism of genes. In addition to conventional bioinformatics, this suite of modules provides protein structure modelling and analysis. A highly intuitive interface guides non-experts through unfamiliar areas, simplifying a technology that often crosses the boundaries between scientific disciplines. Researchers can use Gene Explorer on PCs or Macintoshes, using only a Web browser, such as Netscape Navigator or Microsoft Explorer.
Reader Enquiry No. 105

ADVERTISEMENT

Gramsch Laboratories

- Fast *Peptide Synthesis*: weekend setup:
- 25 µmoles: 10 AA DM 650.00; 15 AA
- DM 730.00; 20 AA DM 780.00
- you will see the HPLC profile before you order
- *Antiserum Production* Service:
Package : DM 2100.00 (Peptide/Conjug./Serum)
New Antisera:
Rab 4/ 5a/ 7 ; G-Protein subunit : α; β; γ
Nociceptin,Hum,Mouse,Rat Somatost.Rec.
1/2A/2B/3/4/5

Distributor for Japan: *FUNAKOSHI CO. Tokio 113*

Phone 08138 1769 or 08131 5679-0
Fax 08138 1260 or 08131 5679-24
Gramsch Laboratories
D-85247 SCHWABHAUSEN, Germany

READER ENQUIRY NO. 91

Wisconsin Package 9.0

From Genetics Computer Group

A comprehensive sequence analysis software package

This version includes the release of SeqLab, designed to be an interactive multiple-sequence editor and analysis tool, which can provide convenient project management capabilities. SeqLab displays data as individual residues or as schematic representations of known sequence features — both are useful for visualizing and manipulating alignment. It can integrate third-party programs into its user interface, directly importing sequences in other poplular file formats, such as FastA, GDE and GenBank, and can annotate sequences based on comparison or analysis. SeqLab provides the user with a 'friendly' interface to about 100 of the company's programs, including database searches (BLAST and FastA), and reference, motif and pattern searches. The major sequence databases are also included with the package (GenBank, EMBL, PIR and Swiss-PROT).
Reader Enquiry No. 106

From Magic Works

A new DNA, RNA and protein sequence editing and analysis tool

This software features a newly designed sequence database retrieval system called the Magic Works artificial neural network. This retrieval system uses similarity searches that are based on artificial intelligence techniques, according to the manufacturer. The editor is fully graphical, providing clear views of DNA, RNA and protein sequences with colour-coded annotation symbols and text. BlueGene provides online analysis to locate restriction sites, open reading frames and to provide more graphical overviews of DNA/RNA and protein sequences, which can be displayed by linear or circular sequence maps. A demonstration version is available at *www.bluegene.com.*
Reader Enquiry No. 107

Image analysis

Image-Pro Plus 3.0

From Media Cybernetics

Image analysis software that includes Internet support

Media Cybernetics has announced the release of Image-Pro Plus 3.0 for Windows 3.1, 95 and NT. Version 3.0 is packed with new functions making it a more robust image analysis software package. In response to the growing use of Internet technology the program provides full Internet support for E-mail, Internet relay chat and FTP protocols. Users can compose

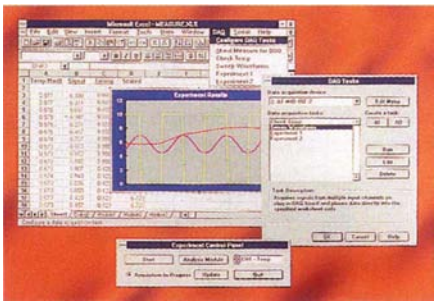

Image-Pro Plus 3.0 with Internet support

and send E-mail messages and images to any location from directly within the Image-Pro application. In addition, the software contains a new report generator, which allows users to create custom formatted reports with images, data and text. Reports can be easily exported to other applications and to spreadsheet programs. An updated and fully featured database has been added, providing the functionality needed to acquire, organize, retrieve and send images. Images can be easily located through keyword searches, image folders, thumbnail gallery or custom fields. The database allows users to print full-size images or a gallery of images. Other features have also been added, including a new 'sequencer' that allows users to acquire and playback sequences of images, intuitive colour segmentation tools, improved filter dialogues and tools that allow users to preview and adjust filters before applying.
Reader Enquiry No. 108

Ultimage for Windows

From Graftek Imaging

A complete image processing and analysis tool developed with LabView 3.1 and the new LabView application builder

Ultimage, which has worked with LabView for the Macintosh for several years, was designed for scientists and researchers in chemistry, the life sciences and biotechnology who need a comprehensive point-and-click image processing program that can handle input, output and processing needs. It features a comprehensive range of algorithms, an assortment of tools for contour detection and object marking, as well as a comprehensive library of more than 400

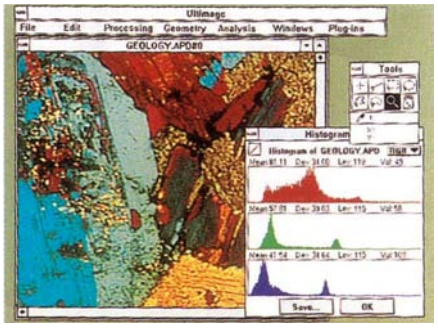

Ultimage image processing and analysis tool

image-acquisition, enhancement and display functions, handling 1-, 8-, 16-, 24- and 32-bit images in a variety of file formats. Ultimage is well suited for morphology applications and a variety of particle-detection, measurement and analysis tasks. It can handle more than 60 shape and density measurements for each object recognized. The software also includes many common imaging functions, such as convolution and nonlinear filters, geometrical transforms, thresholding and colour space conversions. In addition, it can produce statistical reports and charts, and can export results to spreadsheets or other applications. User extensions are written in the LabView graphical programming environment and/or Graftek's Concept Vi, an image processing library for LabView. When these extensions are placed in the proper directory, the modules automatically appear in the pull-down menus.

Reader Enquiry No. 109

IPLab Spectrum 3.1

From Signal Analytics Scientific

Imaging and analysis software that supports the manipulation and analysis of colour images

IPLab Spectrum is now bundled with all its acquisition modules to support a variety of cameras and frame grabbers. The program now allows users to adjust directly the contrast, brightness and 'whiteness' of colour images. A new command in this version lets users directly segment colour images, which may greatly increase productivity in applications such as histology and fluorescence microscopy where objects of interest can be distinguished from the background based only on their colour differences. In addition, users can now read and process 48-bit colour images that come from high-performance scanners, such as the Arcus II from Agfa. The system can now print images at any resolution and size supported by a user's printer. When used in combination with the latest colour printers, this feature allows users to create vivid, high-resolution colour prints of the images seen through the microscope. For users who want to create movies of their time-lapse image sequences, this new version provides enhanced support for creating long QuickTime movies. The program can now perform particle analysis or FFTs (fast Fourier transforms) in the background while capturing images at up to five frames per second. Once the image capture is complete, a new particle classification feature lets users create a colour-coded image that shows how each particle is classified according to any of the measurement criteria. New modules directly control a variety of devices including cameras, frame grabbers and scanners. What is more, these will be placed on the company's worldwide web site

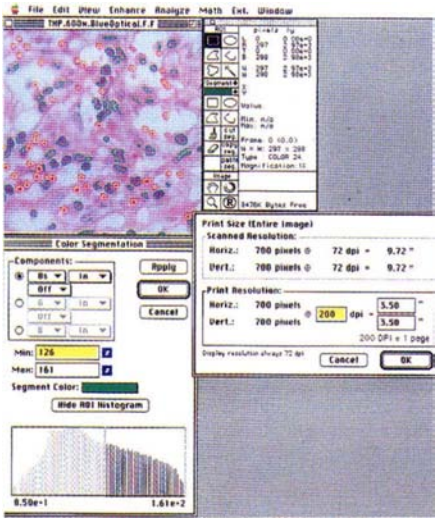

IPLab Spectrum for colour image analysis

(*www.iplab.com/sac*) so users can have access to the latest features in image acquisition.

Reader Enquiry No. 110

Optimas 6

From Optimas

Image analysis software that takes advantage of Pentium processors and Windows 95

This system is stated to run 30–40 per cent faster than the previous version, using 32-bit architecture and PCI-bus frame grabbers on Pentium machines running Windows95. According to the manufacturer, it offers increased accuracy achieved with a set of calibration tools and a flexible range of data sampling options. Some 400 functions can be selected as standard for image processing, measuring, counting and sorting. The new software also simplifies the management of multiple images, views and measurements. Custom interface development tools allow dialogue boxes to be drawn in all resources and can be linked to any system function. A new tool bar enables user-defined image analysis routines to be rapidly selected though a point-and-click icon. The system will run with other development environments, such as Visual Basic, Visual C++ and Delphi. Data can be run out to user-defined reports or exported for further analysis into an Excel spreadsheet, ASCII data file or a custom report created using Visual Basic.

Reader Enquiry No. 111

Maths and statistics

MatLab 5.0

From The MathWorks

An open-environment technical computation program for engineers, scientists and mathematicians

Previously, technical professionals had to choose between maths software packages and general-purpose programming languages, states the manufacturer. MatLab 5.0 provides a single, integrated environment for complex data analysis, visualization, modelling, simulation and large-scale application development and deployment. In the previous release, this program combined tools for numeric and symbolic computation, graphics and visualization, simulation, algorithm prototyping and application development. Building on this foundation, the system's new features include: a suite of tools for application development, including an interactive graphical user interface (GUI) builder, a browser-based function reference and visual editor/debugger, support for multi-dimensional arrays and user-definable data structures. The language enhancements, include object-oriented function overloading, faster and more realistic visualization, updated ODE solvers for stiff equations and expanded sparse-matrix support. It can be used to develop algorithms and applications. New tools, such as graphical user interface development environment (GUIDE), provide a set of graphical tools for designing, constructing and testing interfaces interactively. The visual debugger enables real-time monitoring and debugging of programs. New visualization features include realistic three-dimensional object display, lighting and shading, perspective viewing and true-colour support, which enable users to display more detailed information in a single display. According to the manufacturer, speed improvements of up to a stated 100 times can be realized with the implementation of the new z-buffer algorithm.

Reader Enquiry No. 112

SigmaPlot 4.0 for Windows

From SPSS

A graphical tool that offers scientists and engineers greater flexibility for creating exact technical graphs

This release of SigmaPlot 4.0 for Windows is a flexible graphing tool that can create

ADVERTISEMENT

NEWCASTLE UNIVERSITY
MOLECULAR BIOLOGY UNIT

PROTEIN SEQUENCING

Membrane-bound, solid or solution samples

£12 per cycle

5 cycles minimum - no set up charge

For further information contact Dr. Joe Gray
Phone: +44 191 222 8612
Fax: +44 191 222 8129
Email: JOE.GRAY@newcastle.ac.uk

READER ENQUIRY NO. 69

exact technical graphs for publication. New features include the Regression Wizard with several powerful new graph types and the ability to export to graphic file formats. This feature is said to fit nearly any curve and automatically graphs the results. It allows the program to fit one of over 100 built-in, graphically illustrated equations, as well as the user's own equations. Users should save time using this feature as it provides the equation, determines the initial parameters automatically and creates the resulting graph. The program also offers new graph types: ternary (triangle) plots, time-series graphs, bubble plots and transparent, three-dimensional meshes. SigmaPlot users can export graphs as EPS, TIFF, WMF, BMP and JPEG file formats. Furthermore, these files can be used to create presentation-quality slides, to further customize graphs in drawing packages, to collaborate with graphic artists on Macintosh systems or to allow transmission of graphs to publishers more easily. Users can also use their graphs on the worldwide web with the new JPEG file formats.
Reader Enquiry No. 113

Biotech laboratory

Windmill 4.3 interface software

From Windmill

This version interfaces laboratory instruments to the user's personal computer

Most intruments with a RS232 port can be connected to a personal computer running this software, for example. One Windmill system can handle bar-code readers, chromatographs, gas monitors and weather stations. Its programs include logging, charting, process mimics, alarm monitoring and sequence control. It is said pass data easily to other off-the-shelf Windows programs in real time, so that third-party applications can be integrated seamlessly. There is no programming required with this system. Moreover, it logs data to disk at up to 200 samples per second, handling over 100 input and output channels. Readings are automatically converted to the units chosen by the user. The system also accepts Ethernet, GPIB, Modbus and RS485 linkages. Moreover, it should save libraries of hardware setup files, thus allowing different test and analysis configurations to be quickly restored. According to the manufacturer, the Windows NT software offers added security and reliability over Windows 3.1 and 95 versions with built-in data protection and features that prevent inadvertent or deliberate tampering. The comprehensive security system means users can only access areas specified by the administrator. A record is kept of each user's time on the computer, and exactly which files they used in each session. At regular intervals, Windows NT can automatically create back-up files on tape. The program also supports several types of networks, including Microsoft, Novell and TCP/IP — one operator can therefore access data at any location.
Reader Enquiry No. 114

Shiva process software

From BIA

Control, monitoring and optimization system for biotechnology processes

This system includes a data acquisition module and Microsoft-compatible control software that has been designed for pharmaceutical and chemical research, as well as small-scale production facilities. Intended for use with a variety of bioreactors and shakers, this network-compatible software allows a maximum of 12 channels, which permits the acquisition of data from sensors and custom-built microtransmitters, such as temperature, pH, Rx, pO_2 and pCO_2. Communication with analytical equipment, such as HPLC, GC and FIA can be established. Moreover, the measured data can be analysed in real time, while simultaneously introducing calculated variables and mathematical procedures, such as smoothing and derivation.
Reader Enquiry No. 115

Odds and ends

Densitometry software

From Seescan

Densitometry macroautoradiography software designed specifically for autoradiographers

This program should provide users with rapid and accurate image analysis from direct imaging systems, including Biospace, Fuji and Molecular Dynamics. It allows image calibration and enhancement from a full range of easy-to-use menus, as well as a variety of printing options and a facility with a full audit trail for good laboratory practice compliance. The software runs on Windows 95 and NT and is backed by full technical support and a continuous upgrade programme.
Reader Enquiry No. 116

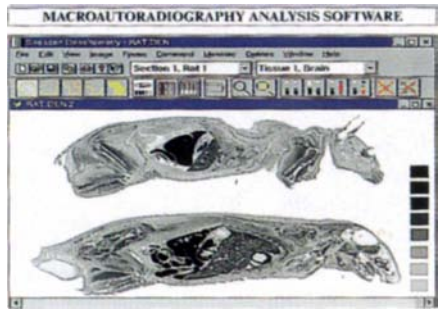

Seescan's macroautoradiograph software

InWords and SciWords

From Inso

Spelling add-ons geared for word processors and scientists using Microsoft Office, Lotus SmartSuite and Word Perfect

InWords is an updated general English dictionary and SciWords is a scientific dictionary for the fields of biology, agriculture, chemistry, environmental science, technology and biochemistry. These dictionaries increase the accuracy of spell checking by enhancing existing dictionaries with up-to-date words or with specialized technical terms. Inso provides multilingual software products and proofing solutions, and supplies technology for use with PC computers.
Reader Enquiry No. 117 □

These notes are compiled by Brendan Horton from information provided by the manufacturers. For more details, fill in the reader service card bound inside the journal.

ADVERTISEMENTS

DNA PEPTIDES
89¢ per base — Deprotected and Desalted 5-10 OD
$15 per residue — Quantity 15 to 40 mg
NEW! DNA Markers
Some Restrictions May Apply. Please Call.
GENEMED SYNTHESIS
1129 Grandview Drive
South San Francisco, CA USA
(800) 344-5337 • Fax (415) 952-9540
E-Mail: Genemed@ix.netcom.com
READER ENQUIRY NO. 90

Check out our homepage at http://www.resgen.com
BACs
YACs
PACs
cDNAs
Research Genetics provides clones and colony membranes for a number of human, mouse, and rat libraries as well as a custom screening service for the libraries.
Research Genetics, Inc.
U.S. or Canada 800-533-4363
U.K. 0-800-89-1393
FAX 205-536-9016
READER ENQUIRY NO. 92